

Distribution Agreement

In presenting this thesis or dissertation as a partial fulfillment of the requirements for an advanced degree from Emory University, I hereby grant to Emory University and its agents the non-exclusive license to archive, make accessible, and display my thesis or dissertation in whole or in part in all forms of media, now or hereafter known, including display on the world wide web. I understand that I may select some access restrictions as part of the online submission of this thesis or dissertation. I retain all ownership rights to the copyright of the thesis or dissertation. I also retain the right to use in future works (such as articles or books) all or part of this thesis or dissertation.

Kenneth Desmond

Date

Structure, Dynamics, and Forces of Jammed Systems

By

Kenneth Desmond
Doctor of Philosophy

Physics

Eric R Weeks
Advisor

Keith Berland
Committee Member

Stefan Boettcher
Committee Member

Daniel Goldman
Committee Member

George Hentschel
Committee Member

Accepted:

Lisa A. Tedesco, Ph.D.
Dean of the James T. Laney School of Graduate Studies

Date

Structure, Dynamics, and Forces of Jammed Systems

By

Kenneth Desmond
B.Sc. Rochester Institute of Technology, 2006

Advisor
Eric R Weeks, Ph.D., University of Texas at Austin, 1997

An abstract of
a dissertation submitted to the Faculty of the
James T. Laney School of Graduate Studies of Emory University
in partial fulfillment of the requirements for the degree of
Doctor of Philosophy
in Physics
2012

Abstract

Structure, Dynamics, and Forces of Jammed Systems
By Kenneth Desmond

Soft materials are commonplace in our daily lives and are unique because they behave solid like in some cases and liquid like in other cases. Examples include shaving cream, mayonnaise, peanut butter, toothpaste, cosmetic products, and paint. The solid like response of a soft material can be controlled by the particle concentration. By increasing the particle concentration the system can undergo a jamming transition, where motion of the individual particles becomes increasingly difficult due to crowding effects. This jamming transition can occur in a variety of materials. In this dissertation, we study the jamming transition in three different scenarios: the jamming/glass transition in colloids, influence of boundaries on the jamming point, and the jamming transition of frictionless emulsion droplets.

The first system we study is a concentrated binary colloidal suspension. We use confocal microscopy to directly observe particle motion within dense samples with packing fractions ranging from 0.40-0.59. To study temporal fluctuations we use the dynamic susceptibility χ_4 , and find that the dynamical heterogeneity of the small and larger particles are qualitatively similar with the smaller particles undergoing slightly larger fluctuations relative to their size. The temporal fluctuations give rise to length scales and time scales which grow as the jamming transition is approached, although the form of this growth is ambiguous with respect to power-law or exponential growth.

The second system we study is random packing of disks and spheres within confined geometries. Studies of random close packing have advanced our knowledge about the structure of systems such as liquids, glasses, emulsions, granular media, and amorphous solids. When these systems are confined, their structural properties change. To understand these changes we study random close packing in finite-sized confined systems, in both two and three dimensions. The presence of confining walls significantly lowers the overall maximum area fraction (or volume fraction in three dimensions). A simple model is presented which quantifies the reduction in packing due to wall-induced structure. This wall-induced structure decays rapidly away from the wall, with characteristic length scales comparable to the small particle diameter.

The final system we explore is a new quasi-two-dimensional model system we have developed to probe the jamming transition. Our system consists of confining oil-in-water emulsion droplets between two parallel plates, so that the droplets are squeezed into quasi-two dimensional disks, analogous to granular photoelastic disks. These droplets have no static friction and are highly deformable. To quantify the internal forces in our experiments, we present an experimental protocol to determine the force law for droplets in contact. We use our model system to characterize various critical scaling phenomena associated with the jamming transition and the force chain network. We also flow our quasi-2D emulsions in a flow geometry analogous to pure shear to better understand the microscopic events and stress relaxations within jammed materials.

Structure, Dynamics, and Forces of Jammed Systems

By

Kenneth Desmond
B.Sc. Rochester Institute of Technology, 2006

Advisor: Eric R Weeks, Ph.D., University of Texas at Austin, 1997

A dissertation submitted to the Faculty of the
James T. Laney School of Graduate Studies of Emory University
in partial fulfillment of the requirements for the degree of
Doctor of Philosophy
in Physics
2012

Structure, Dynamics, and Forces of Jammed Systems

Kenneth W. Desmond

April 9, 2012

Acknowledgements

I thank my advisor Eric R Weeks for his invaluable advice and guidance, and I thank my committee for their support over the years. I would like to express my appreciation to all those that I have interacted with over the years in and outside the research lab (Vikram Prasad, Gianguido Cianci, Umberto Villa, Gary Hunter, Kazem Edmond, James Sebel, Dandan Chen, Xia Hong, and Scott Franklin).

A special thanks to my wife Alejandra, who over the years has been very supportive and patient. Her support and advise has been immeasurable towards finishing my degree.

Finally, this research would not have been possible without a research lab and funding. I want to thank NSF-DMR and the Petroleum Research Fund for funding this work, and I would like to thank the physics department and Emory University for their support over the years.

Contents

| | | |
|----------|--|-----------|
| 1 | Introduction | 1 |
| 1.1 | The Jamming Transition | 1 |
| 1.2 | Ideal Glass Transition and Using Colloids as an Experimental Model | 5 |
| 1.3 | Packing and the Influence of Boundaries | 9 |
| 1.4 | The Ideal Jamming Transition at Zero Temperature | 12 |
| 1.5 | Flow of Disordered Matter Near Jamming | 15 |
| 2 | Dynamic Heterogeneity in Colloidal Glasses | 20 |
| 2.1 | Introduction | 20 |
| 2.2 | Binary Sample | 21 |
| 2.3 | Four-Point Susceptibility | 22 |
| 2.4 | Growing Length & Time Scale | 25 |
| 2.5 | Theory and Expected Results | 27 |
| 2.6 | Comparing Results to Theory | 30 |
| 2.7 | Conclusion | 32 |
| 3 | Packing in Confined Geometries | 33 |
| 3.1 | Introduction | 33 |
| 3.2 | Algorithm | 36 |
| 3.3 | Results on 2D Packing | 41 |
| 3.4 | Results on 3D Packing | 49 |
| 3.5 | Modeling the Effects of Confinement on Volume Fraction | 52 |
| 3.6 | Conclusion | 57 |

| | | |
|----------|---|------------|
| 4 | Imaging and Image Analysis for 2D Experimental Model System | 59 |
| 4.1 | Imaging Droplets | 60 |
| 4.2 | Choosing an Oil Phase and Surfactant | 65 |
| 4.3 | Stitching Images Together | 66 |
| 4.4 | Identifying Droplets and Their Center of Mass | 68 |
| 4.5 | Describing the Perimeter with a Continuous Function | 70 |
| 4.6 | Radical Voronoi Tessellation | 73 |
| 4.7 | Identifying Contacts | 75 |
| 4.8 | Measuring Radius of Curvature | 79 |
| 4.9 | Mean 3D radius of curvature | 83 |
| 5 | Empirical Force Law for 2D Model System | 85 |
| 5.1 | Various Force Laws to be Tested | 86 |
| 5.2 | Adhesion Length l_o | 88 |
| 5.3 | Testing the Quality of an Assumed Force Law | 90 |
| 5.4 | Empirical Force Law for Same Size Droplets in Contact | 94 |
| 5.5 | Empirical Force Law for Different Size Droplets in Contact | 100 |
| 5.6 | Table of Fitting Functions | 103 |
| 6 | Experimental Frictionless 2D Model of Jamming | 107 |
| 6.1 | Introduction | 107 |
| 6.2 | Sample Preparation | 110 |
| 6.3 | Jamming Point | 113 |
| 6.4 | Critical Scaling | 114 |
| 6.5 | Pressure and Effective Force Law for Monodisperse Data | 119 |
| 6.6 | Force Distribution | 122 |
| 6.7 | Force Chains | 123 |
| 6.8 | Conclusions | 131 |
| 7 | Spatial Cooperativity of Stress Relaxation Around Plastic Events in Quasi-Static 2D Flow | 133 |

| | | |
|----------|---|------------|
| 7.1 | Flow Geometry | 134 |
| 7.2 | Droplet-Droplet Forces and Viscous Forces | 136 |
| 7.3 | Determining When Plastic Events Occur | 140 |
| 7.4 | Stress Tensor | 145 |
| 7.5 | Evolution of Stress Around Plastic Event | 147 |
| 7.6 | Conclusion | 151 |
| 8 | Summary | 152 |

List of Figures

| | | |
|------|--|----|
| 2.1 | Percentage of mobile particles | 24 |
| 2.2 | Surface plot of χ_4 | 25 |
| 2.3 | Dynamical susceptibility at various packing fractions | 26 |
| 2.4 | Comparing dynamical heterogeneity between particle sizes | 28 |
| 2.5 | Comparing scaling of dynamical heterogeneity to theory | 29 |
| 3.1 | A flow chart outlining our algorithm for computing <i>rcp</i> configurations. | 37 |
| 3.2 | Images of confined rcp states generated with our algorithm | 38 |
| 3.3 | Finite size effects | 39 |
| 3.4 | 2D System: Area fraction dependence on confinement | 41 |
| 3.5 | 2D System: Number density with distance to the wall at $h = 30$ | 43 |
| 3.6 | 2D System: Image representation of number density with distance to the wall | 44 |
| 3.7 | Rendering of a 2D rcp packing with disks colored by ψ_n | 46 |
| 3.8 | 2D System: Dependence of order parameter with distance to the wall | 48 |
| 3.9 | 3D System: Volume fraction dependence on confinement | 50 |
| 3.10 | 3D System: Number density with distance to the wall at $h = 25$ | 51 |
| 3.11 | 3D System: Image representation of number density with distance to the wall | 52 |
| 3.12 | Illustration of model for the dependence of ϕ_{rcp} on h | 53 |
| 3.13 | Comparing $\phi_{rcp}(h)$ model to data on confinement by two parallel plates | 54 |
| 3.14 | Comparing $\phi_{rcp}(h)$ model to data on confinement by a circular and square boundary | 55 |
| 3.15 | Comparing $\phi_{rcp}(h)$ model to data on confinement by a circular and square boundary | 56 |

| | | |
|------|--|-----|
| 4.1 | Sample chamber for experimental 2D model system | 59 |
| 4.2 | Imaging droplets | 61 |
| 4.3 | Image stitching pattern | 67 |
| 4.4 | A stitched image | 68 |
| 4.5 | Images depicting the steps taken to identify droplets and their centers . . . | 69 |
| 4.6 | Plot of boundary fitted to a Fourier series | 72 |
| 4.7 | Image of boundary fitted to a Fourier series | 72 |
| 4.8 | Radical Voronoi diagram | 74 |
| 4.9 | Identifying if contact exist | 76 |
| 4.10 | Flow chart illustrating how a contact is identified | 77 |
| 4.11 | Droplet-droplet contacts | 80 |
| 4.12 | Measuring radius of curvature | 81 |
| 4.13 | Measurement error in radius of curvature | 82 |
| 4.14 | 3D mean radius of curvature | 83 |
| 5.1 | Incline setup to determine empirical force law | 86 |
| 5.2 | Experimental example demonstrating an adhesive force between droplets . . | 88 |
| 5.3 | Distribution in the adhesion contact lengths | 89 |
| 5.4 | Comparing the quality of different force laws | 95 |
| 5.5 | Variation in contact forces between different force laws | 96 |
| 5.6 | Universal empirical force law for same size droplets | 97 |
| 5.7 | Quality of the empirical force to model the contact forces | 98 |
| 5.8 | Universal empirical force law for different size droplets in contact | 101 |
| 6.1 | Schematic illustrating our method for producing monodisperse droplets . . | 110 |
| 6.2 | Images of three binary samples used to probe the jamming transition | 111 |
| 6.3 | Large field of view image of a binary sample | 112 |
| 6.4 | Computing area fraction in our 2D emulsion system. | 114 |
| 6.5 | Critical scaling in coordination number and pressure | 115 |
| 6.6 | Converting from ϕ_{exp} to ϕ_{theory} | 116 |
| 6.7 | Effective force law for bidisperse sample | 118 |

| | | |
|------|---|-----|
| 6.8 | Effective force law for monodisperse sample | 119 |
| 6.9 | Example illustrating difference in effective force laws | 121 |
| 6.10 | Distribution of contact forces | 122 |
| 6.11 | Definition of force chains | 124 |
| 6.12 | Large image of force chains | 126 |
| 6.13 | Correlation in force chain orientations | 127 |
| 6.14 | Distribution of angle between force chain segments | 129 |
| 6.15 | Distribution in force chain lengths | 130 |
| 7.1 | Schematic of our 2D flow geometry | 135 |
| 7.2 | The three different forces acting on our droplets | 137 |
| 7.3 | Determining the viscous forces between droplets | 139 |
| 7.4 | Defining plastic event | 142 |
| 7.5 | Deformation parameter for plastic event | 143 |
| 7.6 | Duration time of plastic event | 144 |
| 7.7 | Evolution of stress near a plastic event | 148 |
| 7.8 | Stress decay before and after a plastic event | 149 |
| 7.9 | Cooperative length scale for stress relaxation around a plastic event | 150 |

List of Tables

| | | |
|-----|---|-----|
| 2.1 | Fitting coefficients for χ_4 data | 31 |
| 4.1 | Influence of setup on the contact length of hexane droplets | 63 |
| 4.2 | Influence of setup on the contact length of mineral oil droplets | 64 |
| 5.1 | Size of monodisperse droplets | 94 |
| 5.2 | Size of bidisperse droplets | 100 |
| 5.3 | Fitting functions | 106 |
| 6.1 | Size of binary droplets used to probe the jamming transition | 111 |
| 6.2 | Critical scaling fit parameters | 117 |
| 6.3 | Pressure and effective force law scaling parameters for monodisperse data . | 120 |

CHAPTER 1

Introduction

1.1 The Jamming Transition

The familiar three states of matter - gas, liquid, and solid - accurately describe the phases of many materials, and for those that fall under these categories, their phases can be tuned by control parameters like temperature and pressure. By tuning the phase, the structure and mechanical properties of a material can be altered. For instance, in the liquid phase, the molecules are structurally disordered and the material can flow, but in the solid phase the molecules have long range structural order that provides the material with rigidity.

While the familiar three states of matter are adequate for classifying many materials, there are many other materials called soft materials that are more difficult to classify because they share properties common to both liquids and solids. Examples of soft materials are colloids (tiny solid particles suspended in a liquid), emulsions (a mixture of two immiscible liquids), foams (collection of air bubbles), and granular materials (collection of solid particles like sand), and the commonality between these examples is that each material is comprised from a collection of particles (either solid particles or liquid particles). The response of these materials to external stresses consist of a liquid like response (dissipates energy by flowing) and a solid like response (stores energy by internal elastic deformations).

Understanding the mechanical properties of soft materials is important for many applications and natural processes. Colloids are essential in many technical applications ranging from inks and paints to lubricants and drilling fluids [1–4]. Granular materials appear in many industrial applications and geological processes such as silo flows, pharmaceuticals,

landslides, tectonic plates, etc. [5–9]. By usage in tons, only water is manipulated more than granular matter [10]. Foams and emulsions appear are commonly encountered in everyday lives in the household such as shaving cream, mayonnaise, and beer [11–14], and the rheology of soft materials we eat influence the taste [15–17]. Despite the ubiquity of these materials, we still lack the underlying mechanisms that give rise to the diverse behavior observed in these materials, and to this day there is not a single constitutive law that can be derived from fundamental principles to predict the fluid and solid like response of these materials [18, 19].

Similar to traditional liquids and solids, the mechanical properties of soft matter systems can be tuned by controlled parameters such as the packing fraction ϕ , where ϕ is the percentage of the system’s volume occupied by particles [20]. At low ϕ these systems can easily flow like liquids, but at large ϕ they behave more like solids. At a critical ϕ_c the system jams into a disordered state and can no longer flow because particles are too crowded for microscopic rearrangements to occur when external stresses are applied [21, 22]. This liquid to solid like transition for soft materials is known as the jamming transition, and it’s analogous to the dramatic change in the mechanical response of a traditional liquid undergoing a freezing transition [23–25]. Although there are open question as to whether the jamming transition is the result of a true underlying phase transition or if the crossover from liquid to solid like behavior has little universality in the physical mechanism [26]. We note that crystalline systems can jam by forming a single structure such that the particles are too crowded for microscopic rearrangements to occur. However, these materials are classified as crystals and to distinguish from crystals, for which we already have successful theories to describe their mechanical properties, jammed materials are by definition disordered.

The combination of control parameters where a system jams defines the jamming point \mathbf{J} . When a system is jammed it is trapped in a small region of phase space with no possibility of escape, and while ϕ is a crucial parameter underlying jamming, there are also many other parameters that control the ability of system to explore phase space. For instance, by raising the temperature or increasing the stress a jammed system may have enough energy to unjam by jumping to a different region of phase space. For soft matter systems, three commonly discussed control parameters are the temperature T , interaction potential U , and

an externally applied stress σ [27]. In the case of colloids and emulsions the particles may be small enough to undergo Brownian motion and temperature plays a role. In other systems the constituent particles may have electrostatic interactions where U plays a significant role [27]. In highly attractive systems like colloidal gels the constituent particles can form tenuous jammed structures at much lower volume fractions [28, 29], and in cohesive granular materials (i.e. flour), the volume fractions for jamming can be as low as $\phi_c \sim 15\%$ [30]. However, in the case of hard sphere interactions jamming occurs around $\phi_c \sim 64\%$ [21, 22].

When discussing jamming, it doesn't appear necessary to mention if the system is a colloid, emulsion, foam, or granular material. It seems more important to consider the state variables such as ϕ , T , U , and σ and maybe other parameters like deformability and particle size. After all, these materials are distinguishable from one another by how the constituent particles interact and how the constituent particles explore phase space. This led Liu and Nagel [25] to propose that the jamming transition may be universal and determined only by the state variables, but this conjecture is still unclear 14 years later [24].

Before continuing the discussion on the universality of jamming it is worth briefly discussing the origins for the solid and liquid like response of soft materials. In the presence of an external stress the constituent particles of a soft material accommodates that stress by pressing against one another and deforming [22, 31–33]. As the particles deform they store mechanical energy giving rise to a solid like response. If the stress is too large, regions in the sample become unstable, and instead of continuing to deform, groups of neighboring particles release their stored energy and locally rearrange leading to flow of the material [34–37]. As the particles rearrange, they slide past one another dissipating energy, giving rise to a viscous like response [19, 38, 39]. The bulk mechanical properties of soft materials are then related to how the stresses are distributed internally and how groups of particles rearranged [21, 40, 41]. Understanding the links between structure, dynamics, and mechanical properties is crucial in developing theories to predict the liquid and solid like response of soft materials [21, 42, 43]. In this dissertation, we measure some of these links for various experimental setups.

One aspect of the universality of the jamming transition is understanding how certain material properties, like shear modulus or viscosity, scale as a control parameter is varied

towards the jamming point and if these scaling laws are consistent between different soft materials [21, 22, 24, 26]. If a particular scaling relationship is consistent for many different soft materials, then it would suggest that this relationship is governed by a universal mechanism underlying the jamming transition [24, 26]. How to probe these universal mechanisms is not so clear, but establishing why various parameters are related is invaluable towards developing a physical theory.

For a soft matter system, there are many ways to characterize its structure, dynamics, and mechanical properties to establish possible universal scalings [22, 44]. As the jamming transition is approached, many of these characteristics either diverge or tend to zero [21]. For instance, below the jamming transition ($\phi < \phi_c$) in colloids, particles can rearrange with one another on some typically time scale τ , but as the jamming transition is approached, τ diverges as motion cease to exist [45–50]. In foams and emulsions as the jamming transition is approach from above ($\phi > \phi_c$), the shear modulus G vanishes and tends to zero, since below the jamming point droplets are not in contact and there is no resistance to motion [22]. Interestingly in simple numerical models, many of the properties characterizing the structure, dynamics, and mechanical properties show critical scaling analogous to a true phase transition. For instance, $\tau \sim (\phi - \phi_c)^\gamma$ and $G \sim (\phi - \phi_c)^\psi$ [22, 31, 51]. This has led some to speculate that the jamming transition may be like a new phase transition [26]. In the remaining sections of this chapter we elaborate further on the various parameters characterizing soft materials and various critical scaling laws.

In this dissertation we present work on a variety of systems related to the jamming transition, and the rest of this chapter is broken down into sections providing background material on each system studied. The first system we study is the colloidal glass/jamming transition and the scaling laws associated with the diverging time and length scales as the glass/jamming point is approached. Sec. 1.2 provides background on the glass/jamming transition of colloids and our project. The second system we present in this dissertation is a numerical study on the influence of boundaries on the packing of hard disks in 2D and hard spheres in 3D. An important aspect of the jamming transition and other systems is how the boundaries influence the packing of the constituent particles. In Sec.1.3, we provide background on packing and the influence of boundaries. The last topic we present

in this dissertation is a new experimental model system to probe the jamming transition of frictionless 2D disks, and we study both the static and flow properties of this model system. Section 1.4 discusses background material related the theoretical predictions for the jamming properties of the frictionless particles, and Sec. 1.5 discusses theory related to the flow of soft materials near the jamming point. The aim of the last two projects is to verify theoretical predictions for the properties of soft materials, and therefore, we restrict the background discussions in these sections to the untested theoretical results we intend to test.

1.2 Ideal Glass Transition and Using Colloids as an Experimental Model

As the temperature of a molecular glass-forming liquid is lowered it undergoes a liquid to solid like transition, where the viscosity increases by many orders of magnitude until it mechanically behaves like a solid below the glass transition temperature T_g . The ubiquity of glasses in our everyday life and their occurrence in natural processes makes the glass transition an essential field of study. Glasses have been used for years in the optical sciences, many polymers used today are noncrystalline solids, and it's been observed that the glass transition plays a vital role in food preservation [52]. Glassy metals have been useful to scientist and engineers since their material properties differ from the crystalline state [53]. Also, natural processes can form glasses such as volcano eruptions, and it's thought that most of the water in the universe is in the glassy phase [54].

In many scenarios when a traditional liquid is cooled, it undergoes a crystalline phase transition and behaves mechanically as a solid, and so it may not be too surprising to learn that molecular glass-forming liquids behave like solids when cooled. However, unlike a crystalline solid, the molecules within a glass-former are not arranged periodically. Instead, the spatial arrangement of the molecules is identical to the spatial arrangement of the molecules within a liquid [55]. It's this mixed behavior of a glass looking like a liquid, but yet behaving like a solid that make the study of the glass transition fascinating [56]. How can a material with a liquid microscopic structure behave macroscopically like a solid? The

answer to this question has to do with jamming.

As a glass former cools, its volume and thermal energy decrease. Once the glass transition temperature is reached, the molecules are too crowded and lack the thermal energy to relax (or rearrange) fast enough to reach an equilibrium configuration within reasonable human time scales [56]. As the temperature is lowered further below T_g it becomes even more difficult for the molecules to rearrange and the system becomes more rigid. The precise value of T_g is only empirically defined as the temperature below which the material has become too viscous to flow on a reasonable timescale [52]. It's difficult to put a precise definition on "reasonable", but typically the temperature where the viscosity exceeds 10^{13} Pa·s is defined as T_g [55]. For reference, the viscosity of water is 10^{-3} Pa·s.

While the overall motion of the molecules slows upon approaching the glass transition, the dynamics become more spatially and temporally heterogeneous. Some regions of the sample exhibit faster dynamics than the rest, and over time these mobile regions appear and disappear throughout the sample [57]. Particles within the mobile regions move cooperatively, forming spatially extended clusters and strings [58–60]. The length scale of these regions grow as the glass transition is approached, and the length scales are typically on the order of 2-4 particle lengths [58, 61–64]. The connection between the slowing dynamics and spatio-temporal heterogeneity is still not well understood [65, 66].

More formally, the glass transition relates to non-ergodicity, the temperature at which the molecules can not explore all the configurations necessary to reach equilibrium [67]. To make the glass transition temperature well defined, as oppose to the empirical definition, T_g can be defined as the temperature where non-ergodicity sets in. The precise location of the non-ergodicity, and the functional form governing the growth of the relaxation time as T_g is approached, remain largely open issues [51]. Since both the glass transition and the jamming transition relate to the slowing down of the internal dynamics, it has led some to speculate that there is a connection between the two [24, 67]. If glasses are truly governed by a glass transition, then the dramatic changes in the dynamics as T_g is approached are governed by some underlying mechanism related to why non-ergodicity sets in, while a jamming transition picture would suggest that the change in dynamics as T_g is approached is governed by an underlying mechanism related to motion ceasing to exist at a critical

temperature T_c (or jamming point **J**) and non-ergodicity at T_g is a side effect. It is still a controversy as to whether there is a connection between T_g and point **J** [24]. However, a larger contributor to the glass transition in molecular systems is the crowding of the molecules [24, 25, 67], and so the concept of jamming is still applicable.

To simplify the picture of the glass transition, it can be modeled using a hard sphere system, where the only contributor to the glass transition is the crowding of particles. In a hard sphere system, particles can diffuse around, but can never overlap with one another. The key control parameter is the volume fraction ϕ , and an increase in ϕ leads to more crowding of particles and a longer relaxation time, analogous to a decrease in temperature for molecular glass formers. As the volume fraction is increased, the system reaches the glass transition ϕ_g when the system becomes non-ergodic. Similar to the study of molecular glass formers, the location of the non-ergodicity and the functional form governing the growth of the relaxation time as ϕ_g is approached is still unresolved [51]. Most studies report a $\phi_g \approx 0.57$ - 0.59 . Although it is believed that a truly non-ergodic state is obtained at larger ϕ [51].

To experimentally probe the hard sphere glass transition, a common technique is to study the motion of colloids [68]. Colloids are small solid particles suspended in a solvent. For the context of studying the glass transition, the colloids are small enough (roughly 10 – 5000 nm in diameter) so they can undergo Brownian motion. Like the hard sphere model, the colloids can diffuse around, but never overlap. By coating the colloids with poly-12-hydroxystearic acid and adding salt to the solution the interactions between the colloids can be significantly reduced to give a hard sphere interaction between colloids [68–70].

The glass transition in colloidal samples has been studied extensively by light scattering, microscopy, and other techniques. Colloidal samples exhibit many behaviors seen in molecular glasses, such as dramatic increases in viscosity [71, 72], strongly slowing relaxation time scales [45–51], microscopic disorder [73], spatially heterogeneous dynamics [74–77], aging behavior for glassy samples [48, 78–83], and sensitivity to finite size effects [84, 85]. Light scattering allows careful study of the average behavior of millions of colloidal particles, while microscopy techniques observe the detailed behavior of a few thousand particles. These complementary techniques have resulted in connections between different aspects of glassy behavior: for example, showing that aging is temporally and spatially heterogeneous

[45, 48, 75, 76, 78, 79, 86].

The aim of Chapter 2 in this dissertation is to quantify the dynamical heterogeneity in colloidal glasses to test if the slowing of the dynamics are governed by an equation related to a jamming transition or by an equation govern by non-ergodicity (a glass transition). To quantify the dynamical heterogeneity of molecular glasses, Glotzer *et al.* [66] proposed using a four-point susceptibility measure χ_4 to quantify the correlation in the dynamics between any two points in space within some time window Δt . Glotzer *et al.* using numerical and theoretical calculations show that in molecular glasses there is a growing time scale with decreasing temperature associated with larger and larger groups of molecules needing to cooperatively rearrange [87], and this growing time scale was shown experimentally to exist for molecular glass formers [88]. The actual value of χ_4 is a measure of the average number of particles whose dynamics are correlated, which in turn relates back to the spatial heterogeneity [51, 66]. To compute χ_4 , the dynamics must be observed over some time window and the value of χ_4 is sensitive to this time window. There is a particular time window where χ_4 is a maximum corresponding to a relaxation time τ over which the dynamics are most heterogeneous.

Two very popular models predict a divergence in the time scale at a critical ϕ_c . The first model Vogel-Tammann-Fulcher (VTF) is an empirical model and obeys the form

$$\tau = \tau_0 \exp(E/(1 - \phi/\phi_c)), \quad (1.1)$$

where τ_0 , E , and ϕ_0 are all fitting parameters [52, 89–92]. In the VFT law, the divergence in the time scale takes place at ϕ_0 which is expected to be the packing fraction at which diffusive motion should cease [51]. This should occur at the jamming point J or ϕ_J . However, as pointed out by Brambilla *et. al* [51], there is a debate as to whether the divergence predicted by VFT should occur at the jamming point or at a slightly different packing fraction. If the VFT model or a similar model with a divergence in the time scale associate with ϕ_J is an accurate description for the divergence in τ , then it demonstrates a direct link between the glass transition and the jamming transition. The second model, Mode Coupling Theory (MCT), is an exact theoretical prediction for hard sphere systems using ideas related to

non-ergodicity (there is nothing explicit pertaining to jamming in the theory). The model predicts that the time scale should diverge as

$$\tau = \tau_0(1 - \phi/\phi_c)^\gamma, \quad (1.2)$$

where τ_0 , γ , and ϕ_c are the fitting parameters [93]. ϕ_c in this model takes a different meaning with the divergence predicted to occur near the glass transition volume fraction, not at random close packing. In light scattering experiments performed by Brambilla *et al* on 10% polydisperse colloidal samples they found $\phi_c \approx 0.59$, slightly above the glass transition volume fraction [51].

In Chapter 2, we present experimental results on the colloidal glass transition. We characterize the dynamical heterogeneity of the colloids using χ_4 to obtain a relaxation time τ . So far χ_4 has not been applied to the individual motion of colloids to characterize the dynamical heterogeneity as the glass transition is approached. To address the open question of the functional form that governs the growth of the relaxation time as ϕ_g is approached we fit our data to the VFT and mode-coupling models. This question also relates to the precise location of the critical point for the glass transition, since each model has a widely different critical point. With the range of volume fractions presented in Chapter 2 we are not able to conclusively show which model fits better, similar to situations that exists when modeling molecular glasses data [94]. Both models capture and predict the time and length scales associated with dynamic heterogeneity, and the derived fitting parameters of both compare well to expected values.

1.3 Packing and the Influence of Boundaries

Random packings are inherent to a wide range of problems including the packing of living cells [95], the arrangement of molecules in a liquid [96, 97], the processing of ceramics [98], and the molecules in amorphous solids [99]. Essential to the ideal of jamming in granular media [100–103], emulsions [104], and colloids [105] is that the constituent particles are randomly disordered. Knowing how these systems pack is very important for understand-

ing bulk characteristics such as their rheological response, hydrostatics, mass and energy transport, sonic transmission, electrical properties, and optical properties [106]. To learn how particles randomly pack in these complex systems, the jamming of disks in 2D and spheres in 3D is often used as a simple model, making the study of the jamming transition indirectly related to a host of other physical problems.

Interestingly the structure and jamming point ϕ_c of randomly packed disks and spheres is sensitive to a range of external factors, giving the model some flexibility in explaining the variability seen in more complex materials. A large contributor controlling the structure and jamming point is the protocol to initialize the packing. In numerical simulations, random packings are generated using either rate-dependent densification algorithms, energy minimization approaches, Monte Carlo schemes, and “drop and roll” algorithms [95]. These different protocols give $\phi_c \sim 0.60 - 0.68$ [95]. In experiments, often tapping methods or fluidization methods are used giving a $\phi_c \sim 0.55 - 0.64$ [97, 103, 107, 108]. Also polydispersity in particle diameters can influence the jamming point [109–114].

Another critical factor that can influence the jamming of disks and spheres is the container [98, 115–124]. While most studies on random packings focus on infinite systems, real systems have boundaries and often these boundaries are important as highlighted by Carman in 1937 [115]. In the experiments by Carman, the packing fraction dependence on container size was measured for spheres poured into a cylindrical container and shaken for sufficiently long enough time to reach a very dense state. It was found that the packing fraction decreases with decreasing container size which was attributed to the boundaries altering the structure of the packing in the vicinity of the wall.

Since the work of Carman, there have been many other studies which have investigated random packings in confined systems [120, 125–127]. These studies have shown that near the boundary, particles tend to pack into layers giving rise to a fluctuating local porosity with distance from the wall, ultimately affecting the macroscopic properties of highly confined systems. Other studies have examined the packing of granular particles in narrow silos, focusing on the influence of confinement on stresses between particles and the wall [128–131]. Nearly all of these studies did not directly measure the local packing or any local packing parameters with relation to distance from the side wall, with the exception of a few

experiments that used x-ray imaging to view the structure of confined packings. In these experiments the packings were monodisperse, facilitating highly ordered packing near the boundary, with measurements carried out at only a few different container size to particle size ratios [122, 127].

Understanding the character of random packings in confined geometries may be relevant for other confined situations [132]. For example, when a liquid is confined, its structure is dramatically changed; particles form layers near the wall, which ultimately affects the properties of the liquid [133–138]. The shearing of confined dense colloidal suspensions shows the emergence of new structures not seen before since layering near the walls greatly alters the type of structural relaxation events [139]. The flow of granular media through hoppers [140, 141] or suspensions through constricted micro- and nanofluidic devices [142–145] can jam and clog, costing time and money.

Even with the history of work on the study on random packings in confined geometries, there is little known about how sensitive the structure of the packing near the boundary is to small changes in the confining width. For example, prior work found non-monotonic dependence of ϕ on container size but only at extremely small containers with narrow dimensions h only slightly larger than the particle diameter d , that is, $h \approx 3d$ or smaller [115, 121, 123]. However, their data were not strong enough to look for such effects at larger container sizes. Additionally, only confined monodisperse systems have received much attention, and these systems are susceptible to crystallization near flat walls which greatly modify the behavior [146]. (One group did study binary systems but they were unable to directly observe the structure [120].) Furthermore, two-dimensional confined systems have not been studied systematically, although they are relevant for a wide range of granular experiments [147].

In Chapter 3, we numerical study the random packing of disks and spheres in various confining geometries to understand how sensitivity the packing’s structure is to small changes in confinement size. In the chapter, we only consider the case of random close packing (*rcp*) to limit the scope of the study. Typically one loosely defines *rcp* as a collection of particles randomly packed into the densest possible configuration while still remaining structurally disordered. More rigorous definitions are available [95], but it is generally accepted that

the *rcp* density of a packing of disks is $\phi_{rcp} \approx 0.84$ and spheres is $\phi_{rcp} \approx 0.64$ for an infinite system. When the system is confined, ϕ_{rcp} and the structure will change, and we quantify and model those changes in Chapter 3.

1.4 The Ideal Jamming Transition at Zero Temperature

For systems composed of large particles (grains, emulsions, and foams), the gravitational energy of each particle is too large for thermal fluctuations to be important. In this limit only external stresses can allow the system to explore phase space, and therefore, the temperature can be treated as $T = 0$ [20, 22]. Studying the jamming transition in this limit has the advantage of reducing the complexity of the problem by eliminating one of the control parameters [24]. If similarities between the dynamics at $T = 0$ and $T > 0$ can be linked, it may be possible to map the stress variable to a temperature like variable, where many elements of thermal physics can be applied to describe stress driven systems [20, 148, 149]. Since many practical materials exist in this limit, studying the jamming transition at $T = 0$ can also glean valuable information related to many other problems.

To model the jamming transition in this limit a numerical model system known as the ideal jamming transition has emerged over the last decade [22, 31]. This model system is composed of frictionless disks in 2D or spheres in 3D that interact via a soft repulsive potential only when particles overlap. The interaction force between two particles i and j is typically linear $F_{ij} \sim \Theta(\delta r_{ij} < d_{ij})\delta r_{ij}/d_{ij}$ or Hertzian $F_{ij} \sim \Theta(\delta r_{ij} < d_{ij})(\delta r_{ij}/d_{ij})^{3/2}$, where F_{ij} is the force between the two particles, Θ is a Heaviside function, δr_{ij} is the distance between the two particles, and d_{ij} is the sum of the radii of the two particles [21, 22, 31, 150–152]. The only two control parameters are the external stress σ and the packing fraction ϕ [22]. The advantage of this model is that it allows for a precise study of a jamming transition. However, it is still a subject of debate whether this model will be relevant to realistic systems that display more complexity [24]. Nevertheless, this ideal model encompasses the key feature of jamming, the crowding of particles.

The jamming point ϕ_c for this model system is defined as the packing fraction where the system develops a yield stress [22]. To determine ϕ_c one can monitor the pressure

with ϕ . Below the jamming point particles do not overlap and the pressure is zero, while above the jamming point particles overlap and the pressure is greater than zero. ϕ_c is the packing fraction where the pressure is zero, but any amount of compression or shear leads to a mechanically stable state with a non-zero pressure. For binary systems, it is generally accepted that in 2D $\phi_c \sim 0.84$ [21, 22, 153] and in 3D $\phi_c \sim 0.64$ [21, 22, 108]. Recent work has suggested that there is a continuous range for ϕ_c , where ϕ_c depends on the route to the jamming point [150]. This is not surprising given our discussion on the protocol dependence of ϕ_{rcp} in Sec. 1.3. While ϕ_c may vary between different samples, the mechanical properties of this model system are thought to only depend on $\phi - \phi_c$. However, the origin of this universal dependence is still unclear [21, 24].

O’Hern *et al.* [22] was the first to study how various microscopic and macroscopic properties changed with area fraction in the zero stress limit. In their work, they slowly compressed various 2D and 3D packings with either a linear or Hertzian particle-particle force law, while monitoring the pressure P , shear modulus G , and coordination number z with ϕ . Since the bulk modulus B is related to the pressure via $B = \phi dP/d\phi$, one can infer the bulk modulus using $P(\phi)$ [22]. They found a critical like scaling analogous to a classical phase transition in each variable, where $P \sim (\phi - \phi_c)^{\gamma_P}$, $G \sim (\phi - \phi_c)^{\gamma_G}$, and $z - 6 \sim (\phi - \phi_c)^{\gamma_z}$. γ_P and γ_G depend on the dimensionality and the form of the force law, while $\gamma_z = 0.5$ regardless of dimensionality and force law.

The critical scaling observed in the ideal jamming model are related to the microscopic displacements particles undergo to accommodate small changes in external forces. To provide a link between these microscopic displacements and the macroscopic properties, Ellenbroek *et al.* numerically applied small point stresses to a system of frictionless disks at various packing fractions and quantified the motion of particles as the system deformed. They found the motion of the particles to be highly non-affine, where neighboring particles not only press into one another to accommodate the stress, but also slide (or roll) past each other. They found that closer to the jamming point most particles roll past each other rather than press into one another. In their paper, they are able to relate the non-affine motion to the critical exponents found by O’Hern *et al.* [22] through an energy expansion. The results of Ellenbroek *et al.* provide a framework towards linking the microscopic details

of soft materials to their bulk properties. However, their results are still not experimentally verified, but if one can measure the forces or energy between contacting particles in real soft matter systems, then their equations in principle can be tested.

In this dissertation we aim to test the predictions of the ideal jamming model and characterize the jamming transition for the simplest experimental analog to the ideal model, a 2D frictionless disks experiment. To experimentally probe the jamming transition and test many of the results mentioned above, an experiment must be employed where both the position of the particles and the forces between contacting particles are known. Currently there are three known setups where this can be done. One option is photoelastic disks [154–157]. These are elastic frictional disks that when pressed against one another rotate the light passing through each disk. By using cross polarizers and measuring the intensity of light on each disk the contact forces can be determined to 5% accuracy [6, 154–157]. A limitation of this system is that the disks can not be compressed too far from the jamming point without breaking, limiting the range of $\phi - \phi_c < 0.01$. Also for our aim, friction between the disks is a problem. The second option is a 3D emulsion setup [158, 159]. In principle we could work with a 3D setup, but we choose to work with a 2D setup because we also intend to flow our samples (see the discuss in the next section). Currently it is not possible to image flowing materials fast enough in 3D, and if it were possible the computation cost of analyzing 3D data would be enormous. The third option (which did not exist when we began our experiments) is a 2D foam setup [153]. The authors report for the 2D foam setup that they can measure the forces to an accuracy of 80% - 100%. The advantage of the emulsion and foam setup is that there is no static friction between the droplets. In the 3D emulsion work the jamming transition was not studied, and in the 2D foam work only the critical scaling of $z(\phi - \phi_c)$ was studied, and therefore many of the critical scaling results are untested. Experimental finding from other groups related to the jamming transition will be given in Chapter 6.

In Chapters 6 of this dissertation we present a new experimental model system composed of quasi-2D emulsion disks, where the disks have no static friction. We also present a method in Chapters 4 and 5 to determine the contact forces between droplets to less than 15% accuracy. Our model system will allow us to test if the predictions and observations

of the ideal jamming transition are valid. A second aim of this model system is study the flow properties of soft materials. In Chapter 7, we apply our model system to verify the Kinetic Theory of Glassy Flows model used to predict the flow of emulsions and foams. In the next section we provide background on the Kinetic Theory of Glassy Flows model.

1.5 Flow of Disordered Matter Near Jamming

Flow is imposed on a soft material by boundary conditions where one or more of the material's boundaries is moved via some external conditions. Far from the boundary soft materials tend to be solid like (i.e. very few particles ever move) and near the boundary the particles flow at rates comparable to the boundary's rate [7, 154, 160–165]. In many cases, the velocity and stress profiles decay either exponentially or as a power law with distance from the boundary, and the length scale of the decay is on the order of 5 to 15 particle diameters [19, 166]. Since the flow is localized to a narrow region of 5-15 particle diameters, this phenomena is known as shear banding or shear localization.

During slow steady state flow, where the strain rate and shear stress have well defined long time averages, the shear band can exhibit an intermediate between a solid-like and liquid-like response on shorter time scales [154, 167–171]. This mixed behavior leads to large fluctuations in local strain rate and stress, and is due to local groups of particles temporally jamming into disordered spatial configurations [146, 172]. To unjam one of these local groups of particles the stress must build to the point that the local configuration can no longer support the stress [146, 172, 173]. Once the particles unjam, the stress rapidly decreases [174, 175]. The observed average velocity and stress profiles are the cumulative effect of these local jamming and unjamming processes. Intermittent flow at the grain scale has been observed in many experimental and computational soft matter systems with local rearrangements typically involving on the order of 10 particles [34, 167–169, 176–178]. In addition to local rearrangements, intermittent stress fluctuations have also been observed [154, 179–182]. However, there are no experiments to date that quantify the spatial and temporal stress build up and relaxation in the vicinity of individual particle rearrangements.

While there are no direct measurements of the stress build up and relaxation around single plastic events, the details of the stress build up and relaxation have been inferred through indirect methods of fitting data to models [37, 162, 183]. The process involves taking data on a system where the average stress or velocity profiles can be measured. Then a model is used where certain details about the microscopic details are either fixed or left as unknown fitting parameters. By fitting the data one can infer these microscopic characteristics, however, a direction verification is still needed.

Typical models for the flow of soft matter are elastoplastic theories which attempt to explain the elastic and plastic response of soft materials to external stresses [37, 40, 172, 173, 184–190]. The approach of these models is to assume that particles move non-affinely and press into one another when sheared, leading to a spatially heterogeneous build up of stress. As the material is continually sheared, the stress continues to build until local regions within the sample can no longer accommodate this stress, and yield by undergoing plastic rearrangements. During each plastic event the rearranging particles dissipate their stress by sliding past each other, but they also redistribute some of the stress by pressing into their neighboring particles causing a slight change in the local configuration.

One approach of elastoplastic theories is to model the system stochastically, where stress randomly fluctuates, similar to thermal fluctuations [40, 149, 184, 186, 189]. The essential ingredients in these models are that local regions within the sample must cross over energy or stress barriers for plastic events to occur and that the stress is spatially heterogeneous due to the disordered arrangement of the particles. Some theories use energy as the state variable and others use stress, but both are attempting to model the velocity profile. Similar to a Boltzmann distribution for energy fluctuations in thermal systems, different models have certain weighting distributions for either energy or stress fluctuations. In addition to energy or stress fluctuations, there are boundary conditions for the energy or stress and the velocity. In these models, as the system evolves with time, the energy or stress within local regions of the sample fluctuate, where briefly the energy or stress may increase in one region of the sample while decreasing in another region. When the energy or stress in a local region reach a threshold, it undergoes a plastic event and the stress is both locally dissipated and redistributed into the surrounding environment. The strain rate and stress

profiles can be computed numerically or analytically by observing the average number of plastic events and stress in each region of the sample.

The remarkable aspect of some of these models is that testable analytic solutions can be derived for the flow and stress profiles. Three popular models that can make analytic predictions are the Shear Transformation Zone Theory [184, 185], Soft Glassy Rheology [186, 187], and the Kinetic Theory of Glassy Flows (KTGF) [37, 40]. The Shear Transformation Zone Theory and Soft Glassy Rheology model the flow using energy barriers, and so verifying the underlying assumptions of these two model is more difficult since local energy fluctuations are difficult to measure in soft matter systems. The more accessible quantities for experimentalist are particle-particle contact forces and local stresses. In the KTGF the system is modeled using stress barriers.

KTGF is a generalized theory, and for simple geometries and assumptions can produce analytic predictions. One case where the model can produce an analytic prediction is emulsion flow in a microchannel [37, 40]. The flow is modeled on a lattice, where the sample is divided into lattice sites of size a , where a is on the order of a particle diameter. At each site the stress is described stochastically with probability $P_i(\sigma_i, t)$ for lattice site i to have a stress σ_i at some time t . The stress at site i evolves via three mechanisms: (1) an elastic response where the stress increases linearly with an externally imposed shear rate γ_i^o , (2) a stress relaxation due to a plastic event when the stress is above a stress barrier σ_c , and (3) a stress redistribution from neighboring lattice sites where a plastic event has occurred. For a site undergoing a plastic event the model assumes that stress at that site is completely relaxed out ($\sigma_i \rightarrow 0$) and the stress is redistributed to the surrounding lattice sites over some length scale ξ . The length scale ξ implies that not only is the stress at site i modified by the globally imposed strain rate, but also by plastic events occurring at other sites within some distance ξ . Using these assumptions, they predict the following

relationship between the average local stress and local strain rate

$$f(z) = f_{bulk} + \xi^2 \frac{\partial^2 f(z)}{\partial z^2} \quad (1.3)$$

$$f(z) = \frac{\sigma(z)}{\dot{\gamma}(z)} \quad (1.4)$$

$$f_{bulk} = \frac{\sigma(z)}{\dot{\gamma}(z)}, \text{ for large } h \text{ and } z \gg \xi, \quad (1.5)$$

where z is the distance from the boundary, $\sigma(z)$ is the average shear stress, $\dot{\gamma}(z)$ is the average strain rate, and the fluidity f is a local quantity measuring the ratio of the shear stress to strain rate. We note that this equation is a one parameter model, where the single unknown is ξ .

In the work by Goyon *et al.*, they tested the predictions of Eqn. 1.3 by flowing emulsion samples through a microchannel and measuring $\dot{\gamma}(z)$ and $\sigma(z)$ [37]. $\dot{\gamma}(z)$ was measured using fluorescent tracer particles to map out the average flow rate and $\sigma(z)$ was inferred using Newton's 3rd Law. Since the samples were in steady state, the time average stress must be constant everywhere. By knowing the stress at the boundary they were able infer the stress within each sample. Using $\dot{\gamma}(z)$ and $\sigma(z)$ they fitted their data to Eqn. 1.3 and found very good agreement. Their fits gave $\xi = 0$ at the jamming point $\phi = \phi_c$ and increases to $\xi \sim 6$ particle diameters as ϕ approaches 1.

KTGF provides a starting point towards having a universal framework to describe the flow of soft matter. The model has some flexibility to describe the diverse flow of different soft materials because the three basic assumptions of the model can be tuned to match the microscopic details of each material. For instance, ξ may depend on particle-particle interactions, or the time evolution of stress during plastic events may vary for different soft materials. While the Kinetic Theory of Glassy Flows is promising, the three basic assumptions of the model used to predict the flow of emulsions are experimentally untested (linear build up of stress, complete stress relaxation during plastic event, and a cooperative length scale for stress redistribution). Also it is not known if the model can accurately predict the flow when the exact microscopic details of a soft material are inputs into the model. While there is strong evidence from the work Goyon *et al.* to support the theory,

there are no experiments to date that have directly measured the time dependent stress build up and relaxation in the vicinity around individual plastic events.

In Chapter 7, we present preliminary work using our new experimental quasi-2D frictionless model system on the time dependent stress build up and relaxation on individual particles in the vicinity around plastic events. Using our data we can compute ξ directly as a function of ϕ and compare the results to that found by Goyon. Our data shows that there exist a spatially cooperative length scale ξ on the order of 3-4 particle diameters. However, we do not find ξ changing from 0 - 6 particle diameters with increasing $\phi - \phi_c$. Also, more work is needed to test the quality of the theory to predict the observed flow profile in our data. In addition to attempting to verify the KTGF model, our results will be a significant step towards developing constituent equations from physical principles to describe the flow of soft matter since we provide the foundational information needed for any successful model.

CHAPTER 2

Dynamic Heterogeneity in Colloidal Glasses

2.1 Introduction

As the temperature of a glass-forming liquid is lowered, the viscosity rises by many orders of magnitude, becoming experimentally difficult to measure, with little change in the structure [52, 89, 90]. The origin of the slowing dynamics is not yet clear, despite much prior work. One intriguing observation is that as a sample approaches the glass transition, the motion within the sample becomes spatially heterogeneous [62, 65, 191–193]. While overall motion within the sample slows, some regions exhibit faster dynamics than the rest, and over time these mobile regions appear and disappear throughout the sample [57]. Particles within the mobile region move cooperatively, forming spatially extended clusters and strings [58]. The length scale of these regions grows as the glass transition is approached [58, 61–64].

One technique for studying the glass transition is the use of colloidal suspensions [68]. These are composed of small solid particles suspended in a solvent. The particles need to be small enough to undergo Brownian motion, so particle diameters are typically 10 – 5000 nm. The key control parameter is the volume fraction ϕ . For a monodisperse sample (all particles similar in size), the sample becomes glassy for $\phi > \phi_g \approx 0.58$ [45, 68]. The glass transition in colloidal samples has been studied extensively by light scattering, microscopy, and other techniques. Colloidal samples exhibit many behaviors seen in molecular glasses,

such as dramatic increases in viscosity [71, 72], strongly slowing relaxation time scales [45–51], microscopic disorder [73], spatially heterogeneous dynamics [74–77], aging behavior for glassy samples [48, 78–83], and sensitivity to finite size effects [84, 85]. Light scattering allows careful study of the average behavior of millions of colloidal particles, while microscopy techniques observe the detailed behavior of a few thousand particles.

In this chapter, we present results related to the glass transition of binary colloidal suspensions using confocal microscopy. We use binary suspensions (mixtures of two particle sizes) to inhibit crystallization. This allows us to take data over many hours, a time scale in which a monodisperse sample would crystallize [194, 195]. Furthermore, this lets us investigate the role the two particle species play in the dynamics; prior work has suggested that small particles play a lubricating role in the local dynamics [196]. The confocal microscope enables direct visualization of the interior of the sample, and we follow the motion of several thousand colloidal particles within each sample [197]. In Section 2.2, we discuss the specific details of our binary colloidal system.

Colloids undergo large temporal fluctuations in mobility which are thought to be responsible for the viscous response and other macroscopic properties of glasses. In Section 2.4, we characterize these temporal fluctuations for our binary samples using the dynamic susceptibility χ_4 [66, 198, 199], which has not been previously applied to colloidal data, and in Section 2.3 we present the mathematical definition of χ_4 . As measured by this correlation function, the temporal heterogeneity increases as the glass transition is approached. By simultaneously tracking both large and small particles, we can observe the similarities and differences between the two species' dynamics. In section 2.6, we compare our results to the widely used Vogel-Fulcher-Tammann (VFT) scaling law to characterize molecular glasses and the theoretical predictions of Mode-Coupling Theory (MCT) for colloidal glasses [52, 89, 90]. Section 2.5 discusses the details of the VFT scaling law and MCT theory.

2.2 Binary Sample

The data discussed here was taken by Takayuki Narumi and Scott Franklin. For a complete description of the sample preparations and results other than those related to the χ_4 analysis

see our paper [200]. The samples consist of poly-(methyl-methacrylate) (PMMA) colloids stabilized sterically by a thin layer of poly-12-hydroxystearic acid [68]. We use a binary mixture with a large particle mean radius $a_L = 1.55 \mu\text{m}$ and small particle mean radius $a_S = 1.18 \mu\text{m}$, with a polydispersity dispersity for each species of 5%; each individual particle species can crystallize in a monodisperse suspension. Separately from the polydispersity, the mean particle radii each have an uncertainty of $\pm 0.02 \mu\text{m}$. The number ratio of small particles to large particles is $N_S/N_L = 1.56$, resulting in a volume fraction ratio $\phi_S/\phi_L \approx 0.70$. The control parameter is the total volume fraction $\phi = \phi_S + \phi_L$.

Confocal microscopy is used to record the three-dimension particle dynamics of thousands of colloids at ambient temperature [197]. We use a fast confocal microscope (VT-Eye from Visitech, International) to scan a volume $50 \times 50 \times 20 \mu\text{m}^3$ with a resolution of $0.05 \mu\text{m}$ in x and y (parallel to the coverslip) and a resolution of $0.1 \mu\text{m}$ in the z (parallel to the optical axis). To avoid influences from the walls, we focus at least $25 \mu\text{m}$ away from the coverslip. Within each three-dimensional image, we identify both large and small particles using tracking software written by Crocker and Grier [201]. The accuracy in tracking the centers of the colloids is $0.2 \mu\text{m}$. We will be measuring motions that take place on length scales of $1\text{-}3 \mu\text{m}$ which are large enough that tracking noise will not be an issue.

2.3 Four-Point Susceptibility

To quantify the dynamical heterogeneity of molecular glasses Glotzer *et al.* [66] proposed using a four-point susceptibility measure χ_4 to quantify the correlation in the dynamics between any two points in space within some time window Δt . Glotzer *et al.* using numerical and theoretical calculations show that in molecular glasses there is a growing time scale with decreasing temperature associated with larger and larger groups of molecules needing to cooperatively rearrange [87], and this growing time scale was shown experimentally to exist for molecular glass formers [88]. The actual value of χ_4 is a measure of the average number of particles whose dynamics are correlated, which in turn relates back to the spatial heterogeneity and a correlation length scale [51, 66]. To compute χ_4 the dynamics must be observed over some time window and the value of χ_4 is sensitive to this time window.

There is a particular time window where χ_4 is a maximum corresponding to a relaxation time τ over which the dynamics are most heterogeneous.

χ_4 is computed from temporal fluctuations in particle mobility, where a particle is defined to be mobile if its displacement over some time interval Δt is larger than some threshold distance ΔL [199]. Using this definition, each particle at each time can be labeled mobile or immobile and the fraction of mobile particles $Q(t)$ can be computed for each frame recorded. Figure 2.1(a) shows $Q(t)$ for a sample at $\phi = 0.52$ at various Δt using $\Delta L = 0.4a_S$. For $\Delta t = 105$ seconds, the black curve in Fig 2.1(a), we see with time that roughly 50% of the particles displace a distance greater than $0.4a$ and that Q fluctuates with time. In highly dense colloidal samples particles cannot diffuse freely, but instead are “caged” by their nearest neighbor particles. On long enough time scales particles move cooperatively to rearrange, allowing particles to break their cage and briefly diffuse more only to be cage by different particles [202–207]. By examining the average diffusion of single particles, Narumi and Franklin reported in our paper [200] for this data set a cage rearrangement length scale of $\sim 0.4a$ and time scale of ~ 1000 seconds. So it is not too surprising that we find similar results, although, a priori it is not clear if the caging time scales and length scales correspond to when the dynamics are most heterogeneous which χ_4 measures. For larger time windows closer to the cage rearrangement time scale, the average value of $Q(t)$ increases, since each particle has a longer time to diffuse. Also, the variations in $Q(t)$ increase, where the fluctuations between two consecutive frames is roughly the same, but the long time variations are much larger. These long time variations reflect the dynamic heterogeneity of the sample, where there are moments in time with significantly more activity in particle motion, where near $t = 0$ for the blue curve $\sim 75\%$ of the particles are mobile, but 800 seconds later only $\sim 65\%$ on the particles are mobile.

These temporal fluctuations in $Q(t)$, both short and long, are quantified by the self part to χ_4 and written as

$$\chi_4 = N[\langle Q(t)^2 \rangle_t - \langle Q(t) \rangle_t^2], \quad (2.1)$$

where N is the number of particles. N also varies from frame to frame as particles move in and out of the field of view; we average N over all frames and use $\langle N \rangle$ in Eqn (2.1).

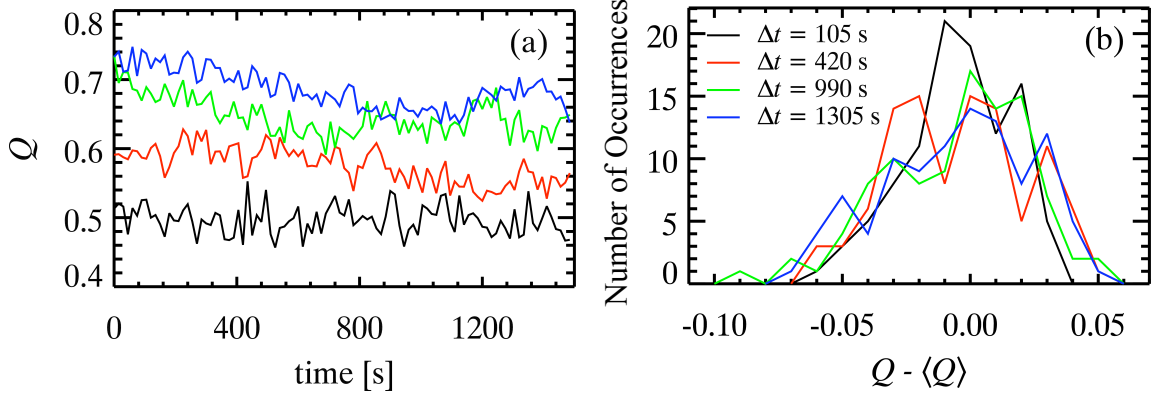


Figure 2.1: (a) Percentage of mobile particles with time using different time windows Δt to define mobility. The legend in (b) applies for this plot as well. (b). The distribution of Q relative to the mean for various Δt used to define particle mobility. The standard deviation for the $P(Q)$ are 0.0208, 0.0256, 0.0278, and 0.0283 for the $\Delta t = 105$ s, 420 s, 990 s, 1305 s data respectively. Since particles are diffusing, some particles leave the field of view after enough time, and the longer the time window used to define particle mobility, the less particle to sample Q . For the data in this figure the average number of particles sampled is 2105, 2059, 1973, and 1640 for the $\Delta t = 105$ s, 420 s, 990 s, 1305 s data respectively. Using the standard deviations and the average number of particles sampled, this gives a $\chi_4 = 44.0$, 52.7, 54.9, and 46.5 for the $\Delta t = 105$ s, 420 s, 990 s, 1305 s data respectively.

The factor of N arises because the variance scales inversely with particle number. Also by including the factor of N , χ_4 is an intensive quantity. Note that χ_4 measures temporal fluctuations in mobility without regard for the spatial correlations between mobile particles. In Fig, 2.1(b) we illustrate the meaning of χ_4 for each data set shown in Fig, 2.1(a) by plotting the histogram of $Q(t) - \langle Q(t) \rangle_t$. In Fig, 2.1(b), we see that the distribution for increasing Δt is slightly wider since the temporal fluctuations are growing, although this may be difficult to see and the caption in Fig, 2.1(b) gives the standard deviations of the distributions. χ_4 is the width of this distribution scaled by the number of particles in the system. For larger Δt the number particles sampled to compute Q is less because particles diffuse out of the field of view, and therefore the width of $P(Q)$ is not the only measure to consider. When the width of the distribution is scaled by the number of particles sampled we see that $\Delta t = 990$ s has a larger χ_4 than $\Delta t = 1305$ s. The caption in Fig, 2.1(b) gives the χ_4 values.

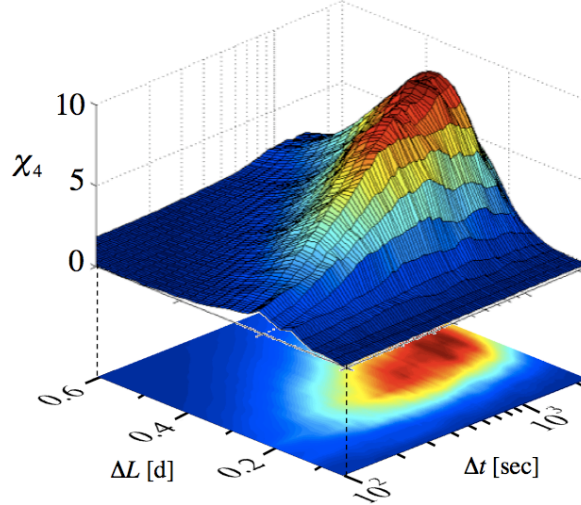


Figure 2.2: Surface plot of χ_4 for large particles within a sample with $\phi = 0.52$.

2.4 Growing Length & Time Scale

From Eqn (2.1) it's evident that χ_4 will depend on our choice of ΔL and Δt as shown in Fig. 2.2, where χ_4 is plotted for the larger particles within a $\phi = 0.52$ sample for various values of Δt and ΔL . This plot shows that χ_4 is characterized by a function that has a maximum at $(\Delta t_{\max}, \Delta L_{\max})$. This maximum in χ_4 indicates a typical timescale Δt_{\max} where the dynamics are most heterogeneous, and likewise ΔL_{\max} indicates a typical length scale distinguishing caged motions from cage rearrangements.

Figure 2.3 shows plots of $\chi_4(\Delta t, \Delta L = \Delta L_{\max})$ for the larger (a) and smaller (b) particles. The value of χ_4 is larger in magnitude for the smaller particles regardless of ϕ , demonstrating that the dynamics of the smaller particles are more temporally heterogeneous. Prior work by Lynch *et al.* [196] showed a similar relative mobility; our results build upon this by showing that smaller particles also experience larger fluctuations, and thus exhibit more anomalous spatial and temporal behavior. We also see that χ_4 grows in amplitude as ϕ increases, but then drops for the glassy sample ($\phi = 0.59$).

The plots in Fig. 2.3 all show a maximum in χ_4 at a well defined Δt_{\max} , and that Δt_{\max} for the various volume fractions occur at timescales close to the timescale where caging rearrangements become prominent. The coincidence of maxima in χ_4 near the time scale associated with cage rearrangements suggests that local cage rearrangements are the largest

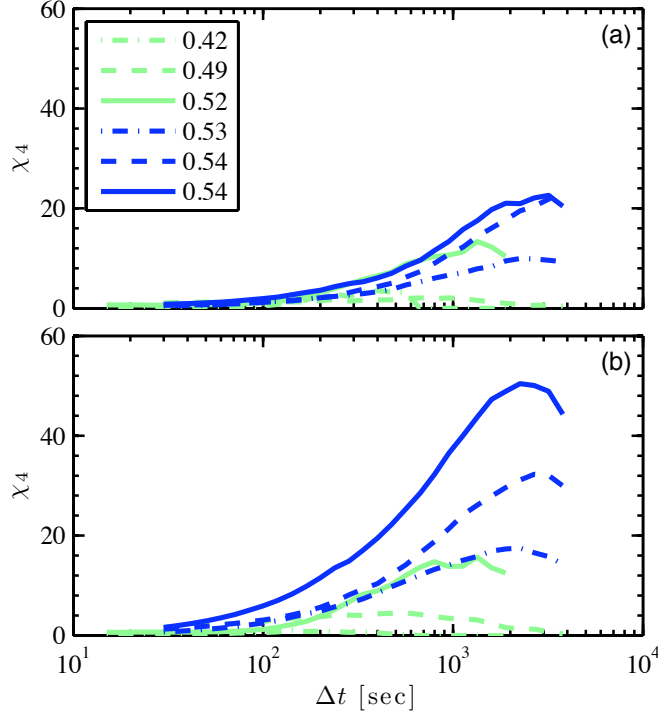


Figure 2.3: (a) is a plot of the susceptibility of large particles for various packing fractions, and (b) is a plot of the susceptibility of small particles for various packing fractions. The legend indicates the packing fraction of the sample.

contributor to temporal fluctuations. Since small particles show larger fluctuations, we infer that they may be largely responsible for facilitating local rearrangements, in agreement with the findings of Lynch *et al.* [196].

χ_4^{\max} , Δt_{\max} , and ΔL_{\max} all vary with ϕ ; this dependence is shown in Fig. 2.4. Both χ_4^{\max} and Δt_{\max} show an increase with ϕ illustrating that upon approaching the glass transition the dynamic heterogeneity and the associated time scale increases. The increasing time scale also suggests that local rearrangements take longer at higher ϕ . On the other hand, the characteristic length scale ΔL decreases with ϕ which is in excellent agreement with prior work, where displacements for cage rearrangements were shown to be smaller as the glass transition is approached [208]. This suggest that with increasing ϕ smaller displacements are required to be an anomalously mobile particle.

Using the χ_4^{\max} data in Fig. 2.4(a) a correlation length scale can be estimated by assuming that the correlations χ_4 measures are correlated particles forming compact clus-

ters [199, 209]. Since χ_4 is the average number of correlated particles, then $\chi_4^{\max} = (4/3)\pi\xi_4^n$, where ξ_4 is the radius of the cluster of correlated particles in units of particle diameters d and $n = 3$ [199, 209]. Although, the particles could form string like clusters where the length scale is $\chi_4^{\max} = \xi_4^n$ and ξ_4 is characteristic length of the string and $n = 1$. The particles could also form string-like and compact-like clusters where the exponent n is between 1-3. The trends that we observe are not susceptible to the exponent we choose, however, later when we fit the data the fitting parameters will depend on our choice of the exponent. Here we only present results assuming that the clusters are compact ($n = 3$) to compare to prior work. In the work of Weeks *et al.* [76], they found clusters of mobile particles to be string-like and cluster-like implying that the exponent is probably somewhere between 1-3. The inset in Fig. 2.4(a) shows the dependence of ξ_4 on ϕ . Similarly as with the relaxation time, we see a tendency in ξ_4 to increase with ϕ . The growth in ξ_4 is about a factor of 4 when the volume fraction is increased from a liquid to a dense supercooled state. Our values of ξ_4 are roughly the same as those measured in a 2D fluidized granular bed on approaching the jamming point [199].

2.5 Theory and Expected Results

The time scales Δt_{\max} associated with the temporal fluctuations measured by the four point susceptibility are analogous to the α relaxation time scales measured in molecular supercooled liquids. In many cases the α relaxation time scales are well described using either a Vogel-Fulcher-Tammann (VFT) model or Mode-Coupling Theory (MCT) [52, 89, 90], although sometimes this is over a limited range of temperatures [91, 92] and it can be hard to distinguish between different functional forms [94].

The first model, VFT, predicts that the time scales should obey the form

$$\Delta t_{\max} = \Delta t_0 \exp(E/(1 - \phi/\phi_0)), \quad (2.2)$$

where Δt_0 , E , and ϕ_0 are all fitting parameters. In the model Δt_0 is an attempt time to undergo relaxation events over some typical length scale. For our experiment, this length

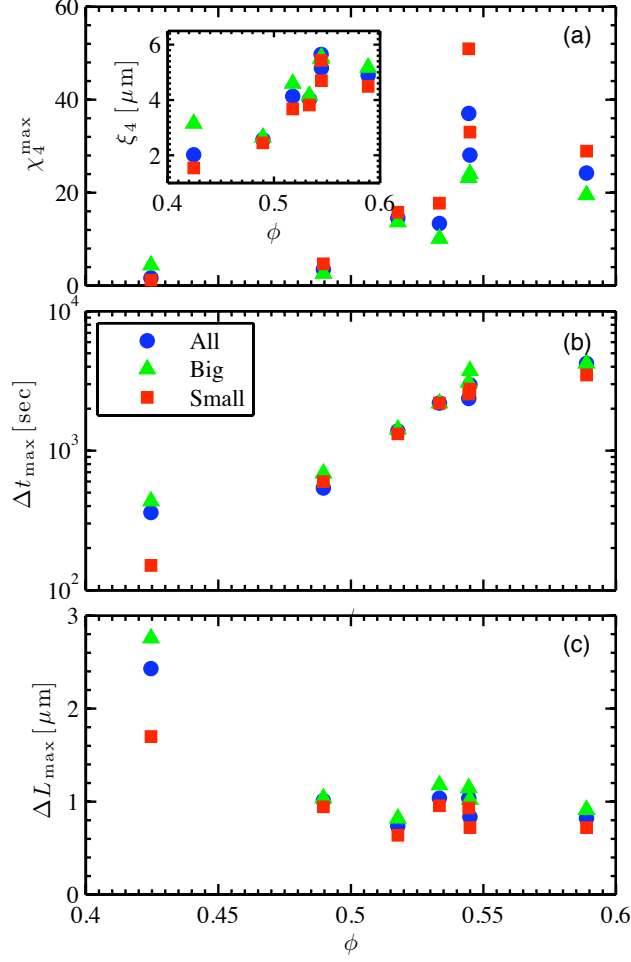


Figure 2.4: (a) Plot of the maximum of χ_4 as a function of ϕ , showing how temporal heterogeneity increases as $\phi \rightarrow \phi_g \approx 0.58$. The inset in (a) shows the dependence of the dynamic heterogeneity length scale $\xi_4 = (\chi_4^{\max})^{1/3}$ on ϕ . (b) Plot of the dynamic heterogeneity time scale as a function of ϕ . (c) Plot of the length scale ΔL as a function of ϕ . For all panels, the symbols are as indicated in the legend of panel (b).

scale would be on the order of a particle diameter and the attempt time would be the time it takes a particle to diffuse over this length scale in the dilute limit. Using the Stokes-Einstein-Sutherland formula and a viscosity of 2.18 mPa·s (measured for the fluid in absence of colloids) we estimate that at room temperature it should take the small particles about 11 seconds and the large particles 25 seconds to diffuse their own diameter [210, 211]. The fitting parameter ϕ_0 is the packing fraction at which diffusive motion should cease. This should occur at random close packing of $\phi \sim 0.65$ (using the value appropriate for our binary suspension). However, as pointed out by Brambilla *et. al* [51], there is a debate as

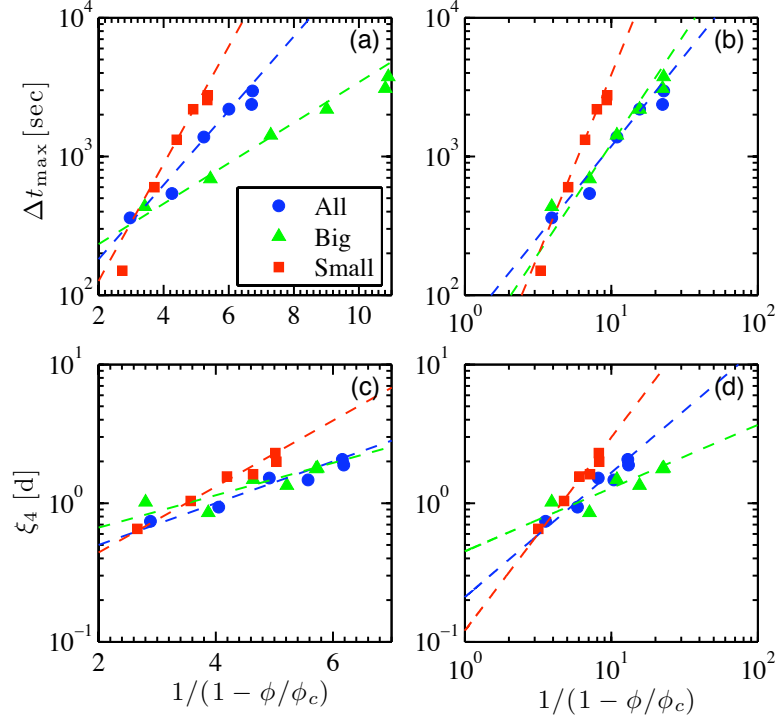


Figure 2.5: (a) Log-linear and (b) log-log plots of temporal dynamical heterogeneity time scale, with fits to Eqn (2.2) in panel (a) and Eqn (2.3) in panel (b). (c) Log-linear and (d) log-log plots of the χ_4 length scales, with fits to Eqn (2.2) in panel (c) and Eqn (2.3) in panel (d).

to whether the divergence predicted by VFT should occur at the jamming point or at a slightly different packing fraction. To definitively show if this is the case one would need very careful measurements extremely close to the jamming point which is beyond the scope of this work. The final fitting parameter is E , the fragility, which is a material dependent value. The fragility is a measure of how sensitive the time scale is to small changes in temperature in molecular glasses and volume fraction colloidal glasses. E typically ranges between ≈ 1 -100 [52]. Materials with low E values are termed fragile glass formers because their relaxation time can be easily reduced by small changes in control parameters leading to a softening of the material. Materials with a large E are termed strong glasses because their relaxation times are insensitive to small changes in control parameters resulting in the material remaining stiff when the control parameter is slightly changed.

The second model, MCT, predicts a scaling of

$$\Delta t_{\max} = \Delta t_0(1 - \phi/\phi_c)^\gamma, \quad (2.3)$$

where Δt_0 , γ , and ϕ_c are the fitting parameters [93]. ϕ_c in this model takes a different meaning with the divergence predicted to occur near the glass transition volume fraction, not at random close packing. In light scattering experiments performed by Brambilla *et al.* on 10% polydisperse colloidal samples they found $\phi_c \approx 0.59$, slightly above the glass transition volume fraction [51]. Their work also showed that near the divergence point the dynamics deviate from the predicted form, but that in the supercooled regime the MCT equation describes the data well. They also found a scaling exponent of $\gamma = 2.5 \pm 0.1$.

2.6 Comparing Results to Theory

We now compare our results to the VFT scaling law and the mode coupling theory by fitting our measured time scales using to the two models. The fit to the VFT scaling law is shown in Fig. 2.5(a), the fit to the mode coupling theory is shown in Fig. 2.5(b), and the corresponding fitting parameters are shown in Table 2.1. In section 2.5 reasonable fitting values were given for some of the different fitting parameters, and these expected values are also included in the table. The Δt_0 values are significantly larger than the dilute concentration diffusive time scales, for both the VFT and MCT fits, although the agreement is off by only a factor of two for the small particles (25 s for VFT, 20 s for MCT, and $\tau_D = 11$ s). For the VFT fit, ϕ_c is near ϕ_{rcp} as predicted. For the MCT fit ϕ_c is near the expected glass transition volume fraction of ≈ 0.58 . The MCT exponent γ is smaller than that found by Brambilla *et. al* [51], who found $\gamma = 2.5$, with the exception of the small particles for which we find $\gamma = 2.6 \pm 0.9$.

Our data gives fragilities on the order of 0.5, consistent with fragility values from a study of a 2D fluidized granular bed [199]. When compared to a molecular system our colloidal system would be considered a very fragile glass former.

In the study on the motion of grains in a 2D fluidized granular bed it was shown

| VFT: | Δt_0 [sec] or ξ_4^0 [d] | E | ϕ_0 |
|-------------------------|-------------------------------------|----------------|-----------------|
| All Δt_{\max} | 70 ± 50 | 0.6 ± 0.3 | 0.64 ± 0.03 |
| Big Δt_{\max} | 200 ± 160 | 0.4 ± 0.2 | 0.6 ± 0.03 |
| Small Δt_{\max} | 25 ± 20 | 0.4 ± 0.35 | 0.67 ± 0.03 |
| All ξ_4 | 0.3 ± 0.2 | 0.4 ± 0.2 | 0.65 ± 0.05 |
| Big ξ_4 | 0.5 ± 0.2 | 0.3 ± 0.2 | 0.66 ± 0.07 |
| Small ξ_4 | 0.2 ± 0.15 | 1.0 ± 0.8 | 0.68 ± 0.07 |

| Power law: | Δt_0 [sec] or ξ_4^0 [d] | γ or δ | ϕ_c |
|-------------------------|-------------------------------------|----------------------|-----------------|
| All Δt_{\max} | 100 ± 90 | 1.3 ± 0.6 | 0.57 ± 0.02 |
| Big Δt_{\max} | 90 ± 70 | 1.6 ± 0.8 | 0.57 ± 0.02 |
| Small Δt_{\max} | 20 ± 10 | 2.6 ± 0.9 | 0.61 ± 0.01 |
| All ξ_4 | 0.2 ± 0.1 | 0.9 ± 0.4 | 0.59 ± 0.03 |
| Big ξ_4 | 0.5 ± 0.1 | 1.4 ± 0.5 | 0.62 ± 0.04 |
| Small ξ_4 | 0.15 ± 0.05 | 0.4 ± 0.2 | 0.57 ± 0.02 |

Table 2.1: This table displays the fitting parameters found when fitting the data to either a VFT scaling or a power law scaling. The uncertainties of the fitting parameters are found by adjusting the fitting parameters until they no longer provide reasonable fits.

that the length scales can also be fitted well to the models used to fit the time scales where the VFT formula becomes $\xi_4 = \xi_4^0 \exp(E/(1 - \phi/\phi_c))$ and the MCT formula becomes $\xi_4 = \xi_4^0(1 - \phi/\phi_c)^\delta$, where δ in work by Berthier *et. al* is predicted to be $2/3$ [212, 213]. The work of Brambilla *et. al* found that $\delta = 2/3$ fitted their light scattering data very well [51].

The fits to the length scales are shown in Fig. 2.5(c) and (d), and the fitting values are shown in Table 2.1. The fitting values found for the VFT fits are physically feasible where the fragilities and divergence points compare well to the fitting parameters previously found for the VFT fits to the time scales. The MCT fits are also reasonable, although our scaling exponents δ is only consistent with the predicted value of $2/3$ due to our large error bars. The MCT divergence at ϕ_c is close to ϕ_g , as expected.

With the range of volume fractions presented in this paper we can not conclusively show which model fits better, similar to the situation which exists for regular glasses [94]. Both models capture and predict the time and length scales associated with dynamic heterogeneity, and the derived fitting parameters of both compare well to expected values.

2.7 Conclusion

We have used confocal microscopy to study the three-dimensional motion of particles in binary colloidal mixture. The volume fraction ϕ was varied from 0.4-0.59 and the dynamical heterogeneity of the small and larger particles were found to be qualitatively similar with the smaller particles undergoing slightly larger fluctuations relative to their size. The temporal fluctuations give rise to length scales and time scales which grow as the glass transition is approached, although the form of this growth is ambiguous with respect to power-law or exponential growth. The spatially and temporally heterogeneous dynamics are similar to the observations of molecular glasses [57, 62, 65, 192, 193]. The coincidence of maxima in χ_4 near the time scale associated with cage rearrangements suggests that local cage rearrangements are the largest contributor to temporal fluctuations. Since small particles show larger fluctuations, we infer that they may be largely responsible for facilitating local rearrangements, in agreement with the findings of Lynch *et al.* [196].

Packing in Confined Geometries

3.1 Introduction

Random close packing (*rcp*) has received considerable scientific interest for nearly a century dating back to the work of Westman in 1930 [106, 125, 214–217] primarily due to the relevance *rcp* has to a wide range of problems including the structure of living cells [95], liquids [96, 97], granular media [100–103], emulsions [104], glasses [105], amorphous solids [99], jamming [218], and the processing of ceramic materials [98]. Typically one defines *rcp* as a collection of particles randomly packed into the densest possible configuration. More rigorous definitions are available [95], but it is generally accepted that the *rcp* density of a packing of spheres is $\phi_{rcp} \approx 0.64$. Packings can have other *rcp* densities when the particles are polydisperse mixture of spheres [109–114], non-spherical in shape [219–223], or confined within a container that is comparable in size to a characteristic particle size [98, 115–124].

While most studies of *rcp* focus on infinite systems, real systems have boundaries and often these boundaries are important as highlighted by Carman in 1937 [115]. In the experiments by Carman, the packing fraction dependence on container size was measured for spheres poured into a cylindrical container and shaken for sufficiently long enough time to reach a very dense state. It was found that the packing fraction decreases with decreasing container size which was attributed to the boundaries altering the structure of the packing in the vicinity of the wall.

Since the work of Carman, there have been many other studies which have investigated

rcp in confined systems [120, 125–127]. These studies have shown that near the boundary, particles tend to pack into layers giving rise to a fluctuating local porosity with distance from the wall, ultimately affecting the macroscopic properties of highly confined systems. Other studies have examined the packing of granular particles in narrow silos, focusing on the influence of confinement on stresses between particles and the wall [128–131]. Nearly all of these studies did not directly measure the local packing or any local packing parameters with relation to distance from the side wall, with the exception of a few experiments that used x-ray imaging to view the structure of confined packings. In these experiments the packings were monodisperse, facilitating highly ordered packing near the boundary, with measurements carried out at only a few different container size to particle size ratios [122, 127].

Even with the history of work on the study of *rcp* in confined geometries, there is little known about how sensitive the structure of the packing near the boundary is to small changes in the confining width. For example, prior work found non-monotonic dependence of ϕ_{rcp} on container size but only at extremely small containers with narrow dimensions h only slightly larger than the particle diameter d , that is, $h \approx 3d$ or smaller [115, 121, 123]. However, their data were not strong enough to look for such effects at larger container sizes. Additionally, primarily only confined monodisperse systems have received much attention, and these systems are susceptible to crystallization near flat walls which greatly modify the behavior [146]. (One group did study binary systems but they were unable to directly observe the structure [120].) Furthermore, two-dimensional confined systems have not been studied systematically, although they are relevant for a wide range of granular experiments [147].

In this chapter we address these questions using computer simulated *rcp* packings in confined geometries. In particular, we study binary mixtures to prevent wall-induced crystallization [224–226]. We create two-dimensional (2D) and three-dimensional (3D) packings with flat confining walls. In some cases the system is confined only along one dimension (with periodic boundaries in the other directions), and in other cases we confine the sample along all directions. Our simulations are carried out at many different and very closely spaced confining thicknesses spanning a large range of values to elucidate the effects small

changes in confining thickness has on the structure.

We find that confinement significantly modifies the *rcp* states, with lowered values for ϕ_{rcp} reflecting an inefficient packing near the walls. This inefficient packing persists several particle diameters away from the wall, although its dominant effects are only within 1-2 diameters. The behavior of ϕ_{rcp} is not monotonic with increasing sample thickness, reflecting the presence of boundary layers near the walls.

Understanding the character of random close packing in confined geometries may be relevant for non-close-packed confined situations [132]. For example, when a liquid is confined, its structure is dramatically changed; particles form layers near the wall, which ultimately affects the properties of the liquid [133–138]. The shearing of confined dense colloidal suspensions shows the emergence of new structures not seen before [139]. The flow of granular media through hoppers [140, 141] or suspensions through constricted micro- and nanofluidic devices [142–145] can jam and clog, costing time and money.

One of our own motivations for this work was to help us understand prior experiments by the Weeks group which studied the confinement of colloidal particles [84]. A dense suspension of colloidal particles behaves similarly to a glass [68]. For traditional glass-formers, many experiments have studied how confinement modifies the glass transition; samples which have a well-characterized glass transition in large samples show markedly different properties when confined to small samples [132, 226–232]. In our experimental work, the colloidal particles had much slower diffusion rates when confined between two parallel walls [84]. However, the experiments were difficult and the authors only examined the behavior of a dense suspension at a few specific thicknesses. As noted above, in this current work we investigate how particles pack for a finely-spaced set of thicknesses, to look for non-monotonic behavior of the packing that might have been missed in the experiment. A second related question is whether confinement effects on glassy behavior are due to boundary effects or finite size effects [233]. Our results show that boundaries significantly modify the packing, which may in turn modify behavior of these confined molecular systems [132].

3.2 Algorithm

Our aim is to quantify how a confining boundary alters the structure of randomly closed packed (*rcp*) disks in 2D and spheres in 3D, and in particular to study how this depends on the narrowest dimension. This section presents our algorithm for 2D packings first, and then briefly discusses differences for the 3D algorithm.

In 2D, our system consists of a binary mixture of disks containing an equal number $N/2$ large disks of diameter d_l and small disks of diameter d_s with size ratio $\sigma = d_l/d_s = 1.4$. For each configuration, disks are packed into a box of dimensions L_x by L_y . For most simulations we discuss, there is a periodic boundary condition along the x -direction and two fixed hard boundaries (walls) along the y -direction, although as discussed below, in some cases we consider periodic boundaries in all directions or fixed boundaries in all directions.

Each configuration is generated using a method adapted from Xu *et al.* [234] which is an extension of a method proposed by Clarke and Wiley [235]. This method is briefly summarized in Fig. 3.1. Infinitesimal particles are placed at random [236] in the system, gradually expanded and moved at each step to prevent particles from overlapping. When a final state is found such that particles can no longer be expanded without necessitating overlap, the algorithm terminates. Near the conclusion of the algorithm, we alternate between expansion and contraction steps to accurately determine the *rcp* state.

In particular, while the final state found is consistent with hard particles (no overlaps allowed), the algorithm uses a soft potential at intermediate steps [234], given by

$$V(r_{ij}) = \frac{\epsilon}{2} (1 - r_{ij}/d_{ij})^2 \Theta(1 - r_{ij}/d_{ij}), \quad (3.1)$$

where r_{ij} is the center to center distance between two disk i and j , ϵ is a characteristic energy scale ($\epsilon = 1$ for our simulations), $d_{ij} = (d_i + d_j)/2$, and $\Theta(1 - r_{ij}/d_{ij})$ is the Heaviside function making V nonzero for $r_{ij} < d_{ij}$. Simulations begin by randomly placing disks within a box of desired dimensions and boundary conditions with the initial diameters chosen such that $\phi_{initial} \ll \phi_{rcp}$. In the initial state particles do not overlap and the total energy $E = 0$.

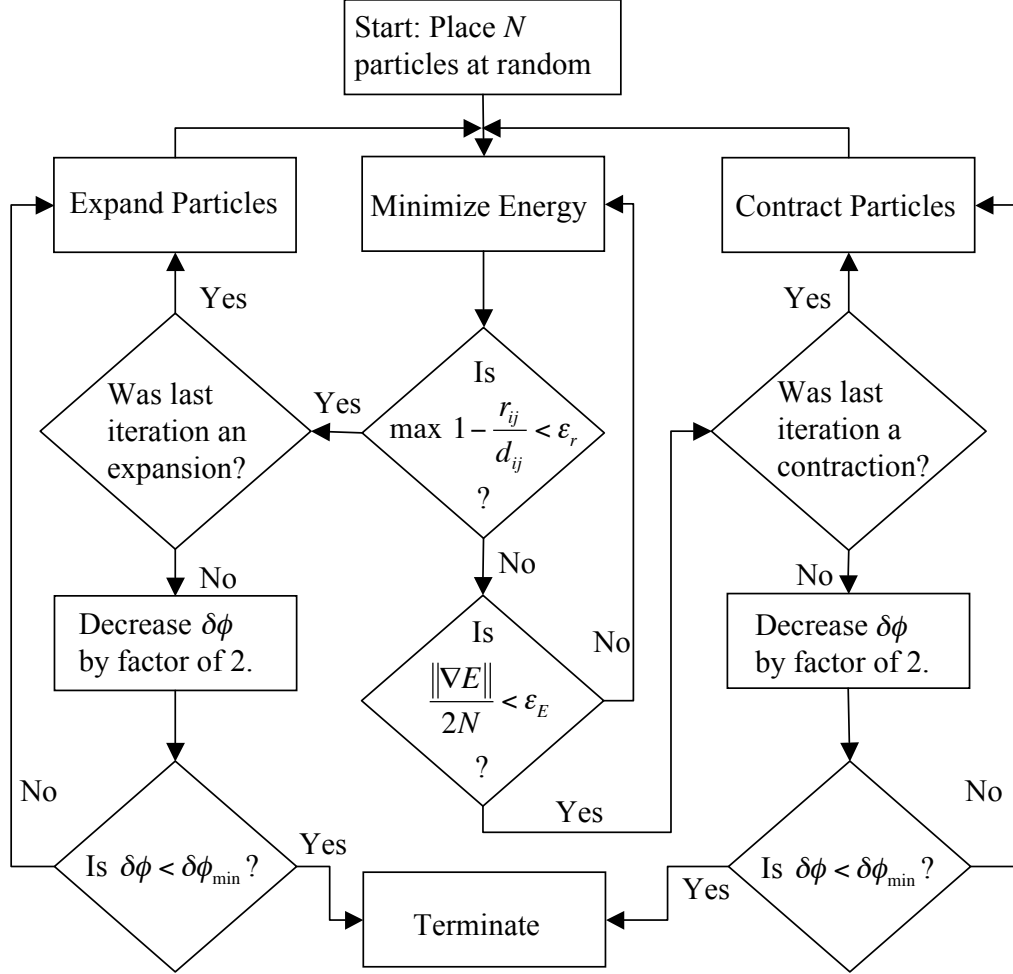


Figure 3.1: A flow chart outlining our algorithm for computing *rcp* configurations.

Next all disk diameters are slowly expanded subject to the fixed size ratio $\sigma = 1.4$ and ϕ changing by $\delta\phi$ per iteration; we start with $\delta\phi = 10^{-3}$. After each expansion step, we check if any disks overlap, by checking the condition $1 - r_{ij}/d_{ij} > \epsilon_r = 10^{-5}$ for each particle pair. Below this limit, we assume the overlap is negligible. If any particles do overlap ($E > 0$), we use the non-linear conjugate gradient method [237] to decrease the total energy by adjusting the position of disks so they no longer overlap ($E = 0$). In practice, one energy minimization step does not guarantee we have reached a minimum within the desired numerical precision. Thus this step can be repeated to further reduce the energy if $E > 0$. We judge that we have reached a nonzero local minimum if the condition $\|\nabla E\|/(2N) < \epsilon_E = 10^{-7}$ is found, where $\|\nabla E\|$ is the magnitude of the gradient of E . Physically speaking this is the average

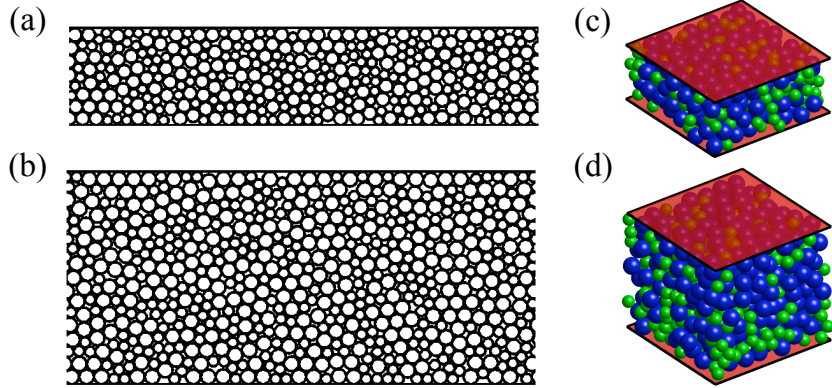


Figure 3.2: Illustrations of 2D and 3D configurations generated using the algorithm described in Sec. 3.2. (a) 2D configuration for $h = 10$. (b) 2D configuration with $h = 20$. (c) 3D configuration with $h = 5$ where blue (dark gray) represents big particles and green (light gray) represents small particles. (d) 3D configuration with $h = 10$.

force per particle, and the threshold value (10^{-7}) leads to consistent results.

If we have such a state with $E > 0$, this is not an *rcp* state as particles overlap. Thus we switch and now slowly contract the particles until we find a state where particles again no longer overlap (within the allowed tolerance). At that point, we once again begin expansion. Each time we switch between expansion and contraction, we decrease $\delta\phi$ by a factor of 2. Thus, these alternating cycles allow us to find an *rcp* state of non-overlapping particles (within the specified tolerance) and determine ϕ_{rcp} to high accuracy. We terminate our algorithm when $\delta\phi < \delta\phi_{\min} = 10^{-6}$. In practice, we have tested a variety of values for the thresholds ϵ_r , ϵ_E , and $\delta\phi_{\min}$ and find that our values guarantee reproducible results as well as reasonably fast computations. Our algorithm gives an average packing fraction of $\phi_{rcp} = 0.8420 \pm 0.0005$ for 40 simulated *rcp* states containing 10,000 particles with periodic boundary conditions along both directions. Our value of ϕ_{rcp} is in agreement with that found by Xu et al. [234].

The above procedure is essentially the same as Ref. [234]; we modify this to include the influence of the boundaries. To add in the wall, we create image particles reflected about the position of the wall; thus particles interact with the wall using the same potential, Eqn. 3.1.

Additionally, we wish to generate packings with pre-specified values for the final confining height $h = L_y/d_s$. (This allows us to create multiple *rcp* configurations with the same

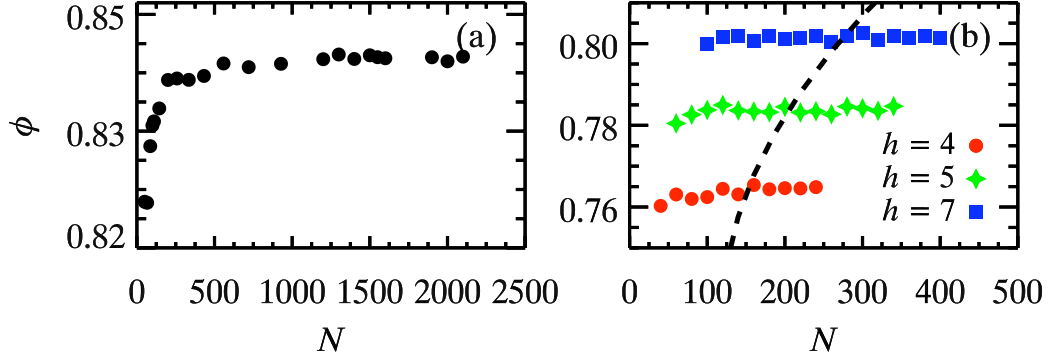


Figure 3.3: (a) Average ϕ_{rcp} for periodic packings of different N . The standard error in the average value is roughly the size of the data symbol. (b) Average ϕ_{rcp} for confined packings of different N . The standard error in the average value is roughly the size of the data symbol. The dashed black line indicates packings with a $L_x/d_s = 40$. To the left of the dashed line are packings with $L_x/d_s < 40$ and to the right are packings with $L_x/d_s > 40$

h .) We impose h by affinely scaling the system after each step, so that the upper boundary is adjusted by $L_y = hd_s$ and each disk's y -coordinate is multiplied by the ratio $L_{y,i+1}/L_{y,i}$, where $L_{y,i}$ and $L_{y,i+1}$ are the confining widths between two consecutive iterations. Thus while d_s gradually increases over the course of the simulation, L_y increases proportionally so that the nondimensional ratio h is specified and constant. Some examples of our final *rcp* states are shown in Fig. 3.2.

To ensure we will have no finite size effects in the periodic direction, we examined how ϕ_{rcp} depends on system size to determine for which L_x there are no finite size effects. In Fig. 3.3(a) we plot the dependence of ϕ_{rcp} on N for a periodic square boundary condition ($L_x = L_y$). In the plot, ϕ_{rcp} is the average ϕ_{rcp} found for multiple runs with the same N . We see that ϕ_{rcp} rapidly increases for small N and levels off to a constant value independent of N once $N > 1500$. For $N = 1500$ this give a box size of roughly $L_x = 40$ by $L_y = 40$. Therefore, we should be able to simulate confined packings of $L_x > 40$ without any finite size effects in the periodic direction. To check this, we simulate highly confined packings of $h = 4, 5$, and 7 for various N , and the results are shown in Fig. 3.3(b). We have also included in the figure, a dashed black line indicating packings with a $L_x/d_s = 40$. To the left of the dashed line are packings with $L_x/d_s < 40$ and to the right are packings with $L_x/d_s > 40$. The figure shows for packings with $L_x/d_s > 40$ (to the right of the black

dashed line), ϕ_{rcp} is independent of the number of particles, confirming that packings with $L_x > 40$ will not have any finite size effects in the periodic direction. Thus, to ensure no finite size effects in the periodic direction we have chosen N for each simulation such that $L_x/d_s \approx 50$.

In 3D, our system consists of a binary mixture of spheres containing an equal number $N/2$ large spheres of diameter d_l and small spheres of diameter d_s with a size ratio $\sigma = d_l/d_s = 1.4$. Spheres are packed into a box of dimensions L_x by L_y by L_z , with periodic boundaries along the x - and z -directions and a fixed hard boundary along the y -direction. Each configuration is generated using the same particle expansion and contraction method described above and the same initial values for $\delta\phi$ and the terminating conditions. For each configuration $L_x = L_z$, $h = L_y/d_s$, and N is chosen so that $L_x/d_s > 10$. Our choice of $L_x/d_s > 10$ is not large enough to avoid finite effects. However, in order to acquire the large amount of data needed in a reasonable amount of time we intentionally choose a value of L_x/d_s below the finite size threshold. Trends observed in the 2D analysis will be used to support that any similar trends seen in 3D are real and not the result of the finite periodic dimensions. Note that in 3D we will show cases where $h > L_x/d_s$ resulting in the confining direction being larger than the periodic direction, and this may affect the structure of final configurations; however, we will not draw significant conclusions from those data.

Overall, it is not known if this algorithm produces mathematically rigorously defined random close packed states [95, 218, 234, 238]. However, the goal of this chapter is to determine empirically the properties of close-packed states in confinement, and we are not attempting to extract mathematically rigorous results. For example, we are not as interested in the specific numerical values of ϕ_{rcp} that we obtain, but rather the qualitative dependence on h . As noted in the introduction, different computational and experimental methods for creating *rcp* systems have different outcomes, and so it is our qualitative results we expect will have the most relevance.

Note that for the remainder of this chapter, we will drop the subscript *rcp*, and it should be understood that discussions of ϕ refer to the final state found in each simulation run, $\phi_{rcp}(h)$.

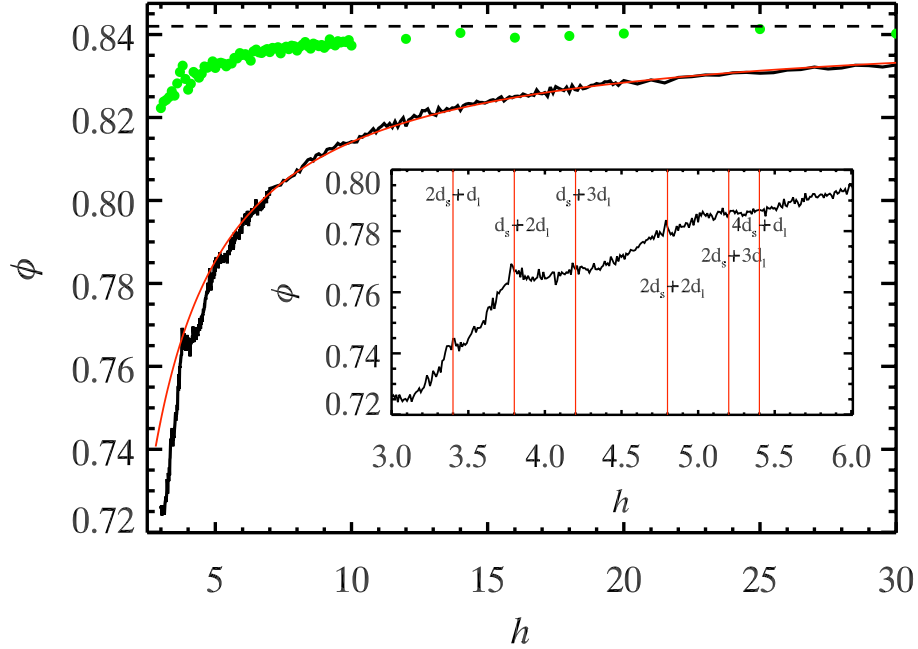


Figure 3.4: The black curve is the average packing fraction ϕ found by averaging at least 10 2D configurations together for various confining widths h ; recall that h has been nondimensionalized by d_s , the small particle diameter. The red curve (dark gray) is a fit using Eqn. 3.5 which finds $\phi_{rcp} = 0.842$ in the limit $h \rightarrow \infty$; the value for ϕ_{rcp} is indicated by the black dashed line. The green (light gray) data points are $\phi(h)$ computed for many configurations with the confining wall replaced by a periodic boundary. The inset is a magnified view of the region for $h \leq 6$ to better show the large variations within this range. The vertical lines in the inset are located at “special” h values where peaks and plateaus appear.

3.3 Results on 2D Packing

We begin by generating many 2D configurations with h between 3 - 30 and computing the packing fraction for each, as shown by the black curve in Fig. 3.4. This plot shows that confinement lowers ϕ , with the influence of the walls being increasingly important at lower h . The lowering of ϕ with confinement is most likely due to structural changes in the packing near the confining boundary. We know that any alteration in particle structure from a *rcp* state must be “near” the wall because as $h \rightarrow \infty$ we expect to recover a packing fraction of ϕ_{rcp} , implying that in the infinite system the “middle” of the sample is composed of an *rcp* region. Extrapolating the data in Fig. 3.4 to $h \rightarrow \infty$ we find $\phi_{h \rightarrow \infty} = \phi_{rcp} = 0.842$ which is essentially a test of our method. The extrapolation (red curve in Fig. 3.4) was carried out

by assuming that to first order $\phi \sim \phi_{h \rightarrow \infty} - C/h$ for large h , where $\phi_{h \rightarrow \infty} = \phi_{rcp}$ (the bulk value for the *rcp* packing) and C is a fitting parameter.

The data in Fig. 3.4 begin to deviate from the fit for $h \lesssim 6$, and furthermore $\phi(h)$ is not monotonic. While some of the variability is simply noise due to the finite number of disks N used in each simulation, some of the variability is real. The inset in Fig. 3.4 shows a magnified view of the region $3 \leq h \leq 6$. The vertical lines in this inset are located at specific values of h that can be expressed as the integer sums of the two particle diameters. For instance, the first vertical line near the y -axis is located at $h = 2d_s + d_l$. These lines are placed at some h values where $\phi(h)$ has notable spikes or plateaus. These lines suggest that there exist special values of h where the confining thickness is the right width so that particles can pack either much more efficiently or much less efficiently than nearby values of h . Intriguingly, these special h values do not appear to be as pronounced at all possible integer sums, but instead only the selected few drawn in the figure. However, given the apparent noisy fluctuations (despite averaging over a very large number of simulations), we cannot completely rule out that local maxima and minima might also exist at other combinations of d_s and d_l . Somewhat surprisingly, we do not observe large peaks corresponding to integer combinations of $(\sqrt{3}/2)d_s$ or $(\sqrt{3}/s)d_l$ which would suggest hexagonal packing, the easiest packing of monodisperse disks in 2D; whereas the observed peaks of $\phi(h)$ suggest square-like packing.

To measure structural changes in particle packing as a result of confinement we start by examining the variations in the local number density ρ with distance y from the confining wall. We define ρ to be the average number of particles per unit of area along the unconfined direction. For a given location y , we count the number of particles in a region of area $L_x \Delta y$ and divide by this area, choosing Δy to be of a size such that the results do not depend sensitively on the choice, but also so that we can get reasonably localized information. Figure 3.5 is a plot of $\rho(y)$ for 100 configurations averaged together at $h = 30$. This plot shows oscillations in particle density which decay to a plateau. The oscillations near the wall are indicative of particles layering in bands. Above $y \gtrsim 6d_s$, noise masks these oscillations. This supports our interpretation, that confinement modifies the structure near the walls but not in the interior. Furthermore, the rapidity of the decay to the plateau seen in Fig. 3.5

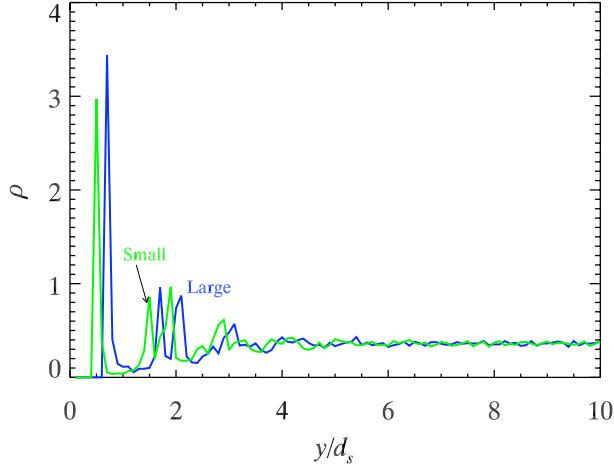


Figure 3.5: A plot of the number density $\rho(y)$ for 100 2D configurations at $h = 30$ averaged together. The plot is constructed by treating the small and big particles separately and using bins along the confining direction of width $\Delta y = 0.1d_s$.

suggests that confinement is only a slight perturbation to systems with overall size $h \gtrsim 6$.

The details of the density profiles in Fig. 3.5 also suggest how particles pack near the wall. The small particle density (solid line) has an initial peak at $y = 0.5d_s$, indicating many small particles in contact with the wall, as their centers are one radius away from $y = 0$. Likewise, the large particle density (dashed line) has its initial peak at $y = 0.7d_s = 0.5d_l$, indicating that those particles are also in contact with the wall. This is consistent with the pictures shown in Fig. 3.2(a,b), where it is clear that particles pack closely against the walls. Examining again the small particle number density in Fig. 3.5 (solid line), the secondary peaks occur at $y = 1.5d_s$ and $y = 1.9d_s = 0.5d_s + 1.0d_l$, which is to say either one small particle diameter or one large particle diameter further away from the first density peak at $y = 0.5d_s$. This again is consistent with particles packing diameter-to-diameter, rather than “nesting” into hexagonally packed regions. Similar results are seen for the large particles (dashed line) which have secondary peaks at $y = 1.0d_s + 0.5d_l$ and $y = 2.1d_s = 1.5d_l$.

To confirm that these density profile results apply for a variety of thicknesses h , and more importantly to see how these results are modified for very small h , we use an image representation shown in Fig. 3.6. To create this image, density distributions of different h are each separately rescaled to a maximum value of 1. Every data point within each distribution is then made into a gray scale pixel indicating its relative value; black is a

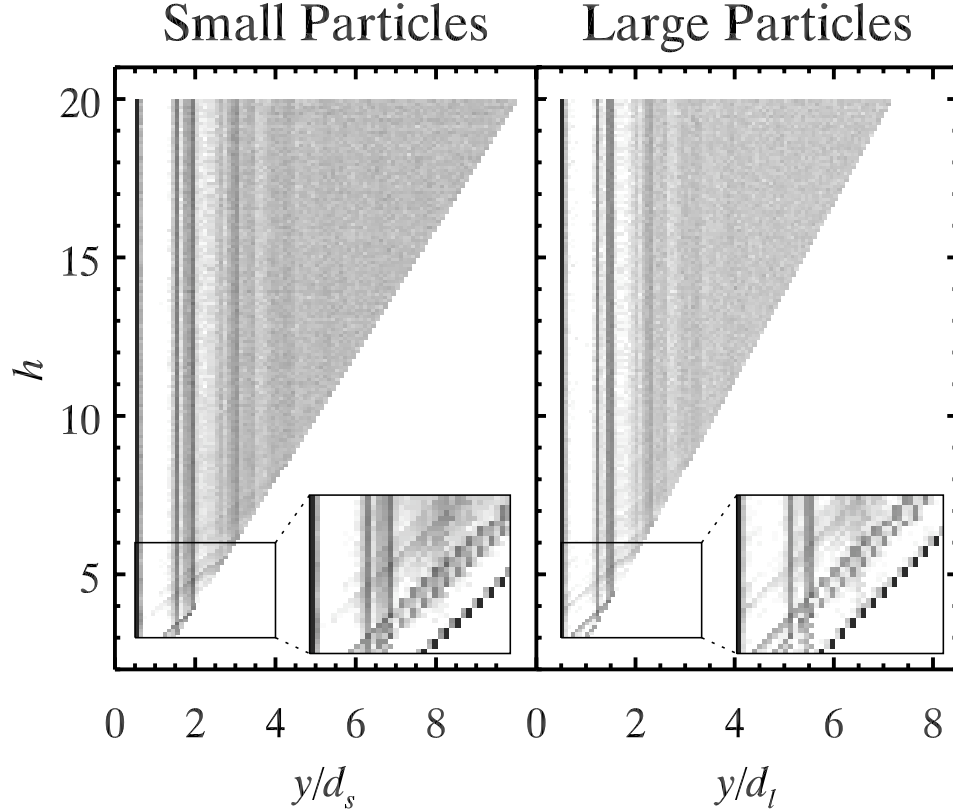


Figure 3.6: An image representation constructed for the purpose of comparing 2D $\rho(y)$ distributions at many different h . The intensities have been logarithmically scaled. The vertical pixel width is 0.1, the left plot horizontal pixel width is 0.2, and the right plot horizontal pixel width is 0.14. The inset include data for $y > h/2$, unlike the entire plot which only shows data for $y < h/2$.

relative value of 1, and white is a relative value of 0. The vertical axis is the confining width and the horizontal axis is the distance y from the bottom wall. Each horizontal slice (constant h) is essentially the same type of distribution shown in Fig. 3.5. The white space on the right side of Fig. 3.6 arises because the distribution is only plotted for the range $0 \leq y \leq h/2$. The distributions are symmetric about $y = h/2$, and by averaging the distribution found for the range $0 \leq y \leq h/2$ with the distribution found for the range $h/2 \leq y \leq h$, the statistics are doubled. The areas shown in the insets are magnified views where the full range $0 \leq y \leq h$ is being shown.

In Fig. 3.6 there are vertical strips of dark areas, once again indicating that particles are forming layers. The width of these strips widens and the intensity lessens farther from

the wall. In each plot, the first vertical black strip is sharply defined and located at one particle radius, illustrating that small and big particles are in contact with the wall. Finally, the location and width of each layer remains essentially the same for different h , suggesting that layering arises from a constraint imposed by the closest boundary. Given that the first layer of particles always packs against the wall, this imposes a further constraint on how particles pack in the nearby vicinity. The consistency in the location and width of the second layer for all h demonstrates that the constraint of the first layer always produces a similar packing in the second layer, essentially independent of h . Continuing this argument, each layer imposes a weaker constraint on the formation of a successive layer, allowing for the local packing to approach rcp far from the wall.

In the magnified views of Fig. 3.6, the vertical dark lines show the layering of particles induced by the left boundary and the angled dark lines show the layering of particles induced by the right boundary. We see that for small h these sets of lines overlap and intersect, meaning that there is a strong influence from one boundary on the packing within the layers produced by the other boundary. This may explain the variations seen in $\phi(h)$ for small h in Fig. 3.4. In particular, it is clear that at certain values of h , the layers due to one wall are coincident with the layers due to the other wall, and this suggests why $\phi(h)$ has a higher value for that particular h . Given that the layer spacings correspond to integer combinations of d_s and d_t , the coincidence of layers from both walls will correspond to integer combinations of d_s and d_t , and this thus gives insight into the peak positions shown in the inset of Fig. 3.4.

As described above, the influence of the walls diminishes rapidly with distance y away from the wall. In particular, for the local number density $\rho(y)$, we observe that the asymptotic limit $\rho(y \rightarrow \infty) = 0.362$ for the curves shown in Fig. 3.5 is in agreement with the theoretical number density of an rcp configuration $\rho_{rcp} = 4\phi_{rcp}/\pi(1 + \sigma)$. To quantify the approach to the asymptotic limit, we define a length scale from a spatially varying function $f(y)$ using:

$$\lambda = \frac{\int y [f(y) - f(y \rightarrow \infty)]^2 dy}{\int [f(y) - f(y \rightarrow \infty)]^2 dy}. \quad (3.2)$$

In this equation $f(y)$ is an arbitrary function where the value of λ quantifies the weighting

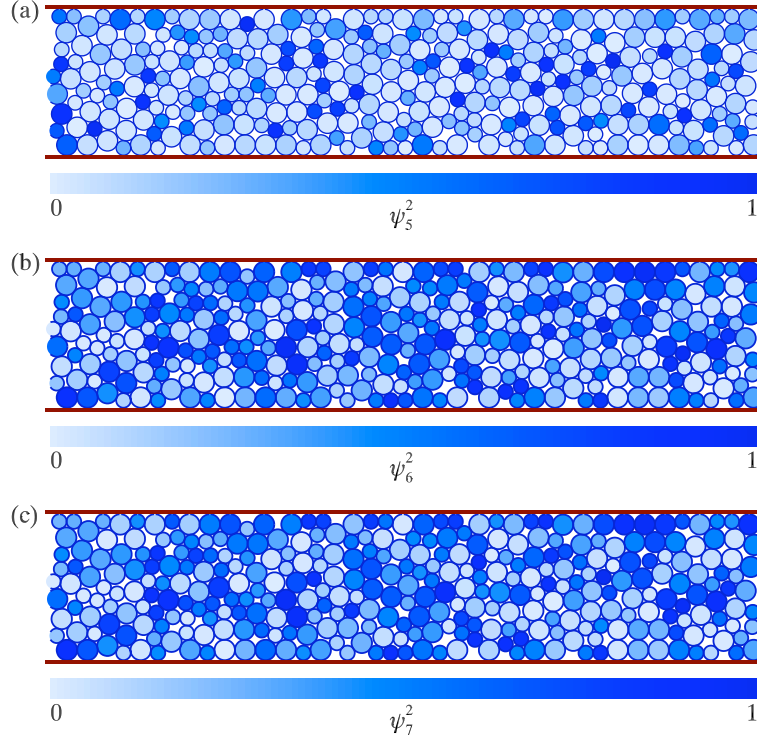


Figure 3.7: Drawings illustrating the conceptual meaning of (a) ψ_5 , (b) ψ_6 , and (c) ψ_7 . Darker colored particles have neighbors that are packed more like an ideal regular n -sided polygon as compared to lighter drawn particles. The configuration of particles is the same for all panels, and are drawn from a simulation with $h = 10$. Note in (b) that there are no large patches of high ψ_6 , demonstrating that there are no large crystalline domains.

of $f(y)$. For simple exponential decay $f(y) = Ae^{(-y/\lambda)}$, Eqn. 3.2 gives $\lambda = \lambda'/2$. Using $f(y) = \rho(y)$ we find $\lambda = 0.85d_s$ and $\lambda = 0.72d_s$ for the small particle curve and big particle curve in Fig. 3.5 respectively, suggesting that the transition from wall-influenced behavior to bulk *rcp* packing happens extremely rapidly.

To further investigate the convergence of the local packing to *rcp* more closely we analyze the local bond order parameters ψ_n , which for a disk with center of mass r_i are defined as

$$\psi_n(r_i) = \frac{1}{n_b} \sum_j e^{ni\theta(r_{ij})}. \quad (3.3)$$

The sum is taken over all j particles that are neighbors of the i th particle, $\theta(r_{ij})$ is the angle between the bond connecting particles i and j and an arbitrary fixed reference axis, and n_b is the total number of $i - j$ bonds [239]. (These are not physical bonds, but indicate

that two particles are nearest neighbors, where the definition of nearest neighbor is set by the first minimum of the pair correlation function.) The square magnitude $\psi_n^2 = \psi_n^* \psi_n$ is bounded between zero and one; the closer ψ_n^2 is to 1, the closer the local arrangement of neighboring particles are to an ideal n -sided polygon. Here ψ_n^* is the complex conjugate of ψ_n . Figures 3.7(a-c) are drawings illustrating the concept of ψ_n^2 using a 2D configuration with $h = 10$. Particles with larger ψ_n^2 are drawn darker. These figures have no large clusters of dark colored particles, demonstrating that there are no large crystalline domains (i.e. particles are randomly packed).

For a highly ordered monodisperse packing $\langle \psi_6^2 \rangle$ would be the most appropriate choice for measuring order because of the ability for monodisperse packings to form hexagonal packing. However for a bidisperse packing with size ratio $\sigma = 1.4$, the average number of neighbors a small particle will have is 5.5 and the average number of neighbors big particles will have is 6.5. Therefore, a bidisperse packing of this kind will have a propensity to form local pentagonal, hexagonal, and heptagonal packing, and to properly investigate how the local packing varies we examine $\langle \psi_5^2 \rangle$, $\langle \psi_6^2 \rangle$, and $\langle \psi_7^2 \rangle$. We compute the average values $\langle \psi_5^2 \rangle$, $\langle \psi_6^2 \rangle$, and $\langle \psi_7^2 \rangle$ for all configurations as a function of y , and averaging together all $\langle \psi_n^2 \rangle$ distributions for configurations with $h \geq 16$ to improve statistics. This averaging can be justified by considering that oscillations in $\rho(y)$ in Fig. 3.5 for $y/d_s > 10$ are quite small. Thus this averaging improves our statistics for the range $0 < y/d_s < 5$ where the largest oscillations occur, without skewing the data. In the end nearly 10,000 configurations are averaged together, producing the curves shown in Fig. 3.8(b-d). This figure shows the spatial variations of $\langle \psi_5^2 \rangle$, $\langle \psi_6^2 \rangle$, and $\langle \psi_7^2 \rangle$ for small and big particles separately and both particles combined. All curves show fluctuations that decay with distance from the wall, and show local order within and between layers. Figure 3.8(a) has been added so comparisons between the location of the oscillations in $\rho(y)$ and $\langle \psi_n^2 \rangle(y)$ can be made.

Each successive layer has less orientational order than the previous layer with $\langle \psi_n \rangle$ eventually decaying to an asymptotic limit. To characterize a length scale for these curves we compute λ using Eqn. 3.2 for each curve shown in Fig 3.8(b-d). From the nine curves, we find that the mean value of $\lambda = (1.00 \pm 0.24)d_s$. The length scales found for these curves are once again less than the largest particle diameter. No striking difference is found

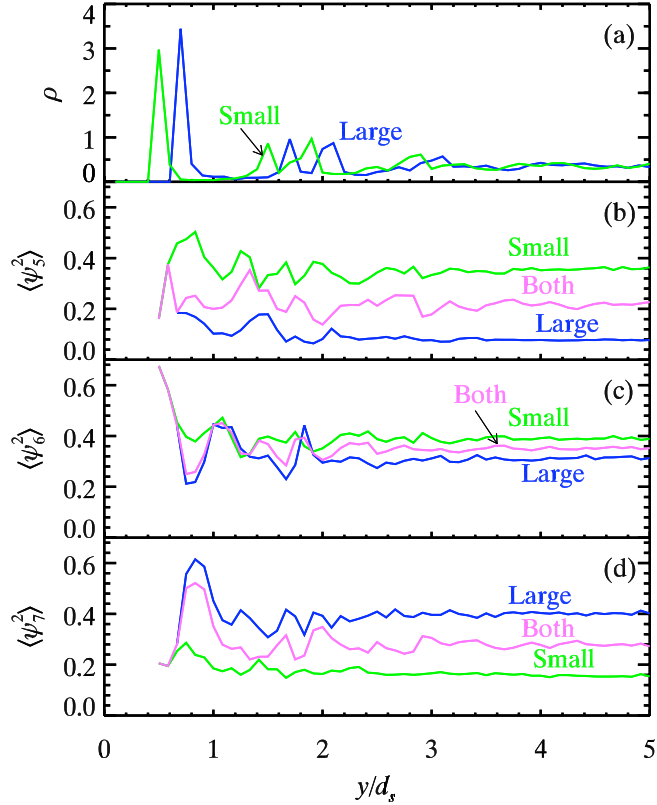


Figure 3.8: (a) is a plot of the local number density $\rho(y)$ for 2D configurations of big and small particles separately. (b) - (d) are plots of $\langle\psi_n^2\rangle(y)$ for small (green/light gray) and big particles (blue/dark gray) separately, and both sizes together (light purple/medium gray) where (b) is $\langle\psi_5^2\rangle$, (c) is $\langle\psi_6^2\rangle$, and (d) is $\langle\psi_7^2\rangle$. The length scales determined from these curves for small, large, and both species are $\lambda_{5,s} = 1.2$, $\lambda_{5,l} = 1.1$, $\lambda_{5,b} = 1.4$, $\lambda_{6,s} = 0.8$, $\lambda_{6,l} = 0.9$, $\lambda_{6,b} = 0.8$, $\lambda_{7,s} = 1.1$, $\lambda_{7,l} = 0.7$, and $\lambda_{7,b} = 1.0$ (all in terms of d_s).

between the different order parameters or between the different particle sizes; specific values of λ are given in the figure caption. (Note that the asymptotic limits of all $\langle\psi_n\rangle$ plots are in agreement with the average values found for 40 unconfined 10,000 particle simulations averaged together, confirming that the local packing converges to an *rcp* arrangement far from the walls.)

Next, we wish to distinguish the structural influence of the flat wall from the finite size effects. We perform simulations where the confining wall is replaced by a periodic boundary with periodicity h ; thus particles cannot form layers. In this case, the packing fraction still decreases as h is decreased, as shown by the green curve (light gray) in Fig. 3.4, although the effect is less striking than for the case with walls (black curve). A likely explanation

for the decrease in ϕ with confinement is the long range structural correlations imposed along the constricted direction; in other words, if there is a particle located at (x, y) that particle is mirrored at $(x, y - h)$ and $(x, y + h)$ by the periodic boundary. We know from the pair correlation function [109, 111] of *rcp* configurations that structural correlations exist over distances of many particle diameters, although of course these are weak at larger distances. Thus the periodicity forces a deviation from the ideal *rcp* packing, that becomes more significant as h decreases. By definition *rcp* is the most random densely packed state, and thus any perturbations away from this state must have lower packing fractions. However, this is not nearly as significant as the constraint imposed by the flat wall, as is clear comparing the green (light gray) data and the black data in Fig. 3.4.

3.4 Results on 3D Packing

For the 3D packings we start by investigating $\phi(h)$, shown as the black points in Fig. 3.9. As observed in the 2D case, ϕ is reduced as a result of confinement. However, unlike the 2D system, there does not appear to be a series of “special values” of h that give rise to peaks and plateaus, other than a hump near $h = 3.75$. The lack of substructure may be due to the smaller size in x and z , in contrast with the 2D simulations which had large sizes in the unconfined direction.

Next we investigate the local number density $\rho(y)$ (the average number of particles per unit area along the unconfined directions) for $h = 25$, shown in Fig. 3.10(a). The data are constructed by averaging together 100 configurations. The curve shows fluctuations that decay with distance from the wall, eventually reaching a plateau. Using Eqn. 3.2, we obtain decay lengths $\lambda_{3D} = 0.77d_s$ and $0.73d_s$ for the small and large particle curves respectively. These length scales are similar to the length scales obtained in the 2D case ($\lambda_{2D} = 0.85d_s$ and $0.72d_s$ for small and large particles).

To compare all 3D $\rho(y)$ distributions for different h we construct the image representation used to compare 2D configurations in Fig. 3.6. The data for the 3D configurations are shown in Fig. 3.11. Again there are dark vertical strips arising from particles forming layers near the wall. Like in 2D, the density approaches the “bulk” *rcp* value far from the

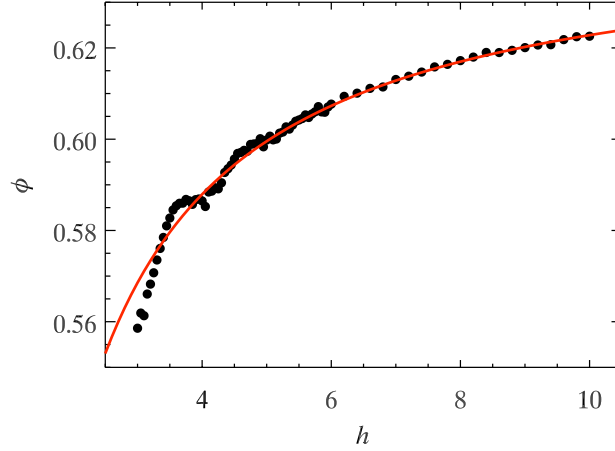


Figure 3.9: The black data points are the average packing fractions of 3D configurations at various h . The red (dark gray) curve is a fit from our model Eqn. 3.5. For each h at least 10 configurations were averaged together.

wall.

In 2D, we also noted that the structure is modified near the wall, as measured by the ψ_n order parameters. To investigate structural ordering in 3D, we use a local structural parameter sensitive to ordering [195, 240]. We start by defining

$$\hat{q}_{i,6} = \frac{1}{n_j K} \sum_j Y_{6m}(\theta_{ij}, \phi_{ij}). \quad (3.4)$$

In the above equation $m = \{-6, \dots, 0, \dots, 6\}$, and thus $\hat{q}_{i,6}$ is a 13 element complex vector which is assigned to every particle i in the system. The sum in Eqn. 3.4 is taken over the j nearest neighbors of the i th particle, n_j is the total number of neighbors, and K is a normalization constant so that $\hat{q}_{i,6} \cdot \hat{q}_{i,6} = 1$. For two particles i and j that are nearest neighbors, $Y_{6m}(\theta_{ij}, \phi_{ij})$ is the spherical harmonic associated with the vector pointing from particle i to particle j , using the angles θ_{ij} and ϕ_{ij} of this vector relative to a fixed axis. Next, any two particles m and n are considered “ordered neighbors” if $\hat{q}_{m,6} \cdot \hat{q}_{n,6} > 0.5$ [195, 240]. Finally, we quantify the local order within the system by the number of ordered neighbors N_b a particle has.

Figure 3.10(b) is a plot of the average number of ordered neighbors particles have $\langle N_b \rangle$ as a function of distance y from the wall. In comparison with Fig. 3.10(a), this plot shows

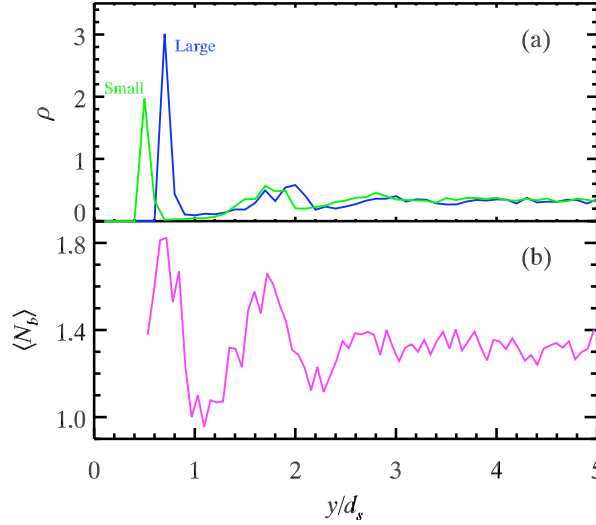


Figure 3.10: (a) is plot of $\rho(y)$ for 3D configurations for small and big particles separately. The plot is constructed using bins of width $\delta y = 0.1d_s$ along the confining directions. (b) is a plot of the average number of ordered bonds $\langle N_b \rangle(y)$.

that local order is mostly seen within layers, not between layers. Also we see that $\langle N_b \rangle$ converges to an asymptotic value of ≈ 1.3 , confirming that the system is disordered. (Values of $N_b \geq 8$ are considered crystalline [195].) We use Eqn. 3.2 to characterize a length scale for the decay in $\langle N_b \rangle$, giving $\lambda = 1.3d_s$. The asymptotic limit of $\langle N_b \rangle(y)$ in Fig. 3.10(b) agrees with the average value of N_b found for 15 large simulations with 2,500 particles and periodic boundary conditions, confirming that the local structure in the confined case converges to the bulk *rcp* state far from the walls.

Our results show that in both 2D and 3D, confinement induces changes in structural quantities near the walls, with a decay towards the “bulk” values characterized by length scales no larger than d_l . The only prior work we are aware of with related results are a computational study [126] and an experimental study [127] of collections of monodisperse particles confined in a large silo. The simulation by Landry et al. primarily focused on the force network within the silo. They show one plot of the local packing fraction as a function of distance from the silo wall. Similar to our results, this local packing fraction showed fluctuations that decayed monotonically. In their paper they state a decay length of $\approx 4d_l$; however, it appears that they drew this conclusion by estimating the value by

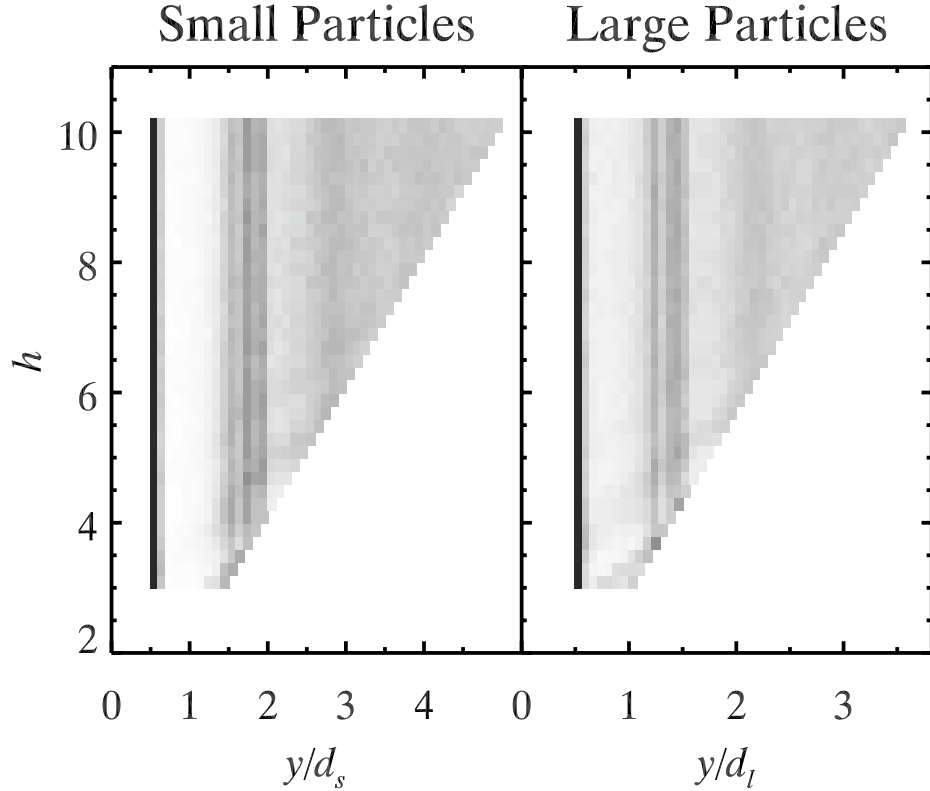


Figure 3.11: An image representation comparing the number density distributions of 3D configurations for many different h . Black pixels represents a relative value of 1 and white represent a relative value of 0. A gray scale is used to represent relative values between 0 and 1. The pixel widths are $0.1d_s$ horizontally and 0.2 vertically.

eye. Applying Eqn. 3.2 to their data we find λ on the order of d_l , close to the value found in our simulations. The experimental study by Seidler et al. reported on the local bond orientational order parameter which showed oscillation that decayed with distance from the wall. They reported a decay length of $\lambda \approx d_l$ using an exponential fit. The length scales from these two studies are slightly larger than those found in our work.

3.5 Modeling the Effects of Confinement on Volume Fraction

Our results for $\phi(h)$ can be understood with a simple model incorporating an effective boundary layer and a bulk like region. This model is an extension of one proposed by Verman, Banerjee, Brown and Hawsley in 1946 [116, 117]. In Fig. 3.12 we show a configuration of particles confined between two plates and divided into two boundary layers and a bulk

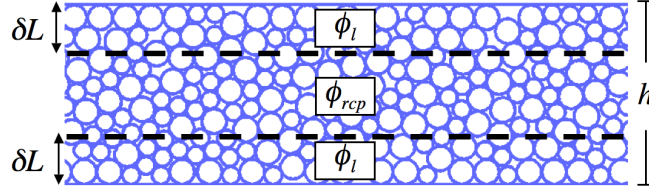


Figure 3.12: Illustration of our model for $\phi(h)$. Our model breaks a configuration with confining width h into three regions. The boundary layers are approximated to have a packing fraction ϕ_l and persist a distance δL into the sample, and the middle “bulk” region is approximated to have a packing fraction ϕ_{rcp} .

region. The model of Refs. [116, 117] approximates the effect of the walls by assuming a lower effective volume fraction, ϕ_l , to the boundary layers. The central region is assumed to have a volume fraction ϕ_{rcp} , equal to the volume fraction for an infinite system. Of course, this model is an over-simplification that coarse-grains the density near the walls, which in reality varies smoothly and non-monotonically in space as Sec. 3.3 and 3.4 demonstrates. Furthermore, this model will not capture the non-monotonic behavior of Figs. 3.4 and 3.9, but it should capture the overall trend with h . In the original model of Refs. [116, 117], it was conjectured that the thickness of the boundary layer is $\delta L = 1d$ for monotonic particles of diameter d . The experimental data they tested the model with were too limited to carefully check this assumption; here, we extend their model by allowing δL to be a free parameter. (Clearly, our results such as Fig. 3.8 confirm that $\delta L \approx 1d_s$ is a reasonable order of magnitude.)

Using this simple model, ϕ can be approximated by the weighted average $\phi = \frac{h-2\delta L}{h}\phi_{rcp} + \frac{2\delta L}{h}\phi_l$ (in either 2D or 3D, with different values of the parameters depending on the dimension). Reducing this equation further we obtain

$$\phi = \phi_{rcp} - \frac{C}{h}, \quad (3.5)$$

where we define the boundary packing parameter $C = 2\delta L(\phi_{rcp} - \phi_l)$, which quantifies how the wall influences the packing fraction near the boundary. Note that this is the same form for $\phi(h)$ obtained from considering a 1st order correction in terms of $1/h$ and is the same empirical form assumed by Scott [217].

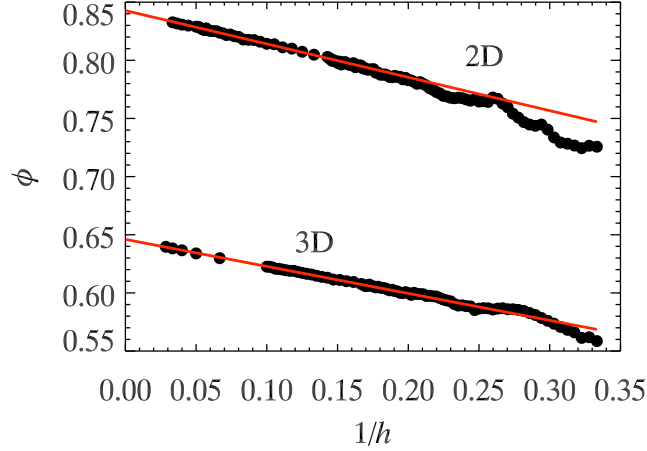


Figure 3.13: The upper black curve is a plot of $\phi(1/h)$ for 2D configurations, and the red (dark gray) line going through the curve, is a fit from our model. Likewise, the lower black curve is a plot of $\phi(1/h)$ for 3D configurations with the red (dark gray) line going through the curve being another fit from our model.

We investigate the merit of this model by fitting the data to Eqn. 3.5 which only contains two fitting parameters, ϕ_{rcp} and C . The data in both Fig. 3.4 and Fig. 3.9 are fitted to Eqn. 3.5. The fits are shown as the red lines in these earlier figures, and also in Fig. 3.13, where the data are plotted as functions of $1/h$ to better illustrate the success of this model. The fits give for 2D $\phi_{rcp} = 0.844$ and $C = 0.317$ and for 3D $\phi_{rcp} = 0.646$ and $C = 0.233$. Both fits give values for ϕ_{rcp} that are slightly larger, but not by much, than ϕ_{rcp} reported earlier in the paper. In Fig. 3.13 it can be seen that the packing fraction for large $1/h$ dip significantly below the fitting line, due to the fluctuations in $\phi(h)$ for small h ; this is responsible for the over estimate in ϕ_{rcp} . When the data for both curves are fitted for $h \geq 8$ ($1/h < 0.125$) the actual values for ϕ_{rcp} are obtained. The dipping of the $\phi(h)$ curve below the line for large $1/h$ is perhaps due to the layering each wall produces affecting the layering produced by the opposite wall (see Figs. 3.6 and 3.11). Another possibility is that this reflects the breakdown of the model when $h \approx 2\delta L$. That is, when the thickness of the sample is such that the two boundary layers begin to overlap, the model would not be expected to work.

To provide further credence to the model we also perform 2D *rcp* simulations with a fixed circular boundary or a fixed square boundary. Figure 3.14 shows a plot of $\phi(h)$

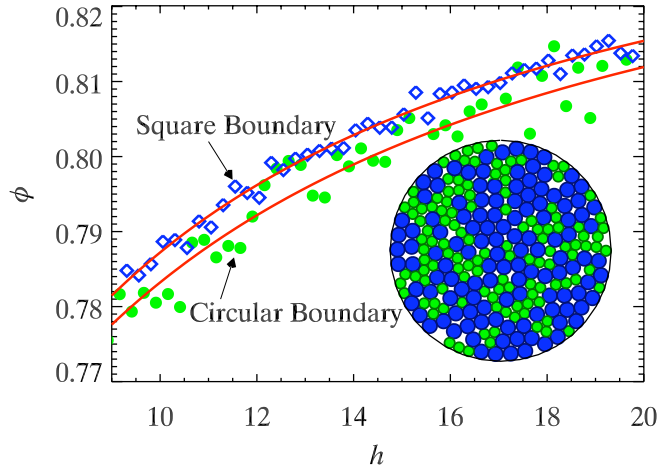


Figure 3.14: The black curve is the packing fraction dependence of random close packed 2D disk enclosed within a circular boundary on the diameter of the enclosure. The red (light gray) curve is a fit from our model, and the image on the lower right is an rcp configuration confined in a circular boundary with $h = 21$. Small particles are rendered as green (medium gray) and large particles are rendered as blue (dark gray).

for both the circular boundary (green points) and the square boundary (blue points). In analogy with our prior results, h is the wall-to-wall distance: for the circular boundary, h is the diameter normalized by d_s , and for the square boundary h is the side length L normalized by d_s . As before with two parallel flat boundaries, we see that ϕ increases to an asymptotic limit. Note that the data are noisier for two reasons. First, given our algorithm (Sec. 3.2, for samples that are confined in all directions, we can only choose the number of particles we start with; we have no control over the final system size when the particles jam. Due to random fluctuations, we can run the simulations many times with the same number of particles and each time find different final value for h (and ϕ_{rcp}). This limits our ability to sample enough data at a particular h to reduce the noise and/or look for non-monotonic effects. Second, there are many fewer particles in these simulations, thus reducing the statistics. Normally this could be compensated by increasing the number of simulation runs, but the first problem (lack of precise control over h) frustrates this.

Adapting the model to a circular boundary with diameter h or to a square boundary

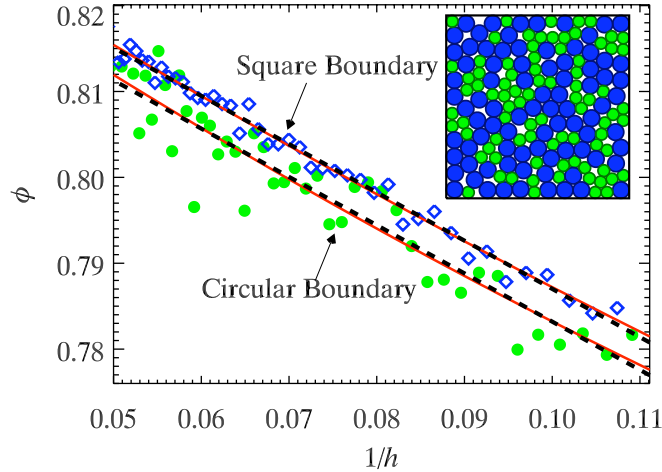


Figure 3.15: $\phi(1/h)$ for disks confined within a circular boundary or square boundary, as indicated; the data are the same as Fig. 3.14 along with the definitions of h . The red (light gray) curves are fits to the data using our model. The black dashed lines are linear fits to the data. The image at the upper right is an rcp configuration confined in a square boundary with $h = 15.5$. Small particles are rendered as green (medium gray) and large particles are rendered as blue (dark gray).

with side length h , we find that both situations give

$$\phi(h) = \phi_{rcp} - \frac{2C}{h} + \frac{2C\delta L}{h^2}, \quad (3.6)$$

where $C = 2\delta L(\phi_{rcp} - \phi_l)$ as before.

Fig. 3.14 is fitted to this model and is shown as the red lines. For the circular boundary the fit gives $\phi_{rcp} = 0.846$, $C = 0.371$, and $\delta L = 1.51$, and for the square boundary the fit gives $\phi_{rcp} = 0.848$, $C = 0.340$, $\delta L = 1.14$. These fits give ϕ_{rcp} values close to the ϕ_{rcp} values reported earlier in the chapter and C values similar, but slightly different, than that found for one fixed flat boundary. Interestingly the fits give values of δL commensurate to the λ values previously computed, demonstrating that the boundary produces a thin boundary layer of about 1-2 characteristic particle sizes thick that is primarily responsible for lowering the global packing fraction.

Finally, to demonstrate the quality of the fits we show a plot of $\phi(1/h)$ in Fig. 3.15. In this figure the red line is the fit from Eqn. 3.6 while the black dashed line is a linear fit in $1/h$. Both fits are reasonable, and the data are not strong enough to determine which

is better. We thus note only that the model suggests we should use the quadratic fit for these cases, and that the values of δL obtained are reasonable ones. δL is a third parameter for the fit; fortunately, extending the model to a 3D case where all directions are confined would predict a cubic fit but without introducing a fourth parameter.

3.6 Conclusion

In this chapter, we have shown how a confining boundary alters the structure of random close packing by investigating simulated *rcp* configurations confined between rigid walls in 2D and 3D. We find that confinement lowers the packing fraction, and induces heterogeneity in particle density where particles layer in bands near the wall. The structure of the local packing decays from a more ordered packing near the wall to a less ordered packing in the bulk. All measures of local order and local density decay rapidly to their bulk values with characteristic length scales on the order of particle diameters. Thus, the influence of the walls is rapidly forgotten in the interior of the sample, with confinement having the most notable effects when the confining dimension is quite small, perhaps less than 10 particle diameters across.

The results are well-fit by a three-parameter model dating back to 1946 [116, 117], with our results suggesting that the third parameter (an effective boundary layer thickness) should be a free parameter rather than constrained. To first order, this model suggests that the primary influence of the boundary is quantified by one parameter, C , which is the product of a length scale and a volume fraction reduction. This parameter, the boundary packing parameter, thus quantifies the overall influence of a boundary, near that boundary. Since the model assumes nothing about container shape, this model should equally apply to other geometries as well.

These findings have implications for experiments investigating the dynamics of densely packed confined systems (i.e. colloidal suspensions or granular materials). For example, our work shows that for small h the packing fraction has significant variations at small h (most clearly seen in 2D, for example Fig. 3.4). For dense particulate suspensions with $\phi < \phi_{rcp}$, flow is already difficult. By choosing a value of h with a local maximum in

$\phi_{rcp}(h)$, a suspension may be better able to flow, as there will be more free volume available. Likewise, a poor choice of h may lead to poor packing and enhanced clogging. A microfluidic system with a tunable size h may be able to vary the flow properties significantly with small changes of h , but our work implies that control over h needs to be fairly careful to observe these effects. Of course, these effects will be obscured by polydispersity in many systems of practical interest; however, our work certainly has implications for microfluidic flows of these sorts of materials, once the minimum length scales approach the mean particle size.

Our work has additional implications for experiments on confined glasses [84, 132, 226–232]. As mentioned in the Sec. 3.1, confinement changes the properties of glassy samples, but it is unclear if this is due to finite size effects or due to interfacial influences from the confining boundaries [233]. Our results show that dense packings have significant structural changes near the flat walls, suggesting that indeed interfacial influences on materials can be quite strong at very short distances, assuming that the structural changes couple with dynamical behavior. Furthermore, the non-monotonic behavior of ϕ_{rcp} that we see suggests that experiments studying confined glassy materials could see interesting non-monotonic effects, if the sample thickness can be carefully controlled.

CHAPTER 4

Imaging and Image Analysis for 2D Experimental Model System

In the work presented in Chapters 6 and 7, our aim is to study the jamming transition and flow of 2D frictionless droplets using a new experimental model system we have developed. Our sample chamber for these experiments is designed to create a system of quasi-2D frictionless emulsion droplets, analogous to 2D granular systems of photoelastic disks, but without static friction [155]. The sample chamber consists of two microscope glass slides separated by a spacer (see Fig. 4.1). The chamber is filled with an oil in water emulsion, where the diameters of the emulsion droplets are larger than the gap distance between the microscope slides.

For the experiments we present in Chapters 6 and 7, it is essential to know the location of each droplet and the contact forces between droplets. In this chapter, we describe various

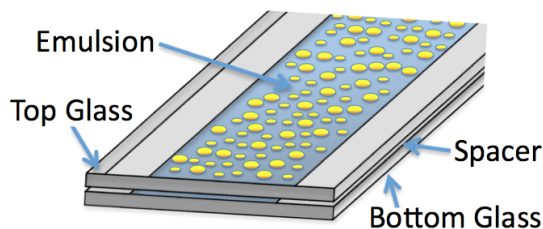


Figure 4.1: The above image is a schematic of our sample chamber where emulsion droplets are confined to a 2D plane by two microscope slides separated by either a $\sim 100 \mu\text{m}$ spacer (transparency film) or $\sim 180 \mu\text{m}$ spacer (glass coverslip).

aspects related to imaging our droplets and our algorithms to determine each droplet's perimeter and the contacts shared between neighboring droplets. Our algorithms were written in the Interactive Data Language (IDL), and at the end of each section the names of our IDL functions are listed. In the next chapter, Chapter 5, we discuss our method to determine the contact forces between droplets.

4.1 Imaging Droplets

To image our samples we use a Leica DM IRB bright field microscope with a MightTex 5 megapixel monochrome CMOS camera (model BCN-B050). For this particular microscope, we have many different objective lenses to control the magnification, and we typically use a $5\times$ or $1.6\times$ lens to image the samples. There is also an eye piece in front of the camera to separately adjust the magnification again, and we use either a $1\times$ and $0.55\times$ eye piece is commonly used.

Depending on our choice of the objective lens, eye piece, and oil phase the boundary of the droplets may look thicker. In Fig. 4.2, we show hexane and mineral oil droplets in water using different objective lenses and eye pieces. In all the images, the droplets are motionless and we imaged the same region within the sample. One obvious difference between the images is that the boundary is much thicker for the mineral oil droplets than the hexane droplets because the mineral oil has a larger index of refraction difference with water than hexane. When light from the microscope is incident on a droplet, the surface of the droplet refracts the light away. The larger the index of refraction difference between the water and oil phase, the larger the refraction. Since light is refracted away from a droplet's surface, the boundary of the droplet appears dark in the image. For hexane droplets in water, the index of refraction difference between the two phases is ≈ 0.04 , and for mineral oil droplets in water, the index of refraction difference between the two phases is ≈ 0.13 .

While the oil phase can dramatically change the thickness of the boundary, changing optical setups does not appear to have nearly as strong an effect. However, when changing optical setups, the intensity of the microscope lamp, the positioning of the condenser, and the optical resolution may all play a role in changing the thickness of the boundary. When

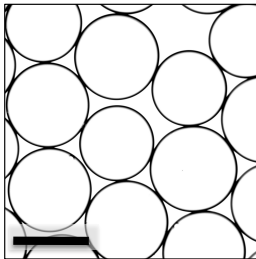
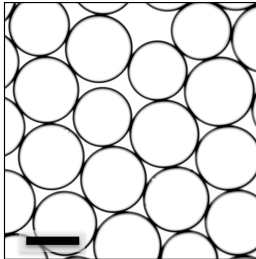
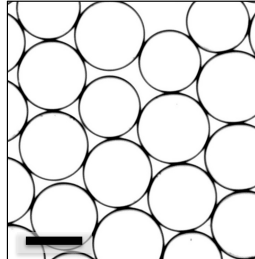
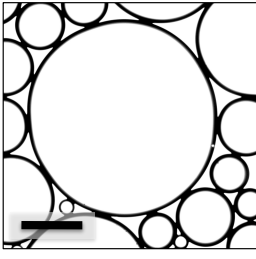
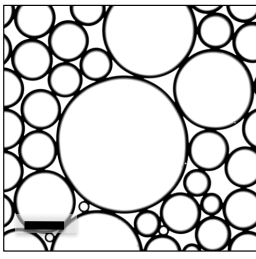
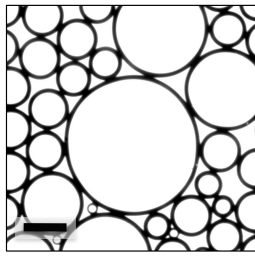
| | 5x Objective 1x Eye Piece | 5x Objective 0.55x Eye Piece | 1.6x Objective 1x Eye Piece |
|-------------|---|--|---|
| Resolution | 0.42 $\mu\text{m}/\text{pixel}$ | 0.77 $\mu\text{m}/\text{pixel}$ | 1.35 $\mu\text{m}/\text{pixel}$ |
| Hexane |  |  |  |
| Mineral Oil |  |  |  |

Figure 4.2: This figure shows hexane in water and mineral oil in water droplets imaged at different magnifications. Above the figures, are the magnifications and pixel size for the object lens and eye pieces used to image the droplets. Each image was taken over a larger region of the sample than seen in the figure. Each image was cropped to roughly the same field of view for easy comparison of any optical effects. Therefore, going left to right the images consist of less pixels per square inch. The scale bar in each image is 200 μm .

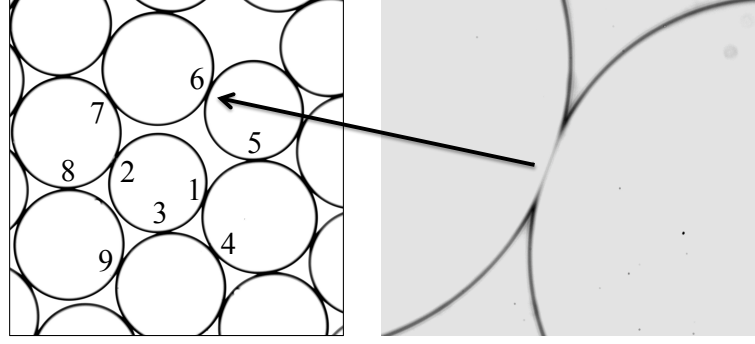
determining an empirical force law data is taken at a smaller pixel sizes than the pixel size we intend to use in studying the physics of jammed system. By using data taken at smaller pixel sizes we can obtain a more accurate force law, and therefore, the optical configuration is different between determining an empirical force law and studying the physics. Also depending on the experiment we may desire to take data at different pixel sizes. If possible, we would like not to have to determine an empirical force law for each optical configuration. An important variable in the empirical force law is a relative contact length Δl (see Sec. 5.2). Even if the contact length changes between two optical configurations, as long as the change in contact length is uniform, then Δl is independent of the optical configuration. Another parameter in the empirical force law is the radius of curvature. Unfortunately the thickness of the boundary does change the radius of curvature by a few microns between optical

configurations. This will introduce a systematic error to the radii of curvatures, in that all the radii will increase or decrease by a constant amount.

To quantify how the contact length changes with optical setup we measure the contact lengths of common droplets in contact in the images shown in Fig. 4.2. In addition to the images shown, we have also taken images of some of the contacts using a $20\times$ objective lens with a $1\times$ eye piece. This gives a pixel size of $0.11\ \mu\text{m}$. In Table 4.1 we show the contact lengths for various hexane droplets in contact. Above the table on the left is an image of hexane droplets taken with a $5\times$ objective and a $0.55\times$ eye piece. The right image is a close up of one of the contacts taken with a $20\times$ object lens and $1\times$ eye piece. In the left image we have numbered the different contacts to provide each contact with an identifier. The top table list the contact lengths for each contact. The contacts we measured individually by hand by looking closely at each contact and identifying the endpoints. We have ordered the contacts by their contact length to make it easier to spot any possible trends in how the contact lengths change with optical setups for larger contacts.

The values in the table show that as the pixel size increases (going right across the top table), the contact lengths increase. While we expect the contact lengths to change it is more important to know if the contact lengths change uniformly for all droplets. To quantify if the contact lengths change uniformly we show in the bottom table the difference δ in the contact lengths relative to the $20\times$ optical setup. Just below the δ values are the the mean and standard deviation in δ for all the data. We see that the mean in δL grows with increasing pixel size, but that the standard deviation in δL is fairly small. When measuring the contacts there is some noise. Judging by eye, the measurement errors are ± 11 pixel ($1.1\ \mu\text{m}$) noise in the $20\times/1\times$ setup, ± 2.8 pixel ($1.2\ \mu\text{m}$) noise in the $5\times/1\times$ setup, ± 1.4 pixel ($1.1\ \mu\text{m}$) noise in the $5\times/0.55\times$ setup, and ± 1.4 pixel ($1.9\ \mu\text{m}$) noise in the $\pm 1.6\times/1\times$ setup. This gives a measurement error of $\pm 2.3\ \mu\text{m}$ for $\delta_{5\times,1\times}$, $\pm 2.2\ \mu\text{m}$ for $\delta_{5\times,0.55\times}$, $\pm 3\ \mu\text{m}$ for $\delta_{1.6\times,1\times}$. Two standard deviations in δ is roughly the measurement error for the data and the range (Max - Min)/2 is close to the measurement error as well. Therefore, we can conclude that all the contact lengths change uniformly with optical setup.

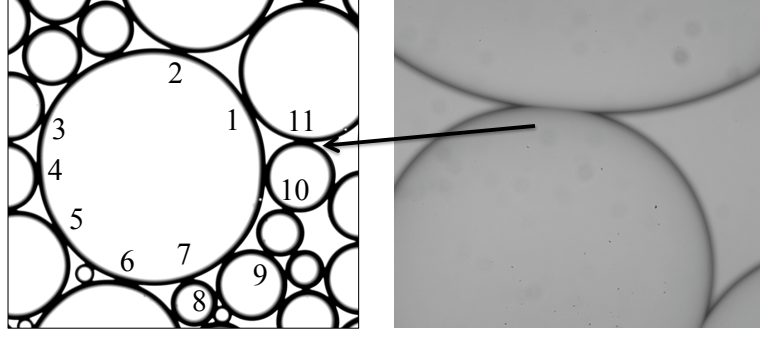
Similar to hexane droplets, we quantified how the different optical setups change the contact lengths for mineral oil droplets. In the case of hexane droplets all the contacts were



| Contact Number | 20× Obj/ 1× eye L [μm] | 5× Obj/1× eye L [μm] | 5× Obj/0.55× eye L [μm] | 1.6× Obj/ 1× eye L [μm] |
|----------------|--|--|---|---|
| 4 | 32.6 | 35.6 | 39.2 | 41.3 |
| 8 | 34.2 | 34.2 | 36.6 | 42.3 |
| 1 | 35.5 | 35.7 | 39.4 | 45.9 |
| 9 | 37.4 | 41.2 | 44.2 | 48.7 |
| 3 | 39.2 | 41.3 | 46.0 | 50.9 |
| 2 | 40.0 | 42.0 | 45.4 | 48.6 |
| 7 | 42.8 | 42.3 | 44.1 | 49.6 |
| 5 | 48.0 | 47.5 | 49.9 | 55.4 |
| 6 | 48.2 | 48.8 | 52.2 | 55.8 |

| Contact | δ [μm] | $\delta_{5\times,1\times}$ [μm] | $\delta_{5\times,0.55\times}$ [μm] | $\delta_{1.6\times,1\times}$ [μm] |
|---------------|----------------------------|--|---|--|
| 4 | - | 2.97 | 6.58 | 8.63 |
| 8 | - | -0.04 | 2.42 | 8.11 |
| 1 | - | 0.249 | 3.90 | 10.4 |
| 9 | - | 3.83 | 6.79 | 11.3 |
| 3 | - | 2.13 | 6.74 | 11.7 |
| 2 | - | 2.04 | 5.41 | 8.67 |
| 7 | - | -0.46 | 1.33 | 6.84 |
| 5 | - | -0.45 | 1.96 | 7.45 |
| 6 | - | 0.62 | 3.98 | 7.62 |
| Mean | - | 1.21 | 4.35 | 8.97 |
| Std | - | 1.49 | 2.02 | 1.65 |
| (Max - Min)/2 | - | 2.14 | 2.73 | 2.43 |

Table 4.1: Table showing the dependence of contact length on different optical setups for hexane droplets. The contacts used to compute a contact length are shown in the left image above the table. In the image various contacts have been labeled with an identifier to distinguish the contacts. The left image was taken with a 5× objective and a 0.55× eye piece. The right image is a close up of one of the contacts taken with a 20× object lens and 1× eye piece. The upper table gives the contact lengths for each optical setup and contact. The lower table gives the contact lengths δ relative to the contact length measured using the 20× objective lens. The final set of numbers at the bottom are the average, standard deviation, and range of minimum to maximum values in δ for each optical setup. When measuring the contacts there is some noise. Judging by eye, there appears to be ~ 11 pixel ($1.1 \mu\text{m}$) noise in the 20×/1× setup, 2.8 pixel ($1.2 \mu\text{m}$) noise in the 5×/1× setup, 1.4 pixel ($1.1 \mu\text{m}$) noise in the 5×/0.55× setup, and 1.4 pixel ($1.9 \mu\text{m}$) noise in the 1.6×/1× setup. This gives a measurement error of $2.3 \mu\text{m}$ for $\delta_{5\times,1\times}$, $2.2 \mu\text{m}$ for $\delta_{5\times,0.55\times}$, and $3 \mu\text{m}$ for $\delta_{1.6\times,1\times}$.



| Contact Number | 20× Obj/ 1× eye L [μm] | 5× Obj/1× eye L [μm] | 5× Obj/0.55× eye L [μm] | 1.6× Obj/ 1× eye L [μm] |
|----------------|--|--|---|---|
| 8 | 16.5 | 20.4 | 21.6 | 23.3 |
| 3 | 26.0 | 26.0 | 28.7 | 32.3 |
| 9 | 27.6 | 31.8 | 33.2 | 33.5 |
| 10 | 28.4 | 33.0 | 35.2 | 34.5 |
| 7 | 33.1 | 36.8 | 38.8 | 40.5 |
| 2 | 42.0 | 44.2 | 47.8 | 51.1 |
| 11 | 46.8 | 51.1 | 53.9 | 55.4 |
| 4 | 56.9 | 60.1 | 61.9 | 64.3 |
| 6 | 61.5 | 66.4 | 66.1 | 69.1 |
| 5 | 71.3 | 73.3 | 73.6 | 76.1 |
| 1 | 72.2 | 75.3 | 77.8 | 79.8 |

| Contact | δ [μm] | $\delta_{5\times,1\times}$ [μm] | $\delta_{5\times,0.55\times}$ [μm] | $\delta_{1.6\times,1\times}$ [μm] |
|---------------|----------------------------|--|---|--|
| 8 | - | 3.86 | 5.09 | 6.80 |
| 3 | - | 0.07 | 2.75 | 6.38 |
| 9 | - | 4.14 | 5.52 | 5.86 |
| 10 | - | 4.65 | 6.83 | 6.17 |
| 7 | - | 3.68 | 5.68 | 7.44 |
| 2 | - | 2.13 | 5.72 | 9.06 |
| 11 | - | 4.31 | 7.09 | 8.58 |
| 4 | - | 3.18 | 5.02 | 7.36 |
| 6 | - | 4.83 | 4.61 | 7.61 |
| 5 | - | 1.97 | 2.36 | 4.84 |
| 1 | - | 3.14 | 5.64 | 7.63 |
| Mean | - | 3.27 | 5.12 | 7.06 |
| Std | - | 1.35 | 1.40 | 1.22 |
| (Max - Min)/2 | - | 2.38 | 2.37 | 2.11 |

Table 4.2: Table showing the dependence of contact length on different optical setups for mineral oil droplets. The contacts used to compute a contact length are shown in the left image above the table. In the image various contacts have been labeled with an identifier to distinguish the contacts. The left image was taken with a 5× objective and a 0.55× eye piece. The right image is a close up of one of the contacts taken with a 20× object lens and 1× eye piece. The upper table gives the contact lengths for each optical setup and contact. The lower table gives the contact lengths δ relative to the contact length measured using the 20× objective lens. The final set of numbers at the bottom are the average, standard deviation, and range of minimum to maximum values in δ for each optical setup. When measuring the contacts there is some noise. Judging by eye, there appears to be ~ 11 pixel ($1.1 \mu\text{m}$) noise in the 20×/1× setup, 2.8 pixel ($1.2 \mu\text{m}$) noise in the 5×/1× setup, 1.4 pixel ($1.1 \mu\text{m}$) noise in the 5×/0.55× setup, and 1.4 pixel ($1.9 \mu\text{m}$) noise in the 1.6×/1× setup. This gives a measurement error of $2.3 \mu\text{m}$ for $\delta_{5\times,1\times}$, $2.2 \mu\text{m}$ for $\delta_{5\times,0.55\times}$, and $3 \mu\text{m}$ for $\delta_{1.6\times,1\times}$.

roughly the same in size, and we can not conclude if contact lengths change by different amount for different contact sizes. To ensure that we have good variability in contact lengths, for the mineral data we took images of highly polydisperse data as shown in Fig. 4.2.

In Table 4.2 we show how the contact lengths change for mineral oil. Similar to the hexane data, two standard deviations in δ is roughly the measurement error and the range (Max - Min)/2 is close to the measurement error. Also, δ does not show any dependence on the contact size, and therefore we can conclude that the optics uniformly adjust the contacts regardless of length.

4.2 Choosing an Oil Phase and Surfactant

We would prefer to use an optical setup with a water-oil mixture that gives images with droplet boundaries as thin as possible. However, there are several practical constraints we must consider. The first and most important constraint is that we must have a water-oil mixture with a large enough density difference between the two liquid phases to determine a force law. To calibrate the forces, we will incline the microscope to allow the droplets to rise up, press into one another, and deform (see Chapter 5). If the density difference between the two phases is too small, then the droplets will not significantly deform under the influence of gravity. The second constraint is that the oil phase cannot be harmful. When imaging the flow of these samples, we must leave the samples open to the atmosphere. Since we are not going to put the microscope and image apparatus in a fume hood and we do not want to expose the microscope to harmful solutions, this eliminates many organic liquids that could be used as an oil phase. Based on the first two constraints, this left us with a few possibilities, and the one we choose is mineral oil because it has a fairly large density difference with water, it's relatively cheap, and safe to use. At first we tried working with hexane droplets in a closed sample chamber since it has such a large density difference with water, but we found it hard to work with hexane because it is so volatile and we had to use a closed chamber.

In our first attempt to determine an empirical force law using mineral oil droplets, we used sodium dodecyl sulfate (SDS) as the surfactant to stabilize the droplets. We used

SDS because it is commonly used in the literature. We found that when the microscope was inclined the droplets were not deformed enough to determine an empirical force law over the range of deformations we are interested in studying. To get the droplets to deform more we changed the surfactant to lower the surface tension of the droplets. Since the deformability of an emulsion droplet is directly proportional to the surface tension, reducing the surface tension will make droplets more deformable under the same weight. We found that Fairy soap, a polymeric surfactant soap commonly used in Britain, gives the droplets a suitable surface tension so that they deform by an appropriate amount when the microscope is inclined.

4.3 Stitching Images Together

When studying a static system we can acquire very large high resolution images by taking a series of high resolution images of neighboring regions within the sample and later stitching the images together to form a single large image. To stitch the images together, we tried using freely available stitching software, but found that none of the software could accurately stitch the images together. The reason the auto stitching software fails for our images is because these algorithms try to identify and overlap distinct unique features shared between pairs of images. In our images, the type of features these stitching softwares look for are not present. Therefore, we had to write our own software. Typically we stitch anywhere from 100-400 images together.

To make it easier to write an in-house stitching software specific for this project, we acquire the images in a manner so that we know which images neighbor each other as shown in Fig. 4.3, and therefore our stitching algorithm does not need to determine which images neighbor each other. Our stitching software is designed to sequentially stitch neighboring images together by first stitching images 1 and 2 together, then stitching image 3 to images 1-2, then stitching image 4 to images 1-2-3 and so on. Therefore, our stitching software only ever needs to stitch two images together.

To stitch two neighboring images together, we overlap one image on top of the other image and shift the overlapping image around to find the best overlap. The algorithm

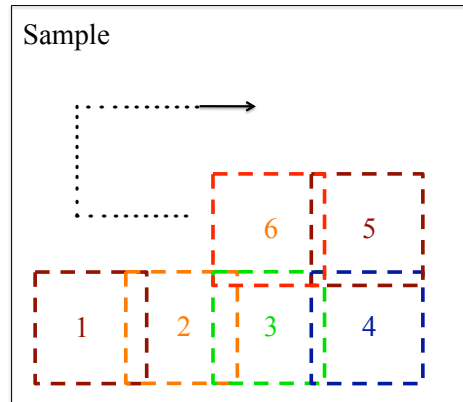


Figure 4.3: This figure illustrates the order in which we image neighboring regions in the sample. We start by taking an image at the left bottom corner. This image is labeled 1. Then we image a region in the sample to the right such that it overlaps with image 1. The second image is labeled 2. We then continue to image more regions in the sample as shown in the diagram.

works by shifting the overlapping image up, down, left, and right in increments of 16 pixels until it finds the best overlap, then shifts the overlapping image in increments of 8 pixels until it finds the best overlap, then shifts in increments of 4 pixels, then in increments of 2 pixels, and finally in increments of 1 pixel. To test how well two images overlap we calculate the cross correlation between the overlapping parts of the two images. If I_1 is the pixel intensities of the overlapping portion of the first image and I_2 is the pixel intensities of the overlapping portion of the second image, the cross correlation is $C = 1/(n - 1) \sum_k (I_1^k - \langle I_1 \rangle)(I_2^k - \langle I_2 \rangle) / (\sigma_{I_1} \sigma_{I_2})$, where n is the number of pixels in I_1 and I_2 , k indexes all the pixels within I_1 and I_2 , σ_{I_1} is the standard deviation in pixel values in I_1 , and σ_{I_2} is the standard deviation in pixel values in I_2 . When two overlapping images match well, they will be well correlated and have a value of C close to 1. For two completely different overlapping images, the correlation will be small and close to 0. We define the best overlap between the two images as the shift that maximizes C . In Fig. 4.4 we show our algorithms ability to automatically stitch neighboring images together.

List Of IDL Functions

- *kautoimage_align.pro*: Automatically determines the shift values for each image.

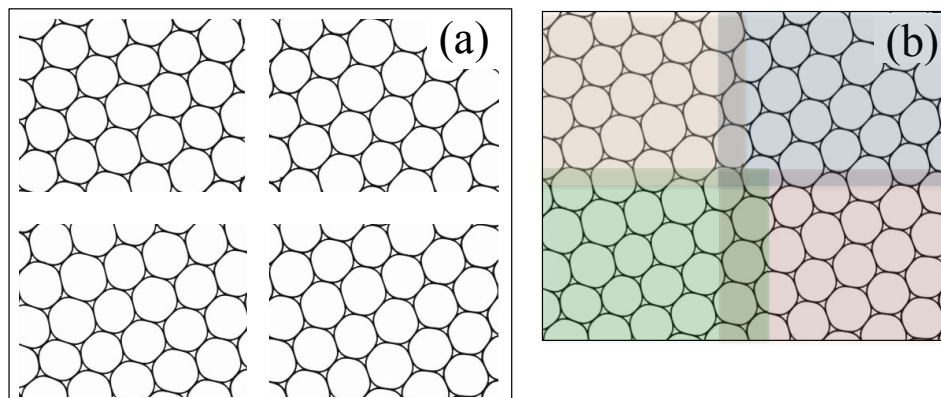


Figure 4.4: This figure shows the stitching of four images to produce a larger image. (a) shows four images of neighboring regions in the sample and (b) shows the four images stitched together to form one large image of a larger image.

- *kimage_merge.pro*: Uses shift values from *kautoimage_align.pro* to merge images into one single image.

4.4 Identifying Droplets and Their Center of Mass

After imaging a sample with the microscope, and possibly stitching together images, we start with a raw 8-bit image as shown in Fig. 4.5(a). We see in the figure that each droplet is defined by a black boundary that enclose a region of white pixels. To simplify the process of identifying the droplets we threshold the image by assigning all pixels below a threshold c equal to 0 and all other pixels are assigned a value of 1. The value of c will depend on how much the sample has been illuminated when the image was taken, but c is chosen so that the 1-bit image looks very similar to the 8-bit image as shown in Fig 4.5(c). By thresholding the image we can use **label_region** (a built IDL function) to easily locate enclosed clusters of pixels with value 1. These clusters are the pixels belonging to each droplet. In Fig. 4.5(d), we show each cluster found by **label_region** as separate regions with different shades of gray.

For each enclosed white region we can easily compute its center of mass from the location of the pixels within that region. The centers for each enclosed white region is shown in Fig. 4.5(d). In the image we see that some of the enclosed regions belong to droplets and others

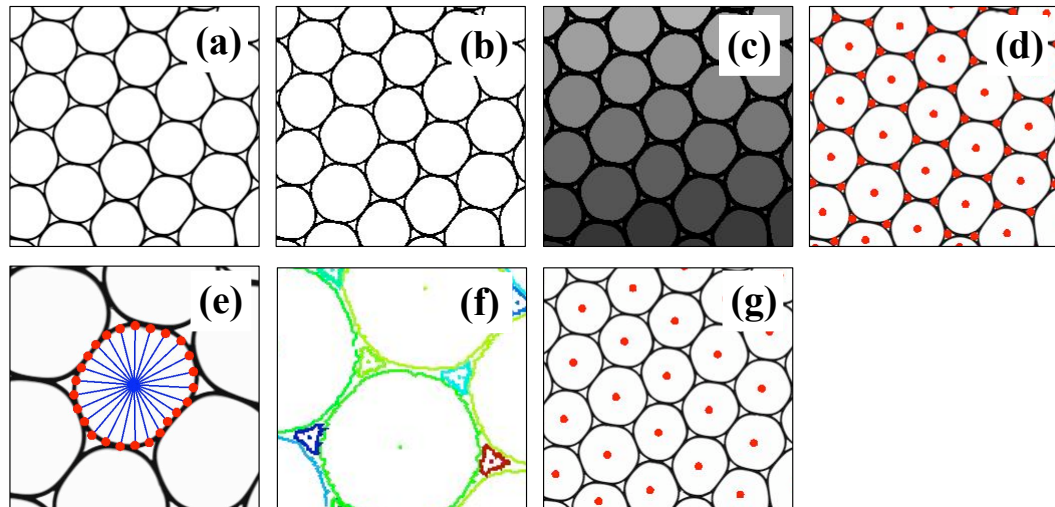


Figure 4.5: A scale bar has not been added, but for a sense of scale, the average droplet size is $210 \mu\text{m}$ in diameter. (a) raw 8-bit image of sample. (b) raw 8-bit image in (a) converted to a 1-bit image. (c) an image showing all the enclosed white regions found by the `label_region` function. Each enclosed white region has been given a unique id with each id shown as a unique shade of gray. (d) raw image with the center of mass of each enclosed white region shown as a red dot. (e) demonstrates how the perimeter of a droplet is found by radially looking outward from the center. (f) shows the perimeter of each droplet and void using different colors. (g) shows which enclosed white regions obey certain criteria defining a droplet.

belong to voids, and we must distinguish the two if we wish to only study the droplets. Before we distinguish the droplets and voids, we first locate the boundaries of each enclosed white region.

To identify the boundary, we look radially outward from the center of mass until we see the pixel value change from 1 to 0. This is shown in Fig. 4.5(e). The blue lines indicate the radial outward search from the center of mass, and the red dots indicate the pixels where the value changes from 0 to 1. After repeating this search on all the enclosed regions, we find the boundaries for each droplet and void, and the boundaries are shown in Fig. 4.5(f).

Two different metrics are used to distinguish between droplets and voids. First, there is a minimum droplet area threshold. For very dense packings as shown in Fig. 4.5, the droplets have an area much larger than the voids, and therefore we can easily distinguish between the two by area. More precisely, for an enclosed region with area A we define it to be a droplet if $A > A_{thres}$, where A_{thres} is the smallest area we expect to find for a

droplet. However, for binary packings near the jamming point, this criterion may not be suitable since the voids can be roughly the same size as a droplet. The second metric uses the convex hull of the perimeters. If a perimeter is convex, such as a droplet, then many of the points belonging to the perimeter will also belong to the convex hull. On the other hand, if the perimeter is concave, such as a void, then many of the points belonging to the perimeter will not belong to the convex hull. For a boundary consisting of n points, the convex hull will return n_h points that defines the largest convex polygon that can be formed using the n points on the boundary, where $n_h \leq n$. For a boundary that is mostly convex, $n_h \approx n$, while a boundary that is concave $n_h \ll n$. We define a boundary to be convex if $n_h > n_{thres}$, where n_{thres} is a user defined threshold. We compute the convex hull using **qhull**, a freely available software. To properly distinguish between droplets and voids, A_{thres} and n_{thres} are chosen by adjusting the values until all the droplets and voids are properly distinguished. Fig. 4.5(f) shows the centers of all enclosed regions satisfying the two criterion.

List Of IDL Functions

- *kfind_emulsions.pro*: Detects center and perimeter of each droplet in an image.

4.5 Describing the Perimeter with a Continuous Function

In this section, we discuss how to describe the perimeter of a droplet as a continuous function using a Fourier series. Once all the droplets have been found, we store each droplet's center of mass and the perimeter. We also fit the perimeter to a Fourier series and store the coefficients for later use. We fit the perimeter so that it can be described by an analytic function and to smooth out the noise present in the raw data. To fit the perimeter of a droplet to a Fourier series we first calculate the polar coordinations of the droplet's perimeter as $r_i = \sqrt{(x_i - x_{cm})^2 + (y_i - y_{cm})^2}$ and $\theta_i = \tan^{-1}((y_i - y_{cm})/(x_i - x_{cm}))$, where (x_i, y_i) are the cartesian coordinates of the perimeter and (x_{cm}, y_{cm}) is the center of mass of the

droplet. We fit the perimeter to Fourier series as

$$r = \sum_{n=0}^{n_c-1} (a_n \cos(n\theta) + b_n \sin(n\theta)), \quad (4.1)$$

where a_n and b_n are the fitting parameters and $2n_c - 1$ is the number of fitting coefficients. Using the following orthogonality relationships the perimeter can be analytically computed for a given n_c as.

$$\text{if } n = 0 \left\{ \begin{array}{l} a_0 = (1/\pi) \sum_i (r_{i+1} - r_i) \cos(n\theta_i - \Delta\theta/2) \\ b_0 = 0 \end{array} \right. \quad (4.2)$$

$$\text{if } n > 0 \left\{ \begin{array}{l} a_n = (2/\pi) \sum_i (r_{i+1} - r_i) \cos(n\theta_i - \Delta\theta/2) \\ b_n = (2/\pi) \sum_i (r_{i+1} - r_i) \sin(n\theta_i - \Delta\theta/2), \end{array} \right. \quad (4.3)$$

where $\Delta\theta$ is the increment in θ in the polar coordinate. In the previous section, we discuss that the perimeter of the droplet is identified by doing radially outward searches from the center. The radially search is done in uniform increments of either $\Delta\theta = 2\pi/201$ or $\Delta\theta = 2\pi/401$. For low resolution images the perimeter is defined by 200 pixels and for high resolution images the perimeter is defined by 400 pixels. These number are chosen because these are roughly the number of actual pixels the boundary of a droplet occupies.

Before fitting the perimeter we must choose a value for n_c . The number of fitting coefficients has to be large enough such that the shape of the perimeter is well represented, but not too large such that a significant amount of the noise is also captured. In Figure 4.6 we show $r(\theta)$ for a droplet as the black data points, and fit $r(\theta)$ to a Fourier series using $n_c = 2, 6,$ and 10 . As n_c increases the fits improve, and for $n_c = 10$, the fit sufficiently describes the perimeter. The actual image of the droplet represented in Fig. 4.6 is shown in Fig. 4.7, with the various $n_c = 2, 6,$ and 10 Fourier fits drawn over the perimeter. For $n_c = 10$, the actual image shows that the perimeter is well described by a Fourier series.

Using the Fourier series fits we can easily calculate many quantities related to a droplet defined not by the experimental data points, but instead by the Fourier series fit. We have

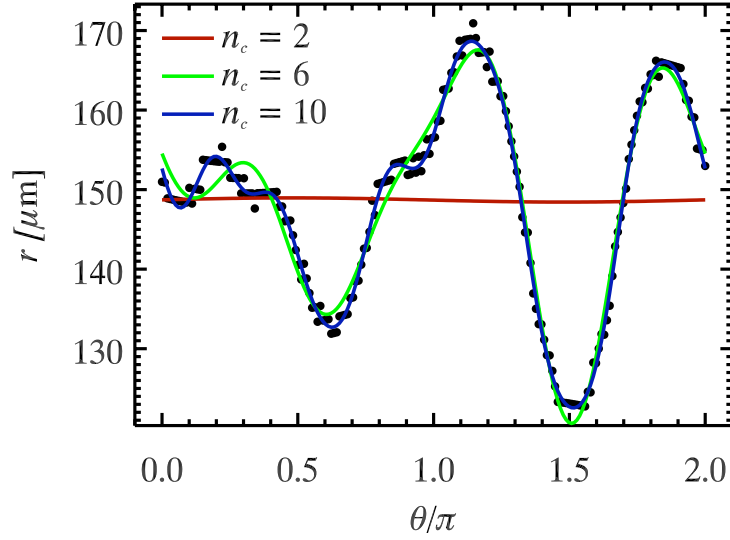


Figure 4.6: The black data points represent the perimeter in polar coordinates of the droplet shown Fig. 4.7. The perimeter is fitted to a Fourier series using different n_c .

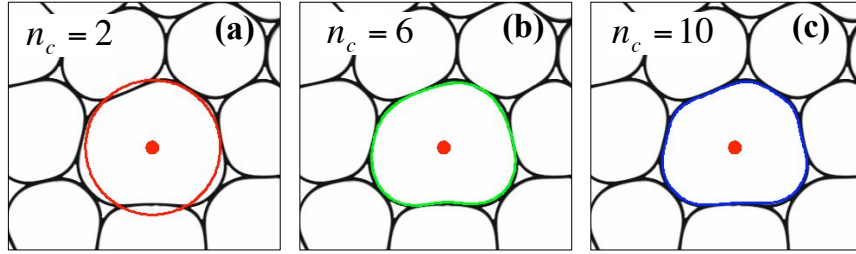


Figure 4.7: (a) droplet boundary fitted to a Fourier series using $n_c = 2$. (b) droplet boundary fitted to a Fourier series using $n_c = 6$. (c) droplet boundary fitted to a Fourier series using $n_c = 10$.

included a few quantities that below are used to define each droplet's center of mass and area.

Center of Mass: For a droplet defined by the Fourier series, the center of mass will be

$$x'_{cm} = x_{cm} + \frac{\int_0^{2\pi} \cos(\theta) r^3 d\theta}{\int_0^{2\pi} r^2 d\theta}$$

$$y'_{cm} = y_{cm} + \frac{\int_0^{2\pi} \sin(\theta) r^3 d\theta}{\int_0^{2\pi} r^2 d\theta},$$

where (x'_{cm}, y'_{cm}) is the center of mass of a droplet defined by the Fourier series and r is

defined in Eqn. 4.1. When computing the center of mass we could try to simplify the above equations, but since the computational cost is so low we numerically integrate the equations. Compared to the experimental data, the center of mass differs by less than a pixel. In most cases this difference is negligible, but when computing the deformation D (shown below) using this center of mass can significantly improve the signal in the data.

Area of droplet: For a droplet defined by the Fourier series the area of the droplet is

$$A_{droplet} = \frac{1}{2} \int_0^{2\pi} r^2 d\theta \quad (4.4)$$

which reduces to

$$A_{droplet} = \pi a_0^2 + \frac{\pi}{2} \sum_{n=1}^{n_c-1} a_n^2 + \frac{\pi}{2} \sum_{n=1}^{n_c-1} b_n^2 \quad (4.5)$$

List Of IDL Functions

- *kfourier_fit.pro*: Fits perimeter to Fourier series.
- *krepair_perimeter.pro*: In some cases a few pixels on the boundary of a droplet may be obscured or not correctly found. This code uses the Fourier series to test if pixels on the boundary deviate too far from the fit. For those pixels that deviate more than a user defined threshold, the program interpolates new pixels on the boundary using the Fourier fit.
- *adjust_center_of_mass.pro*: Adjust the center mass of each droplet to be the center of mass defined by the Fourier fit.
- *kget_deformation.pro*: Computes the deformation D for each droplet.

4.6 Radical Voronoi Tessellation

The radical Voronoi tessellation is a decomposition of the entire space into non-overlapping polygons, where each droplet is assigned its own unique polygonal cell. An example of a Voronoi tessellation for one of our samples is shown in Fig 4.8, where the green lines indicate the boundaries of the polygonal or Voronoi cells. These Voronoi cells are computed using

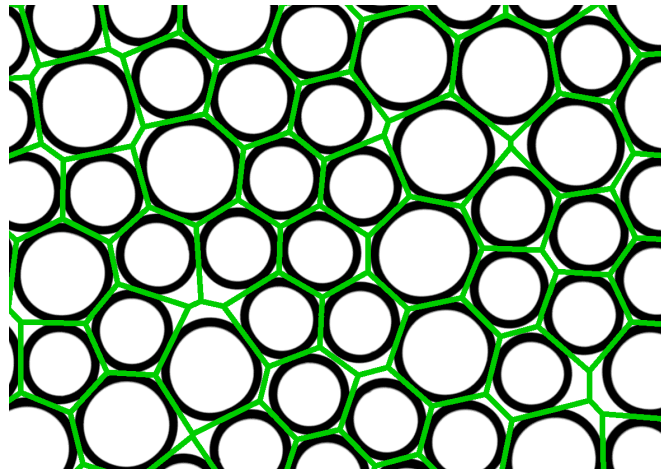


Figure 4.8: Radical Voronoi diagram. The green lines define the Voronoi cells around each droplets.

the power distance $\text{pow}(r_i, v) = (x_i - v_x)^2 + (y_i - v_y)^2 - R_i^2$, where r_i is the center of a droplet of interest, v is an arbitrary point in space, $R_i = \sqrt{A_i/\pi}$, and A_i is the area of the droplet using the Fourier fit to the perimeter [241, 242]. For the power distance to be meaningful, it must be used in conjunction with the coordinates of three neighboring droplets r_1 , r_2 , and r_3 , where the Voronoi coordinate for this pairing of three droplets is defined as the point in space v that satisfies the equations $\text{pow}(r_1, v) = \text{pow}(r_2, v) = \text{pow}(r_3, v)$. The Voronoi cell is then the polygon formed around a droplet by the Voronoi coordinates. While there are many possible combinations for the triplet r_1, r_2 , and r_3 that could be used to compute the Voronoi coordinates, there are rules restricting which triplets to use for the tessellation. It was shown by Aurenhammer that the set of triplets can be found by computing the lower convex hull of the droplet coordinates projected into a parabolic space, where the extra parabolic coordinates for the i th droplet is $x_i^2 + y_i^2 - R_i^2$ such that the parabolic coordinates is $(x_i, y_i, x_i^2 + y_i^2 - R_i^2)$ [241]. To compute the lower convex hull we use **qhull**. Once we have all the triplets, we can easily compute the Voronoi vertices and subsequently the Voronoi cells.

List Of IDL Functions

- *poly_voronoi.pro*: Computes the radical Voronoi tessellation.

- *kemulsion_volfrac2.pro*: Computes the packing fraction of a sample using an image of the droplets, the droplet outlines, and the *poly_voronoi.pro* function.

4.7 Identifying Contacts

For two droplets in contact, they will share a common boundary, and in this section, we discuss our method for determining this common boundary. It is a necessary condition that any two droplets in contact share a common edge between their Voronoi cells, and therefore, we use the Voronoi diagram to generate a list of neighboring droplets that may be in contact. However, it is also possible for two droplets to share an edge between their Voronoi cells even though they are not in contact as can be seen in Fig. 4.8. Once we apply the Voronoi tessellation, we then check each pair of droplets in our neighbor list, first determining if a contact exists, and if the contact exists then we identify the entire contact between the droplets.

To determine if a contact exists between two neighboring droplets, we look at the intensity of pixels along a line that joins the center of the two neighboring droplets as shown in Fig. 4.9(a) and (d). In Fig. 4.9(b), we show the intensity profile between two droplets not in contact, and in Fig. 4.9(e), we show the intensity profile between two droplets in contact. For droplets not in contact, the intensity profile shows two valleys in the intensity, where each valley represents the boundary of each droplet. However, for droplets in contact, they share a single boundary as indicated in the intensity profile by only one valley. Therefore, we can determine whether two droplets are in contact by determining if there is only one valley in the intensity profile.

To locate the valleys in the intensity profile [like those shown in Fig. 4.9(b) and (e)] we use a Schmidt trigger to reassign each pixel a value of 0 or 1, where 0 represents a pixel not in the valley and 1 represents a pixel in the valley. The Schmidt trigger works by starting at the center of one droplet and assigning that pixel a value of 0 or 1 based on one of two rules listed below. Then moving pixel by pixel along the intensity profile towards the other droplet, each pixel is evaluated and reassigned a 0 or 1 using the rules.

Rule 1: If the pixel intensity is greater than I_c , then we assign that pixel a new value

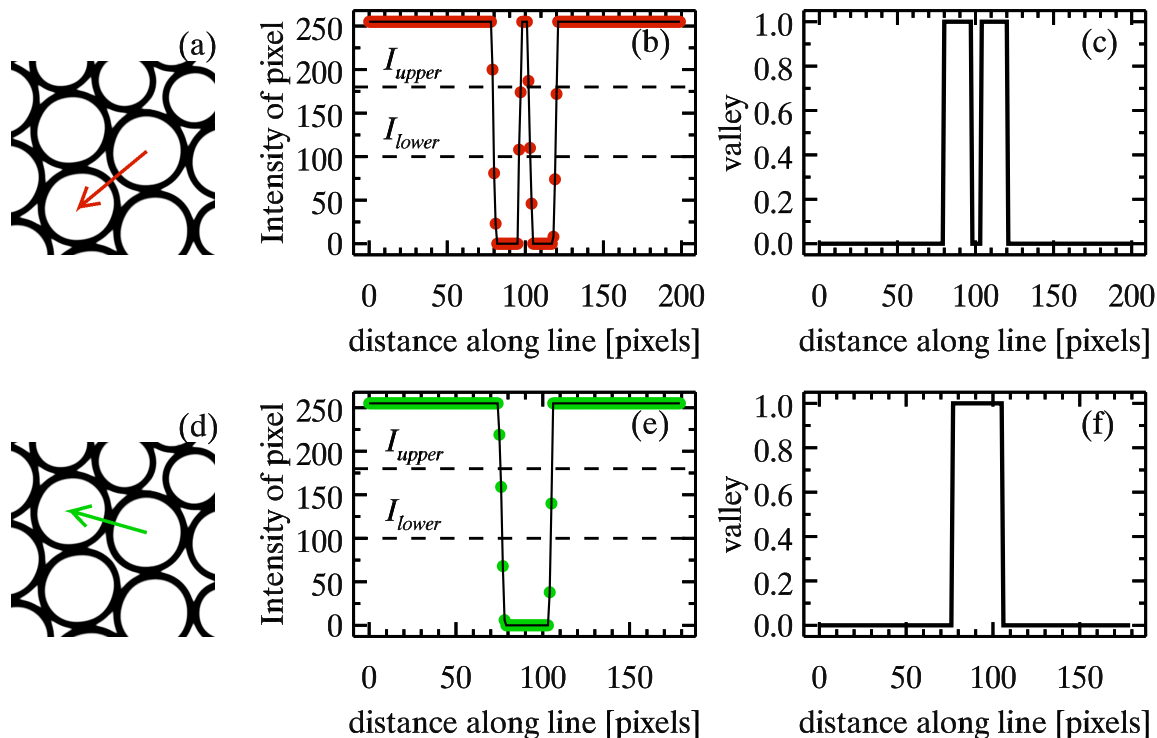


Figure 4.9: (a) [(d)] Image of droplets. The red arrow [green arrow] joins the center of two droplets not in contact [in contact]. In (b) and (c) [(e) and (f)] the pixel intensity is considered along the red [green] arrow starting at the tail and going to the head. (b) [(c)] The red [green] data points with a line going through them represent the pixel intensity along the red [green] arrow. The dashed lines represent the upper and lower thresholds used in the Schmidt trigger. (c) [(d)] The result of applying the Schmidt trigger to (b) [(e)], where 1 indicates a pixel within the valley.

0. Also, if the pixel intensity is greater than I_c and $I_c = I_{upper}$, then we change I_c to $I_c = I_{lower}$. When the algorithm starts $I_c = I_{lower}$.

Rule 2: If the pixel intensity is less than I_c , then we assign that pixel a new value 1. Also, if the pixel intensity is less than I_c and $I_c = I_{lower}$, then we change I_c to $I_c = I_{upper}$.

After applying these rules to the two the intensity profiles in Fig. 4.9, we have the valley curves in Fig. 4.9(c) and (f). In Fig. 4.9(c), the pixels are isolated into two clusters of pixels with value 1, and in Fig. 4.9(f), the pixels are isolated into one cluster of pixels with value 1. Using `label_region` we quickly identify the number of clusters. If `label_region` returns only one cluster of 1's, then we know that the two droplets of interest share a contact.

The idea behind using a Schmidt trigger is that it should trigger when we are confident

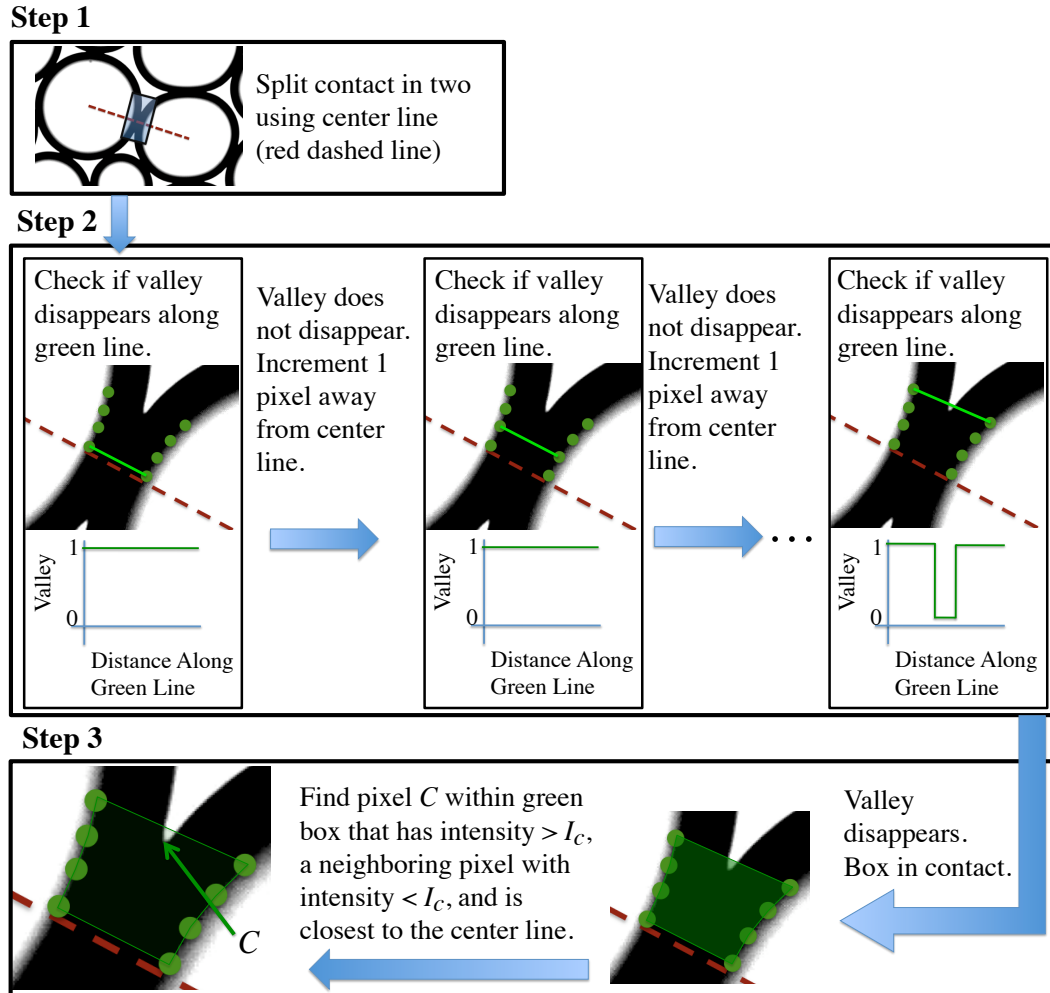


Figure 4.10: Flow chart illustrating how the endpoint of a contact is found.

a pixel belongs to a droplet boundary and turn off when we are confident a pixel is outside the boundary. Since the boundary of a droplet has a very low intensity values, while the other regions in the image have large intensity values we use a low I_{lower} and a high I_{upper} . By using a Schmidt trigger in this manner will avoid issues that may arise due to small noise in the pixel values.

Once we have determined that a pair of droplets share a contact, we then identify the entire contact. The aim here is to identify the endpoints where the two droplets share a common boundary, and in Fig. 4.10, we show a flow chart outlining our algorithm to find the endpoints. We know if we draw a line joining the center of two droplets in contact the line will intersect the contact, dividing the contact into two. Once the contact is divided in

two, we only need to focus on determining the endpoint for one side of the contact. Once we find the endpoint for one side, we repeat the algorithm for the other side. In Step 1 on the flow chart (top left large box), we have drawn a box around the contact of interest and drawn a red dashed center line that divides the contact in two.

After dividing the contact in two, we only focus on the upper half of the contact and move to Step 2 in the flow chart (middle large box). In this step, we look to estimate how far away from the center line does the single boundary shared between the two droplets begin to separate into two boundaries. This is done by looking at the intensity profile along lines joining the inner boundary of one droplet to the inner boundary of the other droplet. In the flow chart, we indicate the pixels on the inner boundary of each droplet using green dots, where the location of the green dots were already known because we had to locate them in Section 4.4 to identify each droplet. We start with the intensity profile along the pixels joining the inner boundary closest to the center line as indicated in the small left most box in Step 2 of the flow chart, where the intensity is checked along the green line joining the inner perimeters. For the first intensity profile, we see that each pixel value along the green line is in the valley, as indicated in the valley curve below the image, and therefore, the boundary for the two droplets has not split. Since the boundary has not yet split, we increment one pixel away from the center line as shown in the small middle box in Step 2. Once again, we look at the intensity profile across the boundary and find that all pixels belong to the valley. We continue to increment away from the center line until we reach the small right box in step (b) where the intensity across the boundary shows a disappearance of the valley.

After estimating where the two boundaries begin to separate, we then move to Step 3 to finally identify the endpoint of the contact. In Step 3 (bottom large box), we start by enclosing the region of space where the endpoint of the contact must exist. This region of space is defined by the center line, the inner boundary of the two droplets, and the last line segment examined in Step 2. We have indicated this region of space as the green shaded box. Within in this box, we can uniquely define the location of the contact's endpoint as the pixel C that satisfies the following criteria.

1. C must have an intensity greater than a threshold I_c .
2. C must have a neighboring pixel with intensity less than I_c .
3. C must be closer to the center line than any other pixel that satisfy other two criteria.

We have indicated the endpoint C in the flow chart. Once we have found C for one side of the center line, the algorithm is repeated to find the endpoint for the other side of the algorithm.

The ability of our algorithm to identify the contacts is shown in Fig. 4.11, where green lines joining the endpoints of the contacts are drawn over the image. Using the endpoints we can calculate the end to end distance l_{ij} of a contact, where i and j index two droplets in contact. Since we can determine the location of each endpoint of a contact to 1 pixel accuracy, this gives a measurement error of 1.4 pixels in l_{ij} . Also, we note that our choice of I_c will also change the length of the contact, however, the force law depends on $\Delta l_{ij} = l_{ij} - l_o$, where l_o is constant to be discussed later. l_o also depends on our choice for I_c , and systematically increases or decreases by the same amount as l_{ij} given the choice for I_c . Therefore, there is no additional measurement error in Δl_{ij} due to our choice of I_c .

List Of IDL Functions

- *klocate_contacts.pro*: Determines which pair of droplets are in contact and finds the endpoints of each contact.

4.8 Measuring Radius of Curvature

In this section, we discuss how the mean radius of curvature along the water-oil interface of a droplet. For a droplet in contact with other droplets only a parts of the perimeter has a water-oil interface, and these parts are the portions of the outer boundary between the two contacts (see Fig. 4.12). To identify these portions of the perimeter, we use the same method discussed in Section 4.4 used to search for the inner perimeter, only this time we use the algorithm to find the outer perimeter between two contacts. Once the outer perimeter is located, we then fit each portion of the perimeter to a circle to obtain a local radius of curvature r_k^i for each portion, where k indexes each portion and i indexes the droplets. In

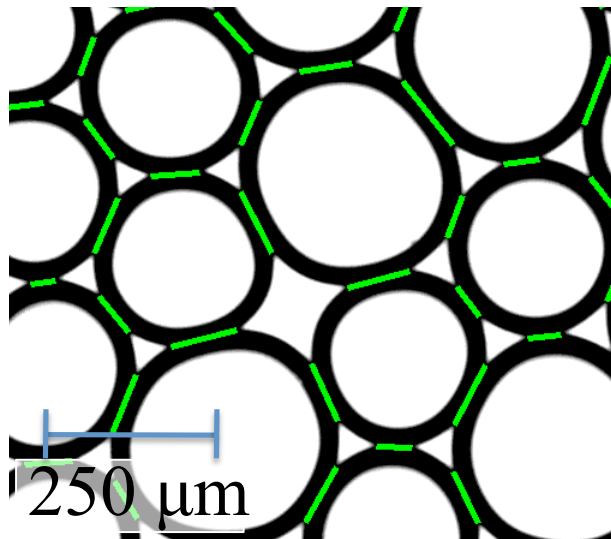


Figure 4.11: The green lines represent the contacts found using our contact finding algorithm. We have shortened the contacts by 6 pixels to expose the tip or endpoint of the contact. This tip will appear as a slight dark pixel at the edge of each green line. Had we covered the entire contact with a green line, we could not argue that our algorithm is working since it would have obscured the endpoints.

Fig. 4.12, we show a droplet with 5 different portions of the outer perimeter fitted to a circle. The average of these radii of curvatures $r_i = \langle r_k^i \rangle_k$ define the mean curvature r_i used in the empirical force law.

In Fig. 4.12, we see that the radius of curvature for each portion varies, and to quantify this variation for all our droplets, we plot in Fig. 4.13(a) the variation in r_k^i relative to the mean curvature for 4 different monodisperse data sets. In Chapter 5.4 we discuss how our monodisperse samples are prepared and provide more details on the samples. For this discussion, the relevant information is that we are using four data sets, where each data set consists of a collection of monodisperse droplets compressed by various amounts (some droplets are highly compressed and others are barely compressed). In Fig. 4.13(a), we are showing the statistics for all droplets in each data set. For all our data sets we see that the variations are fairly large, with the largest variations around 40% and an average variation near 13%. While the variations in the local radii of curvature are fairly significant, it is more important to understand the deviations in the measured mean curvature relative to the actual mean curvature. However, we don't know the true mean curvature for our data,

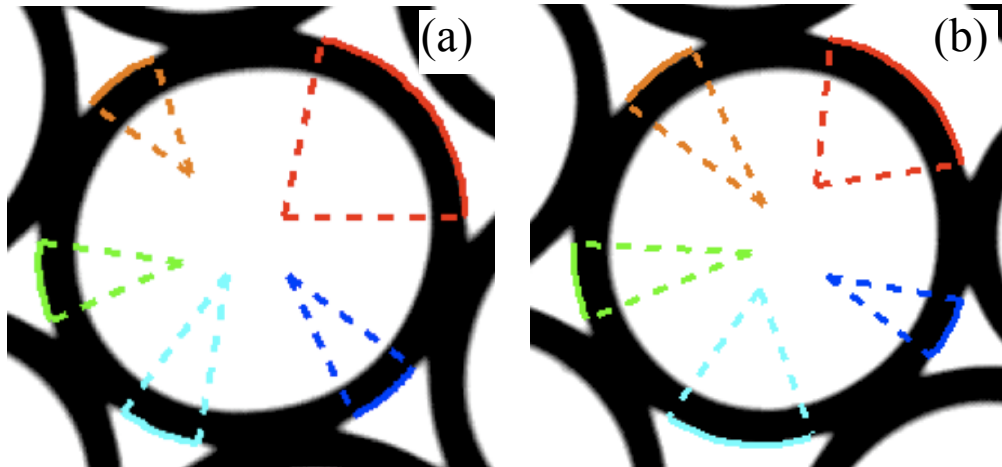


Figure 4.12: The mean curvature r for a droplet is measured by averaging the radius of curvature for each portion of the oil-water interface. In this figure we show a two droplets, each with 5 portions of the oil-water interface fitted to a circle of constant radius of curvature. In (a) the radii of curvature for the portions are $113 \mu\text{m}$ for the red fit, $74.6 \mu\text{m}$ for the orange fit, $89.6 \mu\text{m}$ for the green fit, $107 \mu\text{m}$ for the green fit, and $96.4 \mu\text{m}$ for the blue fit. Averaging the radii from these fits gives $r = (96 \pm 7) \mu\text{m}$ for the droplet. In (b) the radii of curvature for the portions are $102 \mu\text{m}$ for the red fit, $109 \mu\text{m}$ for the orange fit, $114 \mu\text{m}$ for the green fit, $109 \mu\text{m}$ for the green fit, and $89 \mu\text{m}$ for the blue fit. Averaging the radii from these fits gives $r = (104 \pm 4) \mu\text{m}$ for the droplet

but we can estimate measurement error in the mean curvature by adding noise of 1 pixel to the outer perimeter and refitting the data. For each droplet we fit the outer perimeter with added noise 20 times to improve statistics, and we label the new radii fits as r_{noise} . In Fig. 4.13(b), we plot the distribution in $r_i - r_{noise}$. We see that the variation in r_i are much smaller than in r_k^i , and the distribution is Gaussian like with a standard deviation of roughly 3%. To one standard deviation this gives a measurement error of $\sim 3\%$ in r_i .

To check if the estimated measurement errors above are reasonable given our noise in the perimeter, we numerically generate data of a circles with constant radius of curvature $r_i = 125 \mu\text{m}$ and test how r varies when noise is added to the perimeter. Each test circle consist of 400 discrete points (or pixels) defining the perimeter and the perimeter is divided into 5 small portions representing the regions of the perimeter to be fit to small arcs such that the arcs are commensurate in length to the segments fitted in our experimental data. We add 1 pixel noise to each point on the perimeter and then fit them to obtain an r_k^i . In Fig. 4.12(c), we show the variations in r_k^i for the test data, and find that the test data gives

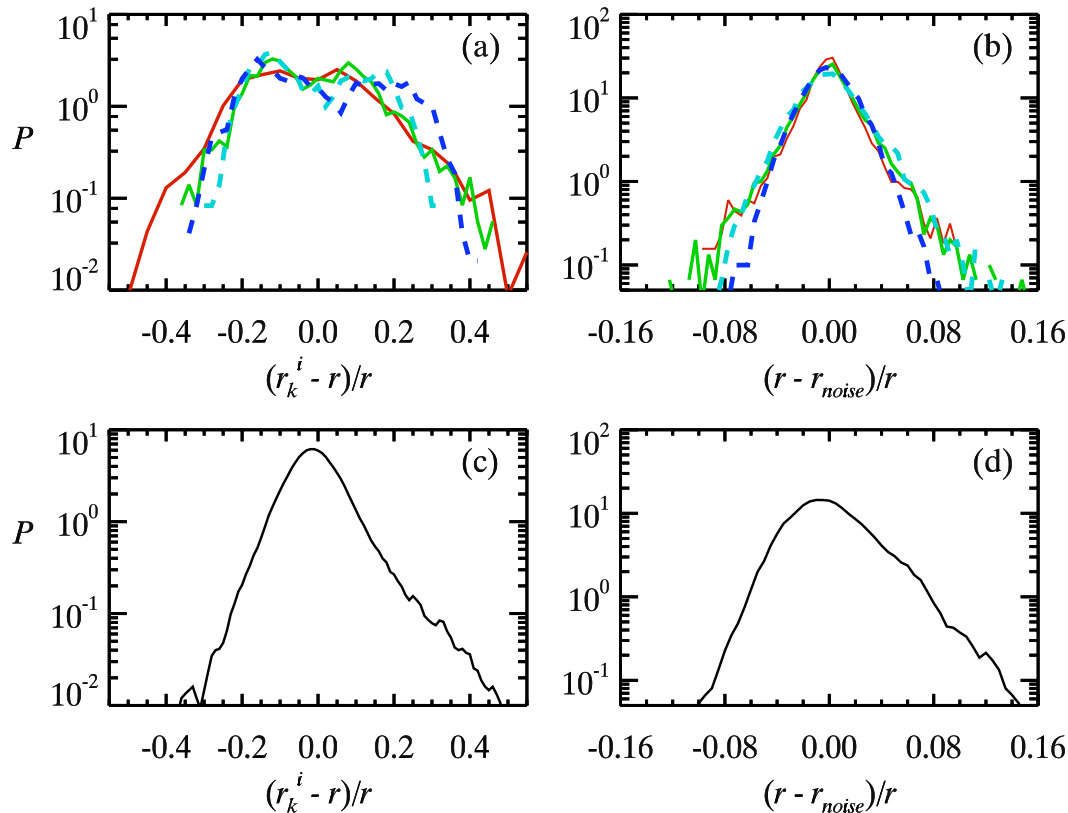


Figure 4.13: (a) Variation in local radii of curvature r_k relative to the mean radii of curvature. (b) Distribution of measurement error in mean radii of curvature.

a narrower distribution than the measured data. The difference in the test and measured data is not understood, but the test data does explain to a large degree the variations in the measured r_k^i . In Fig. 4.12(d), we show the variations in the fitted mean curvature r_{noise} relative to the known mean curvature. Comparing the test data to the experimental data we see that they agree fairly well. The test data gives a distribution that is slightly more skewed to larger values, but the shape and width of the test data and experimental data are very close. Therefore, we find that the pixel noise can explain the variations of r_i relative to the true mean and that the noise in r_i is about 3%.

List Of IDL Functions

- *kget_radii5.pro*: Computes the average radius of curvature for each droplet.

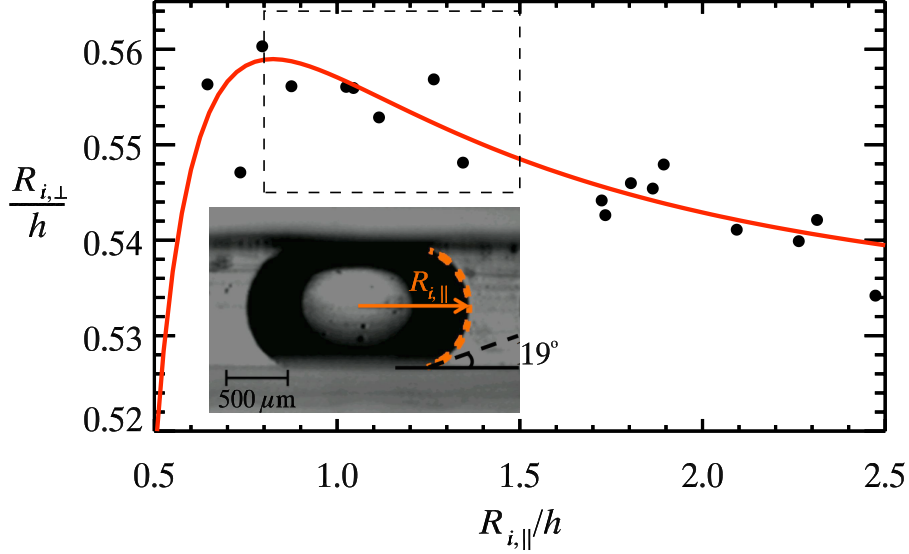


Figure 4.14: The inset is an experimental image of a mineral oil droplet squeezed between two glass slides, where the gap thickness is 1 mm, $R_{i,||} = 0.88$ mm and $R_{i,⊥} = 0.56$ mm. The orange dashed line is a fit to the perimeter of the droplet to obtain an $R_{i,||}$ and $R_{i,⊥}$. The plot is a scatter plot of $R_{i,⊥}$ and $R_{i,||}$ for various size droplets squeezed between two glass plates separated by 1 mm, and both $R_{i,||}$ and $R_{i,⊥}$ are normalized by the gap thickness. The red line is the expected relationship between $R_{i,⊥}$ and $R_{i,||}$ if the droplet has a contact angle of $180^\circ - 19^\circ = 161^\circ$ with the glass plate. The dashed line box encloses the range of $R_{i,||}$ values we use in our typical 2D experiments.

4.9 Mean 3D radius of curvature

The last measurable quantity to consider is \bar{R} which is the mean three dimensional curvature of a compressed emulsion droplet. For scenarios where droplets are asymmetrically deformed in 3D, the local curvature at any point along the water-oil interface has two principle radii, the maximum radius of curvature $R_{i,1}$ and the minimum radius of curvature $R_{i,2}$. For compressed droplets the mean curvature $1/\bar{R}_i = 1/2(1/R_{i,1} + 1/R_{i,2})$ is constant anywhere on the surface since the pressure must be constant across the interface. Laplace's law states that the pressure anywhere on the interface is inversely proportional to the mean curvature, and since the interface of the droplet is not flowing, the pressure on the interface is constant. In this section we discuss the 3D mean curvature for our droplets.

To measure \bar{R} for different droplets we take side view images of isolated droplets in a sample chamber of gap thickness $h = 1$ mm (see inset of Fig. 4.14). Since there is rotational

symmetry in these cross section images, we can fit the outline of the droplets to surfaces of mean curvature \bar{R}_i , where i indexes different droplets. An example of such a fit is shown in the inset of Fig. 4.14 as an orange dashed line overlaid on the outline of the droplet. To fit the outline of each droplet to a surfaces of mean curvature \bar{R}_i we first generate a look up table of 100,000 different surfaces with constant mean curvature using the method of Caboussat and Glowinski [243]. We then fit the outline of each droplet by finding the best surface in the lookup table that matches the droplet's outline. Once an \bar{R}_i is obtained for each droplet, it can be decomposed into two principle radii of curvatures $R_{i,1}$ and $R_{i,2}$. For our geometry, one of the two principle radii $R_{i,1}$ which we label $R_{i,\parallel}$ is the radius of curvature r_i previously discussed. The other principle radius of curvature $R_{i,2}$ which we label $R_{i,\perp}$ is the radius of curvature in the direction perpendicular to the glass. From our side view images, $R_{i,\parallel}$ is trivial to measure (see inset of Fig. 4.14). Once $R_{i,\parallel}$ is measured, $R_{i,\perp}$ can be calculated from $1/R_{i,\perp} = 2/\bar{R}_i - \bar{R}_{i,\parallel}$.

In Fig. 4.14, we plot $R_{i,\perp}/h$ for various $R_{i,\parallel}/h$ as the black data points. The data shows an increase and then slight decrease in $R_{i,\perp}/h$ with increasing $R_{i,\parallel}/h$. For droplets of any size in contact with the glass, they will always be constrained to meet the glass at the same contact angle. We find that the data is well described by a contact angle of 161° , and in the figure the red curve shows the predicted relationship between the curvatures for this contact angle. The box region in the figure show the range of $R_{i,\parallel}/h$ values that we use in our experiments, and we see that over this range $R_{i,\perp}/h$ varies by roughly 2%. Therefore, for simplicity, we treat $R_{i,\perp}$ in our analysis as a constant equal to $0.552h$ for any r_i (since $R_{i,\parallel} = r_i$) while accepting that there is roughly a 2% error in the value. In our 2D images, once we measure r_i , we can immediately calculate \bar{R}_i using $R_{i,\perp} = 0.552h$.

List Of IDL Functions

- *kget_R2.pro*: Fit perimeter of droplet imaged from side view to surface of mean curvature.

List Of MATLAB Functions

- *SqueezeDroplet.pro*: Numerically creates surfaces of 3D droplets squeezed between to glass plates.

CHAPTER 5

Empirical Force Law for 2D Model System

In the last chapter we discussed how to determine r_i , r_j , and l_{ij} for each droplet and contact in an image, but not how to determine the contact force f_{ij} , where i and j index the particles in contact, r is the radius of curvature for each droplet, and l_{ij} is the contact length. The objective of this chapter is to determine the empirical force law $f_{ij}(l_{ij}, r_i, r_j)$ between two droplets in contact. To accomplish this task we image droplets in mechanical equilibrium within a sample chamber that has been inclined to an angle of 28° . As a result of the sample being inclined, gravity applies an upward buoyant force on each droplet. Using our incline setup we are able to span a large range in droplet deformations and contact forces due to hydrostatics, where droplets further up the incline feel larger forces and deform more because they must support the buoyant weight of the droplets below. This can be seen in Fig. 5.1, where droplets further up the incline are more compressed.

From our image we can measure an r_i , r_j , and l_{ij} for each droplet and contact, but the contact force f_{ij} is unknown. While the individual forces between droplets in contact are unknown, the collective contribution of the forces to the mechanical stability of sample is known from Newton's Laws of motion. Newton's 2nd law states that for each droplet (1) the sum of the forces in the direction up the incline equals the droplet's buoyant weight and (2) in the perpendicular direction the sum of the forces is zero. (3) Newton's 3rd law says that the forces acting between two touching droplets are equal and opposite. These

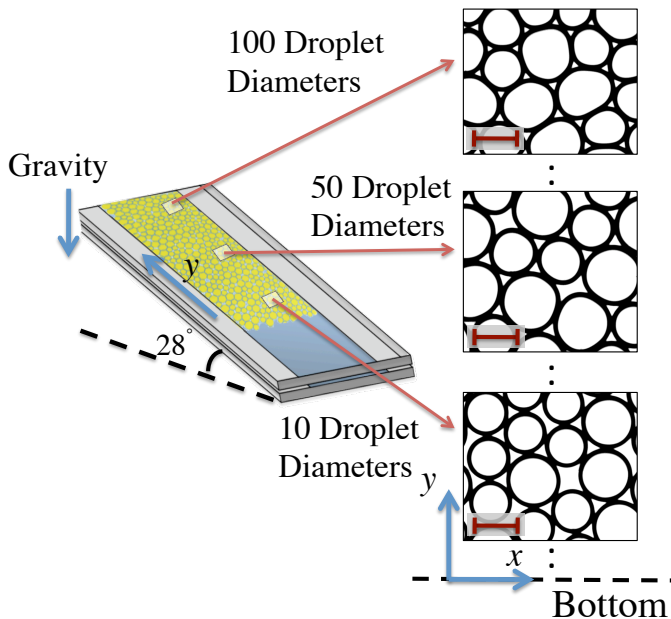


Figure 5.1: Illustration of our experimental approach to determine an empirical force law. The oil droplets rise to the top of the sample chamber due to buoyancy. At the bottom of the droplet “pile,” droplets barely touch and are not deformed. At the top, droplets are compressed due to the buoyant weight of the droplets below them. The scale bar is $200\ \mu\text{m}$.

three statements using Newton’s Laws establish constraints on the collective behavior of the individual contact forces.

To find an empirical force law, we test many different force laws to find the force law that predicts contact forces that best match the constraints set by Newton’s Laws of motion. In the next section we discuss the various force laws we will test. Since there is a slight adhesion between our droplets, we discuss in Sec. 5.2 how to account for this in our model. In Sec. 5.3, we develop an expression to quantify how well an assumed force law predicts a set of contact forces that match the constraints from Newton’s Laws of motion, and in the last two sections, we test various force laws using experimental data to find the best empirical force law.

5.1 Various Force Laws to be Tested

To find an empirical force law we must decide on which functions to test, and to determine these force laws we need to understand how the r_i , r_j , and l_{ij} relate to force. We can gain

insight into how r_i , r_j , and l_{ij} contribute to the forces between droplets by considering two ideal cases where the force law can be written explicitly. The first case is for two ideal 2D disks in contact, and the second case is for two ideal 3D spheres in contact. A system is considered ideal, if the contact between two droplets has a contact angle of zero and there is no adhesion between droplets, which in most cases is not true due to interaction between the surfactant molecules at the contacting interface [244, 245]. For the ideal 2D or 3D case, the force between two droplets in contact can be modeled using Princen's 2D model [246–248] or Zhou's 3D model [249]. We use lower case to indicate 2D variables and upper case to indicate 3D variables. In 2D, the contact between two droplets has a contact length l_{ij} , and in 3D, the contact has contact area A_{ij} . The force law for the two models are

$$\text{2D Model: } f_{ij} = \gamma_{2D} \frac{l_{ij}}{r_{ij}}, \text{ where } r_{ij} = \frac{r_i + r_j}{r_i r_j} \quad (5.1)$$

$$\text{3D Model: } F_{ij} = \gamma_{3D} \frac{A_{ij}}{R_{ij}}, \text{ where } R_{ij} = \frac{R_i + R_j}{R_i R_j} \quad (5.2)$$

In the above equations, γ_{2D} is a 2D line tension and γ_{3D} is a 3D surface tension. For scenarios where droplets are asymmetrically deformed in 3D, the radius of curvature R_{ij} in the 3D model must be replaced by the mean curvatures $\bar{R}_{ij} = (\bar{R}_i + \bar{R}_j) / (\bar{R}_i \bar{R}_j)$.

From the two ideal models, we learn that if the forces between our droplets is best described by a 2D force law, the relevant parameters are l_{ij} and r_{ij} , both of which we can measure for each pair of droplets in contact. If our force law is best described by a 3D force law, then the relevant parameters are A_{ij} and \bar{R}_{ij} . Since the contact area is related to the contact length, we can write that the relevant parameters for a 3D force law are l_{ij} and \bar{R}_{ij} . As of yet, we do not know if the forces between our droplets are better described by 2D variables or 3D variables, and therefore we will test force laws consisting of 2D variables and force laws consisting of 3D variables.

Generalizing the ideal models to be arbitrary function of the relevant measurable quantities, we write the empirical force laws to be tested of the form $f_{ij}^{(2D)}(l_{ij}, 1/r_{ij}; \vec{\alpha})$ for 2D or $f_{ij}^{(3D)}(l_{ij}, 1/\bar{R}_{ij}; \vec{\alpha})$ for 3D. We take the approach of using generalized functions since we only know that the forces increase monotonically with l_{ij} and $1/r_{ij}$. As to the functional form for how the force depends on these two quantities, we have no acceptable model to

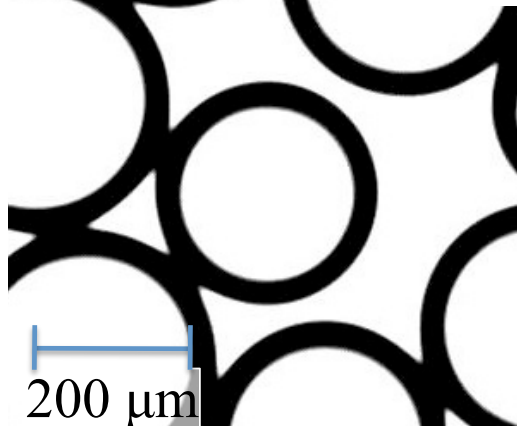


Figure 5.2: Experimental image of a rattler droplet being held in contact with two neighboring droplets due to a slight adhesion. In this image the droplets are motionless and the system is not inclined.

use, and since the scope of the work is to have an adequate force law, we take the approach of assuming any possible function. For the generalized expressions, $\vec{\alpha} = \alpha_1, \alpha_2, \dots$ are the n_α adjustable parameters associated with the functional form. In all, we will test a total of 86 various 2D and 3D force laws of different functional forms that include exponentials, hertzians, power laws, and polynomials in l_{ij} , $1/r_{ij}$, and $1/\bar{R}_{ij}$, and combinations of these forms, and we restrict the number of adjustable parameters to $n_\alpha \leq 4$. To give an example, one of the force laws we will test is $f_{ij}^{2D} = \alpha_1 (l_{ij}/r_{ij})^{\alpha_2}$, where α_1 and α_2 are the parameters and $n_\alpha = 2$. In the Sec. 5.4 and Sec. 5.5 we test these different force laws using experimental data, and at the end of this section we provide a table listing all the functions we test along with a measure quantifying how well they model the forces between our droplets. We find a simple polynomial function with $n_\alpha = 2$ works well.

5.2 Adhesion Length l_o

In our system, we have observed a slight adhesive interaction between our droplets as shown in Fig. 5.2, where the central droplet is held in contact with two neighboring droplets due to adhesion. In the configuration shown in the image, the droplets are motionless, and therefore the net force on each droplet is zero. Since the central droplet shares a contact with adhesion length l_o with the two neighbors, then there should be a repulsive force

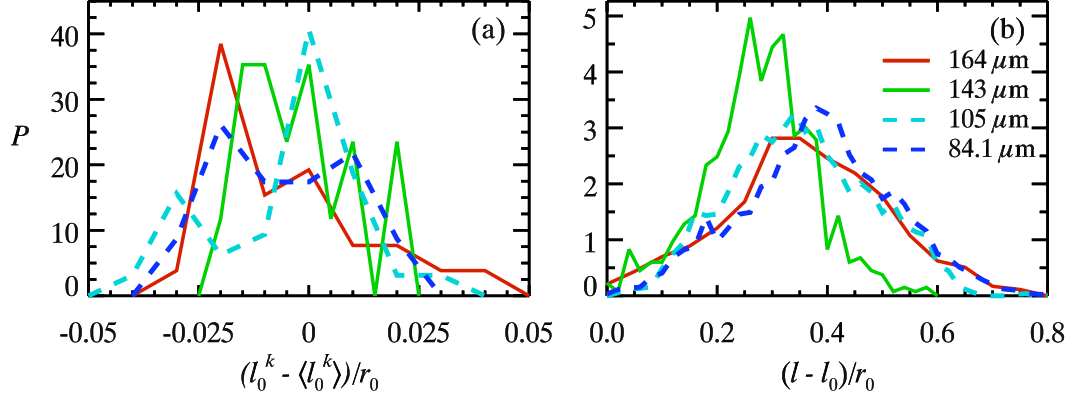


Figure 5.3: (a) Distribution showing the variation in the adhesion contact lengths l_o^k between droplets in contact, where the distribution has been centered around zero. The distribution is normalized by the droplet size r_0 . (b) Distribution of contact lengths for droplets pressed into one another. These contact lengths are the contact lengths due to adhesion and a compressive force at the contact and $l_0 = \langle l_o^k \rangle_k$. The distribution has been normalized by the droplet size r_0 . The legend in (b) applies to (a) as well.

$f_{ij}(l_0)$ pushing the central droplet away, however, this is not the case. Therefore, to balance the repulsive force there must be an adhesive force. In addition to the adhesion, some of the finite contact length is due to optical resolution limits (see Chapter 4.1), but most of the contact length seen is due to the adhesion and not optical resolution. While there is some adhesion between the droplets, the strength of the interaction does not appear to be significant, given that there is no noticeable deformation in droplets being held together by adhesion. Taking into account the attraction and optical resolution limit, we recognize that our force law must be constrained to satisfy $f_{ij}(l_0) = 0$. To apply this constraint to our force law, we rewrite the generalized 2D and 3D force laws as $f_{ij}^{(2D)}(\Delta l_{ij}, 1/r_{ij}; \vec{\alpha})$ and $f_{ij}^{(3D)}(\Delta l_{ij}, 1/\bar{R}_{ij}; \vec{\alpha})$, where $\Delta l_{ij} = l_{ij} - l_0$. Using the variable Δl_{ij} , the constraint on the force laws are $f_{ij}^{(2D)}(\Delta l_{ij} = 0) = 0$ and $f_{ij}^{(3D)}(\Delta l_{ij} = 0) = 0$. For our data, l_0 can be determined by measuring the average contact length for droplets in contact at the very bottom of the sample chamber.

To quantify the consistency in l_0 between actual droplets in contact we measure investigate l_0 using four different monodisperse data sets. In Chapter 5.4 we discuss how our monodisperse samples are prepared and provide more details on the samples. For this discussion, the relevant information is that we are using four different monodisperse samples.

Each sample contain different size droplets, the samples are inclined on a microscope, and the droplets imaged. At the bottom of the sample chamber droplets are circle and undeformed since the forces between droplets are small, and at the top of the chamber droplets are highly compressed. Each sample contains hundreds to thousands of droplets. Using our algorithm to determine contact lengths, we measure the contact length l_0^k for roughly 25-50 droplet contacts at the bottom of the sample chamber, where k indexes the contacts. In Fig. 5.3(a), we show the distribution of l_0^k for our four monodisperse data sets. To compare the data between different samples we have centered the data around zero, and normalized the distribution by the average droplet size since we expect the contact lengths should grow in proportion to the droplet radius. The distribution of l_0^k is fairly narrow with a standard deviation of roughly 2%. While these variations are fairly small, they are larger than the measurement error in computing a contact length, indicating that l_0 is not a single number, but varies for different droplets in contact. In the experiments, we intend to measure the forces between droplets with contacts lengths $l_{ij} > l_0$. To understand if the variation in l_0 will be an issue we compare l_{ij} to l_0 in Fig. 5.3(b) for each monodisperse data set, where $l_0 = \langle l_0^k \rangle_k$. Comparing the distribution in Fig. 5.3(a) to the distribution in Fig. 5.3(b) we see that the variations in l_0^k is 1 to 2 orders of magnitude less than the size of l_{ij} relative to l_0 . While the variations in l_0 is an unfortunate byproduct of the system, these variations can be ignored because they are significantly smaller than the contact lengths we are interested in studying.

5.3 Testing the Quality of an Assumed Force Law

Each force law tested has a set of adjustable parameters $\vec{\alpha}$ and the goal is to determine an $\vec{\alpha}$ that gives the best agreement between the set of contact forces given by the force law and Newton's Laws. To determine $\vec{\alpha}$ we minimize a goodness of comparison χ^2 with a smaller minimal χ^2 indicating the function better models the forces on each droplet. Once a minimal χ^2 has been found for each force law to be tested, we can then compare χ^2 between all the forces laws to find the best empirical force law. In this section, we develop an expression for χ^2 using Newton's Laws of motion. We start by considering the constraints

in the y -direction and then in x -direction. Lastly, we combine these constraints to have one equation for the goodness of comparison

In the y -direction, the sum of the forces on any given droplet is equal to the buoyant weight $W_D = 4\pi\Delta\rho g/3R_0^3\sin(\theta)$, and since the oil phase is less dense than water, the droplets will rise to the top of the chamber compressing one another as shown in Fig. 5.1. In the equation R_0 is the radius of the droplets before placing them into the sample chamber, $\Delta\rho$ is the density difference between the water and the oil phase (for water and mineral oil $\Delta\rho = 0.17 \text{ g/cm}^3$). For our inclined configuration we use $\theta = 28^\circ$. This gives $W_D = 3280(\text{N/m}^3)R_0^3$, where R_0 ranges from $75 \mu\text{m}$ to $200 \mu\text{m}$ giving a range of $W_D = 1.38 \text{ nN} - 26.2 \text{ nN}$.

When the droplets rise up the sample chamber, they must slide pass the glass microscope slides and there is a slight dynamic friction between the droplets and the glass plates. When the droplets come to rest there is still a slight static friction between the droplets and the glass slide. To quantify the static friction, the slide is tilted until the droplets begin to rise upward. The angle at which the droplets start to rise varies from droplet to droplet and slide to slide and is between $4 - 5^\circ$, giving an average friction force on each droplet of $f_{friction} = 4\pi\Delta\rho g/3R_0^3\sin(4.5^\circ) = 548(\text{N/m}^3)R_0^3$. For our range of R_0 values this gives $f_{friction} = 0.231 \text{ nN} - 4.38 \text{ nN}$. Since droplets float to the top of the sample chamber, the friction force will point in the downward direction to oppose the motion. To account for this friction force we can define an effective buoyant weight on each droplet $W'_D = c(\sin(28^\circ) - \sin(4.5^\circ)) = 0.391c$, where $c = 4\pi\Delta\rho g/3R_0^3 = 3280(\text{N/m}^3)R_0^3$ and the friction force is subtracted from the buoyant force. While this seems like a reasonable approach, the situation is a little more complicated. Once droplets start to reach the top of the sample chamber, they begin to make slight adjustments as they settle into mechanical equilibrium. Sometimes groups of droplets rearrange with some droplets moving up and down the sample chamber and others moving horizontal. In many cases, the last direction a droplet moves before coming to rest is not always directly upward and therefore the direction of the friction force on any droplet is unknown. Since the direction of the friction force is unknown, we must make some simple assumption that only consider the average effect the friction force has on the buoyant weight of each droplet. First, we assume that

the friction force on each droplet is $f_{friction} = c \sin(4.5^\circ)$, and second, we assume that the last motion taken by a droplet before resting into mechanical equilibrium is always up the incline and any amount of motion left and right is equally probable. These are reasonable assumptions since in granular compaction experiments the trajectory of individual grains resemble Brownian like motion [250]. Using this assumption, the average friction force in the x -direction is zero and the average friction force in the y -direction is downward with magnitude $f_{friction} = c \sin(4.5^\circ)/2$. This gives an effective buoyant weight on each droplet of $W'_D = c(\sin(28^\circ) - \sin(4.5^\circ/2)) = 0.430c$.

Using our effective buoyant weight, we look to write down a constraint using Newton's 2nd Law. We could write as a constraint that our force law must give the sum of the forces in the y -direction on each droplet as close as possible to W'_D . However, we don't know the actual values of W'_D , only the average. Also W'_D is small compared to the contact forces further up the incline, and therefore we need to take a slightly different approach to writing down a constraint. While the average net upward force on a droplet is independent of its location up the incline, droplets are more compressed with increasing y due to hydrostatic effects. For droplets located at a given y they must support the collective effective buoyant weight W_{below} of droplets below them. The way in which these droplets support this buoyant weight is through contact forces, and for an assumed force law $f_{ij}(\Delta l_{ij}, r_{ij}; \vec{\alpha})$ we can determine these contact forces by substituting our measured values for Δl_{ij} and r_{ij} into the function. If the assumed force law accurately predicts the forces, then the sum of these contact forces $\sum F_y^{down}$ at a given y will correctly predict W_{below} , where F_y^{down} is the y -component of only those forces pointed in the downward directions. The reason we only consider the downward facing forces is because the collective buoyant weight is pushing upward, and to satisfy Newton's 3rd law, the balancing forces must be facing downward. Therefore, we have the constraint that $W_{below} = \sum F_y^{down}$ which can also be written as a force per unit length $\lambda^{obs} = \lambda^{mod}$, where $\lambda^{obs} = W_{below}/w$, $\lambda^{mod} = \sum F_y^{down}/w$, and w is the width of the chamber. Since we know the location of each droplet and their size, we can calculate W_{below} for any given y without knowing individual contact forces. To quantify how well an assumed force law predicts the forces we define a goodness of comparison in

the y -direction as

$$\chi_y^2 = \sum_y [(\lambda(y)_{obs} - \lambda(y)_{mod}) / \langle \lambda(y)_{obs} \rangle]^2, \quad (5.3)$$

where smaller values of χ_y^2 indicate a better match between the assumed force law and the actual forces. In the equation, y indexes discrete evenly spaced distances up the incline where $\lambda(y)_{mod}$ and $\lambda(y)_{obs}$ are sampled and the angle brackets are an average over y . To make χ_y^2 dimensionless, we normalize by $\langle \lambda(y)_{obs} \rangle$ which is independent of the assumed force law. We sample λ at intervals of $5r_0$ up the incline. At each y sampled, λ_{mod} is calculated using the contact lengths and droplet radii for all droplets found between a distance $y - 5r_0$ and $y + 5r_0$ up the incline, and λ_{obs} is calculated using the position and radii of all droplets below a distance y up the incline.

Similar to the y -direction, we can construct a goodness of comparison for how well an assumed force law models the forces in the x -direction. However, unlike the y -direction, there are no gravitational forces or any other external forces, and therefore, the sum of the forces on each droplet in the x -direction is zero. Using Newton's second law we can construct the following goodness of comparison

$$\chi_x^2 = \sum_i \left[\left(\sum_j f_{x,ij} \right) / \langle |\vec{f}_i| \rangle \right]^2, \quad (5.4)$$

where the $f_{x,ij}$ is the x component of the force at a contact between droplet i and droplet j and $\langle |\vec{f}_i| \rangle$ is the average net contact force exerted on droplet i . In the equation, $f_{x,ij}$ are the forces predicted by the assumed force law. Due to measurement error, forces will not sum to zero, and the deviation from zero grows with $\langle |\vec{f}_i| \rangle$. We assume that the deviation will grow linearly with $\langle |\vec{f}_i| \rangle$ and to fairly weight the contributions of each droplet to χ_x^2 , we normalize the sum of the forces by $\langle |\vec{f}_i| \rangle$.

Finally, we can combine the goodness of comparisons in the y and x directions to define a net goodness of comparison $\chi^2 = \chi_x^2 \chi_y^2$ which indicates how well an assumed force law models the forces in both the x and y directions. When testing an assumed force law, χ^2 will be minimized to obtain the best adjustable parameters $\vec{\alpha}$. Since we know the buoyant weight of our droplets in units of μN , this will allow us to find a force law in units of μN . To

| R_0 [μm] | r_0 [μm] | h [μm] | poly (%) | l_0 [μm] |
|-------------------------|-------------------------|-----------------------|----------|-------------------------|
| 164 | 183 | 186 | 5.5 | 50.8 |
| 143 | 156 | 180 | 1.6 | 48.8 |
| 105 | 128 | 96 | 1.9 | 36.6 |
| 84 | 89 | 96 | 2.5 | 30.3 |

Table 5.1: In the above table we provide various parameters characterizing the droplets in our 4 different monodisperse samples. R_0 is the 3D radius of the droplets, r_0 is the 2D radius, h is the gap thickness of the chamber, poly is the polydispersity of the sample, and l_0 is the length of contact for two droplets just in contact. The polydispersity is the standard deviation in droplet radii normalized by the mean droplet radius. Our uncertainties for the various measures are $\pm 1 \mu\text{m}$ in R_0 , $\pm 2 \mu\text{m}$ in r_0 , $\pm 2 \mu\text{m}$ in h . The variability in l_0 grows with droplet size and the measurement uncertainty can be expressed as $\pm 0.04r_0$ in l_0 .

minimize χ^2 we use the default built in `fminsearch` in MATLAB which applies a simplex method developed by Lagarias *et al.* [251].

5.4 Empirical Force Law for Same Size Droplets in Contact

We now apply our method to experimental data to find an empirical force law. We start by determining the force law for same size droplets in contact using data taken on four different monodisperse samples. The samples are prepared by placing droplets with 3D radius R_0 into a sample chamber with gap thickness of either $\sim 100 \mu\text{m}$ or $\sim 180 \mu\text{m}$, and once in the chamber, the droplets have a 2D radius of r_0 . After the sample chambers are filled, they are sealed to prevent evaporation, and then placed on a microscope inclined to an angle of 28° . Initially droplets rise to the top of the chamber and finally come to rest in mechanical equilibrium, at which point we acquire high resolution images of the sample, where each droplet occupies 100,00 - 200,000 pixels depending on the droplet size. Various parameters characterizing each sample are shown in Table 5.1.

To determine the best force law we apply our routine to test and obtain a χ^2 for various assumed force laws, and we compare χ^2 for the different functions by plotting their values in Fig. 5.4. In the figure, χ^2 has been plotted in a sorted format, where χ^2 is first separated based on n_α (or number of terms in $\vec{\alpha}$) and then sorted in order from smallest to largest. The x -axis indicates the number of parameters and the vertical dashed lines separate the regions between different n_α . Each triangle represents a χ^2 for an assumed force law.

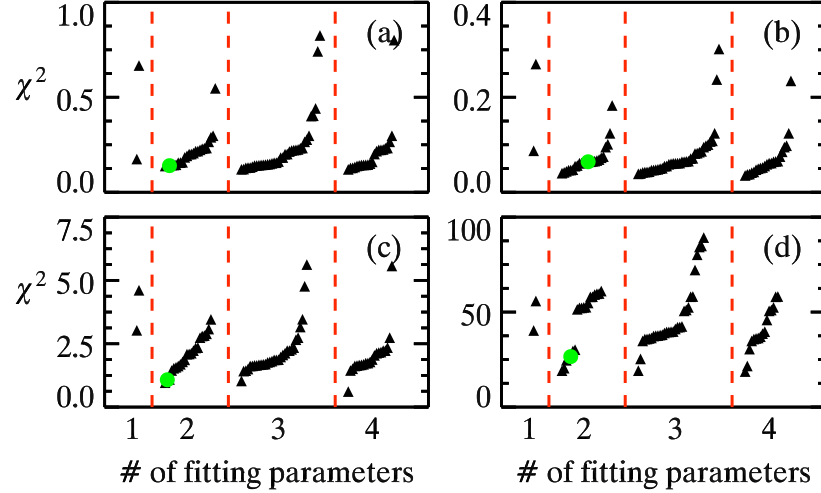


Figure 5.4: (a)-(d): The mean goodness of comparison χ^2 are plotted for all force laws for each data set in a sorted format. χ^2 are sorted in order from smallest to biggest and separated by n_α , as labeled on the horizontal axis. Plot (a) is data for $R_0 = 164 \mu\text{m}$, (b) is for $R_0 = 142 \mu\text{m}$, (c) is for $R_0 = 105 \mu\text{m}$, and (d) is for $R_0 = 84.1 \mu\text{m}$. The green circles indicate the function that we will use to compute the forces between droplets in future experiments.

The functions of interest in Fig. 5.4 are those with the lowest χ^2 , since these force laws better model the contact forces. The first observation of the data is that the lowest values of χ^2 for $n_\alpha = 2, 3$, and 4 are roughly the same in magnitude, which indicates that adding more parameters does not significantly improve the accuracy in modeling the forces. The second observation is that, except for Fig. 5.4(d), there are many small χ^2 values that are all roughly the same in magnitude. This second observation implies two possible scenarios; one, that all the force laws with “small” χ^2 are converging to the same contact forces, but because they are constrained by different functional forms they can not converge to the exact same contact forces, or two, that these different force laws are returning significantly different contact forces. Recall, to obtain a χ^2 we apply the assumed force law to compute a contact force for each contact giving a list of contact forces \vec{f} . If two different assumed force laws give the same contact forces, then \vec{f} will be the same for the two force laws.

We will consider the likely force laws to be the 10 smallest χ^2 $n_\alpha = 2$ functions, 10 smallest χ^2 $n_\alpha = 3$ functions, or 10 smallest χ^2 $n_\alpha = 4$ functions. To test if the contact forces are the same or vary between the best force laws, we will compute the variation in

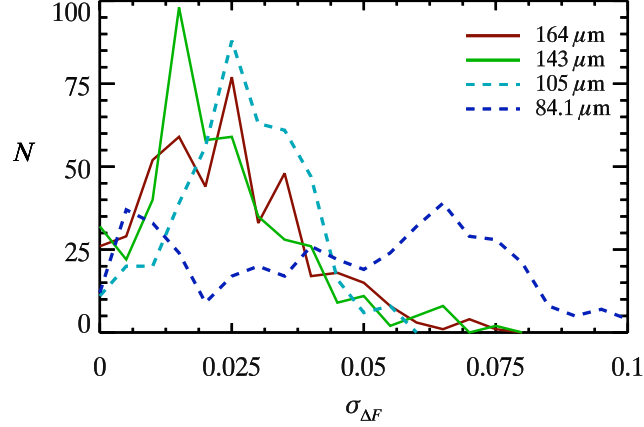


Figure 5.5: Histogram of $\sigma_{\Delta F}$ for each data set, where $\sigma_{\Delta F}$ quantifies the variation in forces between two force laws. The solid lines are samples with a gap thickness of approximately $h \approx 180 \mu\text{m}$ and the dashed lines are samples with a gap thickness of approximately $h \approx 110 \mu\text{m}$. The legend indicates R_0 .

the contact forces between any two force laws a and b as the standard deviation $\sigma_{\Delta f}$ in $\Delta \vec{f}$, where $\Delta \vec{f} = (\vec{f}_a - \vec{f}_b)/(\vec{f}_a + \vec{f}_b)$. Since there are 30 likely force laws, comparing any two of these functions gives 435 different comparisons. If all the likely force laws are giving roughly the same contact forces, then the distribution in $\sigma_{\Delta f}$ will be narrow and small, however, if the force laws are giving different contact forces, then the distribution in $\sigma_{\Delta f}$ will have multiple peaks or be broad. In Fig. 5.5, the distribution of $\sigma_{\Delta f}$ is shown for all four data sets, and in all the data, except (d), $\sigma_{\Delta f}$ is typically less than 5%. Although in (d), most of the values are less than 8%. Therefore, we can conclude that all the likely force laws are converging to one solution with about 5% variation, and that we can pick any likely force law, as long as we recognize that in addition to measurement error, we have an additional 5% error in the forces due to how well we know the force law.

Since there are 30 likely forces laws to choose from, we apply Occam's razor, and choose the one simplest in form. We start by noting that measuring r_{ij} is simpler than measuring \bar{R}_{ij} , and that 2 parameter functions are simpler than higher order ones. Second, having a function that treats Δl_{ij} and r_{ij} as a single variable, such as $\Delta l_{ij}/r_{ij}$, as oppose to the two separable variables, is simpler because in the first case the force law is a 1D curve while in the second case it's a 2D surface. Finally, of those functions that meet the two previous conditions, we choose the function that closely resembles the ideal 2D force model

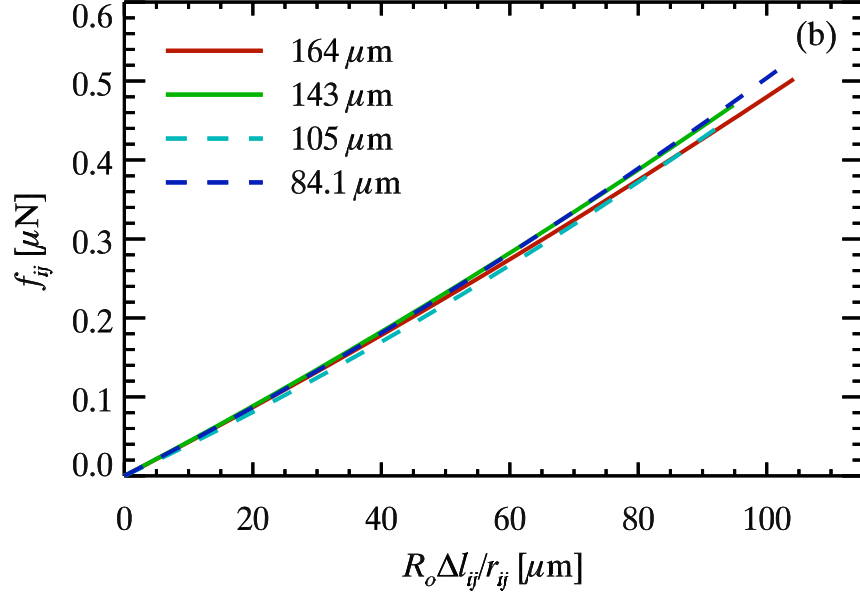


Figure 5.6: A plot of the universal empirical force law for each data set. The solid lines are samples with a gap thickness of approximately $180 \mu\text{m}$ and the dashed lines are samples with a gap thickness of approximately $110 \mu\text{m}$. The legend indicates R_0 .

(Eqn. 5.2), giving $F_{ij} = \alpha_1 \Delta l_{ij}/r_{ij} + \alpha_2 (\Delta l_{ij}/r_{ij})^2$. This function is indicated in Fig. 5.4 as the green circular data points. We also choose this function because we find that we can easily rescale it for all four data sets to give a universal force law. The rescaled force law is

$$F_{ij} = \alpha_1 R_0 \Delta l_{ij}/r_{ij} + \alpha_2 (R_0 \Delta l_{ij}/r_{ij})^2. \quad (5.5)$$

where $\alpha_1 = 4.18 \text{ dynes/cm}$ and $\alpha_2 = (0.0909 \text{ dynes}^{1/2}/\text{cm})^2$, and is shown in Fig. 5.6. The rescaled force law shows that all the data nearly collapse onto a single universal curve, and that these curves only slightly deviate between each other at larger $\Delta l_{ij}/r_{ij}$. We note that for these larger values in $\Delta l_{ij}/r_{ij}$, the area fraction is close to 96% which is the upper limit where we can still confidently measure r_{ij} because few pixels occupy the water-oil interface and the radius of curvature becomes difficult to measure. Intriguingly, α_1 has units of surface tension and the value of α_1 is the correct order of magnitude for the surface tension of most water-oil interfaces.

To show the quality of the universal force law in a little more detail, we show in Fig. 5.7(a) the sum of the forces in the x -direction with distance up the incline for the $R_0 = 84.1 \mu\text{m}$

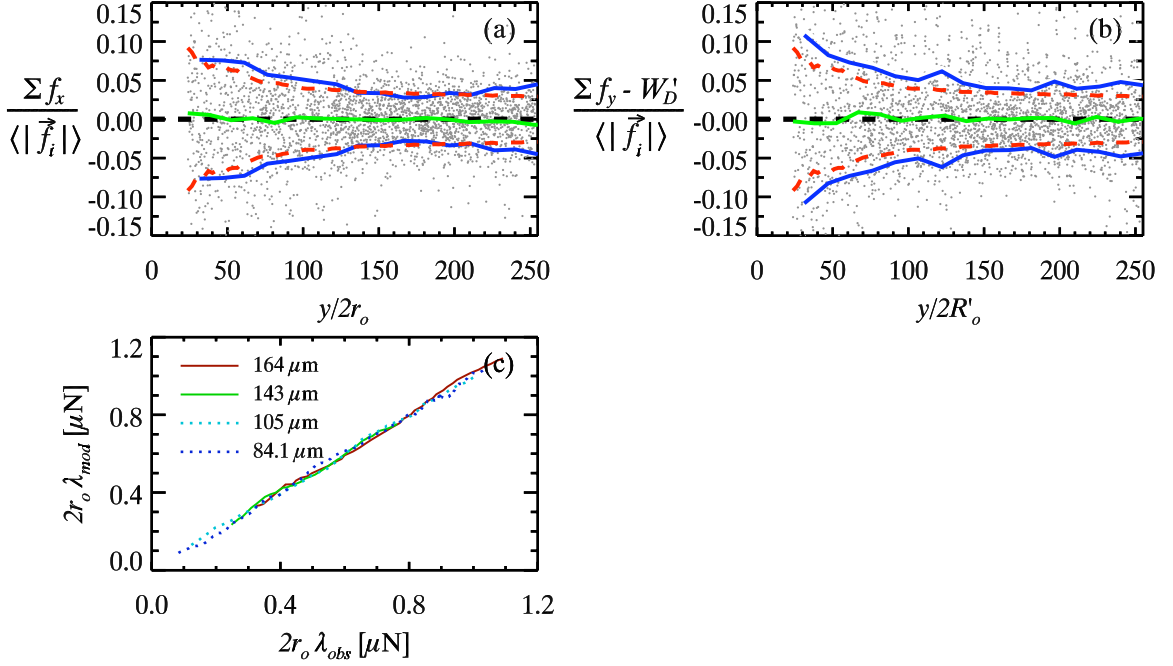


Figure 5.7: (a) is a scatter plot for the sum of the forces in the x -direction and (b) is a scatter plot for the sum of the forces in the y -direction relative to the effective buoyant weight with distance up the incline. Both (a) and (b) are data for the $R_0 = 84.1 \mu\text{m}$ sample. In (a) and (b) the blue solid line is the standard deviation in the scatter of the data points, the red dashed line is the expected standard deviation in the scatter based on our measurement errors, and the green line is the mean in the scatter of the data. In (a) and (b) the sum of the forces have been normalized by the average contact force on the droplet. In (c) λ_{mod} is plotted against the known λ_{obs} at various points up the incline. The dashed lines in (c) are samples with a gap thickness of $\approx 100 \mu\text{m}$ and the solid lines are samples with a gap thickness of $\approx 180 \mu\text{m}$. The legend indicates R_0 .

data set, which is representative of the other data sets. The figure shows the net force is very close to zero, only deviating by about 5% on average. This deviation arises because of measurement errors. Since we know the form of the force law and the size of the measurement errors, we can predict the deviation from zero. In the figure, the blue line is the standard deviation of the data points and the red dashed line is the standard deviation expected based on the known measurement errors. The red dashed line is computed in the following way. For each droplet i we compute the average $\langle \Delta l_{ij} \rangle_j$ and $\langle r_{ij} \rangle_j$ for all the contacts. Then we assume each droplet has 6 neighbors arranged in a hexagonal packing and we assign each contact a contact length equal to $\langle \Delta l_{ij} \rangle_j$ and a radius of curvature equal to $\langle r_{ij} \rangle_j$. Since the packing is hexagonal, assigning each contact the same contact length

and radius of curvature gives the sum of the forces equal to zero. Next, we randomly add noise within the experimental uncertainty to each contact length and radius of curvature, and then recompute the sum of the forces in the x -axis. Repeating this processes thousands of times for different orientations of the hexagonal packing and for each droplet gives a new set of values for the sum of forces in the x -direction. Using these new values we can compute the standard deviation shown as the red dashed line in the figure. We see that the red dashed line agrees very well with the blue line. We would only achieve this level of agreement if our force law is significantly more precise than our measurement error. Therefore, the agreement between the measured and predicted variations indicates that our method is returning a very precise force law.

In the y -direction, the forces should sum to the effective buoyant weight of the droplets, but due to measurement errors the sum of the forces will vary around a mean W'_D . We have verified that the mean in the sum of force in the y -direction is W_D . We repeat the above analysis shown Fig. 5.7(a) for the forces in the y -direction, and the data is shown in Fig. 5.7(b). The data is scattered around W'_D as expected. However, the variations around W'_D are larger than expected, probably due to the distribution of friction forces.

In Fig. 5.7(c), λ_{mod} is plotted against λ_{obs} for all four data sets. If the force law is a good model of the contact force, then we expect the data to fall along the $\lambda_{mod} = \lambda_{obs}$ line, and in all four cases the lines are linear, falling along the line $\lambda_{mod} = \lambda_{obs}$ with only small deviations.

When we minimize χ^2 to find the adjustable parameters $\vec{\alpha}$ for an assumed force we had a finite number of droplets and there was noise in each measurement. Even if we tested the correct force law, these two factors may give slight errors in $\vec{\alpha}$. To quantify the error in the adjustable parameters $\vec{\alpha}$, we create two test data sets of 1000 droplets with a known force law, and each droplet is assigned a r_i and each contact is assigned l_{ij} such that the forces sum to W'_D in the y -direction and zero in the x -direction. The number of droplets chosen and the values of r_i and r_j are commensurate to our experiments. The force law for the first test case is $f_{ij} = \alpha_1(l_{ij}/r_{ij})^{\alpha_2}$ and for the other test case the force law is $f_{ij} = (\alpha_1 l_{ij} + \alpha_2 l_{ij}^2)(1/r_{ij} + \alpha_3/r_{ij}^2)$. For different values of $\vec{\alpha}$, different values of r_{ij} and l_{ij} are assigned to satisfy force balance. For each test case, different values of $\vec{\alpha}$ are chosen and

| σ | n_r | $R_0^{(b)}$ [μm] | $R_0^{(s)}$ [μm] | $r_0^{(b)}$ [μm] | $P^{(b)}$ % | $r_0^{(s)}$ [μm] | $P^{(s)}$ % | h [μm] | $l_0^{(ss)}$ [μm] | $l_0^{(sb)}$ [μm] | $l_0^{(bb)}$ [μm] |
|----------|-------|----------------------------------|----------------------------------|----------------------------------|----------------|----------------------------------|----------------|--------------------------|-----------------------------------|-----------------------------------|-----------------------------------|
| 1.25 | 0.684 | 102 | 86.5 | 126 | 3.4 | 102 | 3.1 | 104 | 52.0 | 56.0 | 63.0 |
| 1.42 | 0.849 | 91.8 | 80.0 | 130 | 3.0 | 105 | 3.4 | 106 | 46.8 | 50.9 | 58.5 |
| 1.52 | 0.806 | 108 | 79.2 | 137 | 3.3 | 90.1 | 3.1 | 104 | 45.0 | 51.0 | 58.7 |

Table 5.2: This table provides various parameters characterizing the droplets in our 3 binary samples. The first column $\sigma = r_0^{(b)}/r_0^{(s)}$ is the size ratio and the second column is the number ratio n_r (number of big droplets to number of small droplets). In the table a superscript (s) indicates a value representing small droplets and a superscript (b) indicates a value representing big droplets. P indicates the polydispersity in droplet size. The polydispersity is the standard deviation in droplet radii normalized by the mean droplet radius. There are also three contact types small-small contacts (ss), small-big contacts (sb), and big-big contacts (bb), and therefore there are three l_0 values. Our uncertainties are $\sim 0.1\%$ in σ , $\pm 1 \mu\text{m}$ in R_0 , $\sim 2 \mu\text{m}$ in r_0 , $< 0.1\%$ in polydispersity, and $\pm 2 \mu\text{m}$ in h . The variability in l_0 grows with droplet size and the measurement uncertainty can be expressed as $\pm 0.04\langle r_0 \rangle$. Since we can observe every single droplet there is no measurement error in n_r .

χ^2 minimized. We choose values of $\vec{\alpha}$ close to the values we found for the experiments. We find that minimizing χ^2 gives $\vec{\alpha}$ to floating point precision. Now we add noise to r_i and l_{ij} commensurate to the data, and minimize χ^2 for different $\vec{\alpha}$. In the case of noise, we find that minimizing χ^2 gives a force law close to the true force law, but each time the force law is a little different. The variation from the true force law is 1.4% (2 standard deviations). Therefore, when we compare the forces laws in Fig. 5.6 to each other we expect to find $\sim 3\%$ variation between any two curves, which is in agreement with the data in the figure.

5.5 Empirical Force Law for Different Size Droplets in Contact

So far, we have discussed the force law between droplets of the same size in contact, however, in many cases we are interested in the forces between droplets of different sizes. To obtain a force law between droplets of different sizes, we apply our method to find an empirical force law using data taken on three different binary samples. The binary samples are prepared in the same manner as the monodisperse case, however, this time we use a mixture of two different droplet sizes. Table 5.2 summarizes the various parameters of our binary systems.

For the case of a binary sample, there are 3 possible contact types to consider; a small

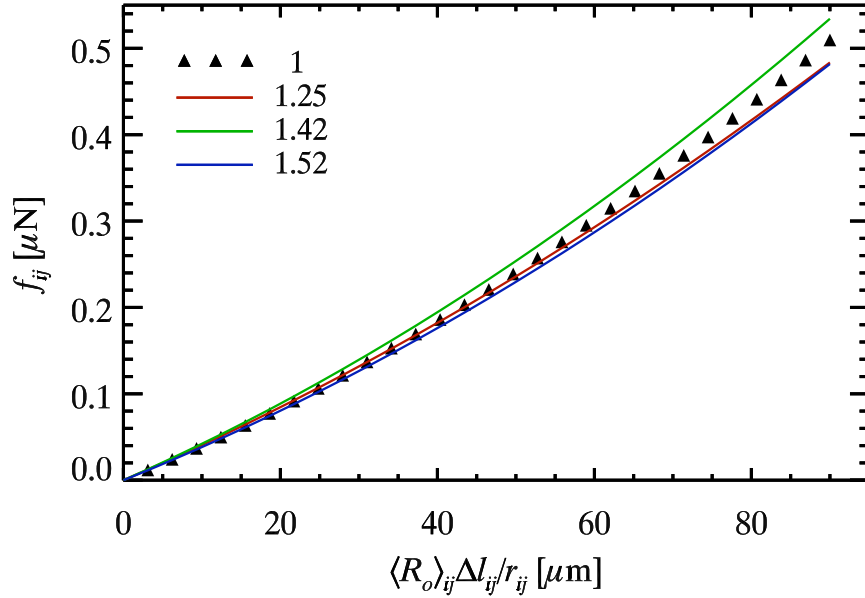


Figure 5.8: Binary force law for the experimental data. The legend indicates the size ratio. The triangle data points is the force law Eqn. 5.5 for same size droplets in contact.

droplet in contact with a small droplet (small-small contact), a small droplet in contact with a big droplet (small-big contact), and a big droplet in contact with a big droplet (big-big contact). Using our previous results, we know the forces between small-small contacts and big-big contacts while the forces between small-big contacts are unknown. We will assume for the small-big contacts that the force law obeys the same functional form as that found for the monodisperse case (Eqn. 5.5), where α_1 and α_2 are different and are considered as unknowns to be found by minimizing χ_x^2 . Recall that Eqn. 5.5 contains a term R_0 that rescales the force law and makes it universal. For the small-big contacts there are two different radii or R_o values, one for the small droplets and one for the big droplets. To account for these two radii we assume that we need to substitute R_0 with the arithmetic mean of the two radii $\langle R_0 \rangle$ giving as our binary empirical force law $F_{ij} = \alpha_1 \langle R_0 \rangle \Delta l_{ij} / r_{ij} + \alpha_2 (\langle R_0 \rangle \Delta l_{ij} / r_{ij})^2$, where α_1 and α_2 are unknown. To obtain α_1 and α_2 for our binary samples we minimize χ_x^2 , and find that α_1 and α_2 are very close to that found for the monodisperse case. The binary force laws are shown in Fig. 5.8, along with the monodisperse force law. We see that the binary force law is in very good agreement with the same size force law. There are slight variations between the curves, however, there is no

trend in the data. This binary data was taken at half the resolution as the monodisperse data sets, giving twice as much error in $\vec{\alpha}$ when minimizing χ_x^2 . Therefore we expect the variations between any two curves to be $\sim 5\%$ which is consistent with the results in the figure. We can conclude that for our experimental setup, the universal force law is

$$F_{ij} = \alpha_1 \langle R_0 \rangle \Delta l_{ij} / r_{ij} + \alpha_2 (\langle R_0 \rangle \Delta l_{ij} / r_{ij})^2, \quad (5.6)$$

where $\alpha_1 = 4.18$ dynes/cm and $\alpha_2 = (0.0909 \text{ dynes/cm})^2$.

5.6 Table of Fitting Functions

The table below have been provided for completeness and does not need to be read in full. The table list the minimal χ^2 values found for each function tested for each data set. The first column list the number of adjustable parameters, the second column list the tested force laws, and the last column list the minimized χ^2 value for each data set. The table has been sorted first by n_α and then by the minimal χ^2 for the $R_0 = 164 \mu\text{m}$ data set. The force law written in green indicates the force law we chose as the best.

| | | minimal χ^2 | | | |
|------------|---|-------------------|-------------------|-------------------|--------------------|
| | | R_0 | R_0 | R_0 | R_0 |
| n_α | Function | 164 μm | 143 μm | 105 μm | 84.1 μm |
| 1 | $\alpha_1 \Delta l_{ij}/r_{ij}$ | 0.17 | 0.09 | 3.03 | 40.30 |
| 1 | $\alpha_1 \Delta l_{ij}/\bar{R}_{ij}$ | 0.67 | 0.27 | 4.61 | 55.83 |
| 2 | $\alpha_1 \Delta l_{ij}/\bar{R}_{ij} + \alpha_2 (\Delta l_{ij}/\bar{R}_{ij})^2$ | 0.14 | 0.04 | 1.44 | 19.16 |
| 2 | $\alpha_1 (1 - e^{-\alpha_2 \Delta l_{ij}/r_{ij}})$ | 0.14 | 0.06 | 1.09 | 26.39 |
| 2 | $\alpha_1 \Delta l_{ij}/r_{ij} + \alpha_2 (\Delta l_{ij}/r_{ij})^2$ | 0.14 | 0.06 | 1.08 | 26.39 |
| 2 | $\alpha_1 (1 - e^{-\alpha_2 \Delta l_{ij}})/r_{ij}$ | 0.14 | 0.06 | 189.02 | 123.30 |
| 2 | $\alpha_1 (\Delta l_{ij}/r_{ij})^{\alpha_2}$ | 0.14 | 0.07 | 0.96 | 30.19 |
| 2 | $(\alpha_1 \Delta l_{ij} + \alpha_2 \Delta l_{ij}^2)/r_{ij}$ | 0.14 | 0.06 | 1.86 | 122.41 |
| 2 | $\alpha_1 \Delta l_{ij}^{\alpha_2}/r_{ij}$ | 0.16 | 0.07 | 1.78 | 125.40 |
| 2 | $\alpha_1 (\Delta l_{ij}/\bar{R}_{ij})^{\alpha_2}$ | 0.16 | 0.05 | 1.53 | 24.59 |
| 2 | $\alpha_1 (1 - e^{-\alpha_2 \Delta l_{ij}/\bar{R}_{ij}})$ | 0.16 | 0.04 | 1.62 | 20.49 |
| 2 | $\alpha_1 \Delta l_{ij} e^{\alpha_2/r_{ij}}$ | 0.18 | 0.06 | 2.89 | 59.20 |
| 2 | $\alpha_1 (\Delta l_{ij}/\bar{R}_{ij})^{3/2} + \alpha_2 (\Delta l_{ij}/\bar{R}_{ij})^{5/2}$ | 0.19 | 0.07 | 1.57 | 29.51 |
| 2 | $\alpha_1 \Delta l_{ij} e^{\alpha_2/\bar{R}_{ij}}$ | 0.20 | 0.04 | 3.08 | 58.01 |
| 2 | $\alpha_1 \Delta l_{ij} (1/r_{ij} + \alpha_2/r_{ij}^2)$ | 0.20 | 0.06 | 2.13 | 51.44 |
| 2 | $\alpha_1 \Delta l_{ij}/r_{ij}^{\alpha_2}$ | 0.21 | 0.06 | 2.09 | 54.77 |
| 2 | $\alpha_1 \Delta l_{ij} (1/\bar{R}_{ij}^{3/2} + \alpha_2/\bar{R}_{ij}^{5/2})$ | 0.22 | 0.05 | 2.80 | 61.07 |
| 2 | $\alpha_1 \Delta l_{ij}/\bar{R}_{ij}^{\alpha_2}$ | 0.22 | 0.65 | 26.82 | 59.64 |
| 2 | $\alpha_1 \Delta l_{ij} (1/\bar{R}_{ij} + \alpha_2/\bar{R}_{ij}^2)$ | 0.22 | 0.05 | 2.74 | 59.75 |

| | | minimal χ^2 | | | |
|------------|---|-------------------|-------------------|-------------------|--------------------|
| | | R_0 | R_0 | R_0 | R_0 |
| n_α | Function | 164 μm | 143 μm | 105 μm | 84.1 μm |
| 2 | $\alpha_1 \Delta l_{ij} (1/r_{ij}^{3/2} + \alpha_2/r_{ij}^{5/2})$ | 0.23 | 0.07 | 2.09 | 52.22 |
| 2 | $\alpha_1 (1 - e^{-\alpha_2 \Delta l_{ij}}) / \bar{R}_{ij}$ | 0.23 | 0.07 | 115.70 | 52.46 |
| 2 | $(\alpha_1 \Delta l_{ij} + \alpha_2 \Delta l_{ij}^2) / \bar{R}_{ij}$ | 0.23 | 0.08 | 2.23 | 52.23 |
| 2 | $(\alpha_1 \Delta l_{ij}^{3/2} + \alpha_2 \Delta l_{ij}^{5/2}) / r_{ij}$ | 0.27 | 0.12 | 1.69 | 151.60 |
| 2 | $(\alpha_1 \Delta l_{ij}^{3/2} + \alpha_2 \Delta l_{ij}^{5/2}) / \bar{R}_{ij}$ | 0.29 | 0.10 | 2.33 | 58.07 |
| 2 | $\alpha_1 \Delta l_{ij}^{\alpha_2} / \bar{R}_{ij}$ | 0.30 | 0.10 | 2.35 | 52.56 |
| 2 | $\alpha_1 (\Delta l_{ij} / r_{ij})^{3/2} + \alpha_2 (\Delta l_{ij} / r_{ij})^{5/2}$ | 0.55 | 0.18 | 3.46 | 109.71 |
| 3 | $(\alpha_1 \Delta l_{ij} + \alpha_2 \Delta l_{ij}^2) e^{\alpha_3 / r_{ij}}$ | 0.12 | 0.24 | 5.62 | 36.39 |
| 3 | $\alpha_1 (1 - e^{-\alpha_2 \Delta l_{ij}}) e^{\alpha_3 / r_{ij}}$ | 0.12 | 0.05 | 51.20 | 37.63 |
| 3 | $\alpha_1 (1 - e^{-\alpha_2 \Delta l_{ij}}) / r_{ij}^{\alpha_3}$ | 0.13 | 0.06 | 43.54 | 35.80 |
| 3 | $\alpha_1 \Delta l_{ij}^{\alpha_2} e^{\alpha_3 / r_{ij}}$ | 0.13 | 0.05 | 1.50 | 39.76 |
| 3 | $(\alpha_1 \Delta l_{ij} + \alpha_2 \Delta l_{ij}^2) / r_{ij}^{\alpha_3}$ | 0.13 | 0.06 | 1.67 | 34.82 |
| 3 | $\alpha_1 \Delta l_{ij} / \bar{R}_{ij} + \alpha_2 (\Delta l_{ij} / \bar{R}_{ij})^2 + \alpha_3 (\Delta l_{ij} / \bar{R}_{ij})^3$ | 0.13 | 0.04 | 1.44 | 19.15 |
| 3 | $\alpha_1 \Delta l_{ij} / r_{ij} + \alpha_2 (\Delta l_{ij} / r_{ij})^2 + \alpha_3 (\Delta l_{ij} / r_{ij})^3$ | 0.14 | 0.06 | 1.03 | 25.35 |
| 3 | $\alpha_1 (1 - e^{-\alpha_2 \Delta l_{ij}}) e^{\alpha_3 / \bar{R}_{ij}}$ | 0.14 | 0.04 | 51.24 | 37.55 |
| 3 | $(\alpha_1 \Delta l_{ij} + \alpha_2 \Delta l_{ij}^2 + \alpha_3 \Delta l_{ij}^3) / r_{ij}$ | 0.14 | 0.05 | 1.62 | 122.13 |
| 3 | $\alpha_1 (1 - e^{-\alpha_2 \Delta l_{ij}}) (1/r_{ij} + \alpha_3 / r_{ij}^2)$ | 0.14 | 0.06 | 34.21 | 123.32 |
| 3 | $(\alpha_1 \Delta l_{ij} + \alpha_2 \Delta l_{ij}^2) (1/r_{ij} + \alpha_3 / r_{ij}^2)$ | 0.14 | 0.06 | 1.86 | 89.20 |
| 3 | $(\alpha_1 \Delta l_{ij} + \alpha_2 \Delta l_{ij}^2) / \bar{R}_{ij}^{\alpha_3}$ | 0.15 | 0.04 | 1.86 | 36.12 |
| 3 | $\alpha_1 \Delta l_{ij}^{\alpha_2} / r_{ij}^{\alpha_3}$ | 0.15 | 0.06 | 1.62 | 38.08 |
| 3 | $\alpha_1 \Delta l_{ij}^{\alpha_2} e^{\alpha_3 / \bar{R}_{ij}}$ | 0.15 | 0.04 | 1.64 | 39.54 |
| 3 | $(\alpha_1 \Delta l_{ij} + \alpha_2 \Delta l_{ij}^2) (1/\bar{R}_{ij}^{3/2} + \alpha_3 / \bar{R}_{ij}^{5/2})$ | 0.15 | 0.05 | 1.87 | 72.14 |
| 3 | $\alpha_1 (1 - e^{-\alpha_2 \Delta l_{ij}}) (1/\bar{R}_{ij}^{3/2} + \alpha_3 / \bar{R}_{ij}^{5/2})$ | 0.16 | 0.05 | 54.97 | 84.27 |
| 3 | $\alpha_1 \Delta l_{ij}^{\alpha_2} (1/r_{ij} + \alpha_3 / r_{ij}^2)$ | 0.16 | 0.07 | 1.78 | 125.40 |
| 3 | $\alpha_1 \Delta l_{ij}^{\alpha_2} / \bar{R}_{ij}^{\alpha_3}$ | 0.16 | 0.05 | 1.76 | 39.52 |

| | | minimal χ^2 | | | |
|------------|---|-------------------|-------------------|-------------------|--------------------|
| | | R_0 | R_0 | R_0 | R_0 |
| n_α | Function | 164 μm | 143 μm | 105 μm | 84.1 μm |
| 3 | $(\alpha_1 \Delta l_{ij}^{3/2} + \alpha_2 \Delta l_{ij}^{5/2}) e^{\alpha_3/r_{ij}}$ | 0.18 | 0.09 | 1.42 | 42.43 |
| 3 | $\alpha_1 \Delta l_{ij}^{\alpha_2} (1/\bar{R}_{ij}^{3/2} + \alpha_3/\bar{R}_{ij}^{5/2})$ | 0.18 | 0.06 | 1.81 | 84.84 |
| 3 | $(\alpha_1 \Delta l_{ij}^{3/2} + \alpha_2 \Delta l_{ij}^{5/2}) e^{\alpha_3/\bar{R}_{ij}}$ | 0.20 | 0.07 | 2.66 | 42.13 |
| 3 | $\alpha_1 \Delta l_{ij} (1/r_{ij} + \alpha_2/r_{ij}^2 + \alpha_3/r_{ij}^3)$ | 0.20 | 0.11 | 1.65 | 41.10 |
| 3 | $(\alpha_1 \Delta l_{ij}^{3/2} + \alpha_2 \Delta l_{ij}^{5/2})/r_{ij}^{\alpha_3}$ | 0.21 | 0.08 | 1.70 | 42.03 |
| 3 | $(\alpha_1 \Delta l_{ij}^{3/2} + \alpha_2 \Delta l_{ij}^{5/2})/\bar{R}_{ij}^{\alpha_3}$ | 0.22 | 0.08 | 1.68 | 80.18 |
| 3 | $(\alpha_1 \Delta l_{ij}^{3/2} + \alpha_2 \Delta l_{ij}^{5/2})(1/\bar{R}_{ij}^{3/2} + \alpha_3/\bar{R}_{ij}^{5/2})$ | 0.22 | 0.08 | 1.68 | 80.18 |
| 3 | $\alpha_1 \Delta l_{ij} (1/\bar{R}_{ij} + \alpha_2/\bar{R}_{ij}^2 + \alpha_3/\bar{R}_{ij}^3)$ | 0.22 | 0.05 | 2.74 | 58.17 |
| 3 | $(\alpha_1 \Delta l_{ij} + \alpha_2 \Delta l_{ij}^2 + \alpha_3 \Delta l_{ij}^3)/\bar{R}_{ij}$ | 0.23 | 0.06 | 2.23 | 51.12 |
| 3 | $\alpha_1 (1 - e^{-\alpha_2 \Delta l_{ij}}) (1/\bar{R}_{ij} + \alpha_3/\bar{R}_{ij}^2)$ | 0.23 | 0.07 | 52.67 | 52.47 |
| 3 | $(\alpha_1 \Delta l_{ij} + \alpha_2 \Delta l_{ij}^2) (1/\bar{R}_{ij} + \alpha_3/\bar{R}_{ij}^2)$ | 0.23 | 0.07 | 2.23 | 35.83 |
| 3 | $(\alpha_1 \Delta l_{ij}^{3/2} + \alpha_2 \Delta l_{ij}^{5/2}) (1/r_{ij} + \alpha_3/r_{ij}^2)$ | 0.27 | 0.12 | 1.69 | 38.99 |
| 3 | $(\alpha_1 \Delta l_{ij}^{3/2} + \alpha_2 \Delta l_{ij}^{5/2}) (1/\bar{R}_{ij} + \alpha_3/\bar{R}_{ij}^2)$ | 0.28 | 0.10 | 2.06 | 58.07 |
| 3 | $\alpha_1 \Delta l_{ij}^{\alpha_2} (1/\bar{R}_{ij} + \alpha_3/\bar{R}_{ij}^2)$ | 0.30 | 0.10 | 2.35 | 39.67 |
| 3 | $\alpha_1 \Delta l_{ij}^{\alpha_2} (1/r_{ij}^{3/2} + \alpha_3/r_{ij}^{5/2})$ | 0.40 | 0.08 | 4.77 | 333.36 |
| 3 | $(\alpha_1 \Delta l_{ij} + \alpha_2 \Delta l_{ij}^2) (1/r_{ij}^{3/2} + \alpha_3/r_{ij}^{5/2})$ | 0.40 | 0.11 | 3.47 | 307.26 |
| 3 | $\alpha_1 (1 - e^{-\alpha_2 \Delta l_{ij}}) (1/r_{ij}^{3/2} + \alpha_3/r_{ij}^{5/2})$ | 0.44 | 0.10 | 156.15 | 308.29 |
| 3 | $(\alpha_1 \Delta l_{ij}^{3/2} + \alpha_2 \Delta l_{ij}^{5/2}) (1/r_{ij}^{3/2} + \alpha_3/r_{ij}^{5/2})$ | 0.74 | 0.30 | 3.16 | 331.52 |
| 3 | $(\alpha_1 \Delta l_{ij} + \alpha_2 \Delta l_{ij}^2) e^{\alpha_3/\bar{R}_{ij}}$ | 0.83 | 0.04 | 2.28 | 37.39 |
| 3 | $\alpha_1 (1 - e^{-\alpha_2 \Delta l_{ij}}) / \bar{R}_{ij}^{\alpha_3}$ | 2.19 | 0.04 | 1.98 | 37.38 |
| 4 | $(\alpha_1 \Delta l_{ij} + \alpha_2 \Delta l_{ij}^2 + \alpha_3 \Delta l_{ij}^3) e^{\alpha_4/r_{ij}}$ | 0.12 | 0.23 | 5.57 | 36.38 |
| 4 | $\alpha_1 \Delta l_{ij} / \bar{R}_{ij} + \alpha_2 (\Delta l_{ij} / \bar{R}_{ij})^2 + \alpha_3 (\Delta l_{ij} / \bar{R}_{ij})^3 + \alpha_4 (\Delta l_{ij} / \bar{R}_{ij})^4$ | 0.13 | 0.04 | 1.44 | 18.67 |
| 4 | $(\alpha_1 \Delta l_{ij} + \alpha_2 \Delta l_{ij}^2 + \alpha_3 \Delta l_{ij}^3) / r_{ij}^{\alpha_4}$ | 0.13 | 0.05 | 1.67 | 34.81 |
| 4 | $(\alpha_1 \Delta l_{ij} + \alpha_2 \Delta l_{ij}^2 + \alpha_3 \Delta l_{ij}^3) (1/r_{ij} + \alpha_4/r_{ij}^2)$ | 0.13 | 0.05 | 1.74 | 30.80 |

| | | minimal χ^2 | | | |
|------------|---|-------------------|-------------------|-------------------|--------------------|
| | | R_0 | R_0 | R_0 | R_0 |
| n_α | Function | 164 μm | 143 μm | 105 μm | 84.1 μm |
| 4 | $\alpha_1 \Delta l_{ij}/r_{ij} + \alpha_2 (\Delta l_{ij}/r_{ij})^2 + \alpha_3 (\Delta l_{ij}/r_{ij})^3 + \alpha_4 (\Delta l_{ij}/r_{ij})^4$ | 0.14 | 0.06 | 0.61 | 21.62 |
| 4 | $(\alpha_1 \Delta l_{ij} + \alpha_2 \Delta l_{ij}^2 + \alpha_3 \Delta l_{ij}^3 + \alpha_4 \Delta l_{ij}^4)/r_{ij}$ | 0.14 | 0.05 | 1.62 | 120.16 |
| 4 | $\alpha_1 (1 - e^{-\alpha_2 \Delta l_{ij}})(1/r_{ij} + \alpha_3/r_{ij}^2 + \alpha_4/r_{ij}^3)$ | 0.14 | 0.06 | 1.88 | 123.29 |
| 4 | $(\alpha_1 \Delta l_{ij} + \alpha_2 \Delta l_{ij}^2)(1/r_{ij} + \alpha_3/r_{ij}^2 + \alpha_4/r_{ij}^3)$ | 0.14 | 0.06 | 1.74 | 122.38 |
| 4 | $(\alpha_1 \Delta l_{ij} + \alpha_2 \Delta l_{ij}^2 + \alpha_3 \Delta l_{ij}^3)(1/\bar{R}_{ij}^{3/2} + \alpha_4/\bar{R}_{ij}^{5/2})$ | 0.14 | 0.04 | 1.64 | 38.64 |
| 4 | $(\alpha_1 \Delta l_{ij} + \alpha_2 \Delta l_{ij}^2 + \alpha_3 \Delta l_{ij}^3)/\bar{R}_{ij}^{\alpha_4}$ | 0.15 | 0.04 | 1.66 | 36.11 |
| 4 | $\alpha_1 \Delta l_{ij}^{\alpha_2} (1/r_{ij} + \alpha_3/r_{ij}^2 + \alpha_4/r_{ij}^3)$ | 0.15 | 0.07 | 1.78 | 125.35 |
| 4 | $(\alpha_1 \Delta l_{ij} + \alpha_2 \Delta l_{ij}^2 + \alpha_3 \Delta l_{ij}^3)(1/r_{ij}^{3/2} + \alpha_4/r_{ij}^{5/2})$ | 0.16 | 0.09 | 2.04 | 243.95 |
| 4 | $\alpha_1 \Delta l_{ij} (1/r_{ij} + \alpha_2/r_{ij}^2 + \alpha_3/r_{ij}^3 + \alpha_4/r_{ij}^4)$ | 0.20 | 0.06 | 2.13 | 50.61 |
| 4 | $(\alpha_1 \Delta l_{ij}^{3/2} + \alpha_2 \Delta l_{ij}^{5/2})(1/\bar{R}_{ij} + \alpha_3/\bar{R}_{ij}^2 + \alpha_4/\bar{R}_{ij}^3)$ | 0.22 | 0.10 | 2.15 | 58.06 |
| 4 | $\alpha_1 \Delta l_{ij} (1/\bar{R}_{ij} + \alpha_2/\bar{R}_{ij}^2 + \alpha_3/\bar{R}_{ij}^3 + \alpha_4/\bar{R}_{ij}^4)$ | 0.22 | 0.05 | 2.74 | 58.17 |
| 4 | $(\alpha_1 \Delta l_{ij} + \alpha_2 \Delta l_{ij}^2 + \alpha_3 \Delta l_{ij}^3 + \alpha_4 \Delta l_{ij}^4)/\bar{R}_{ij}$ | 0.22 | 0.06 | 2.17 | 51.08 |
| 4 | $(\alpha_1 \Delta l_{ij} + \alpha_2 \Delta l_{ij}^2 + \alpha_3 \Delta l_{ij}^3)(1/\bar{R}_{ij} + \alpha_4/\bar{R}_{ij}^2)$ | 0.23 | 0.04 | 2.23 | 35.80 |
| 4 | $\alpha_1 (1 - e^{-\alpha_2 \Delta l_{ij}})(1/\bar{R}_{ij} + \alpha_3/\bar{R}_{ij}^2 + \alpha_4/\bar{R}_{ij}^3)$ | 0.23 | 0.07 | 52.65 | 52.46 |
| 4 | $(\alpha_1 \Delta l_{ij} + \alpha_2 \Delta l_{ij}^2)(1/\bar{R}_{ij} + \alpha_3/\bar{R}_{ij}^2 + \alpha_4/\bar{R}_{ij}^3)$ | 0.23 | 0.08 | 2.23 | 45.85 |
| 4 | $(\alpha_1 \Delta l_{ij}^{3/2} + \alpha_2 \Delta l_{ij}^{5/2})(1/r_{ij} + \alpha_3/r_{ij}^2 + \alpha_4/r_{ij}^3)$ | 0.27 | 0.12 | 1.69 | 151.60 |
| 4 | $\alpha_1 \Delta l_{ij}^{\alpha_2} (1/\bar{R}_{ij} + \alpha_3/\bar{R}_{ij}^2 + \alpha_4/\bar{R}_{ij}^3)$ | 0.30 | 0.10 | 2.35 | 39.68 |
| 4 | $(\alpha_1 \Delta l_{ij} + \alpha_2 \Delta l_{ij}^2 + \alpha_3 \Delta l_{ij}^3)e^{\alpha_4/\bar{R}_{ij}}$ | 0.80 | 0.04 | 1.51 | 39.03 |

Table 5.3: This table provides a list of all the force laws tested and the minimum χ^2 for each data set.

Experimental Frictionless 2D Model of Jamming

6.1 Introduction

A wide variety of materials, from those composed of small scale particles, like colloids, to larger scale particles like emulsions, foams, and sand, all exhibit a liquid to solid like transition when the particle concentration is increased. This transition arises from the crowding of the particles to the point that microscopic rearrangements are unable to occur when external stresses are applied. This phenomena has been termed jamming and has been observed in a wide range of materials and scenarios [24, 27, 252]. Working from the premise that all jammed materials share many common features, Cates *et al.* [23] and Liu and Nagel [25] propose the idea that jammed systems can be viewed as a new class of materials that can be described using a universal conceptual and mathematical framework.

Over the last decade, an ideal model for the jamming transition has emerged to explain many of the characteristics observed in all jammed materials [22, 24, 31, 95, 253]. This ideal model system is composed of frictionless disks in 2D or spheres in 3D and the particles only interact through a soft repulsive potential when overlapping. There is a single control parameter, the volume fraction ϕ , and the system jams when ϕ is increased to a critical volume fraction ϕ_c . ϕ_c is thought to coincide with previous ideas of ‘random close packing’ of hard spheres, although a clear definition is in debate; see [22, 95, 218, 238]. Above

ϕ_c , this model system shows critical-like behavior. For example, the pressure increases as $P \sim (\phi - \phi_c)^\alpha$, with α depending on the details of the inter-particle interaction [156, 253], and the coordination number z also shows power law growth with $\phi - \phi_c$ [22, 31]. The advantage of this model is it allows for a precise study of a jamming transition, however, it is still a subject of debate whether this model will be relevant to more realistic systems [24].

To have a full understanding of the jamming transition in an experiment both the particle-particle forces and the particle positions must be known, and currently the role of friction and deformability in jammed systems is unclear since experimental efforts have mostly been limited to 2D frictional disks. A primary tool for experimentalists to study the jamming transition and verify numerical and theoretical results has been photoelastic disks [154–157]. These are frictional elastic disks that allow for direct visualization of the internal forces [6, 154–157]. Some experimental behaviors of frictional particles [156] agree with simulations of frictionless particles [253]; in particular, several of the critical-like behaviors match. Other simulations where friction is varied find that some behaviors change as friction tends to zero [21, 254, 255]; for example, the coordination number at jamming changes smoothly from $z \approx 4$ for frictionless particles to $z \approx 3$ for particles with a large friction coefficient (in 2D). This difference may be important if the contact number is the crucial quantity governing much of the critical behavior, rather than $\phi - \phi_c$ [21]. In addition to friction, deformability presents an essential difference between how grains and emulsions or foams flow. Since grains can not significantly deform they must dilate to flow, while bubbles can easily deform and rearrange with no dilatation [38]. In granular studies, the inability for grains to significantly deform without breaking limits the study of the jamming transition to near ϕ_c , and it is unclear if the scaling laws found for granular materials apply at larger $\phi - \phi_c$.

There have been other experimental techniques to study jamming and granular physics that include emulsions [158, 159], bubble rafts [169, 256, 257], plastic bead rafts [258, 259], and 2D foams [162, 163, 183], but only in two emulsion studies [158, 159] and one 2D foam study were the forces measured [153]. In the two emulsion studies the jamming transition was not probed. In the 2D foam study, the authors only investigate the distribution of forces at different ϕ and the critical scaling in z , leaving much to be studied. In Sec. 6.4 and

6.6, we discuss the jamming properties and critical scaling laws explored in the numerical study of O’Hern *et al.* [22], the photoelastic study of Majmudar *et al.* [156], and foam study of Katgert *et al.* [153] in more detail. We will also study the jamming transition using an experimental setup analogous to photoelastic disks, but without static friction, and we will compare our results to the previous numerical and experimental studies of [22, 153, 156].

Another important aspect of jammed materials are the emergence of force chains, chain like structures of large forces that bear the majority of the load [154, 155, 159, 260–263]. Force chains are responsible for mechanical rigidity and are related to many bulk material properties [23, 260, 261, 264]. There have been many theoretical attempts to understand force chains, such as the q -model of Coppersmith *et al.* [265], directed-force chain networks of Socolar’s group [266], and simulations [267–269]. Some of these ideas assume friction is present, and others ignore friction. Others have taken an ensemble approach to describe force chains, where each approach has its own meaning for an ensemble and how the ensemble is sampled [148, 158, 270–275]. While some of these models can successfully predict certain properties of the force network, they can not explain the physical origins of force chains. A model recently proposed by Bruijic *et al.* [158, 276] and extended by Zhou *et al.* [159, 272] provides a physical description for the origin of force chains and can accurately predict the statistics of the force chain network. An essential untested assumption of the model is that the forces on neighboring droplets are uncorrelated.

In this chapter, we introduce a new experimental tool for studying the jamming transition of frictionless soft deformable droplets using a quasi-2D emulsion setup. We outline a method to determine the force law between droplets in contact. Our method can determine forces to an accuracy of about 10% - 15% which is a factor of 5-10 in improvement from the forces reported for a similar system [153]. We use this model system to characterize the critical scaling of the jamming transition and compare our results to other numerical and experimental models of the jamming transition. We also characterize the statistics and randomness of the force network and compare our results to the Bruijić-Zhou model.

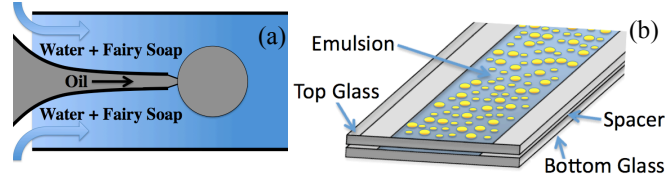


Figure 6.1: (a) is a schematic of our co-flow apparatus where oil is pumped at a constant rate through a micropipet centered within a capillary tube of larger diameter. Around the inner micropipet, a 5 g/mL water Fairy soap mixture is pumped through the capillary tube, and as oil leaves the micropipet it forms spherical droplets that repeatedly break off with the same diameter. (b) is a schematic of our sample chamber where emulsion droplets are confined to a 2D plane by two microscope slides separated by either a $\sim 100 \mu\text{m}$ spacer (transparency film) or $\sim 180 \mu\text{m}$ spacer (glass coverslip).

6.2 Sample Preparation

Our sample chamber is designed to create a system of quasi-2D frictionless emulsion droplets, analogous to 2D granular systems of photoelastic disks but without static friction [155]. The sample chamber consist of two microscope glass slides of dimensions $25 \text{ mm} \times 75 \text{ mm}$ (Corning) separated by $\sim 100 \mu\text{m}$ spacer (transparency film) or $\sim 180 \mu\text{m}$ spacer (Corning No. 1 glass coverslip) placed along the two longer edges (see Fig. 6.1(b)). The chamber is filled with an oil in water emulsion, where the diameters of the emulsion droplets are larger than the gap distance between the microscope slides. The emulsion droplets are produced using a standard co-flow micro-fluidic technique [277], see Fig. 6.1(a). The inner diameter is $\sim 35 \mu\text{m}$ and the outer diameter is $\sim 500 \mu\text{m}$. The flow rate of the water Fairy soap mixture is $\sim 1 \text{ mL/min}$ and the flow rate of the oil is $\sim 0.5 \mu\text{L/hr}$. After the sample chambers are loaded, they are placed on a microscope for imaging. To acquire very accurate measurements of each droplets deformation we take high resolution images on the order of 10,000 by 50,000 pixels². We achieve this resolution by taking a series of images with resolution 2000×2400 pixels of neighboring regions within the sample and later merge all the images together to form a single high resolution image. Each high resolution image has about 1,000 to 5,000 droplets in the field of view depending on the droplet radius.

To study the jamming transition, we use data taken in Chapter 5.5 on three separate binary samples. In Fig. 6.2, we show an image within a small region of each sample, and in Table 6.1, we list the droplet sizes and polydispersity for each data set. In Fig. 6.3,

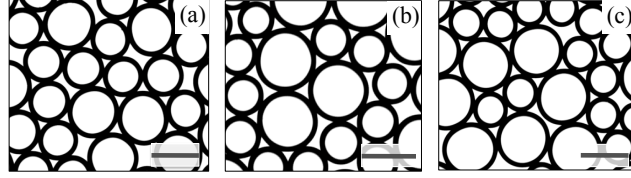


Figure 6.2: Close up view of regions within our three binary samples. The scale bar in each image is $250 \mu\text{m}$. (a) is an image for our sample with size ratio 1.25. (b) is an image for our sample with size ratio 1.42. (c) is an image for our sample with size ratio 1.52.

| σ | n_r | $r_0^{(big)}$ | poly ^(big) | $r_0^{(small)}$ | poly ^(small) |
|----------|-------|-------------------|-----------------------|--------------------|-------------------------|
| 1.25 | 0.684 | $126 \mu\text{m}$ | 3.4% | $102 \mu\text{m}$ | 3.1% |
| 1.42 | 0.849 | $130 \mu\text{m}$ | 3.0% | $105 \mu\text{m}$ | 3.4% |
| 1.52 | 0.806 | $137 \mu\text{m}$ | 3.3% | $90.1 \mu\text{m}$ | 3.1% |

Table 6.1: This table provides various parameters characterizing the droplets in our 3 binary samples. The first column $\sigma = r_0^{(big)}/r_0^{(small)}$ is the size ratio and the second column is the number ratio n_r (number of big droplets to number of small droplets). The polydispersity in droplet sizes for the big droplets is indicated by poly^(big) and for the small droplets by poly^(small). The polydispersity is defined as the standard deviation in droplet sizes normalized by the mean size. Our uncertainties for the various measures are $\sim 2 \mu\text{m}$ in r_0 , $\sim 0.1\%$ in σ , and $< 0.1\%$ in polydispersity. Since we can count every single droplet there is no measurement error in n_r .

we show an experimental image for one of the samples over a larger field of view. The samples were prepared by loading droplets of two different sizes into a chamber, and then placing this sample onto a microscope inclined to an angle 28° . The droplets rise to the top of the chamber and rest into a jammed state. The advantage of this system is that the area fraction increases with distance up the incline, and therefore, we can easily study how various jamming properties depend on area fraction. Also by inclining the samples, we were able to use the data in Chapter 5.5 to determine an empirical force law. To identify the center and outline of the droplets from our images we use the algorithms discussed in Chapter 4, and to determine the contact forces we use the force law determined in Chapter 5.5.

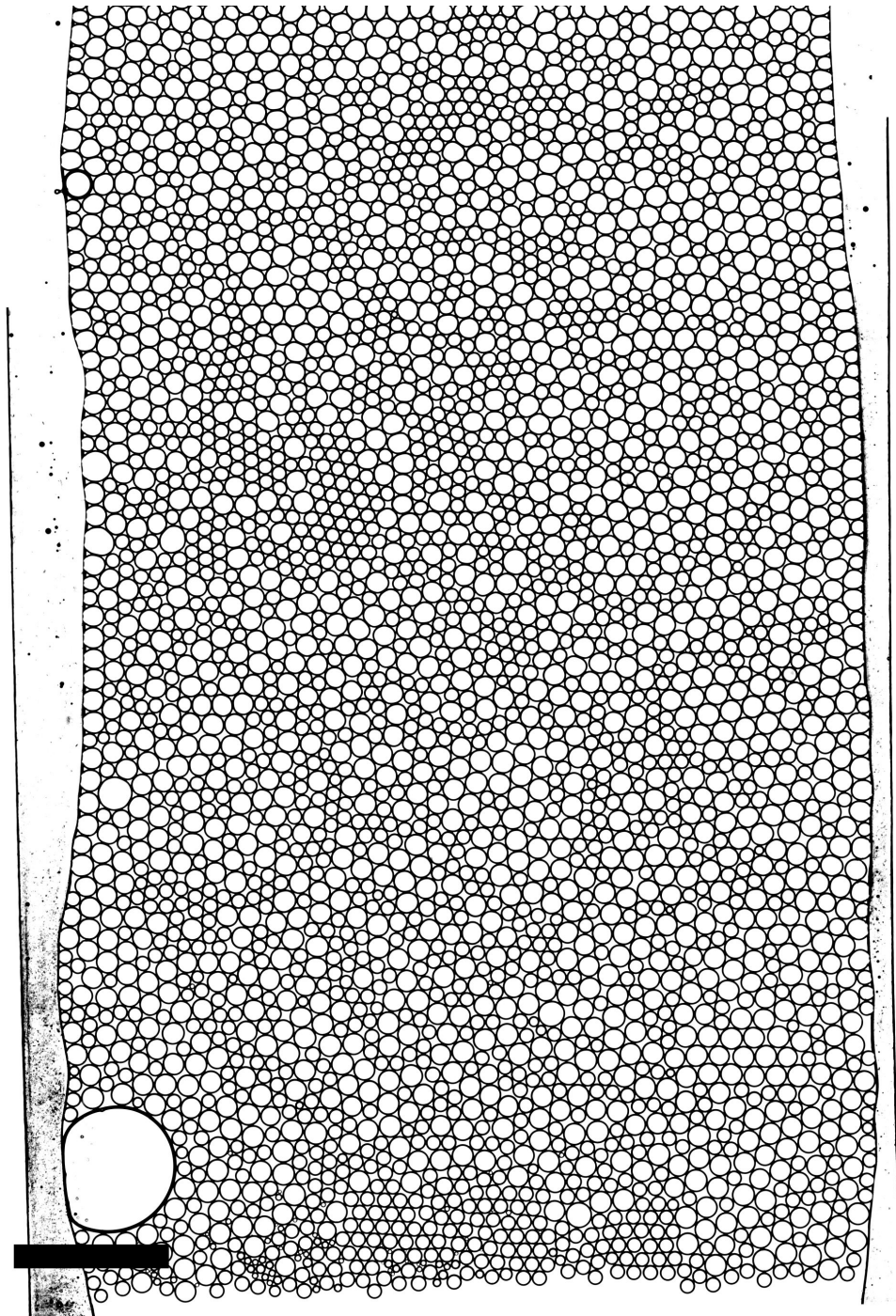


Figure 6.3: Image of an inclined sample with size ratio 1.52. This image only shows 1/3 of the sample in the vertical direction. When analyzing data, we only consider droplets that are at least 4 particles diameters from the wall. The scale bar at the bottom left is 2 mm.

6.3 Jamming Point

To characterize various critical scaling laws with $\phi - \phi_c$ we must first identify the jamming point ϕ_c for each data set. We can treat the area fraction at the bottom of the droplet pile $y = 0$ (see Fig. 5.1) in our data as the jamming point since the forces between droplets at $y = 0$ are nearly zero, and for any small increase in area fraction (which is like a small increase in y) leads to an increase in the forces between droplets. To compute the area fraction, we must determine how much of the system's area is occupied by droplets. If we only consider droplets at $y = 0$ in computing the area fraction, the statistics will be poor. If we include more droplets near $y = 0$ in the calculation of the area fraction to improve the statistics, the center of mass of the droplets is greater than $y = 0$ and the area fraction does not represent $\phi(y = 0)$. Therefore, to determine ϕ_c we will compute the area fraction for a collection of droplets at various y and extrapolate the area fraction to $y = 0$. We calculate the area fraction directly from our images of the droplets in four steps. First, using the centers and radii of the droplets we compute the radical voronoi cells [241, 242] for each droplet (see Chapter 4.6). Second, we locate the pixels in the image that are within each droplet's voronoi cell and the pixels that belong to each droplet. Third, we compute the voronoi area A_v and the droplet area A_d for each droplet using the pixels identified in step two. Finally, the area fraction $\phi(y)$ at some distance y is computed as $\phi(y) = \sum_k A_{d,k} / \sum_k A_{v,k}$, where k indexes all droplets with a center of mass within $y - \Delta y/2$ and $y + \Delta y/2$. We choose $\Delta y = 6r_0$, giving roughly 150 droplets per y sampled. In Fig. 6.4, we illustrate how ϕ is computed on a set of droplets. Using the computed $\phi(y)$, we find for the three data sets $\phi_c = 0.855, 0.861, \text{ and } 0.858$ for the $\sigma = 1.25, 1.42, \text{ and } 1.52$ data, respectively, where σ is the big to small size ratio of the droplets. In simulations on frictionless disk and experiments on 2D foams it has been reported that $\phi_c \sim 0.84$ for binary systems [153, 253, 278], which is a little lower than the values we found.

We note that our measured area fractions depend on our choice for where we define the outer perimeter of a droplet. From the images our choice of the outer perimeter has an uncertainty of 2-3 pixels which leads to a systematic uncertainty in the area fraction of roughly 1%. Since this is a systematic uncertainty our choice in defining the boundary also

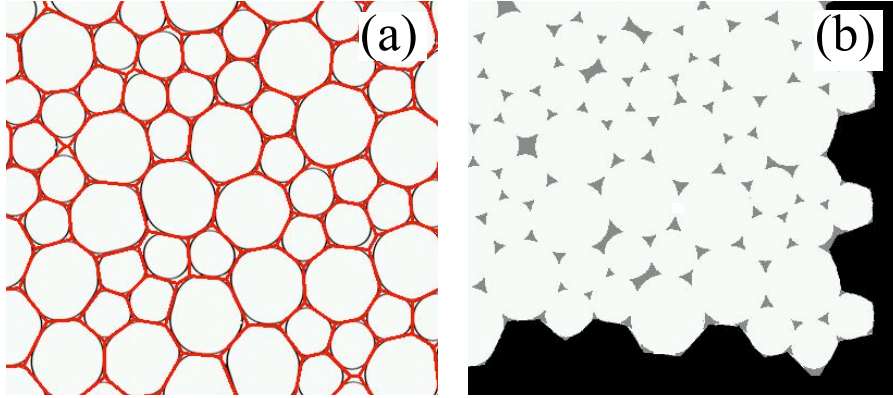


Figure 6.4: These two figures illustrate how the area fraction around a certain group of droplets is computed. In the above images, we show a close up view of a region where the area fraction is to be computed. The first step in computing the area fraction is to compute the radical Voronoi tessellation. In (a) we show the radical Voronoi tessellation as the red polygonal cells (see Chapter 4.6 for how the Voronoi tessellation is computed). To compute the area fraction around only certain droplets of interest, the other Voronoi cells are ignored. This can be seen in (b) where the pixels belonging to the Voronoi cells not of interest have been turned to black. For those droplets of interest, the pixels inside of the droplet have been turned to white and the pixels outside the droplets have been turned to grey. The area fraction is simply the total number of white pixels divided by the total number of grey and white pixels.

shifts ϕ_c by the same amount, and therefore, the control parameter $\phi - \phi_c$ is insensitive to this systematic error.

6.4 Critical Scaling

The first critical scaling we investigate is the coordination number z for each packing. In the inset of Fig. 6.5(a), we plot the average coordination number z as a function of area fraction for the 3 separate packings, where z and ϕ are found at various points up the incline. The data show a linear relationship between z and ϕ for all three packings, and we have added a line to highlight the linearity. We see that this line extrapolates to a coordination number of $z_c = 4.8$ at $\phi = \phi_c = 0.86$. In prior numerical studies on jamming in frictionless systems, it has been shown that the coordination number and area fraction obey a power law scaling of $z - z_c = (\phi - \phi_c)^{\beta_z}$, where $z_c = 4$ and $\beta_z = 1/2$, which is inconsistent with the results in the inset of Fig. 6.5(a) [253].

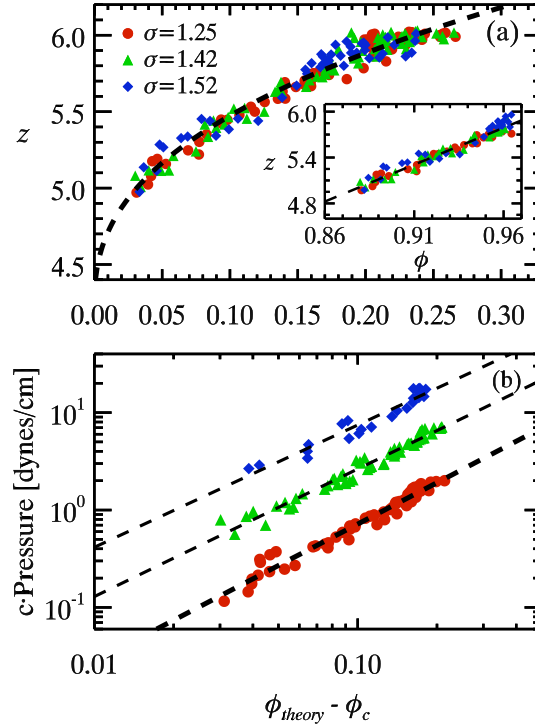


Figure 6.5: (a) Scatter plot of coordination number and the equivalent theoretical area fraction. All data were fit together to $z - z_c = A(\phi - \phi_c)^{\beta_z}$, where the fit is shown as the black dashed line with fit parameters $z_c = 4.57 \pm 0.03$, $A = 2.73 \pm 0.06$, and $\beta_z = 0.46 \pm 0.01$. Fitting the different data sets separately gives slightly different fit values, and the fit values are shown in Table 6.2. Inset of (a): Scatter plot of coordination number and area fraction. The dashed line is a linear fit to all the data with slope 8.22 with $z_c = 4.8$ at $\phi = \phi_c = 0.86$. (b) A scatter plot between pressure and the equivalent theoretical area fraction. The pressure has been scaled by a prefactor $c = 1, 3.5$, and 10 for the $\sigma = 1.25, 1.42$, and 1.52 data respectively. Each data set is fitted to $\mathcal{P} = A(\phi_{theory} - \phi_c)^{\beta_P}$, and the fits are shown as the black dashed lines. The fit values are shown in Table 6.2.

However, as pointed out by Katgert *et al.* [153], the definition of area fraction is different between numerical and experimental studies. In numerical studies, the area fraction is defined as $\phi_{theory} = A_{disks}/A_c$, and in experiments, $\phi = A_{total}/A_c$, where A_{disks} is the sum of all the disk areas, A_{total} is the total area of the container occupied by droplets, and A_c is the area of the container. The difference in the definitions is subtle and has to do with disks being allowed to overlap in the simulations, but in experiments the droplets are not allowed to overlap and instead deform. In experiments and numerical studies, the total area of the container occupied by disks is $A_{total} = A_{disks} - 2A_{over}$, where A_{over} is total area of all overlapping disks. For numerical studies, $A_{over} > 0$ when the system is compressed

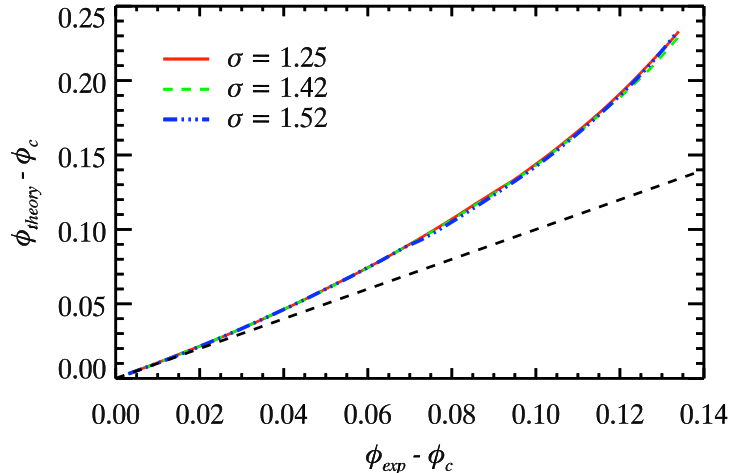


Figure 6.6: This plot shows the relationship between ϕ_{exp} and ϕ_{theory} for simulations of randomly packed disks for three different size ratios indicated in the legend. The data was generated by swelling packings of 1000 disks to different area fractions. The size and number ratio for each packing was chosen to match the parameters given in Table 6.1. The dashed black line represents $\phi_{exp} = \phi_{theory}$.

since disks overlap, and in experiments, $A_{over} = 0$ for all compressions since disks can not overlap. In the numerical studies where the critical scaling was observed, they used ϕ_{theory} as their area fraction, and therefore, to properly compare our results to theory we can convert our experimentally measured ϕ_{exp} into the appropriate numerical ϕ_{theory} by accounting for any overlap area of neighboring disks. By computing how A_{over}/A_c depends on ϕ_{exp} we can convert our area fraction using $\phi_{theory} = \phi_{exp} + 2A_{over}/A_c$. We compute A_{over}/A_c by swelling random packings of 1000 disks to different values of ϕ_{exp} using our method in Chapter 3.2, where each packing had the appropriate size ratio and number ratio to match the parameters as given in Table 6.1. In Fig. 6.6, we show the relationship between ϕ_{exp} and ϕ_{theory} for the different samples, and find that this relationship is the same for all the data.

For each data set, we determine the equivalent ϕ_{theory} at each y using our simulations to convert ϕ_{exp} to ϕ_{theory} . In Fig. 6.5(a) we plot z as function of distances to the jamming point $\phi_{theory} - \phi_c$. Using ϕ_{theory} we find that the relationship is no longer linear and looks more like the scaling $z - z_c = (\phi_{theory} - \phi_c)^{\beta_z}$ with $\beta_z < 1$. Since all the data overlap well, we fit all the data together to this critical scaling law to improve statistics, and find an exponent

| $z - z_0 = A_z(\phi - \phi_{theory})^{\beta_z}$ | | | |
|---|-------------------------|-----------------|---------------|
| σ | A_z | β_z | z_c |
| 1.25 | 3.22 ± 0.06 | 0.45 ± 0.05 | 4.3 ± 0.2 |
| 1.42 | 3.25 ± 0.07 | 0.43 ± 0.05 | 4.3 ± 0.2 |
| 1.52 | 3.21 ± 0.14 | 0.34 ± 0.07 | 4.0 ± 0.3 |
| $\mathcal{P} = A(\phi - \phi_{theory})^{\beta_P}$ | | | |
| σ | A_P [dynes/cm] | β_P | |
| 1.25 | 18.5 ± 0.3 | 1.41 ± 0.01 | |
| 1.42 | 15.4 ± 0.3 | 1.30 ± 0.01 | |
| 1.52 | 13.4 ± 0.4 | 1.26 ± 0.01 | |
| $f_{ij} = F_0(\delta r_{ij}/d_{ij})^{\beta_f}$ | | | |
| σ | F_0 [μN] | β_f | |
| 1.25 | 3.30 ± 0.05 | 1.40 ± 0.01 | |
| 1.42 | 2.34 ± 0.06 | 1.29 ± 0.01 | |
| 1.52 | 2.02 ± 0.03 | 1.25 ± 0.01 | |

Table 6.2: This table shows the fitting parameters for data fitted to various critical scaling laws. The first column indicates the size ratio and the other columns indicate the fit values. The uncertainties in the fit values were obtained by adding noise commensurate with the measurement errors and refitting the data. The uncertainties are the standard deviation in the fit values after refitting the data 100 times.

of $\beta_z = 0.44$ which is close to the previously found $\beta_z = 1/2$ [153, 253]. The fit also gave $z_c = 4.2$. Fitting the data separately gives different fit parameters, and the fit parameters are shown in Table 6.2. For $\sigma = 1.25$ and $\sigma = 1.42$, β_z is $1/2$ within the uncertainty, but for $\sigma = 1.52$, β_z is less than $1/2$. We also find that β decreases with increasing σ . Interestingly, in 2D photoelastic disk experiments, they found $z - z_c = (\phi - \phi_c)^{\beta_z}$ with $\beta_z = 1/2$ without needing to convert their experimental ϕ to ϕ_{theory} [156].

The second critical scaling we investigate is the dependence of pressure with distance to the jamming point. To determine the 2D pressure at various ϕ , we consider the pressure at various distances up the incline. For k droplets located a distance $y - \Delta y/2$ and $y + \Delta y/2$ up the incline, the 2D pressure, which has units of force/length, can be computed from the contact forces using the expression $\mathcal{P} = \left(\sum_i \sum_{j>i} F_{ij} r_{ij} \right) / \sum_k A_{k,v}$, where i and j index all contacts on the k droplets and $\sum_k A_{k,v}$ is the sum of the voronoi areas of all k droplets [22, 279]. Here we use $\Delta y = 5r_0$. In Fig 6.5(b), we plot the pressure for all three packings against $\phi_{theory} - \phi_c$ at various y . We scaled the pressure by a prefactor c in the figure to separate the curves. In previous studies it was found that the pressure should obey

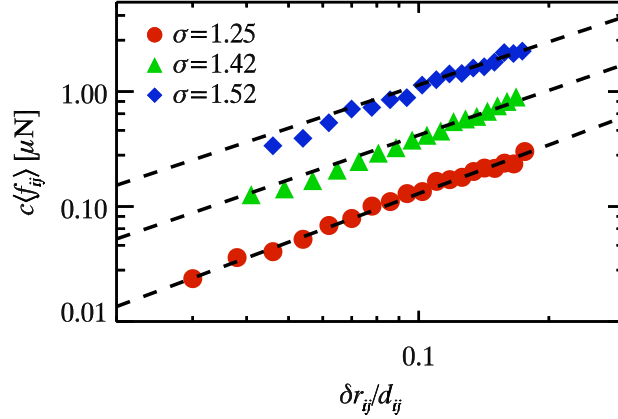


Figure 6.7: The average force between droplets in contact is plotted against the amount of compression between the droplets. The average force has been scaled by a prefactor of $c = 1, 3.5,$ and 10 for the $\sigma = 1.25, 1.42,$ and 1.52 data respectively. Each data set is fitted to $\langle f_{ij} \rangle = \epsilon (\delta r_{ij}/d_{ij})^{\beta_f}$ and the fits are shown as the black dashed lines. The fit values are shown in Table 6.2.

the critical scaling $\mathcal{P} = (\phi_{theory} - \phi_c)^{\beta_P}$ [22, 156]. To see how well our data is described by this scaling, we fit each data set to $\mathcal{P} = A(\phi_{theory} - \phi_c)^{\beta_P}$. The fit values are shown in Table 6.2 and each fit is shown in Fig 6.5(b) as the dashed lines. In the figure, we see that the data is well fitted by the critical scaling law, where the exponents for the critical scaling are between 1.25-1.41. In 2D photoelastic disk experiments, β_P was found to be 1.1 [156].

In the numerical study by O’Hern *et al.* [22], where the scaling $\mathcal{P} = (\phi_{theory} - \phi_c)^{\beta_P}$ was observed, they used frictionless disks that interacted via the force law $f_{ij} = F_0(\delta r_{ij}/d_{ij})^{\beta_f}$, where F_0 is a scale, δr_{ij} is the distance between two particles in contact, and d_{ij} is the sum of the radii of the particles in contact. In their paper, they showed that $\beta_P = \beta_f$. To see if this relationship is consistent with our data, we computed an effective force law $\langle f_{ij} \rangle$ for various $\delta r_{ij}/d_{ij}$ between droplets in contact. We obtain this effective force law by computing a $\delta r_{ij}/d_{ij}$ for each contact force, and then we average together all the contact forces with roughly the same $\delta r_{ij}/d_{ij}$. In Fig. 6.7, we plot $\langle f_{ij} \rangle$ for each binary sample and fit each data to $\langle f_{ij} \rangle = F_0(\delta r_{ij}/d_{ij})^{\beta_f}$ to obtain a β_f . Since all the effective force laws overlap fairly well with each other, we have scaled each force law by a prefactor c to separate the data. In the figure, the fits are shown as the red dashed lines and we see that the data are well described by the fits. The fit values for each data set are given in Table 6.2. Confirming

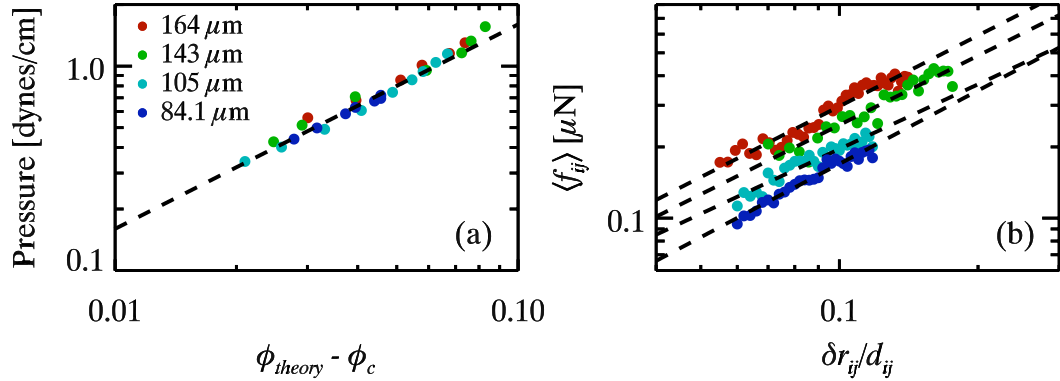


Figure 6.8: (a) A scatter plot between pressure and the equivalent theoretical area fraction for our monodisperse data sets. The legend indicates the size of the droplets. The black dashed line is a guide to eye and indicates a linear relationship. (b) The dependence of the average force on compression is shown for our monodisperse data sets. Each data has been fitted to a power law as indicated by the black dashed lines. The fit values are given in Table 6.3. The legend in (a) applies to (b) as well.

the results of O’Hern [22], the fits gave exponents for β_f that are in agreement with β_P .

6.5 Pressure and Effective Force Law for Monodisperse Data

In addition to the binary force calibration data presented in the last chapter, we also have incline data on four different monodisperse packings presented in Chapter 5.4. Each packing consists of droplets with radius $R_0 = 164 \mu\text{m}$, $143 \mu\text{m}$, $105 \mu\text{m}$, or $84.1 \mu\text{m}$, where R_0 is the 3D radius of the droplets before placing them in the sample chamber. Repeating the above analysis on our monodisperse data, we can test if crystalline packings also give a critical scaling in the pressure and if the effective force law obeys a power law scaling. By measuring the area fraction with distance up the incline, we determine $\phi_c = 0.910$, 0.900 , 0.903 , 0.905 for the $R_0 = 164 \mu\text{m}$, $143 \mu\text{m}$, $105 \mu\text{m}$, or $84.1 \mu\text{m}$ packings respectively. For a crystalline packing we expect $\phi_c = \sqrt{3}\pi/6 \approx 0.906$, which is close to the measured values.

We start by measuring the pressure and area fraction with distance up the incline. In Fig. 6.8(a), we plot the dependence of the pressure with distance to the jamming point $\phi_{theory} - \phi_c$, and find that the pressure scales linearly with distance to the jamming point, where the black dashed line illustrates a linear scaling relationship. Fitting each data set separately to a power law gives exponents that are given in Table 6.3. The fits gave

| $\mathcal{P} = A(\phi - \phi_{theory})^{\beta_P}$ | | |
|---|-------------------------|-----------------|
| R_0 [μm] | A_P [dynes/cm] | β_P |
| 164 | 14.8 ± 0.3 | 0.94 ± 0.01 |
| 143 | 16.7 ± 0.4 | 0.99 ± 0.01 |
| 105 | 18.5 ± 0.5 | 1.05 ± 0.01 |
| 84.1 | 13.5 ± 0.5 | 0.95 ± 0.01 |
| $f_{ij} = F_0(\delta r_{ij}/d_{ij})^{\beta_f}$ | | |
| R_0 [μm] | F_0 [μN] | β_f |
| 164 | 2.93 ± 0.03 | 0.99 ± 0.01 |
| 143 | 2.33 ± 0.04 | 0.97 ± 0.01 |
| 105 | 1.59 ± 0.06 | 0.91 ± 0.01 |
| 84.1 | 1.81 ± 0.05 | 1.03 ± 0.01 |

Table 6.3: This table shows the fitting parameters for our monodisperse data fitted to two scaling laws. The first column indicates the droplet radius and the other columns indicate the fit values. The uncertainties in the fit values were obtained by adding noise commensurate with the measurement errors and refitting the data. The uncertainties are the standard deviation in the fit values after refitting the data 100 times.

exponents of nearly unity, ± 0.05 . These exponents are smaller than the exponents found for the bidisperse case in the previous section.

Using the repulsive forces and relative distances between contacts, we show in Fig. 6.8(b) the relationship between the average force and compression $\delta r_{ij}/d_{ij}$ for each data set. The dashed lines in the figure are power law fits to the data. The power law fits gave exponents of roughly unity, where the fitting parameters are shown in Table 6.3. In the previous section, it was shown that the exponents β_P from fitting the pressure data and the exponents β_F from fitting the effective force law data agreed very well. For the monodisperse data, we see that the exponents are close, but do not agree as well as before.

Our monodisperse force data in Fig. 6.8(b) indicates that the effective force law is Hookean, in contrast to the non-Hookean effective force law observed for our binary samples. Using the simple examples shown in Fig. 6.9, we will reason why the effective force law for the monodisperse and bidisperse packings may differ. Although, from these examples it will not be clear if we should expect an effective force law that is Hookean, non-Hookean, or Hertzian. First, we note that the force between two droplets is not determined by the center to center distance δr_{ij} . Instead, as we have shown in the last chapter, the force is determined by the contact length and the curvature of the droplets. In our above analysis, we have

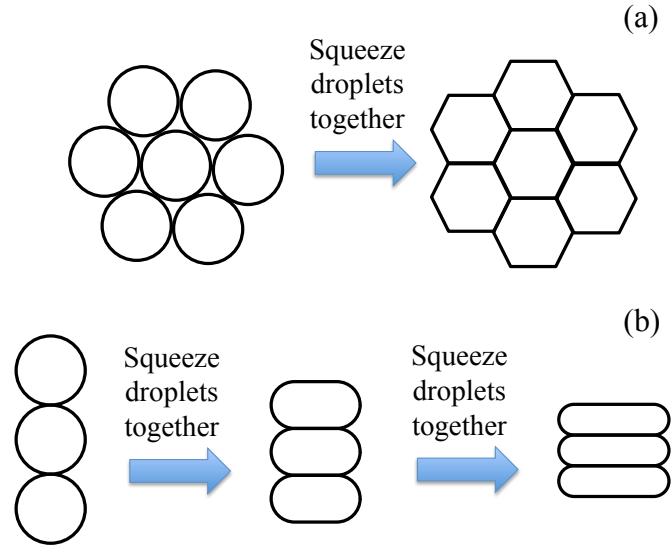


Figure 6.9: (a) A crystalline packing of droplets pressed together. In this example, the force at the contacts goes to infinity while the center to center distance δr_{ij} is finite. (b) A chain of droplets pressed together. In this example, the force at the contacts goes to infinity as the center to center distance δr_{ij} goes to zero.

computed an “effective” force law between droplets. This “effective” force law is the average, not actual, force between two droplets separated by a common center to center distance δr_{ij} . In Fig. 6.9(a) and (b), we show two examples illustrating how the force between droplets can be greatly different for the same δr_{ij} . In Fig. 6.9(a), we show a crystalline packing of droplets pressed together so tightly that the force at the contact goes to infinity. Regardless of how much force is acting on the droplets, the center to center distance is always finite. In Fig. 6.9(b), we show a chain of droplets being pressed together. In this example, as the force on the droplets increase, the center to center distance between the droplets goes to zero. Comparing both examples, we can conclude that for the same δr_{ij} the force at the contacts will differ and be highly depended on the local packing geometry. For our monodisperse data, the packing will be analogous to Fig. 6.9(a), while for our bidisperse data, the packing will be somewhere between Fig. 6.9(a) and (b). Therefore, from this simple example we can understand why the effective force law between monodisperse packings and bidisperse packings is different. Also, since the local packing geometry can vary between different bidisperse packings, it also hints as to why in the last section β_F differed between the three binary packings.

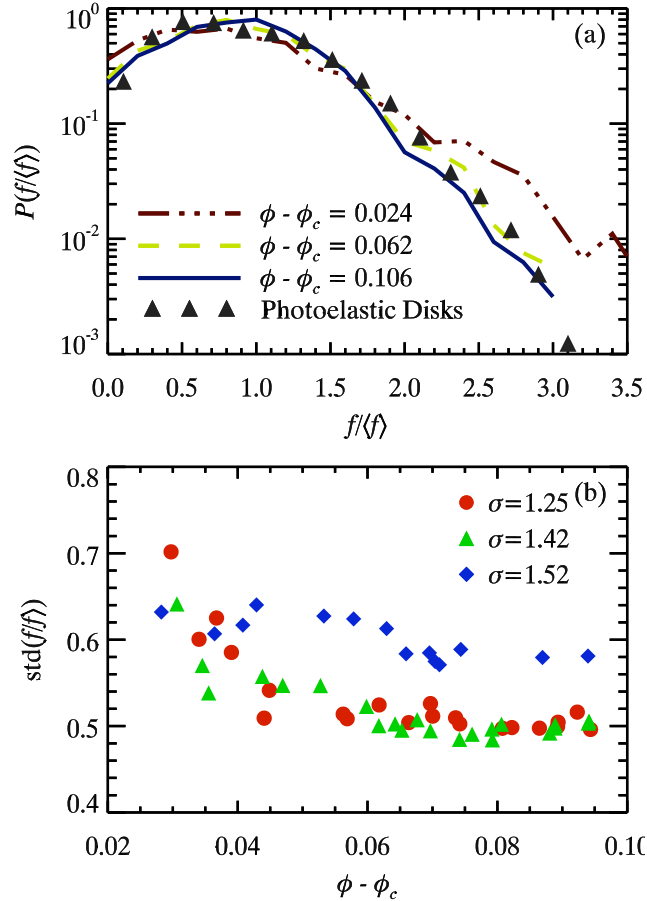


Figure 6.10: (a) Distribution of contact forces relative to the mean contact force at different ϕ for the $\sigma = 1.25$ packing, $\langle f \rangle = 0.011 \mu\text{N}$, $0.045 \mu\text{N}$, and $0.13 \mu\text{N}$ for the $\phi = 0.88, 0.92$, and 0.96 distributions respectively. The distribution of forces for a 2D photoelastic system at $\phi - \phi_c \sim 0.016$ performed by Majmudar *et al.* is shown as well [155]. (b) The standard deviation if the $P(f/\langle f \rangle)$ distributions for each packing at different ϕ are shown.

6.6 Force Distribution

We now consider the distribution of contact forces for each packing at different area fractions. Like before, we sample the contacts forces at various points up the incline using a window of $y - \Delta y/2$ and $y + \Delta y/2$. However, we need many contacts to obtain a good distribution of contact forces, and therefore, we use $\Delta y = 30r_0$. This gives roughly 2500 contacts for each y sampled. In Fig. 6.10(a), we show the distribution of contact forces normalized by the mean contact force at 3 distances up the incline for the $\sigma = 1.25$ packing, where the values of ϕ at each y are reported. We have also included in the figure the distri-

bution of normal forces from Majmudar *et al.* [155] on frictional 2D photoelastic disks. In their photoelastic disks experiment, the particles were isotropically compressed to an area fraction ~ 0.016 above the critical area fraction. We see that in all our data most forces are near or less than the mean force $\langle f \rangle$ and that the maximum force is about $3\langle f \rangle$. We also find that the shape and magnitude of all the curves are roughly the same. These distributions are also similar to simulations and experiments on 2D and 3D frictionless systems on foams and emulsions [153, 159, 253, 276]. This suggest that the distribution of forces is a fairly universal property of all jammed systems.

As observed by Katgert *et al.* [153], our force distributions slightly narrow with area fraction in Fig. 6.10(a). To see how the width of the distributions depend on area fraction for each packing, we plot the standard deviation of each force distribution in Fig. 6.10(b). For the $\sigma = 1.25$ and $\sigma = 1.42$ packings, the width of the force distributions decrease quickly near the jamming point and saturates to a constant width of ~ 0.5 further from the jamming point. However, the $\sigma = 1.52$ packing has a broader distribution of forces at larger $\phi - \phi_c$ compared to the other two packings, and the decrease in the width as $\phi - \phi_c$ increases is more subtle. It's not clear why the $\sigma = 1.52$ data does not show the same decay in width of the force distribution as the other two packings.

6.7 Force Chains

We now investigate the characteristics of the force chain network for each binary packing and test the randomness of each network. Having established in the previous section that our model system shares many common features with other numerical and experimental model systems, this analysis will serve to provide a broad conceptual understanding of force chains in jammed systems.

In Fig. 6.11(a) we show an experimental image with the contact forces between droplets drawn as lines. The forces are heterogeneous in magnitude, with the large forces organized along chain like structures (termed force chains) that bear most of the load. This type of forces network is common in many jammed systems [6, 154–157]. To characterize the force chains of our jammed systems we need to provide a precise definition for a force chain.

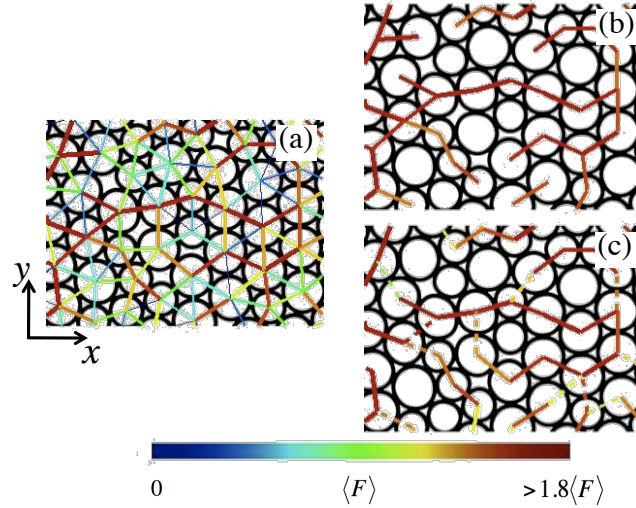


Figure 6.11: (a) shows the forces between droplets within a region of our $\sigma = 1.25$ sample. (b) The same image and forces as in (a) with only the forces that are larger than $1.4\langle f \rangle$ being shown. (c) Using our definition for a force chain only the forces in (a) belonging to a force chain (solid lines) and the merging/branching forces (dashed lines) are shown.

A common definition for force chains are those force segments within the force network that are larger than some threshold $c\langle f \rangle$ [154, 159, 262, 263]. In Fig. 6.11(b) we show such a force chain network for our data using $c = 1.4$, where the forces above $1.4\langle f \rangle$ form chain like structures that branch and merge. The branching and merging of the force network makes it difficult, but not impossible to describe the statistics of the network. To simplify the network we propose a new alternative definition that divides the network into isolated force chains.

Staying consistent with the meaning of a force chain, we define a force segment to belong to a force chain if it is one of the two largest forces on both droplets joined by the force segment. Under this definition, each droplet can only have a maximum of two force segments that belong to a force chain, and therefore, no force chain can branch or merge because that would require at least three force chain segments on a single droplet. However, we do know that the network of large forces does indeed branch and merge and therefore we also define another type of force segment, the branching/merging force segments which are those force segments that are one of the two largest forces on one of the droplets joined by the force segment, but not one of the two largest forces on the other droplet. The essential idea of

these definitions are that the force segments belonging to a force chain are “locally” the largest forces being transmitted through a sequence of droplets, and that at certain points along the chain there are secondary large forces that branch off and can merge two chains together.

To see how our new definitions compare to the previous definition we show in Fig. 6.11(c) the force chain segments as the solid lines and the branching/merging force segments as the dashed lines. Comparing the force structure Fig. 6.11(b) to Fig. 6.11(c) we see that our definition is consistent with the old definition, where now the force chain structure has been isolated into individual chains (the solid lines in Fig. 6.11(c)). Figure 6.12 show force chains using our definition for a larger region in the sample. The image shows force chains that are fairly linear and heterogenous in length with some force chains spanning more than 10 droplets while others only span 1 or 2 droplets.

In this section we consider various statistical measurements on the randomness of the force chain network, and then we apply the Brujić-Zhou model [158, 159, 272, 276] to compare to our data. The branching/merging force segments will not be considered. When analyzing data in this section we consider all droplets and contacts between $40 \leq y/2r_o \leq 80$ unless otherwise specified, and over this range ϕ increases from ~ 0.93 to 0.96. We found that many of the statistical measures we discuss do not depend on ϕ at larger area fractions. Such a large window size is necessary to provide the best statistics.

Due to the protocol for how the system was initialized we may expect there to be anisotropies in the force chain network. We measured the distribution in the orientation of force segments and found there to be a slight bias for force chain segments to be orientated in the direction of the incline. This is not too surprising giving the protocol for initializing the packing was to allow the droplets to flow up the chamber until they settled into mechanical equilibrium. It’s been shown that force chains tend to align in the flowing direction [23, 155, 280]. Also, since there is a small buoyant force in the y -direction, this will result in slightly larger vertical forces.

Given that force chains form linear like structures and that there is a slight anisotropy for the force chains to align along the incline we may expect there to be correlations in the orientation of neighboring force chain segments. To quantify such correlations we define

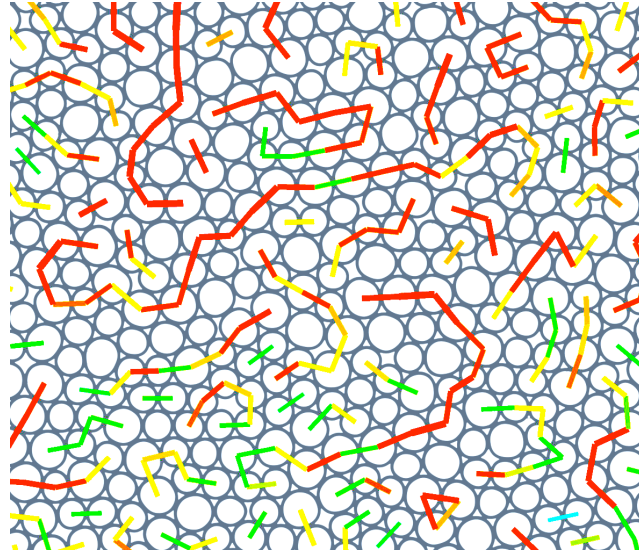


Figure 6.12: This image shows only the forces belonging to a force chain within a region of the $\sigma = 1.25$ sample. The thick red lines indicate large forces and the thinner green lines indicate forces closer to the mean. See the scale bar in Fig. 6.11. On average, the forces are larger further up the image because the sample is inclined, and this can be observed in the image by the increasing redness of the force segments.

two relative angles θ_1 and θ_2 between joining force segments, where the definition of θ_1 and θ_2 are shown in the inset of Fig. 6.13. Using this definition, if there is a correlation in the relative orientations that tend to make the chains linear, then θ_1 and θ_2 would be positively correlated. We compute the correlation C of θ_1 and θ_2 at various distances up the incline and the data are shown in Fig. 6.13. Surprisingly, for all the data C is very small or zero, indicating that there is no correlation between the orientation of neighboring force segments.

To further explore the tendency for force chains to be linear without exhibiting any correlation between the orientation of neighboring force chain segments, we consider the distribution of θ , where θ_1 and θ_2 are treated as a single variable θ . In Fig. 6.14 we plot the distribution in θ for all three packings. The distribution shows that most force chain segments form at an angle $|\theta| < 60^\circ$, indicating that two force segments tend to form a linear chain because it's more probable. The analysis of both the correlation in θ_1 and θ_2 and the distribution $P(\theta)$ leads to the conclusion that the orientation θ of any given force chain segment is independent of the orientation of a neighboring segment and that θ is

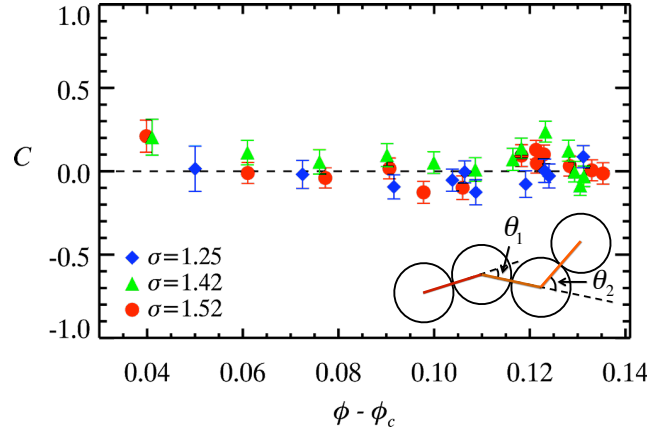


Figure 6.13: Plot of the correlation between θ_1 and θ_2 for the three different binary packings. Inset: Definitions of the relative orientations θ_1 and θ_2 between joining force segment. In the image both θ_1 and θ_2 are positive. θ_1 is defined to be positive if the extended dashed line is a counter clockwise rotation relative to the center force segment, and θ_2 is positive if the third force segment is a counter clockwise rotation relative to center force segment. If there is a correlation between θ_1 and θ_2 that tends to make force chains linear, then the correlation between θ_1 and θ_2 is positive.

randomly chosen from a distribution that is biased towards forming linear chains.

To understand from physical origins why force chains are biased towards being linear we apply a model proposed by Brujić *et al.* [158, 276] and extended by Zhou *et al.* [159, 272] to our data. The Brujić-Zhou model is a method for generating ensembles of local particle configurations (a central particle and contacting first neighbors) and the forces acting on a central particle by its first neighbors. Each local configuration is generated by randomly placing z_i contacting neighbors such that any two neighboring particles do not overlap. Next, the contact forces between the central particle and $z_i - 2$ neighboring particles are chosen at random from a distribution $P(f)$, leaving two unknown contact forces. By invoking force balance, the two remaining contact forces are found algebraically. In the work of Zhou *et al.* they used $P(f) \sim f \exp(-(f/2\sigma)^2)$, where $f > 0$, since it closely matched the force distribution in experiments. Once a sufficient number of local configurations are generated the distribution of force chains orientations can be studied. The basic assumptions of this model is force balance, randomness in the magnitude of forces, and randomness in the orientation of forces. For our data the first assumption applies because the system is in mechanical equilibrium and in the previous paragraphs we have shown that the other two

assumptions reasonably apply.

One issue in using the Brujić-Zhou model to predict $P(\theta)$ is that the model only gives the forces between a central particle and first neighbors. In order to define a force chain segment we also need to know all the forces acting on each first neighbor as well. On the central particle there are only two forces that could potentially be a force chain segment; the two largest forces f_1 and f_2 between the central particle and the first neighbors and we label these first neighbors as j_1 and j_2 . To determine if both of these large force segments are force chain segments we add onto our local configuration the first neighbors around j_1 and j_2 . Fixing all the forces previously generated on the central particle we now randomly generate forces on j_1 and j_2 such that force balance is satisfied. With these new forces we determine if f_1 and f_2 are force chain segments, and if both are force chain segments we calculate the angles θ between these two segments. We repeat of the process of generating these local configurations and only keep those configurations that return a force chain segment for both j_1 and j_2 .

Clearly, the distribution for $P(\theta)$ returned by our modified Brujić-Zhou model depends on the choice of $P(f)$ and the protocol for generating local configurations. To make the inputs into the Brujić-Zhou model as consistent as possible with our experimental data we use the experimentally measured $P(f)$ (Fig. 6.10) and instead of randomly generating local configurations we randomly select local configurations from our experimental data. Applying our modified Brujić-Zhou and using our data as inputs, we obtain a distribution for each of our three packings, and the distributions are shown Fig. 6.14(b), (c), and (d) for the $\sigma = 1.25, 1.42,$ and 1.52 data respectively. In each figure, the experimentally measured $P(\theta)$ is shown as the black line and the $P(\theta)$ found from the model is shown as the red line. We see that quantitatively the model is in good agreement with the experiment, but there is some discrepancy in the magnitude of the peaks. The model is able to capture significant changes between the data. For instance, the peak around $\theta = 0$ is much different between Fig. 6.14(b) and Fig. 6.14(d), and the model is able to capture this difference.

The discrepancy between the model and data may be the result of slight correlations in the forces and orientations between neighboring droplets. While the correlations in Fig. 6.13 are nearly zero, there is still some correlation. Also, we did not consider all the

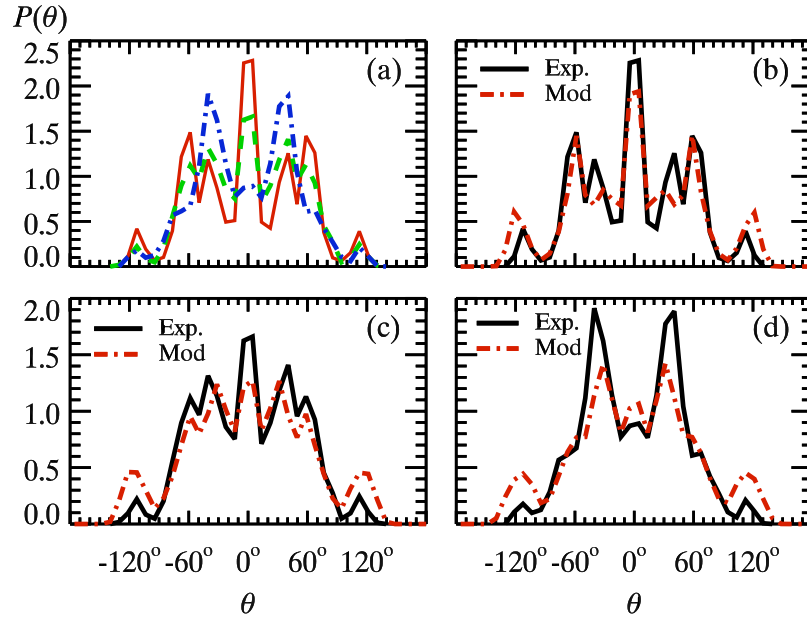


Figure 6.14: (a) Distribution of θ for each packing, where both θ_1 and θ_2 are treated as a single variable θ . The red solid line is the distribution for the $\sigma = 1.25$ packing, the green dashed line is the distribution for the $\sigma = 1.42$ packing, and the blue dashed-dot line is the distribution for the $\sigma = 1.52$ packing. (b) is a comparison between the distribution for $\sigma = 1.25$ and the Brujić-Zhou model. (c) is a comparison between the distribution for $\sigma = 1.42$ and the Brujić-Zhou model. (d) is a comparison between the distribution for $\sigma = 1.52$ and the Brujić-Zhou model.

second neighbors in our modified Brujić-Zhou model, we only considered a select few. Also to define a θ_1 and θ_2 we would need to consider out to the third nearest neighbors. It may be possible that structural constraints in the packing out to the second and third nearest neighbors constrain the allowable distributions in forces for which the force balance can be satisfied. However, adding these complexity into the model starts to make the model less computationally feasible and less appealing.

From the prior analysis it suggest that the force chain network can be thought of as a random network, and therefore, we may also expect the distribution of chain lengths to obey a random process. If there is a probability p for a force chain segment to have a neighboring force chain segment, then the distribution of chain lengths should obey the scaling $P(n) = (1 - p)p^n$ for a random process, where n is the length of a force chain (or number of force segments that belongs to an isolated force chain). In Fig. 6.15 we plot the distribution of chain lengths for each packing. The data decay exponentially over 3 orders of

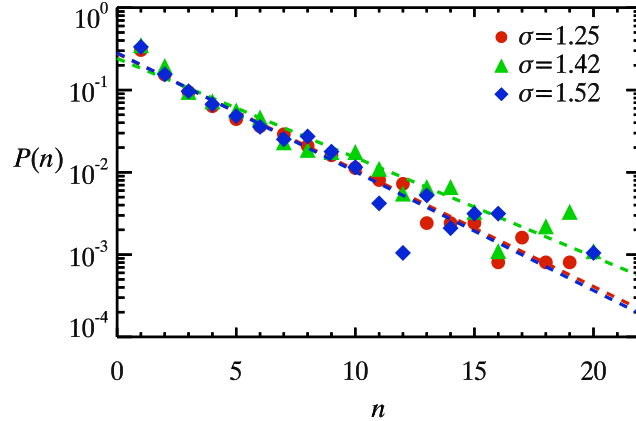


Figure 6.15: Distribution of the number of force segments making up distinct force chains. The data points are experimental observed values and the dashed lines are fits to the data of the form $P(n) = (1 - p)p^n$, where p is found to be 0.722, 0.758, and 0.717 for the $\sigma = 1.25$, 1.42, and 1.52 packings, respectively.

magnitude. To obtain the probability p for our packings, we fit the data to $P(n) = (1-p)p^n$, which is a one parameter fit, and find $p = 0.722$, 0.758, and 0.717 for the $\sigma = 1.25$, 1.42, and 1.52 packings, respectively. The fits are shown as the dashed lines and show good agreement with the data other than at $n = 1$. The discrepancy at $n = 1$ may suggest that this distribution is only valid when there is a least 2 force segments because for $n = 1$ the force chain has not spanned an entire droplet and the meaning of a force chain is nebulous.

To check how our $P(n)$ results compare to a simple model system, we simulated the isotropic compression of a binary mixture of 10,000 2D disks with size ratio 1.4 and a particle-particle force law $f_{ij} = F_o(\delta r_{ij}/d_{ij})$ (same as O'Hern's model [22] previously discussed). In the simulation, we start with a packing of disks below the jamming point and compress the container in small increments until the area fraction is 0.98. At each increment, we allow the disks to rearrange until they settle into mechanical equilibrium before compressing the container again. At various area fractions above the jamming point we apply our force chain analysis, and found the same distribution as in Fig. 6.15 with $p \sim 0.75$, regardless of ϕ . We also note that Peters *et al.*, using a much more sophisticated 11 step process for defining and breaking up force chains into countable lengths, also found an exponential distribution in chain lengths [281]. In their work, they simulated an intruder penetrating a sample of polydisperse 2D frictional disks and recorded the distribution in

force chain lengths during the intruding process. From their reported data on $P(n)$, we estimate a value of $p = 0.65$ regardless of how far the intruder had penetrated the sample. For our compression experiments and the penetration experiment of Peters *et al.*, we expect to find different force networks due to grain rearrangements upon further compression or penetration, and therefore, we may expect to find different $P(n)$. However this is not the case, and it appears that statistically the “formation” of a force chain can be thought of as a random process with probability p for the force chain to propagate.

6.8 Conclusions

In this work, we have introduced a new model system composed of quasi-2D emulsions droplets to experimentally probe the jamming transition. We have introduced a method for determining an empirical force law that is not limited to our setup, and could be used to determine forces in 2D foams, 3D emulsions, and 3D foams. For our system, we have found a universal force law that works for any droplet size and gap thickness. Our model system is an additional tool for studying internal forces in jammed systems with its own unique advantages. Compared to photoelastic disks our droplets can be compressed to a larger area fraction to probe properties farther from the jamming point, our droplets are significantly cheaper and easier to make (thousands of any size can be made in minutes), our droplets are highly monodisperse, and there is no static friction between droplets. Compared to 2D foam experiments, foam droplets coarsen quickly while our emulsions are stable over several days, and we can easily make controlled sizes down to very small droplets which is difficult for foams because coarsening is even more troublesome. Also with our calibration technique we are able to obtain internal forces to an accuracy of 5-10 times better than reported for the 2D foam setup [153]. An advantage of our 2D setup over 3D setups is for the case of flowing droplets. We can image our system quickly, limited only by the camera’s frame rate while 3D imaging is limited by the technique to roughly 1 image per second [84, 282]. Also 3D image analysis to determine droplet locations and forces is very computationally expensive, while 2D image analysis is much less expensive allowing for analysis of very long movies.

In our first work with this new model system, we have probed the jamming transition and found that various critical scaling relationships agree well with other numerical and experimental model systems. This demonstrates that 2D deformable droplets serve as a good ideal model system to study the jamming transition. In this work, we have also characterized the force chain network by applying various statistical measures. We found that the relative orientation in force chain segments are random, but the distribution in orientations is biased toward force chains being linear. Other statistical measures on chain lengths and correlations between the orientation of neighboring force chain segments also demonstrated that the network is random. To explain the bias in the relative orientations using a physical description, we applied the Brujić-Zhou model with a few modifications to include second neighbors, and found that the model predicts the distribution fairly well.

CHAPTER 7

Spatial Cooperativity of Stress Relaxation Around Plastic Events in Quasi-Static 2D Flow

Soft materials like colloids, foams, and emulsions are a collection of discrete particles, and when the particle concentration is above a critical point, these materials can behave like solids in some cases, but can easily flow in other cases. For instance, shaving cream (a foam) will rest in your hand like a solid, but will flow like a liquid when squeezed. There are many applications of health care products, pastes, coatings, and foods where understanding and optimizing the flow properties are important. When soft materials are flowing, many microscopic plastic changes take place, involving groups of particles rearranging with one another. While steady state flow of a soft material may have well defined time averages in strain rate and stress, on shorter time scales the flow is intermediate between a solid and a liquid with large fluctuations in local strain rate and stress.

At shorter time and length scales the discrete nature of soft materials is important since individual plastic events are the only characteristic feature of the flow. The flow is punctuated by local groups of particles temporally jamming into disordered configurations [168, 171, 172, 256, 283] and unjamming by plastically rearranging with one another [172]. The observed average velocity and stress profiles are the cumulative effect of these local jamming and unjamming processes. Intermittent flow at the particle scale

has been observed in many experimental and computational studies with local rearrangements typically involving on the order of 10 particles [34, 167–169, 176–178]. In addition to local rearrangements, intermittent macroscopic stress fluctuations have also been observed [154, 179–182]. However, there are no experiments that quantify the spatial and temporal stress build up and relaxation in the vicinity of individual particle rearrangements.

The flow of soft materials is typically modeled using elastoplastic theories [188]. Our current understanding within the elastoplastic framework is that plastic events occur when the local stress on a group of particles is too large for the particles to support and some of the stress on the particles is dissipated or redistributed through a plastic event [40, 284]. Bocquet *et al.* recently proposed an elastoplastic model that can accurately predict the spatial stress and velocity profiles observed in 3D microchannel flow [37, 40]. Essential to their model is that during a plastic event the stress on the rearranging particles completely relaxes to zero and that the relaxation process is spread over neighboring particles with a cooperative length scale ξ .

In this Chapter, we apply our 2D experimental model system developed in Chapters 4, 5, and 6 to study the evolution and relaxation of stress near a plastic event, and to confirm if there exist a cooperative length scale. We show for our system that the only dominant term to the stress is the repulsive force between droplets (viscous forces are negligible), and that our results represent the most idealized example of flow, the flow of 2D frictionless droplets where the only contributor to the rheology is the crowding or jamming of the droplets. We measure a spatial length scale $\xi \sim 3 - 4$ particle diameters which is roughly that found by Goyon *et al.* [37], however, we do not observe the area fraction dependence they had measured. The work presented in this chapter is ongoing and the results are preliminary.

7.1 Flow Geometry

Our sample chamber for this study is nearly the same as the one described in Chapter 6, where droplets are squeezed between two glass microscope slides. The droplets are a binary mixture of mineral oil in water stabilized using Fairy soap. The droplets are produced using

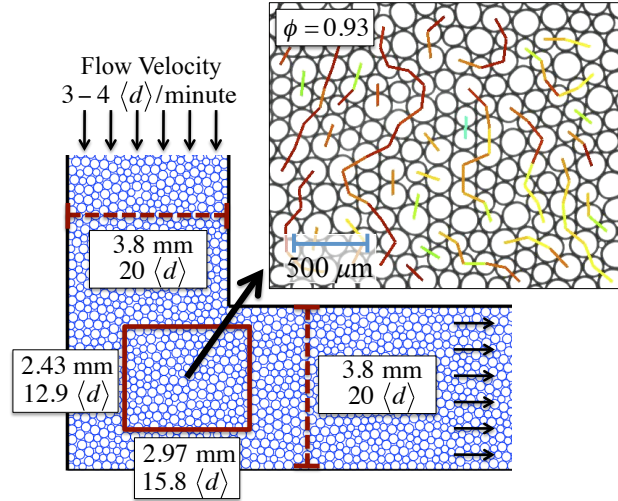


Figure 7.1: Schematic of our 2D flow geometry. The sample chamber consists of droplets squeezed between two glass slides. The sample chamber rests on top of a microscope with gravity pointing into the page. To offset some of the friction between the glass slides and the droplets, the microscope is inclined by 4.5° such that a component of gravity points in the flowing direction of the vertical chamber. Using a syringe pump droplets are pushed down the channel. The red box overlaid on the schematic indicates the region where the droplets are imaged. The viewing region is offset from the corner by 0.63 mm to the right and 0.48 mm down. The image in the upper right is an image of the sample taken with a microscope. On the image the largest contact forces have been drawn as lines. The more red and thicker the line, the larger the force.

the same co-flow setup discussed in Chapter 6. For this study, the sample chamber consists of two channels that meet at a right angle. In Fig. 7.1, we present a schematic of the setup. Droplets are driven through the channel using a syringe pump, and at the bend droplets will rearrange due to the change in direction. There are eight data sets ranging in area fraction $\phi = 0.881 - 0.956$, where the jamming point is $\phi_c \sim 0.86$ (see Chapter 6.3). The size ratio of big droplets to small droplets is 1.28 ± 0.01 and the number ratio of big droplets to small droplets is 0.65 ± 0.05 . The diameters of the small droplets are $171 \mu\text{m}$ with polydispersity 4.4% and the diameters of the big droplets are $218 \mu\text{m}$ with 5.2% polydispersity, where the polydispersity is defined as the ratio of the standard deviation in droplet diameters to the mean droplet diameter. The average particle diameter is $\langle d \rangle = 188 \mu\text{m}$. Droplets are driven through the channel at an average speed of ~ 3.5 particle diameters per minute, and for each data set and between the data sets the average velocity fluctuates by ~ 0.5 particle diameters per minute. Each sample is imaged at a frame rate of 2 frames/second over a

duration of ~ 20 minutes.

7.2 Droplet-Droplet Forces and Viscous Forces

There are three possible forces acting on each droplet as shown in Fig. 7.2. There is a repulsive force f_{ij}^c between the two particles i and j in contact, a viscous drag force f_{dw} on droplets from the two glass microscope slides, and a viscous drag f_{dd} as one droplet slides past another droplet. To properly characterize the stress around rearranging droplets we must quantify each of these forces. The analysis in this section will be on each of these forces for a single data set at $\phi = 0.93$. The analysis still needs to be repeated for the other data sets to check for consistency in the results. Although a priori, we may expect f_{dw} to be independent of ϕ , since the contacting interface between the droplets and the glass slides should not change much with ϕ . However, f_{dd} may depend on ϕ , since the interfacial area between droplets in contact will change with ϕ .

The repulsive force f_{ij}^c is found for each pair of droplets i and j in contact using the methods discussed in Chapters 4, 5, and 6. These forces can be computed using the curvatures and the contact length of droplets in contact. In pure shear experiments on granular materials using photoelastic disks, it was shown that large forces tend to be linear forming chain like structures [155]. Pure shear is a process where a sample is slowly compressed in one direction, while simultaneously expanded in the orthogonal direction such that the area of the sample remains fixed. In the granular pure shear experiments, it was also found that the force chains align along the compression direction. The flow geometry used in this study was chosen since it is analogous to pure shear and will result in force chains aligning with the vertical direction. Force chains are known to provide a sample with mechanical rigidity by resisting flow and are thought to be related to many other bulk material properties [23, 260, 261, 264]. By establishing a preferred direction for the force chains in our samples it will make it easier to spot any trends in droplet motion relative to the force chain direction. Using our algorithm to compute contact forces and using our definition of a force chain presented in Chapter 6.7, we show in Fig. 7.1 the force chain structure for a snapshot in time of our $\phi = 0.93$ data set. We see that the forces chains tend to align with

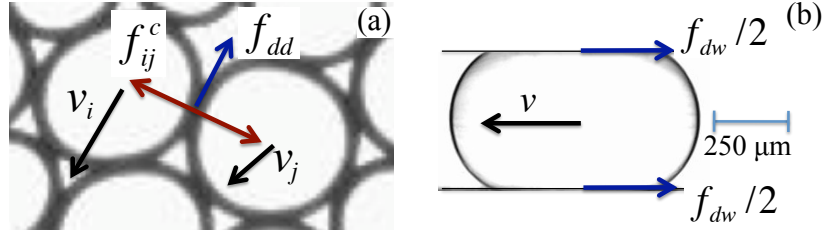


Figure 7.2: (a) The image shows two droplets sliding past each other. One droplet is moving with velocity v_i and the other with velocity v_j . There is a repulsive contact force f_{ij}^c between the droplets and a viscosity force f_{dd} that depends on the velocity difference of the two droplets. (b) The image shows a droplet moving with velocity v between two glass slides. As the droplet slides past the glass, there is a velocity dependent viscous friction force $f_{dw}/2$ on each wall. This gives a total friction force of f_{dw} on the droplet.

the vertical direction. Other images were also inspected to ensure that the forces chains are on average aligned along the vertical direction, but a more quantitative analysis is needed.

The second force we quantify is the viscous force f_{dw} which is exerted on a droplet as it slides past the two glass microscope slides. This force will depend on the velocity v_i of the droplet, and can be deduced using Newton's 2nd Law. Since our system is in steady state, the long time average of the sum of the forces on each droplet must be zero. In this analysis, we will ignore the other viscous force f_{dd} , and we will determine f_{dw} by considering the net force on each droplet along the direction of motion \hat{v}_i of the droplet. We will assume that the viscous drag force f_{dd} is randomly distributed about \hat{v}_i , and therefore, the contribution of f_{dd} from all contacts to the net force along \hat{v}_i is zero. More analysis is needed to verify this assumption, but we can still learn to first order the magnitude of the drag forces. As we will show, these drag forces are small enough to ignore, and currently more sophisticated analysis is not needed. We start our analysis by considering the net force on each droplet which can be written as $\sum_j \vec{f}_{ij}^c - f_{dw}(v_i)\hat{v}_i = 0$, where the left term is the sum of the repulsive forces f_{ij}^c on each droplet and the right term is the viscous force on droplet i with magnitude $f_{dw}(v_i)$ pointing in the opposite direction of \hat{v}_i . Here \hat{v}_i is a unit vector pointing in the direction of motion of droplet i . In the net force equation, $f_{dw}(v_i)$ is collinear to the motion of the droplet and only contributes to the net force along the direction v_i . Therefore, to deduce $f_{dw}(v_i)$ we only need to consider the net force along the direction \hat{v}_i . To consider the net force along this direction, we take the dot product of the net force equation with \hat{v}_i ,

and then rearrange the terms to have a new equation $(\sum_j \vec{f}_{ij}^c) \cdot \hat{v}_i = f_{dw}(v_i)$. To determine $f_{dw}(v_i)$, we plot in Fig. 7.3(a) the average of $(\sum_j \vec{f}_{ij}^c) \cdot \hat{v}_i$ for all droplets at all times with roughly the same velocities. We have rescaled the y -axis by the average repulsive force to illustrate how the magnitude of $f_{dw}(v_i)$ compares to the average repulsive force. The figure shows that $(\sum_j \vec{f}_{ij}^c) \cdot \hat{v}_i$ increases linearly with velocity, where velocity is measured in units of particle diameters per minute. At most we find that the friction from the glass plate is 0.4% of the repulsive force and is on average 2% of the repulsive force. We fit the data to a line to obtain the expression

$$f_{dw}(v_i) = (6.72 \times 10^{-4} \mu\text{N}/(\langle d \rangle/\text{min}))v_i + 1.13 \times 10^{-5} \mu\text{N}. \quad (7.1)$$

In the figure, the fit is shown as the red dashed line, and we see that the data agrees well with the fit. The fit has a slight y -intercept, but this y -intercept is small and only $0.0001 \langle f_{ij}^c \rangle$, where $\langle f_{ij}^c \rangle$ is mean repulsive force acting on all the droplets. Recall, that these droplets have a yield force to flow (see Chapter 5.3), and that the microscope has been inclined to an angle of 4.5° to offset this yield force. The small y -intercept in the above equation indicates that the sample was inclined to the appropriate angle.

The third force we compute is the viscous force f_{dd} which arises when one droplet slides past another droplet. This force will depend on the velocity difference $\Delta v_{ij,\hat{a}}$ (see Fig. 7.3(d) for a definition of $\Delta v_{ij,\hat{a}}$). Similar to the above analysis, $f_{dd}(\Delta v_{ij,\hat{a}})$ can be determined using Newton's 2nd Law, where the sum of the forces on droplet i is $f_{bw}(v_i)\hat{v}_i + \sum_j \vec{f}_{ij}^c - \sum_j f_{dd}(\Delta v_{ij,\hat{a}})\hat{a}_{ij} = 0$. In the equation, the first term is the viscous force from the glass plate on droplet i which we know from Eqn. 7.1, the second term is the net repulsive force exerted on droplet i by its neighbors, and the last term is the net viscous drag forces exerted on droplet i by its neighbors. To simplify the net force equation, we define two new variables $\vec{F}_{net}^{(glass,rep)} = f_{bw}(v_i)\hat{v}_i + \sum_j \vec{f}_{ij}^c$ and $\vec{F}_{net}^{dd} = \sum_j f_{dd}(\Delta v_{ij,\hat{a}})\hat{a}_{ij}$. Using these new variables we can rewrite Newton's 2nd Law for each droplet as $\vec{F}_{net}^{(glass,rep)} = \vec{F}_{net}^{dd}$. Similar to before, we can make the net force vector equation into a scalar equation by taking a dot product of both sides with \hat{F}_{net}^{dd} giving $\vec{F}_{net}^{(glass,rep)} \cdot \hat{F}_{net}^{dd} = \vec{F}_{net}^{dd} \cdot \hat{F}_{net}^{dd}$, where \hat{F}_{net}^{dd} is a unit vector in the direction of \vec{F}_{net}^{dd} . However, unlike before, the direction of \hat{F}_{net}^{dd} is unknown

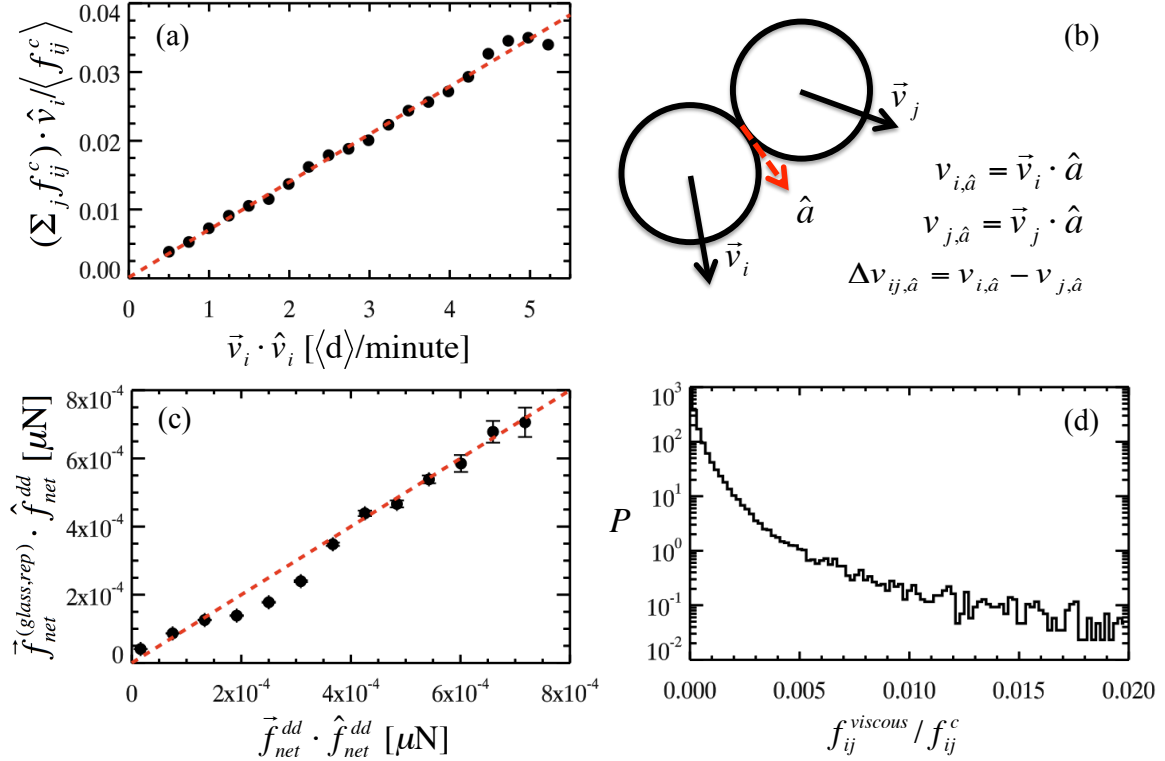


Figure 7.3: (a) Plot of the average net repulsive force on a droplet traveling with velocity v_i , where the data has been normalized by the mean repulsive $\langle f_{ij}^c \rangle$. The red dashed line is a linear fit to the data, and the error bars in the data are significantly smaller than the diameter of the data points. (b) Two droplets are shown moving with velocity \vec{v}_i and \vec{v}_j . The vector \hat{a} is defined to be parallel to the contact such that $\vec{v}_i \cdot \hat{a} > 0$. (c) Plot demonstrating how well force balance on a droplet is satisfied when assuming a viscous force law between droplets of $f_{dd} = b\Delta v_{ij}^{1.5}$. If the assumed force law is correct, then the data will fall along a line of slope 1. The red dashed line has a slope of 1. (d) Probability distribution to find a contact with a ratio of viscous force $f_{ij}^{viscous}$ to repulsive force f_{ij}^c .

and will depend on the magnitude of $f_{dd}(\Delta v_{ij,\hat{a}})$ at each contact. Therefore, to determine $f_{dd}(\Delta v_{ij,\hat{a}})$ we guess different functional forms until we find one that reasonably satisfies the previous scalar equation. We find

$$f_{dd}(\Delta v_{ij,\hat{a}}) = b\Delta v_{ij,\hat{a}}^{1.5} \quad (7.2)$$

can adequately satisfy the scalar force balance equation, where $b = 5.97 \times 10^{-5} \mu\text{N}/(\langle d \rangle/\text{min})^{1.5}$.

In Fig. 7.3(b) we plot the data on the average value of $\vec{F}_{net}^{(glass,rep)} \cdot \hat{F}_{net}^{dd}$ for droplets with different values of $\vec{F}_{net}^{dd} \cdot \hat{F}_{net}^{dd}$. If the correct function for $f_{dd}(\Delta v_{ij,\hat{a}})$ was chosen, then the

data in this figure would fall along a straight line with slope 1. The data falls along this line, but there is some variations in the data. A better function could be chosen for $f_{dd}(\Delta v_{ij,\hat{a}})$ to get the data in Fig. 7.3(b) to be more linear, but as we will show, the magnitude of the viscous force is so small that it can be neglected. Therefore, the effort to determine the exact form is not necessary.

Using Eqn. 7.2, we can compute the magnitude of the viscous force $f_{ij}^{(viscous)}$ for each pair of droplets in contact and compare it to the repulsive forces f_{ij}^c . In Fig. 7.3(c), we plot the probability distribution to find the ratio of the viscous force to the repulsive force at each contact. First we note that 96% of the contacts have a viscous force less than 0.1% of the repulsive force, and second, the mean of $f_{ij}^{(viscous)}/f_{ij}^c$ is 0.0002. Therefore, in comparison to the repulsive forces, the viscous force can be considered small enough to be neglected. Even though we did not have the best possible function describing $f_{dd}(\Delta v_{ij,\hat{a}})$, improving on the exact functional form would not have much effect of the distribution seen in Fig. 7.3(c).

7.3 Determining When Plastic Events Occur

In prior studies, plastic events have traditionally been defined as a loss of contact between neighboring droplets. Two examples are shown in Fig. 7.4(b) and (c), where a contact breaks. However, there are two other types of structural changes that can take place which we show in Fig. 7.4(d) and (e). In the first example, no contact is broken or formed, but two droplets move closer together while the other two move apart. In the second example, no contact is broken, but two droplets move apart, while the other two form a contact. Clearly, the size of the structural changes in the four examples in Fig. 7.4(b)-(e) are different, but topologically these four examples involve a structural change. In this section, we present a looser definition for a plastic event based on topology that captures the four examples in Fig. 7.4(b)-(e) and a deformation parameter to characterize the size of the structural change associated with a plastic event. An advantage of this deformation parameter is that it can be used to define the size and duration of a plastic event. We also note, that in this section we only discuss the position and rearrangement of droplets, and not the forces acting on

the droplets.

We define a plastic event to be any structural change that leads to an altering in the Delaunay triangulation. The Delaunay triangulation is a tessellation of the entire space into triangles, where the triangulation provides a precise definition for which droplets are neighbors based on the topology or position and diameters of the droplets. In Fig. 7.4(a), we show the Delaunay triangulation as the green lines at different times for our $\phi = 0.93$ sample. The red lines in the figure indicate the pair of droplets where the Delaunay network will change. At $t = 0$ one of the red bonds is broken and a new red bond is formed as two droplets move towards each other and become neighbors. We see in the figure that when a bond is broken there are two triangles in the Delaunay network that are destroyed. A constraint of the Delaunay network is that the space must be tiled with triangles, and therefore, the destruction of two triangles leads to two new triangles. A refined definition of a plastic event is any grouping of four droplets involved in the altering of the Delaunay network.

To characterize the size of the plastic event we adapt the deformation parameter introduced by Utter and Behringer to characterize shear transformation zones, where a larger deformation parameter indicates a larger structural change [185]. The deformation parameter of Utter and Behringer characterizes the change in shape of a grouping of particles. Here shape refers to the shape formed by the centers of the particles and not the shape of individual particles. In our case, a plastic event involves four droplets and the shape formed by these four droplets is a diamond. In Fig. 7.5, we show the variables defining the local deformation parameter. At some time $t - t_w/2$, the center of mass of the four droplets constituent a diamond shape illustrated as the green lines. A little time t_w later, the center of mass of the droplets have moved and potentially the shape of the diamond has changed as well. At each time a bond length l_{AB} , l'_{AB} , l_{CD} , and l'_{CD} can be defined. The strain in each bond length over the time period t_w is $\epsilon_{AB} = (l_{AB} - l'_{AB})/l_{AB}$ and $\epsilon_{CD} = (l_{CD} - l'_{CD})/l_{CD}$. Using Utter and Behringer's definition, the deformation parameter is defined as $D = |\epsilon_{AB} - \epsilon_{CD}| = |l_{AB}/l'_{AB} - l_{CD}/l'_{CD}|$. One issue with this parameter is that it is not time symmetric. To make our expression for the deformation parameter time

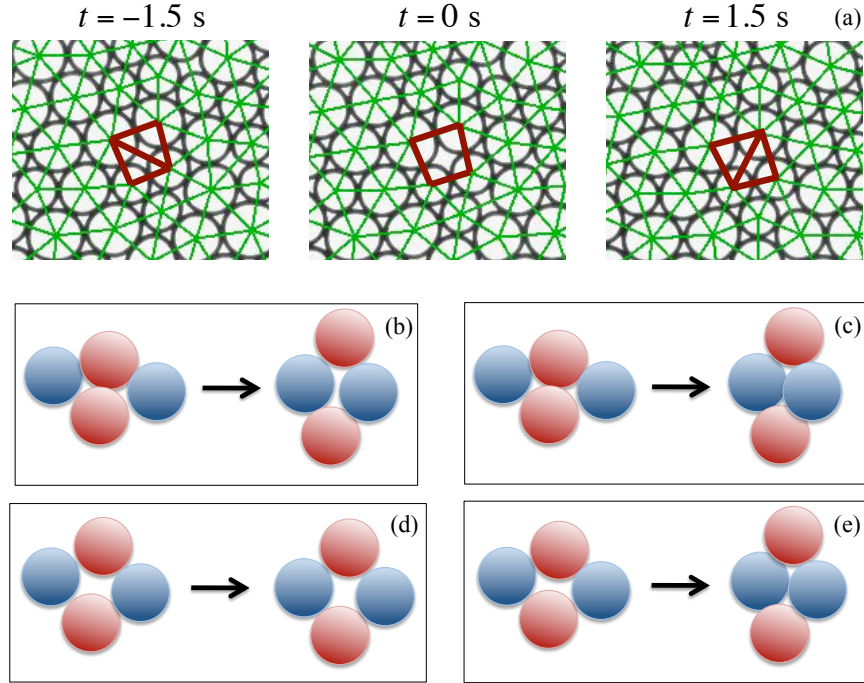


Figure 7.4: (a) Delaunay network at different times, where the green lines indicate neighbors defined by the Delaunay triangulation. The red lines show four droplets involved in a change of neighbors. (b), (c), (d), and (e) are various examples of Delaunay neighbor changes with various amounts of structure change. (b) involves a neighbor change with a contact breaking and no new contact forming. (c) involves a neighbor change where a contact breaks and forms. (d) involves a neighbor change with no contacts breaking and forming. (e) involves a neighbor change with a contact not breaking and a new contact forming. The deformation parameter for the four examples are $D = 1.04$ for (b), $D = 1.15$ for (c), $D = 0.29$ for (d), and $D = 0.89$ for (e).

symmetric, we introduce logarithms in the following manner

$$D(t, t_w) = \left| \ln \left(\frac{l_{AB}}{l'_{AB}} \right) - \ln \left(\frac{l_{CD}}{l'_{CD}} \right) \right|. \quad (7.3)$$

With this definition, if the shape of the diamond does not change during a plastic event then $D = 0$, but if it does change $D > 0$. For instance, if the diamond shape undergoes a pure dilation or compression $D = 0$, since $l_{AB}/l'_{AB} = l_{CD}/l'_{CD}$. However, if droplets A and B move apart and C and D move together, then $D > 0$, since $l_{AB}/l'_{AB} > l_{CD}/l'_{CD}$. The more A and B move apart and the more C and D move together the larger D .

By investigating the deformation parameter with time for a plastic event, the duration

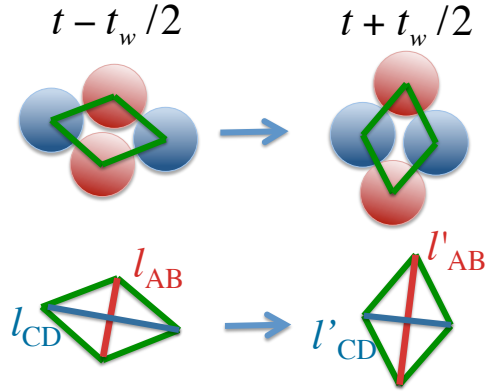


Figure 7.5: A structural change is defined by the relative motion of four neighbors. The centers of these neighbors produce a diamond shape characterizing the structure of the neighbors. To quantify the change in structure of the diamond we use the bond lengths l_{AB} and l_{CD} at two points in time. The deformation parameter for this example is $D = 0.90$.

time of the event can easily be determined. In Fig. 7.6(a), we show D as a function of time for a plastic event in our $\phi = 0.93$ sample. To compute D we used a time window of $t_w = 0.5t_d$, where t_w is measured in the time t_d it takes for the rearranging droplets to move a droplet diameter. The data shows two humps in the figure, where there is a slight change in the structure at $t \sim -12$ seconds and a larger structural change around $t \sim 0$. The peak defines the origin of the plastic event and the width of the larger structural change defines the duration of the event. For this particular group of droplets, the duration of the plastic event is roughly 10 seconds, where this duration time measures the time over which the droplets are physically moving. In this work, we do not investigate smaller structural changes immediately next to large structural changes. We only consider the dynamics of the stress centered in time around the large hump. We also note that smaller secondary peaks before and after a plastic event are not consistently reproduced between events.

Using $D(t, t_w)$ for all plastic events, an average duration time τ_{pl} can be determined for each sample. τ_{pl} can also be viewed as an average structural relaxation time since it measures the average time it takes droplets to transition between two configurations. To determine τ_{pl} we start by normalizing each $D(t, t_w)$ by the maximum deformation $D(t = 0, t_w)$. Then we average all deformation curves $D(t, t_w)/D(t = 0, t_w)$ together. In Fig. 7.6(b), we plot the average $D(t, t_w)/D(t = 0, t_w)$ curve for all plastic events for our $\phi = 0.93$ sample. The

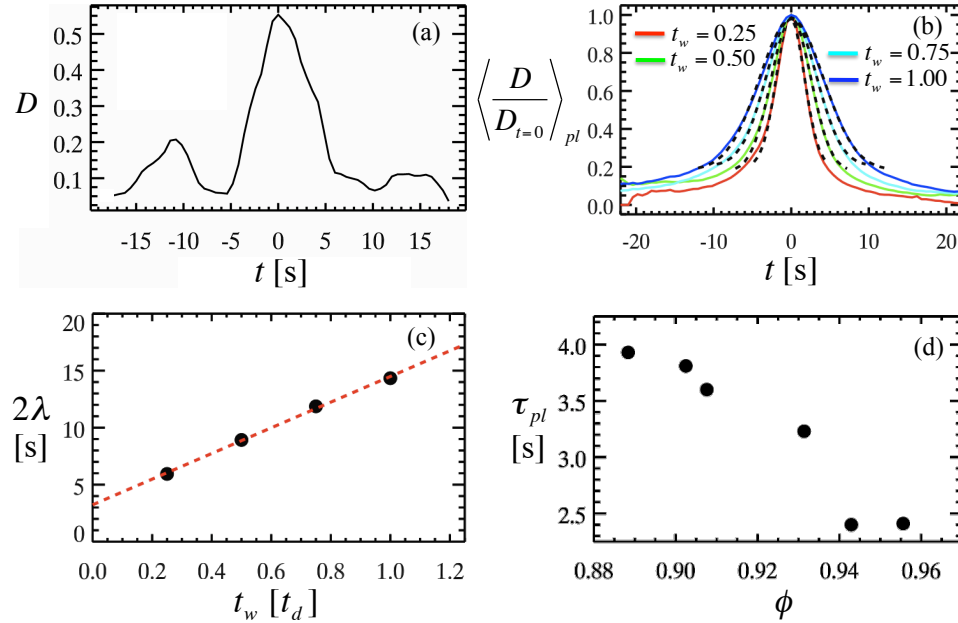


Figure 7.6: (a) D with time for a single plastic event, where the maximum in D defines $t = 0$. To compute $D(t)$ a time window of $t_w = 0.5t_d$ is used. (b) The average $\langle D/D_{t=0} \rangle_{pl}$ for all plastic events is plotted against time, where $D(t)$ for a single plastic event is normalized by the peak $D(t = 0)$ before taking an averaging over all plastic events. The data is shown for different t_w and the black dashed lines are gaussian fits to the data with standard deviation λ . t_w is in units of t_d . (c) The dependence of 2λ on t_w is shown as the black data points. The red dashed line is a linear fit with y -intercept of $\tau_{pl} = 3.23$ seconds. (d) Dependence of the duration time τ_{pl} with area fraction.

data show a center peak around $t = 0$ and the width of the central peak increases with t_w . The peak is wider with larger t_w because using a larger time window coarse grains the data causing it to be smoothed out. Ideally, the best measure of the deformation parameter is in the limit t_w tends to zero, since this would give an instantaneous measure of $D(t)$. To determine the average duration time in the limit t_w tends to zero, we start by fitting the central peak in each $D(t, t_w)/D(t = 0, t_w)$ curve to a Gaussian with standard deviation λ . For each $D(t, t_w)/D(t = 0, t_w)$ we define the average duration time as 2λ . In Fig. 7.6(c), we plot the average duration time 2λ as a function of t_w . 2λ has a linear dependence on t_w , and to extrapolate to the $t_w \rightarrow 0$ limit we fit the data to a line. The fit gives an x -intercept of $\tau_{pl} = 3.23$ seconds.

We repeat the analysis to determine τ_{pl} for all our other data sets and the results are shown in Fig. 7.6(d). We see τ_{pl} decreases by about a factor of 2 with increasing area

fraction. This indicates that the average time it takes for droplets to transition between configurations decreases with area fraction. Since packings at higher area fractions are under more stress and have little space for voids during rearrangements, it seems reasonable that droplets will transition between configurations quicker.

For our samples, the channel width is ~ 20 particle diameters and the average flow rate is ~ 3.5 particle diameters per minute giving a strain rate $\dot{\gamma} \sim 0.2$ 1/min. From the strain rate we can define a time scale $t_\gamma = 1/\dot{\gamma} \sim 300$ seconds as the time it takes for the sample to strain by 1. Microscopically, this time scale quantifies the time it takes for one droplet to slide past a neighboring droplet if the motion of the droplets followed the superimposed strain. The ratio of the two time scales gives $t_{pl}/t_\gamma \sim 0.01$, indicating that droplets rearrange much faster than the superimposed strain. Since droplets rearrange much faster than required by the flow rate, this implies that the system may be quasi-static and that the external flow is not superimposing secondary effects on the behavior of individual rearrangements. To confirm that the system is quasi-static, we will need to perform experiments to test if the results are the same at different flow rates .

7.4 Stress Tensor

The stress acting on a 2D body can be written as a 2×2 tensor σ . The diagonal terms σ_{xx} and σ_{yy} are the pressure on the body in the x and y -directions respectively. The off diagonal terms σ_{xy} and σ_{yx} are the shear stress in the x and y -directions respectively. Note that in 2D the stress is force per unit length and not force per unit area. The stress tensor for a 2D body can be computed directly by knowing the forces acting on the boundary. However, the stress tensor can also be computed using the internal forces, as is the case with our data where the individual contact forces are known. For a sample of size A_{system} the stress can be computed from the internal forces using the expression

$$\sigma = \sum_i \hat{\sigma}_i / A_{system} \quad (7.4)$$

$$\hat{\sigma}_i = \sum_j \vec{r}_{ij}^c \otimes \vec{f}_{ij}^c, \quad (7.5)$$

where $\hat{\sigma}_i$ is defined as the force moment tensor of a droplet, \vec{r}_{ij}^c is a vector from the center of droplet i to contact ij , \vec{f}_{ij}^c is the repulsive force at the contact, and \otimes is an outer product [22, 279, 285]. A_{system} is the area occupied by the i droplets the sum is performed over in the top expression. In the bottom expression, the force moment tensor quantifies the contribution of the forces acting on a droplet to the stress tensor. By observing changes in the force moment tensor for droplets undergoing rearrangements, we can understand how the macroscopic stress is influenced by rearranging droplets.

In pure shear, which our system is analogous to, the sample is compressed in one direction and expanded in the other direction such that the area of the sample remains fixed. In such an experiment, there are only two body forces. One body force is along the compression direction, and this force is responsible for compressing the sample. The second body force is along the expansion direction, and this force is responsible for maintaining constant area. When computing the stress tensor using a coordinate system aligned with the compression and expansion directions, these two body forces only contribute to the pressure term, and therefore, the shear stress or off diagonal components of σ are zero. By rotating the coordinate system by 45° the shear stress or off diagonal components of σ are maximal. This rotated coordinate system defines the shear direction for a pure shear experiment. In our flow geometry (see Fig. 7.1), the compression direction is the y -axis and the expansion direction is the x -axis. Since our setup is not identical to pure shear, we may expect the shear direction to be slightly different than 45° to the vertical direction (compression direction). To determine the shear direction in our setup, we first compute the stress tensor in an arbitrary coordinate system. Then we diagonalize σ to find the principle coordinate directions associated with pure shear. We find that this direction is roughly $1.5^\circ \pm 1^\circ$ relative to the lab frame for all samples. By rotating the principle coordinate system by 45° this establishes the shear direction. We define the off diagonal term of $\hat{\sigma}_i$ in the shear direction as Γ_i . In this work, we are interested in understanding how the contribution of individual particles to the shear stress of the system evolves with time. This only requires studying the evolution of Γ_i . Note that Γ_i/A_i is the actual stress on droplet i , where A_i is the Voronoi area around a droplet [148]. Therefore, we can treat Γ_i as analogous to the stress on droplet i , however, we do not use Γ_i/A_i since $\sum_i \Gamma_i/A_i \neq \sum_i \hat{\sigma}_i/A_{system}$.

7.5 Evolution of Stress Around Plastic Event

In this section, we discuss the average stress build up and relaxation in the vicinity of a plastic event. We start by apply our definition in Sec. 7.3 to identify all plastic events in each sample, and we find roughly 500 plastic events for each sample. To determine the size of each plastic event we use $D(t = 0, t_w = 0.5t_d)$. In Fig. 7.7(a), we show the distribution in $D(t = 0, t_w = 0.5t_d)$ for our $\phi = 0.93$. $D(t = 0, t_w = 0.5t_d)$ is broadly distributed with a peak around 0.4. To restrict the analysis in this section to plastic events undergoing larger structural changes we only consider those events with $D(t = 0, t_w = 0.5t_d) > 0.4$ for all samples. This gives roughly 300 plastic events for each sample.

During a plastic event the stress on the rearranging droplets and their neighboring droplets are expected to change. To characterize this change, we investigate the average dependence of Γ with time t in the vicinity of the plastic event. As in Sec. 7.3, $t = 0$ defines the midpoint in time when the droplets are rearranging and t_{pl} defines the average duration time droplets take to rearrange. To understand the spatial spreading of $\Gamma(t)$ around a plastic event, we bin the space into rings of width $0.5\langle d \rangle$ at distances ΔR to the center of the plastic event. See Fig. 7.7(b) for a diagram defining each bin. At each time and each spatial bin, there are $n_{\Delta R, t}$ droplets, and the average force moment within one of these bins is $\bar{\Gamma}_{\Delta R, t} = (\sum_k \Gamma_k) / n_{\Delta R, t}$, where the average is over all droplets k within bin ΔR at time t . We also define the average force moment for all the droplets within t_d before and after a plastic event as $\bar{\Gamma}_{all}$.

In Fig. 7.7(c) and (d), we plot the average stress build up and relaxation for all plastic events for our $\phi = 0.93$ sample. Since there is a natural asymmetry in the plastic event with two of the droplets coming closer together and the other two droplets moving farther apart, the data is divided along two axes. We may expect the evolution of the stress near the expanding droplets to be different than near the compressing droplets. In each plot, the average behavior is computed by first determining the temporal and spatial dependence of $\bar{\Gamma}_{\Delta R, t} / \bar{\Gamma}_{all}$ for each plastic event, and then averaging $\bar{\Gamma}_{\Delta R, t} / \bar{\Gamma}_{all}$ over all plastic events. To compare the stress build up and relaxation to the motion of the droplets, time t has been normalized by τ_{pl} . Therefore, $t / \tau_{pl} = -0.5$ indicates when droplets start moving/rearranging

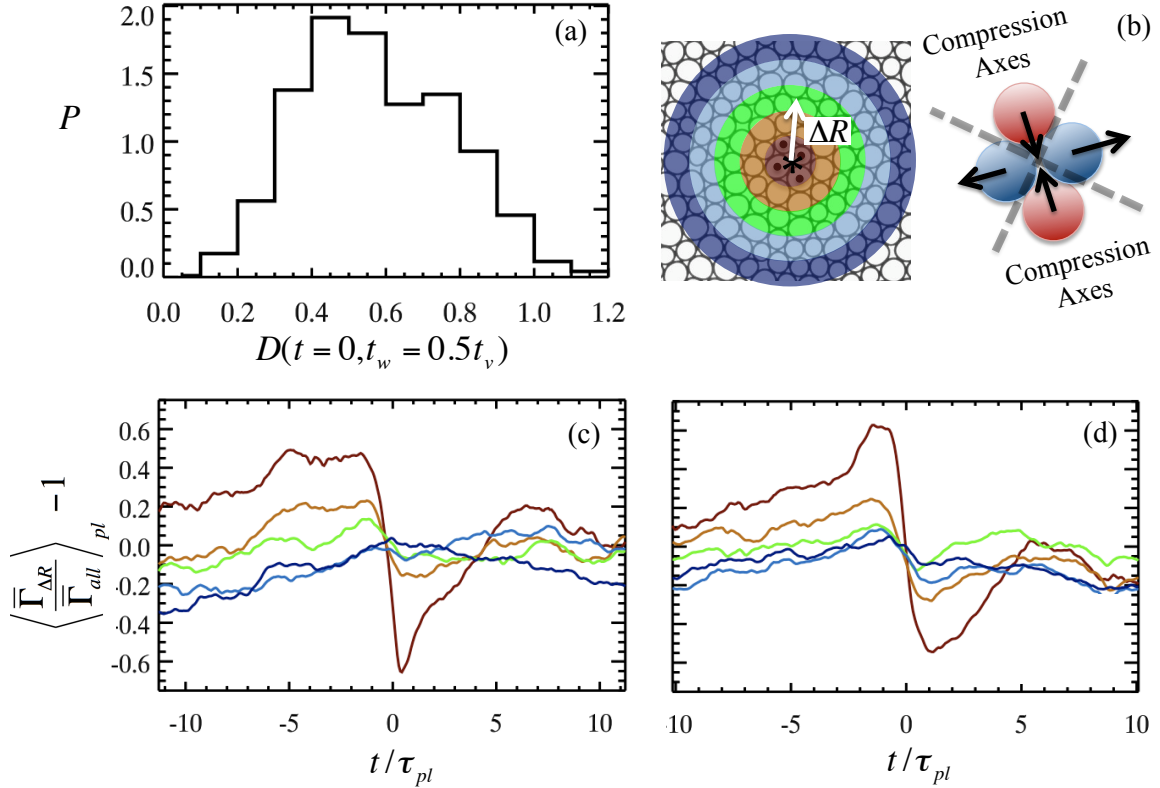


Figure 7.7: (a) Distribution in the size of plastic events for our $\phi = 0.93$ sample. (b) In the left image ΔR is defined as the distance from the plastic event, where the four rearranging droplets are marked with black dots. The center of mass of those four droplets is marked with an asterisks. Each ring around the center of the droplets indicates a bin where the average stress is computed, and the colors correspond to the curves shown in the other plots. The right illustrations demonstrates how the droplets move. Two droplets move towards each other and two move away from each other. Using these two directions of motion, the space is broken into 4 quadrants. (c) The average stress for all plastic events along the compression axes. (d) The average stress for all plastic events along the expansion axes.

on average and $t/\tau_{pl} = 0.5$ indicates when droplets stop moving/rearranging on average.

In Fig. 7.7(c), we show the average stress for all the plastic events as a function of time along the compression axes for different distances to the plastic event. The data show that before the droplets start to rearrange the stress builds for all ΔR , where the largest $\Delta R = 5\langle d \rangle$. Around $t/\tau_{pl} = -1$, the stress starts to relax, where the relaxation begins first for the droplets constituting the plastic event. At each subsequent distance, the stress begins relaxing at slightly different times, indicating a propagating stress relaxation. At larger distances, the stress slowly relaxes to the sample's mean stress. However, at $\Delta R = 1\langle d \rangle$, the stress relaxes far below the sample's mean stress and quickly recovers.

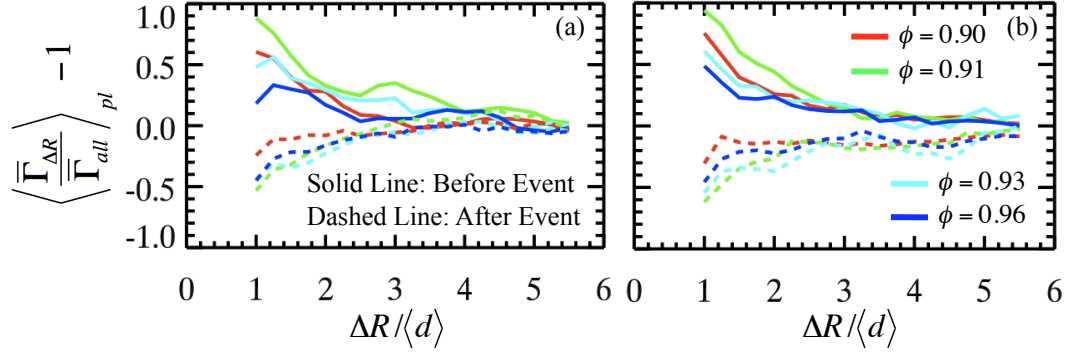


Figure 7.8: (a) is the compression direction and (b) is the expanding direction. The data in both plots show the stress in the vicinity of a plastic event immediately before a plastic event and immediately after a plastic event. The time immediately before a plastic event is defined as $t/\tau_{pl} = -1$ and the time immediately after a plastic event is defined as $t/\tau_{pl} = 1$. Both plots include data for samples at different ϕ . The legends in (a) and (b) apply to both plots.

In Fig. 7.7(d), we plot the average stress for all the plastic events as a function of time along the expanding axes for different distances to the plastic event. Similar to the compression direction, the data show a stress build up before the particles rearrange. Although, unlike the compression direction, the stress build up for smaller ΔR is much quicker and is slightly larger. Similar to the compression direction, the stress starts to relax around $t/\tau_{pl} = -1$ for all ΔR . The recovery of the stress at $\Delta R = 1\langle d \rangle$ is longer than the stress recovery in the compression direction. The data also show that before the plastic event there is more stress in the expanding direction.

To elucidate the spatial dependence of the stress build and relaxation, we show in Fig. 7.8(a) and (b) the stress as a function of ΔR for both the compression and expansion axes immediately before the plastic event and immediately after the plastic event. Since the stress is maximum around $t/\tau = -1$ and minimum around $t/\tau = 1$ we define the time immediately before the plastic event as $t/\tau_{pl} = -1$ and the time immediately after the plastic event as $t/\tau_{pl} = 1$. Right before the plastic event, we see that the stress in both the compression and expansion axes are roughly the same and decay with distance from the center of the event. We have included data for different ϕ , and the data show no trend in ϕ . Immediately after the plastic event, the stress increases with distance, converging to the mean stress at larger ΔR . Likewise, the data immediately after the plastic event show no

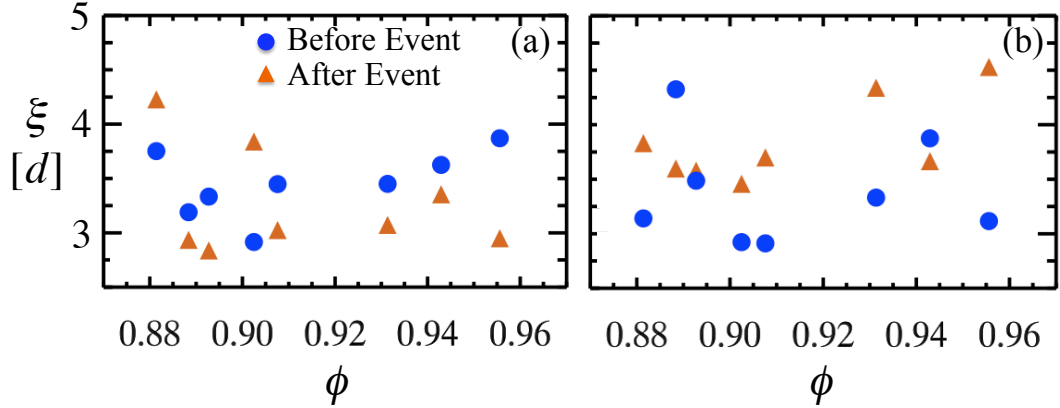


Figure 7.9: Length scale for stress decay with distance to plastic event immediately before the event and after the event. (a) is the length scale along the compression axis and (b) is the length scale along the expansion axis. The time immediately before a plastic event is defined as $t/\tau_{pl} = -1$ and the time immediately after a plastic event is defined as $t/\tau_{pl} = 1$. We estimate an uncertainty of ~ 0.5 particle diameters in ξ .

trend in ϕ .

The data in Fig. 7.8 indicate a spatial spreading in the stress during a plastic event. Since there is no conclusive theory to describe how the stress should decay, we avoid fitting the data to an empirical function to obtain a length scale and instead use

$$\xi = \frac{2 \int_0^\infty x [f(x) - f(x \rightarrow \infty)]^2 dx}{\int_0^\infty [f(x) - f(x \rightarrow \infty)]^2 dx} \quad (7.6)$$

which characterizes the decay in the stress with distance from the center of the plastic event. In the expression, $x = \Delta R$ and $f = \langle \bar{\Gamma}_{\Delta R, t} / \bar{\Gamma}_{all} \rangle_{pl} - 1$. This function was introduced as Eqn. 3.2 in Chapter 3.3 to characterize boundary effects in our confinement work. For simple exponential decay, $f(z) = Ae^{(-z/\lambda)}$, Eqn (7.6) gives the appropriate length scale of $\xi = \lambda$.

In Fig. 7.9(a) and (b) we show the ξ for our different samples immediately before and after the plastic event along the expansion and compression axis. The length scale is roughly 3 – 4.5 particle diameters with no dependence on ϕ . In the work of Goyon *et al.* [37], they observed for microchannel flow a length scale of 0 – 6 particle diameters, where ξ was obtained indirectly by fitting the average stress and velocity profile. In their work, they observed an ϕ dependence, where ξ increased with volume fraction and was 0 particle

diameters at the jamming point. For reasons we do not understand, we have not observed an area fraction dependence.

7.6 Conclusion

In this chapter, we have provided a new insight into the evolution of the stress in the vicinity of a plastic event. We have introduced a deformation parameter to precisely define the size, location in time, and duration of a plastic event. Analyzing the larger plastic events, we have shown that particle rearrangements are driven by an asymmetric process involving a compression and expansion mode. Right before droplets undergo a plastic rearrangement, the stress increases significantly and extends 4 particle diameters from the center of the plastic event. Once the rearrangement occurs, the stress drops precipitately by a factor of 3 in both directions. The stress recovery in the expansion direction is slow taking a time scale of $4\tau_{pl}$ while in the compression direction the stress recovery is much quicker.

In the Bocquet *et al.* model, an essential aspect of the model is a flow cooperativity length scale ξ characterizing “how the plastic activity spreads spatially over the system due to non-local elastic relaxation” [40]. Clearly in our data we see a stress build up and relaxation that spreads roughly four particle diameters from the center of a plastic event, and is solely the result of an elastic response. In the work of Goyon, where this length scale was measured indirectly by fitting average stress and velocities profiles predicted by the Bocquet *et al.* model, they found length scales on the order of $\xi \sim 0 - 6$ particle diameters. They found the length scale to depend on volume fraction, where at the jamming point $\xi = 0$ and near a volume fraction 1 they found $\xi \sim 5$ particle diameters. In our work, we do not see a trend in the length scale with ϕ , but our length scale is within the length scale observed by Goyon. Even though we see no trend in ϕ , we have confirmed the hypothesis of a flow cooperativity length scale. Our results stand as an important step in developing a quantitative and conceptual understanding for the evolution of the stress near a plastic event.

CHAPTER 8

Summary

Soft materials are well suited for a variety of applications because their mechanical response is an intermediate between a solid and a liquid. For instance, shaving cream is useful because it easily spreads onto the face like a liquid, but once applied, it's solid enough to hold to the face. Likewise, peanut butter easily spreads onto bread, but doesn't run off. Similar reasons apply to the use of toothpaste, cosmetic products, paints, plasters, drilling fluids, and firefighting agents to name a few others. By controlling the degree of the solid like and liquid like response, a soft material can be tuned for a particular application, and understanding the origins of this mixed solid and liquid like response is very important for designing soft materials to be useful in our everyday experience. In addition to the industrial applications, soft materials pose rich and difficult scientific questions such as the nature of the jamming transition which was the topic of this dissertation.

Changing the particle concentration is the simplest approach to tune the response of a soft material from behaving more liquid like to behaving more solid like. By increasing the particle concentration, the system can undergo a jamming transition, where motion of the individual particles becomes increasingly difficult because of crowding effects. This jamming transition can occur in a variety of materials composed of discrete particles such as colloids, granular materials, emulsions, and foams. At first glance, materials like colloids, granular materials, emulsions, and foams may seem vastly different, but under the umbrella of jamming, the physics of these materials can be linked to a singular concept, the crowding of particles.

In this dissertation, we studied this crowding effect in a wide range of scenarios that include colloids, packing of disks and spheres into small spaces, static emulsion packings, and the flow of emulsions. We found many trends in the scaling of microscopic parameters with particle concentration that confirm existing models. We found that boundaries can alter the structure of soft materials and shift the jamming transition to lower particle concentrations. Most importantly, we introduced a new model system to study the internal forces within a soft material, and using this model system, we verified a hypothesis that there is a spatial cooperative length scale for stress relaxation.

In our colloidal studies, we applied an analytic tool χ_4 , commonly used to characterize the dynamical heterogeneity of molecules in molecular glass formers, to quantify the dynamical heterogeneity as the particle concentration increases. Empirical and theoretical models predict for colloidal systems a divergence in the dynamical heterogeneity with increasing concentration. Verifying which models correctly predict the dynamical heterogeneity can elucidate if the properties of dense colloids are completely governed by a jamming transition or by an analogous glass transition. Using our measurements, we tested two models, however, we were unable to conclusively show which model is better, and if the growing dynamical heterogeneity is governed solely by a jamming transition. Both models capture and predict the time and length scales associated with dynamical heterogeneity, and fitting our data to the models gave fitting parameters that agreed well to derived fitting values.

In our confinement studies, we investigated how boundaries alter the packing of hard disks and spheres to learn how boundaries affect the microstructure of real soft materials. Knowing the structure of soft materials is very important for understanding many bulk characteristics such as their rheological response, hydrostatics, mass and energy transport, sonic transmission, electrical properties, and optical properties. In molecular, colloidal, and granular systems, as a material is confined the internal dynamics and structure are modified leading to changes in many material properties. If we want to understand how confinement alters the behavior of soft materials, it is essential to understand how confinement alters the internal structure. To first order, we modeled the structure of soft materials using disks in 2D and spheres in 3D. We found that the boundaries can alter how particles pack near the walls and that the jamming transition is shifted to lower particle concentrations with

increasing confinement. We also presented and verified a model predicting how boundaries shift the jamming point to lower particle concentrations. Another important aspect of this work relates to how one studies packing in general. How big does an experiment need to be before confinement effects are important, and how far do perturbation in the packing extend from the wall? We found that the boundaries have a pronounced effect on the packing up to 4 particle diameters from the boundary. Therefore, if one wishes to conduct an experiment where boundary effects are less important, the system must be at least 8 particle diameters wide and the properties of the system must be quantified using particles at least 4 particle diameters away from the boundary.

For our last two experiments we introduced a new model system to study the jamming behavior and flow properties of deformable 2D emulsion droplets. We also introduced a method to determine the repulsive forces between droplets in contact and the viscous drag force between droplets. The advantage of our system is that the position of the particles and forces are known, we can easily tune the droplet size to create monodisperse, bidisperse, and polydisperse packings, it's cheap, and there is no static friction between droplets. Therefore, we can apply our model system to easily probe various jamming properties related to forces, polydispersity, and friction.

For static systems composed of frictionless disks or spheres, the jamming transition is expected to obey many critical scaling relationships analogous to a true phase transition. Experimentally, many of these critical scaling relationships have not been tested for frictionless particles. Taking advantage of the fact that our system has no static friction between droplets, we used our new model system to verify these critical scaling laws. Also an important property of soft matter systems is the formation of force chains since they are thought to provide mechanical rigidity, and therefore, it is highly valuable to have a model that can accurately predict the statistics of these force chains. Using our model system, we also quantified the force chains in our static experiments, and verified the assumptions of a model that can accurately predict the statistics of force chains using physical principles.

Using our model system we also explored the quasi-static flow of our 2D deformable droplets. In general, the flow of soft matter is the result of microscopic events taking place at the grain scale. To elucidate the physics of these microscopic events, we used our 2D

model system to explore the local stresses acting on groups of particles rearranging. Our results are preliminary, but we have found that before a group of droplets rearrange there is a large build up of stress, and that this stress is quickly dissipated when these droplets rearrange. We find that the stress build up is spatially spread out over a cooperativity length scale, and that this length scale is on the order of 4 particle diameters independent of droplet concentration. This observation is in contrast to a model that predicts a spatial cooperativity length scale that grows with area fraction. Currently it is not understood why the length scale in our data is independent of droplet concentration, but nonetheless, our results are beginning to illuminate the physical aspects of the stress build up and relaxation of microscopic events in soft materials.

Bibliography

- [1] H. Löwen, “Colloidal soft matter under external control,” *J. Phys-Condens. Mat.*, vol. 13, no. 24, p. R415, 2001.
- [2] A.-P. Hynninen, M. Dijkstra, and R. Roij, “Effect of triplet attractions on the phase diagram of suspensions of charged colloids,” *J. Phys-Condens. Mat.*, vol. 15, no. 48, p. S3549, 2003.
- [3] J. Zhang, Z. Sun, and B. Yang, “Self-assembly of photonic crystals from polymer colloids,” *Current Opinion in Colloid & Interface Science*, vol. 14, no. 2, pp. 103–114, 2009.
- [4] D. T. N. Chen, Q. Wen, P. A. Janmey, J. C. Crocker, and A. G. Yodh, “Rheology of Soft Materials,” *Condens. Matter Phys.*, vol. 1, no. 1, pp. 301–322, 2010.
- [5] A. Samadani, L. Mahadevan, and A. Kudrolli, “Shocks in sand flowing in a silo,” *J. Fluid Mech.*, vol. 452, pp. 293–301, 2002.
- [6] H. M. Jaeger, S. R. Nagel, and R. P. Behringer, “Granular solids, liquids, and gases,” *Rev. Mod. Phys.*, vol. 68, no. 4, pp. 1259–1273, 1996.
- [7] D. M. Mueth, G. F. Debregeas, G. S. Karczmar, P. J. Eng, S. R. Nagel, and H. M. Jaeger, “Signatures of granular microstructure in dense shear flows,” *Nature*, vol. 406, no. 6794, pp. 385–389, 2000.
- [8] D. R. Scott, “Seismicity and stress rotation in a granular model of the brittle crust,” *Nature*, vol. 381, pp. 592–595, 1996.

- [9] J. Duran, *Sands, Powders, and Grains: An Introduction to the Physics of Granular Materials*. Springer, 2000.
- [10] P. G. de Gennes, “Granular matter: a tentative view,” *Rev. Mod. Phys.*, vol. 71, no. 2, pp. 374–382, 1999.
- [11] R. Mezzenga, P. Schurtenberger, A. Burbidge, and M. Michel, “Understanding foods as soft materials,” *Nature Materials*, vol. 4, no. 10, pp. 729–740, 2005.
- [12] D. J. Durian, D. A. Weitz, and D. J. Pine, “Scaling behavior in shaving cream,” *Phys. Rev. A*, vol. 44, no. 12, pp. R7902–R7905, 1991.
- [13] J. C. Earnshaw and A. H. Jaafar, “Diffusing-wave spectroscopy of a flowing foam,” *Phys. Rev. E*, vol. 49, pp. 5408–5411, 1994.
- [14] C. W. Bamforth, “The Relative Significance of Physics and Chemistry for Beer Foam Excellence: Theory and Practice,” *The Institute & Guild of Brewing*, vol. 110, no. 4, pp. 259–266, 2004.
- [15] P. Fischer and E. J. Windhab, “Rheology of food materials,” *Current Opinion in Colloid & Interface Science*, vol. 16, no. 1, pp. 36–40, 2011.
- [16] B. J. D. Le Révérend, I. T. Norton, P. W. Cox, and F. Spyropoulos, “Colloidal aspects of eating,” *Current Opinion in Colloid & Interface Science*, vol. 15, no. 1-2, pp. 84–89, 2010.
- [17] J. Ubbink, A. Burbidge, and R. Mezzenga, “Food structure and functionality: a soft matter perspective,” *Soft Matter*, vol. 4, no. 8, pp. 1569–1581, 2008.
- [18] Y. Forterre and O. Pouliquen, “Flows of dense granular media,” *Annual Review of Fluid Mechanics*, vol. 40, no. 1, pp. 1–24, 2008.
- [19] P. Schall and M. van Hecke, “Shear Bands in Matter with Granularity,” *Annual Review of Fluid Mechanics*, vol. 42, no. 1, pp. 67–88, 2010.
- [20] M. Dennin, “Discontinuous jamming transitions in soft materials: coexistence of flowing and jammed states,” *J. Phys-Condens. Mat.*, vol. 20, no. 28, p. 283103, 2008.

- [21] M. V. Hecke, “Jamming of soft particles: geometry, mechanics, scaling and isostaticity,” *J. Phys-Condens. Mat.*, vol. 22, no. 3, p. 033101, 2010.
- [22] C. S. O’Hern, L. E. Silbert, A. J. Liu, and S. R. Nagel, “Jamming at zero temperature and zero applied stress: The epitome of disorder,” *Phys. Rev. E*, vol. 68, no. 1, p. 011306, 2003.
- [23] M. E. Cates, J. P. Wittmer, J. P. Bouchaud, and P. Claudin, “Jamming, Force Chains, and Fragile Matter,” *Phys. Rev. Lett.*, vol. 81, no. 9, pp. 1841–1844, 1998.
- [24] A. J. Liu and S. R. Nagel, “The Jamming Transition and the Marginally Jammed Solid,” *Condens. Matter Phys.*, vol. 1, no. 1, pp. 347–369, 2010.
- [25] A. J. Liu and S. R. Nagel, “Nonlinear dynamics: Jamming is not just cool any more,” *Nature*, vol. 396, no. 6706, pp. 21–22, 1998.
- [26] G. Biroli, “Jamming: A new kind of phase transition?,” *Nat. Phys.*, vol. 3, no. 4, pp. 222–223, 2007.
- [27] V. Trappe, V. Prasad, L. Cipelletti, P. N. Segre, and D. A. Weitz, “Jamming phase diagram for attractive particles,” *Nature*, vol. 411, no. 6839, pp. 772–775, 2001.
- [28] H. Tanaka, J. Meunier, and D. Bonn, “Nonergodic states of charged colloidal suspensions: Repulsive and attractive glasses and gels,” *Phys. Rev. E*, vol. 69, no. 3, p. 031404, 2004.
- [29] V. Trappe and P. Sandkühler, “Colloidal gelslow-density disordered solid-like states,” *Current Opinion in Colloid & Interface Science*, vol. 8, no. 6, pp. 494–500, 2004.
- [30] P. B. Umbanhowar and D. I. Goldman, “Low density fragile states in cohesive powders,” *American Journal of Physics*, vol. 74, no. 8, pp. 720–721, 2006.
- [31] W. G. Ellenbroek, E. Somfai, M. van Hecke, and W. van Saarloos, “Critical Scaling in Linear Response of Frictionless Granular Packings near Jamming,” *Phys. Rev. Lett.*, vol. 97, no. 25, p. 258001, 2006.

- [32] W. G. Ellenbroek, Z. Zeravic, W. van Saarloos, and M. van Hecke, “Non-affine response: Jammed packings vs. spring networks,” *Europhys. Lett.*, vol. 87, no. 3, p. 34004, 2009.
- [33] S. S. Datta, D. D. Gerrard, T. S. Rhodes, T. G. Mason, and D. A. Weitz, “Rheology of attractive emulsions,” *Phys. Rev. E*, vol. 84, p. 041404, 2011.
- [34] O. Dauchot, G. Marty, and G. Biroli, “Dynamical Heterogeneity Close to the Jamming Transition in a Sheared Granular Material,” *Phys. Rev. Lett.*, vol. 95, no. 26, p. 265701, 2005.
- [35] P. Hébraud, F. Lequeux, J. P. Munch, and D. J. Pine, “Yielding and rearrangements in disordered emulsions,” *Phys. Rev. Lett.*, vol. 78, no. 24, pp. 4657–4660, 1997.
- [36] T. Mason, “Yielding and Flow of Monodisperse Emulsions,” *J. Colloid Interface Sci.*, vol. 179, no. 2, pp. 439–448, 1996.
- [37] J. Goyon, A. Colin, G. Ovarlez, A. Ajdari, and L. Bocquet, “Spatial cooperativity in soft glassy flows,” *Nature*, vol. 454, no. 7200, pp. 84–87, 2008.
- [38] L. Berthier, G. Biroli, J.-P. Bouchaud, L. Cipelletti, and W. van Saarloos, *Dynamical Heterogeneities in Glasses, Colloids, and Granular Media (International Series of Monographs on Physics)*. Oxford University Press, USA, 2011.
- [39] A. Lemaître and C. Maloney, “Sum Rules for the Quasi-Static and Visco-Elastic Response of Disordered Solids at Zero Temperature,” *J. Stat. Phys.*, vol. 123, no. 2, pp. 415–453, 2006.
- [40] L. Bocquet, A. Colin, and A. Ajdari, “Kinetic Theory of Plastic Flow in Soft Glassy Materials,” *Phys. Rev. Lett.*, vol. 103, no. 3, p. 036001, 2009.
- [41] E. Aharonov, E. Bouchbinder, H. G. E. Hentschel, V. Ilyin, N. Makedonska, I. Procaccia, and N. Schupper, “Direct identification of the glass transition: Growing length scale and the onset of plasticity,” *Europhys. Lett.*, p. 56002, 2007.

- [42] E. Bouchbinder, J. S. Langer, and I. Procaccia, “Athermal shear-transformation-zone theory of amorphous plastic deformation. I. Basic principles,” *Phys. Rev. E*, vol. 75, p. 036107, 2007.
- [43] J. S. Langer and L. Pechenik, “Dynamics of shear-transformation zones in amorphous plasticity: Energetic constraints in a minimal theory,” *Phys. Rev. E*, vol. 68, no. 6, p. 061507, 2003.
- [44] Z. Zhang, N. Xu, D. T. N. Chen, P. Yunker, A. M. Alsayed, K. B. Aptowicz, P. Habdas, A. J. Liu, S. R. Nagel, and A. G. Yodh, “Thermal vestige of the zero-temperature jamming transition,” *Nature*, vol. 459, no. 7244, pp. 230–233, 2009.
- [45] W. van Meegen and P. N. Pusey, “Dynamic light-scattering study of the glass transition in a colloidal suspension,” *Phys. Rev. A*, vol. 43, no. 10, pp. 5429–5441, 1991.
- [46] T. G. Mason and D. A. Weitz, “Linear viscoelasticity of colloidal hard sphere suspensions near the glass transition,” *Phys. Rev. Lett.*, vol. 75, no. 14, pp. 2770–2773, 1995.
- [47] E. Bartsch, “Scattering experiments for the microscopic understanding of the glass transition,” *J. Non-cryst. Solids*, vol. 192-193, pp. 384–392, 1995.
- [48] W. van Meegen, T. C. Mortensen, S. R. Williams, and J. Müller, “Measurement of the self-intermediate scattering function of suspensions of hard spherical particles near the glass transition,” *Phys. Rev. E*, vol. 58, no. 5, pp. 6073–6085, 1998.
- [49] W. van Meegen and S. R. Williams, “Comment on “probing the equilibrium dynamics of colloidal hard spheres above the mode-coupling glass transition”,” *Phys. Rev. Lett.*, vol. 104, no. 16, p. 169601, 2010.
- [50] G. Brambilla, D. E. Masri, M. Pierno, L. Berthier, L. Cipelletti, G. Petekidis, and A. Schofield, “Brambilla et al. reply:,” *Phys. Rev. Lett.*, vol. 104, no. 16, p. 169602, 2010.
- [51] G. Brambilla, D. E. Masri, M. Pierno, L. Berthier, L. Cipelletti, G. Petekidis, and A. B. Schofield, “Probing the Equilibrium Dynamics of Colloidal Hard Spheres above

- the Mode-Coupling Glass Transition,” *Phys. Rev. Lett.*, vol. 102, no. 8, p. 085703, 2009.
- [52] C. A. Angell, “Formation of Glasses from Liquids and Biopolymers,” *Science*, vol. 267, no. 5206, pp. 1924–1935, 1995.
- [53] L. A. Greer, “Metallic Glasses,” *Science*, vol. 267, no. 5206, pp. 1947–1953, 1995.
- [54] P. Jenniskens and D. F. Blake, “Structural transitions in amorphous water ice and astrophysical implications,” *Science*, vol. 265, no. 5173, pp. 753–756, 1994.
- [55] P. G. Debenedetti and F. H. Stillinger, “Supercooled liquids and the glass transition,” *Nature*, vol. 410, no. 6825, pp. 259–267, 2001.
- [56] L. Berthier and G. Biroli, “Theoretical perspective on the glass transition and amorphous materials,” *ArXiv*, 2011.
- [57] E. Donth, “Characteristic length of the glass transition,” *J. Polym. Sci. B Polym. Phys.*, vol. 34, no. 17, pp. 2881–2892, 1996.
- [58] C. Donati, J. F. Douglas, W. Kob, S. J. Plimpton, P. H. Poole, and S. C. Glotzer, “Stringlike cooperative motion in a supercooled liquid,” *Phys. Rev. Lett.*, vol. 80, no. 11, pp. 2338–2341, 1998.
- [59] W. Kob, P. Scheidler, and K. Binder, “The relaxation dynamics of a simple glass former confined in a pore,” *Europhys. Lett.*, vol. 52, no. 3, pp. 277–283, 2000.
- [60] M. T. Cicerone, F. R. Blackburn, and M. D. Ediger, “How do molecules move near T_g ? molecular rotation of six probes in o-terphenyl across 14 decades in time,” *J. Chem. Phys.*, vol. 102, no. 1, pp. 471–479, 1995.
- [61] E. W. Fischer, E. Donth, and W. Steffen, “Temperature dependence of characteristic length for glass transition,” *Phys. Rev. Lett.*, vol. 68, no. 15, pp. 2344–2346, 1992.
- [62] E. Hempel, G. Hempel, A. Hensel, C. Schick, and E. Donth, “Characteristic length of dynamic glass transition near t_g for a wide assortment of glass-forming substances,” *The Journal of Physical Chemistry B*, vol. 104, no. 11, pp. 2460–2466, 2000.

- [63] H. Huth, M. Beiner, and E. Donth, “Temperature dependence of glass-transition cooperativity from heat-capacity spectroscopy: Two post-adam-gibbs variants,” *Phys. Rev. B*, vol. 61, no. 22, pp. 15092–15101, 2000.
- [64] R. Kurita and E. R. Weeks, “Glass transition of two-dimensional binary soft-disk mixtures with large size ratios,” *Phys. Rev. E*, vol. 82, no. 4, p. 041402, 2010.
- [65] H. Sillescu, “Heterogeneity at the glass transition: a review,” *J. Non-cryst. Solids*, vol. 243, no. 2-3, pp. 81–108, 1999.
- [66] S. C. Glotzer, V. N. Novikov, and T. B. Schröder, “Time-dependent, four-point density correlation function description of dynamical heterogeneity and decoupling in supercooled liquids,” *J. Chem. Phys.*, vol. 112, no. 2, pp. 509–512, 2000.
- [67] D. Chandler and J. P. Garrahan, “Dynamics on the Way to Forming Glass: Bubbles in Space-Time,” *Annual Review of Physical Chemistry*, vol. 61, no. 1, pp. 191–217, 2010.
- [68] P. N. Pusey and W. van Meegen, “Phase behaviour of concentrated suspensions of nearly hard colloidal spheres,” *Nature*, vol. 320, no. 6060, pp. 340–342, 1986.
- [69] A. D. Dinsmore, E. R. Weeks, V. Prasad, A. C. Levitt, and D. A. Weitz, “Three-dimensional confocal microscopy of colloids,” *Applied Optics*, vol. 40, no. 24, pp. 4152–4159, 2001.
- [70] L. Antl, J. W. Goodwin, R. D. Hill, R. H. Ottewill, S. M. Owens, S. Papworth, and J. A. Waters, “The preparation of poly(methyl methacrylate) latices in non-aqueous media,” *Colloids and Surfaces*, vol. 17, no. 1, pp. 67–78, 1986.
- [71] P. N. Segrè, S. P. Meeker, P. N. Pusey, and W. C. K. Poon, “Viscosity and structural relaxation in suspensions of hard-sphere colloids,” *Phys. Rev. Lett.*, vol. 75, no. 5, pp. 958–961, 1995.
- [72] Z. Cheng, J. Zhu, P. M. Chaikin, S.-E. Phan, and W. B. Russel, “Nature of the divergence in low shear viscosity of colloidal hard-sphere dispersions,” *Phys. Rev. E*, vol. 65, no. 4, p. 041405, 2002.

- [73] A. van Blaaderen and P. Wiltzius, “Real-space structure of colloidal hard-sphere glasses,” *Science*, vol. 270, pp. 1177–1179, 1995.
- [74] A. H. Marcus, J. Schofield, and S. A. Rice, “Experimental observations of non-Gaussian behavior and stringlike cooperative dynamics in concentrated quasi-two-dimensional colloidal liquids,” *Phys. Rev. E*, vol. 60, no. 5, pp. 5725–5736, 1999.
- [75] W. K. Kegel and A. van Blaaderen, “Direct observation of dynamical heterogeneities in colloidal hard-sphere suspensions,” *Science*, vol. 287, no. 5451, pp. 290–293, 2000.
- [76] E. R. Weeks, J. C. Crocker, A. C. Levitt, A. Schofield, and D. A. Weitz, “Three-dimensional direct imaging of structural relaxation near the colloidal glass transition,” *Science*, vol. 287, no. 5453, pp. 627–631, 2000.
- [77] H. König, R. Hund, K. Zahn, and G. Maret, “Experimental realization of a model glass former in 2d,” *Euro. Phys. J. E*, vol. 18, no. 3, pp. 287–293, 2005.
- [78] R. E. Courtland and E. R. Weeks, “Direct visualization of ageing in colloidal glasses,” *J. Phys.-Condens. Mat.*, vol. 15, no. 1, pp. S359–S365, 2003.
- [79] L. Cipelletti, H. Bissig, V. Trappe, P. Ballesta, and S. Mazoyer, “Time-resolved correlation: a new tool for studying temporally heterogeneous dynamics,” *J. Phys.: Condens. Matter*, vol. 15, pp. S257–S262, 2003.
- [80] N. B. Simeonova and W. K. Kegel, “Gravity-induced aging in glasses of colloidal hard spheres,” *Phys. Rev. Lett.*, vol. 93, no. 3, p. 035701, 2004.
- [81] D. El Masri, M. Pierno, L. Berthier, and L. Cipelletti, “Ageing and ultra-slow equilibration in concentrated colloidal hard spheres,” *J. Phys.-Condens. Mat.*, vol. 17, no. 45, pp. S3543–S3549, 2005.
- [82] G. C. Cianci, R. E. Courtland, and E. R. Weeks, “Correlations of structure and dynamics in an aging colloidal glass,” *Solid State Communications*, vol. 139, no. 11–12, pp. 599–604, 2006.

- [83] P. Yunker, Z. Zhang, K. Aptowicz, and A. Yodh, “Irreversible rearrangements, correlated domains, and local structure in aging glasses,” *Phys. Rev. Lett.*, vol. 103, no. 11, p. 115701, 2009.
- [84] C. R. Nugent, K. V. Edmond, H. N. Patel, and E. R. Weeks, “Colloidal glass transition observed in confinement,” *Phys. Rev. Lett.*, vol. 99, no. 2, p. 025702, 2007.
- [85] P. S. Sarangapani and Y. Zhu, “Impeded structural relaxation of a hard-sphere colloidal suspension under confinement,” *Phys. Rev. E*, vol. 77, no. 1, p. 010501, 2008.
- [86] J. C. Conrad, P. P. Dhillon, E. R. Weeks, D. R. Reichman, and D. A. Weitz, “Contribution of slow clusters to the bulk elasticity near the colloidal glass transition,” *Phys. Rev. Lett.*, vol. 97, no. 26, p. 265701, 2006.
- [87] N. Lacevic and S. C. Glotzer, “Dynamical heterogeneity and jamming in glass-forming liquids†,” *The Journal of Physical Chemistry B*, vol. 108, no. 51, pp. 19623–19633, 2004.
- [88] L. Berthier, G. Biroli, J. P. Bouchaud, L. Cipelletti, D. E. Masri, D. L’Hote, F. Ladieu, and M. Pierno, “Direct experimental evidence of a growing length scale accompanying the glass transition,” *Science*, vol. 310, no. 5755, pp. 1797–1800, 2005.
- [89] F. H. Stillinger, “A topographic view of supercooled liquids and glass formation,” *Science*, vol. 267, no. 5206, pp. 1935–1939, 1995.
- [90] C. A. Angell, K. L. Ngai, G. B. McKenna, P. F. McMillan, and S. W. Martin, “Relaxation in glassforming liquids and amorphous solids,” *Journal of Applied Physics*, vol. 88, no. 6, pp. 3113–3157, 2000.
- [91] F. Stickel, E. W. Fischer, and R. Richert, “Dynamics of glass-forming liquids. I. temperature-derivative analysis of dielectric relaxation data,” *J. Chem. Phys.*, vol. 102, no. 15, pp. 6251–6257, 1995.
- [92] F. Stickel, E. W. Fischer, and R. Richert, “Dynamics of glass-forming liquids. II. detailed comparison of dielectric relaxation, dc-conductivity, and viscosity data,” *J. Chem. Phys.*, vol. 104, no. 5, pp. 2043–2055, 1996.

- [93] W. Götze, “Recent tests of the mode-coupling theory for glassy dynamics,” *J. Phys-Condens. Mat.*, vol. 11, no. 10A, pp. A1–A45, 1999.
- [94] T. Hecksher, A. I. Nielsen, N. B. Olsen, and J. C. Dyre, “Little evidence for dynamic divergences in ultraviscous molecular liquids,” *Nature Physics*, vol. 4, no. 9, pp. 737–741, 2008.
- [95] S. Torquato, T. M. Truskett, and P. G. Debenedetti, “Is Random Close Packing of Spheres Well Defined?,” *Phys. Rev. Lett.*, vol. 84, no. 10, pp. 2064–2067, 2000.
- [96] O. K. Rice, “On the Statistical Mechanics of Liquids, and the Gas of Hard Elastic Spheres,” *J. Chem. Phys.*, vol. 12, no. 1, pp. 1–18, 1944.
- [97] J. D. Bernal and J. Mason, “Packing of Spheres: Co-ordination of Randomly Packed Spheres,” *Nature*, vol. 188, no. 4754, pp. 910–911, 1960.
- [98] R. K. Mcgeary, “Mechanical Packing of Spherical Particles,” *J. Am. Ceram. Soc.*, vol. 44, no. 10, pp. 513–522, 1961.
- [99] R. Zallen, *Physics of Amorphous Solids*. Wiley, 1983.
- [100] W. O. Smith, P. D. Foote, and P. F. Busang, “Packing of Homogeneous Spheres,” *Phys. Rev. Lett.*, vol. 34, no. 9, pp. 1271–1274, 1929.
- [101] S. F. Edwards, *Granular Matter*. Springer-Verlag, 1994.
- [102] C. Radin, “Random Close Packing of Granular Matter,” *J. Stat. Phys.*, vol. 131, no. 4, pp. 567–573, 2008.
- [103] M. Jerkins, M. Schröter, H. L. Swinney, T. J. Senden, M. Saadatfar, and T. Aste, “Onset of Mechanical Stability in Random Packings of Frictional Spheres,” *Phys. Rev. Lett.*, vol. 101, no. 1, p. 018301, 2008.
- [104] R. Pal, “A new linear viscoelastic model for emulsions and suspensions,” *Polym. Eng. Sci.*, vol. 48, no. 7, pp. 1250–1253, 2008.
- [105] G. Lois, J. Blawdziewicz, and C. S. O’Hern, “Percolation Model for Slow Dynamics in Glass-Forming Materials,” *Phys. Rev. Lett.*, vol. 102, no. 1, pp. 015702–4, 2009.

- [106] D. P. Haughey and G. S. G. Beveridge, “Structural properties of packed beds - A review,” *Can. J. Chem. Eng.*, vol. 47, no. 2, pp. 130–140, 1969.
- [107] D. I. Goldman and H. L. Swinney, “Signatures of glass formation in a fluidized bed of hard spheres,” *Phys. Rev. Lett.*, vol. 96, no. 14, p. 145702, 2006.
- [108] R. Kurita and E. R. Weeks, “Experimental study of random-close-packed colloidal particles,” *Phys. Rev. E*, vol. 82, no. 1, p. 011403, 2010.
- [109] A. R. Kansal, S. Torquato, and F. H. Stillinger, “Computer generation of dense polydisperse sphere packings,” *J. Chem. Phys.*, vol. 117, no. 18, pp. 8212–8218, 2002.
- [110] R. Al-Raoush and M. Alsaleh, “Simulation of random packing of polydisperse particles,” *Powder Technol.*, vol. 176, no. 1, pp. 47–55, 2007.
- [111] K. Lochmann, L. Oger, and D. Stoyan, “Statistical analysis of random sphere packings with variable radius distribution,” *Solid State Sci.*, vol. 8, no. 12, pp. 1397–1413, 2006.
- [112] H. J. H. Brouwers, “Particle-size distribution and packing fraction of geometric random packings,” *Phys. Rev. E*, vol. 74, no. 3, pp. 031309–031322, 2006.
- [113] T. Okubo and T. Odagaki, “Random packing of binary hard discs,” *J. Phys-Condens. Mat.*, vol. 16, no. 37, pp. 6651–6659, 2004.
- [114] P. Richard, L. Oger, J. P. Troadec, and A. Gervois, “A model of binary assemblies of spheres,” *Eur. Phys. J. E*, vol. 6, no. 4, pp. 295–303–303, 2001.
- [115] P. C. Carman, “Fluid flow through granular beds,” *Trans. Inst. Chem. Eng.-Lond.*, vol. 15, pp. 150–166, 1937.
- [116] L. C. Verman and S. Banerjee, “Effect of Container Walls on Packing Density of Particles,” *Nature*, vol. 157, p. 584, 1946.
- [117] R. L. Brown and P. G. W. Hawksley, “Effect of Container Walls on Packing Density of Particles,” *Nature*, vol. 157, p. 585, 1946.
- [118] G. D. Scott and D. M. Kilgour, “The density of random close packing of spheres,” *J. Phys. D Appl. Phys.*, vol. 2, no. 6, pp. 863–866, 1969.

- [119] K. Ridgway and K. J. Tarbuck, “Random packing of spheres,” *Brit. Chem. Eng. Pr. Tec.*, vol. 12, no. 3, p. 384, 1967.
- [120] B. R. Aïm and L. P. Goff, “Effet de paroi dans les empilements désordonnés de sphères et application à la porosité de mélanges binaires,” *Powder Technol.*, vol. 1, no. 5, pp. 281–290, 1967.
- [121] A. G. Dixon, “Correlations for wall and particle-shape effects on fixed-bed bulk voidage,” *Can. J. Chem. Eng.*, vol. 66, no. 5, pp. 705–708, 1988.
- [122] M. Suzuki, T. Shinmura, K. Iimura, and M. Hirota, “Study of the Wall Effect on Particle Packing Structure Using X-ray Micro Computed Tomography,” *Powder Technol.*, vol. 19, no. 2, pp. 183–195, 2008.
- [123] R. Zou, “The packing of spheres in a cylindrical container: the thickness effect,” *Chem. Eng. Sci.*, vol. 50, no. 9, pp. 1504–1507, 1995.
- [124] R. P. Zou and A. B. Yu, “Wall effect on the packing of cylindrical particles,” *Chem. Eng. Sci.*, vol. 51, no. 7, pp. 1177–1180, 1996.
- [125] R. M. German, *Particle Packing Characteristics*. Metal Powder Industries Federation, 1989.
- [126] J. W. Landry, G. S. Grest, L. E. Silbert, and S. J. Plimpton, “Confined granular packings: Structure, stress, and forces,” *Phys. Rev. E*, vol. 67, no. 4, pp. 041303–041311, 2003.
- [127] G. T. Seidler, G. Martinez, L. H. Seeley, K. H. Kim, E. A. Behne, S. Zaranek, B. D. Chapman, S. M. Heald, and D. L. Brewster, “Granule-by-granule reconstruction of a sandpile from x-ray microtomography data,” *Phys. Rev. E*, vol. 62, no. 6, pp. 8175–8181, 2000.
- [128] L. Vanel, P. Claudin, Bouchaud, M. E. Cates, E. Clément, and J. P. Wittmer, “Stresses in Silos: Comparison Between Theoretical Models and New Experiments,” *Phys. Rev. Lett.*, vol. 84, no. 7, pp. 1439–1442, 2000.

- [129] U. Marconi, “Janssen’s law and stress fluctuations in confined dry granular materials,” *Physica A*, vol. 280, no. 3-4, pp. 279–288, 2000.
- [130] P. Claudin and J.-P. Bouchaud, “Static Avalanches and Giant Stress Fluctuations in Silos,” *Phys. Rev. Lett.*, vol. 78, no. 2, pp. 231–234, 1997.
- [131] J. Landry, “Discrete element simulations of stress distributions in silos: crossover from two to three dimensions,” *Powder Technol.*, vol. 139, no. 3, pp. 233–239, 2004.
- [132] M. Alcoutlabi and G. B. McKenna, “Effects of confinement on material behaviour at the nanometre size scale,” *J. Phys-Condens. Mat.*, vol. 17, no. 15, pp. R461–R524, 2005.
- [133] P. Gallo, M. Rovere, and E. Spohr, “Glass transition and layering effects in confined water: A computer simulation study,” *J. Chem. Phys.*, vol. 113, no. 24, pp. 11324–11335, 2000.
- [134] S. Granick, “Motions and Relaxations of Confined Liquids,” *Science*, vol. 253, no. 5026, pp. 1374–1379, 1991.
- [135] J. R. Henderson, “Oscillatory structure of confined fluids,” *Mol. Phys.*, pp. 2345–2352, 2007.
- [136] J. Mittal, V. K. Shen, J. R. Errington, and T. M. Truskett, “Confinement, entropy, and single-particle dynamics of equilibrium hard-sphere mixtures,” *J. Chem. Phys.*, vol. 127, no. 15, pp. 154513–154520, 2007.
- [137] J. Mittal, J. R. Errington, and T. M. Truskett, “Does confining the hard-sphere fluid between hard walls change its average properties?,” *J. Chem. Phys.*, vol. 126, no. 24, pp. 244708–244715, 2007.
- [138] J. Mittal, T. M. Truskett, J. R. Errington, and G. Hummer, “Layering and Position-Dependent Diffusive Dynamics of Confined Fluids,” *Phys. Rev. Lett.*, vol. 100, no. 14, pp. 145901–145904, 2008.

- [139] I. Cohen, T. G. Mason, and D. A. Weitz, “Shear-Induced Configurations of Confined Colloidal Suspensions,” *Phys. Rev. Lett.*, vol. 93, no. 4, pp. 046001–046004, 2004.
- [140] K. To, P.-Y. Lai, and H. K. Pak, “Flow and jam of granular particles in a two-dimensional hopper,” *Physica A*, vol. 315, no. 1-2, pp. 174–180, 2002.
- [141] I. Zuriguel, L. A. Pugnaloni, A. Garcimartín, and D. Maza, “Jamming during the discharge of grains from a silo described as a percolating transition,” *Phys. Rev. E*, vol. 68, no. 3, pp. 030301–030304, 2003.
- [142] S. Redner and S. Datta, “Clogging Time of a Filter,” *Phys. Rev. Lett.*, vol. 84, no. 26, pp. 6018–6021, 2000.
- [143] S. B. Fuller, E. J. Wilhelm, and J. M. Jacobson, “Ink-jet printed nanoparticle microelectromechanical systems,” *J. Microelectromech. S.*, vol. 11, no. 1, pp. 54–60, 2002.
- [144] K. Sharp and R. Adrian, “On flow-blocking particle structures in microtubes,” *Microfluid. Nanofluid.*, vol. 1, no. 4, pp. 376–380, 2005.
- [145] G. M. Whitesides, “The origins and the future of microfluidics,” *Nature*, vol. 442, no. 7101, pp. 368–373, 2006.
- [146] D. M. Mueth, “Measurements of particle dynamics in slow, dense granular Couette flow,” *Phys. Rev. E*, vol. 67, no. 1, pp. 011304–4, 2003.
- [147] J. Ritvanen and P. Jalali, “On near-wall effects in hard disk packing between two concentric cylinders,” *Physica A*, vol. 387, no. 22, pp. 5381–5386, 2008.
- [148] S. Henkes, C. S. O’Hern, and B. Chakraborty, “Entropy and Temperature of a Static Granular Assembly: An Ab Initio Approach,” *Phys. Rev. Lett.*, vol. 99, no. 3, p. 038002, 2007.
- [149] D. Bi and B. Chakraborty, “Rheology of granular materials: dynamics in a stress landscape,” *Philosophical Transactions of the Royal Society A: Mathematical, Physical and Engineering Sciences*, vol. 367, no. 1909, pp. 5073–5090, 2009.

- [150] P. Chaudhuri, L. Berthier, and S. Sastry, “Jamming transitions in amorphous packings of frictionless spheres occur over a continuous range of volume fractions,” *Phys. Rev. Lett.*, vol. 104, no. 16, p. 165701, 2010.
- [151] N. Xu and E. S. C. Ching, “Effects of particle-size ratio on jamming of binary mixtures at zero temperature,” *Soft Matter*, vol. 6, no. 13, pp. 2944–2948, 2010.
- [152] L. E. Silbert and M. Silbert, “Long-wavelength structural anomalies in jammed systems,” *Phys. Rev. E*, vol. 80, no. 4, p. 041304, 2009.
- [153] G. Katgert and M. van Hecke, “Jamming and geometry of two-dimensional foams,” *Europhys. Lett.*, p. 34002, 2010.
- [154] D. Howell, R. P. Behringer, and C. Veje, “Stress Fluctuations in a 2D Granular Couette Experiment: A Continuous Transition,” *Phys. Rev. Lett.*, vol. 82, no. 26, pp. 5241–5244, 1999.
- [155] T. S. Majmudar and R. P. Behringer, “Contact force measurements and stress-induced anisotropy in granular materials,” *Nature*, vol. 435, no. 1079, pp. 1079–1082, 2005.
- [156] T. S. Majmudar, M. Sperl, S. Luding, and R. P. Behringer, “Jamming Transition in Granular Systems,” *Phys. Rev. Lett.*, vol. 98, no. 5, pp. 058001–058004, 2007.
- [157] J. Geng, D. Howell, E. Longhi, R. P. Behringer, G. Reydellet, L. Vanel, E. Clément, and S. Luding, “Footprints in Sand: The Response of a Granular Material to Local Perturbations,” *Phys. Rev. Lett.*, vol. 87, no. 3, pp. 035506–1–035506–4, 2001.
- [158] J. Brujic, S. Fedwards, I. Hopkinson, and H. Makse, “Measuring the distribution of interdroplet forces in a compressed emulsion system,” *Physica A*, vol. 327, no. 3-4, pp. 201–212, 2003.
- [159] J. Zhou, S. Long, Q. Wang, and A. D. Dinsmore, “Measurement of Forces Inside a Three-Dimensional Pile of Frictionless Droplets,” *Science*, vol. 312, no. 5780, pp. 1631–1633, 2006.

- [160] D. Fenistein, J. W. van de Meent, and M. van Hecke, “Universal and Wide Shear Zones in Granular Bulk Flow,” *Phys. Rev. Lett.*, vol. 92, no. 9, p. 094301, 2004.
- [161] R. Gutfraind, “Study of the origin of shear zones in quasi-static vertical chute flows by using discrete particle simulations,” *Mechanics of Materials*, vol. 24, no. 4, pp. 273–285, 1996.
- [162] G. Debrégeas, H. Tabuteau, and J. M. di Meglio, “Deformation and Flow of a Two-Dimensional Foam under Continuous Shear,” *Phys. Rev. Lett.*, vol. 87, no. 17, p. 178305, 2001.
- [163] G. Katgert, M. E. Möbius, and M. van Hecke, “Rate Dependence and Role of Disorder in Linearly Sheared Two-Dimensional Foams,” *Phys. Rev. Lett.*, vol. 101, no. 5, p. 058301, 2008.
- [164] Y. Wang, K. Krishan, and M. Dennin, “Impact of boundaries on velocity profiles in bubble rafts,” *Phys. Rev. E*, vol. 73, no. 3, p. 031401, 2006.
- [165] W. Losert, L. Bocquet, T. C. Lubensky, and J. P. Gollub, “Particle dynamics in sheared granular matter,” *Phys. Rev. Lett.*, vol. 85, no. 7, pp. 1428–1431, 2000.
- [166] D. Weaire, J. D. Barry, and S. Hutzler, “The continuum theory of shear localization in two-dimensional foam,” *J. Phys-Condens. Mat.*, vol. 22, no. 19, p. 193101, 2010.
- [167] M. Dennin and C. M. Knobler, “Experimental Studies of Bubble Dynamics in a Slowly Driven Monolayer Foam,” *Phys. Rev. Lett.*, vol. 78, no. 12, pp. 2485–2488, 1997.
- [168] M. Dennin, “Statistics of bubble rearrangements in a slowly sheared two-dimensional foam,” *Phys. Rev. E*, vol. 70, no. 4, p. 041406, 2004.
- [169] J. Lauridsen, G. Chanan, and M. Dennin, “Velocity Profiles in Slowly Sheared Bubble Rafts,” *Phys. Rev. Lett.*, vol. 93, no. 1, p. 018303, 2004.
- [170] C. Heussinger and J. L. Barrat, “Jamming transition as probed by quasistatic shear flow,” *Phys. Rev. Lett.*, vol. 102, no. 21, p. 218303, 2009.

- [171] C. Heussinger, P. Chaudhuri, and J.-L. Barrat, “Fluctuations and correlations during the shear flow of elastic particles near the jamming transition,” *Soft Matter*, vol. 6, no. 13, pp. 3050–3058, 2010.
- [172] B. Miller, C. O’Hern, and R. P. Behringer, “Stress Fluctuations for Continuously Sheared Granular Materials,” *Phys. Rev. Lett.*, vol. 77, no. 15, pp. 3110–3113, 1996.
- [173] P. Coussot, “Rheophysics of pastes: a review of microscopic modelling approaches,” *Soft Matter*, vol. 3, no. 5, pp. 528–540, 2007.
- [174] S. Tewari, D. Schiemann, D. J. Durian, C. M. Knobler, S. A. Langer, and A. J. Liu, “Statistics of shear-induced rearrangements in a two-dimensional model foam,” *Phys. Rev. E*, vol. 60, pp. 4385–4396, 1999.
- [175] A. Kabla and G. Debrégeas, “Local Stress Relaxation and Shear Banding in a Dry Foam under Shear,” *Phys. Rev. Lett.*, vol. 90, no. 25, p. 258303, 2003.
- [176] A. Gopal, “Shear-Induced Melting of an Aqueous Foam,” *J. Colloid Interface Sci.*, vol. 213, no. 1, pp. 169–178, 1999.
- [177] A. D. Gopal and D. J. Durian, “Nonlinear Bubble Dynamics in a Slowly Driven Foam,” *Phys. Rev. Lett.*, vol. 75, no. 13, pp. 2610–2613, 1995.
- [178] A. Kabla, J. Scheibert, and G. Debregeas, “Quasi-static rheology of foams. Part 2. Continuous shear flow,” *J. Fluid Mech.*, vol. 587, no. -1, pp. 45–72, 2007.
- [179] G. Hill, S. Yeung, and S. A. Koehler, “Scaling vertical drag forces in granular media,” *Europhys. Lett.*, vol. 72, no. 1, pp. 137–143, 2005.
- [180] M. Schröter, S. Nägle, C. Radin, and H. L. Swinney, “Phase transition in a static granular system,” *Europhys. Lett.*, vol. 78, no. 4, p. 44004, 2007.
- [181] M. B. Stone, R. Barry, D. P. Bernstein, M. D. Pelc, Y. K. Tsui, and P. Schiffer, “Local jamming via penetration of a granular medium,” *Phys. Rev. E*, vol. 70, no. 4, p. 041301, 2004.

- [182] J. Geng and R. P. Behringer, “Slow drag in two-dimensional granular media,” *Phys. Rev. E*, vol. 71, p. 011302, 2005.
- [183] G. Katgert, A. Latka, M. E. Möbius, and M. van Hecke, “Flow in linearly sheared two-dimensional foams: From bubble to bulk scale,” *Phys. Rev. E*, vol. 79, no. 6, p. 066318, 2009.
- [184] M. L. Falk and J. S. Langer, “Dynamics of viscoplastic deformation in amorphous solids,” *Phys. Rev. E*, vol. 57, no. 6, pp. 7192–7205, 1998.
- [185] B. Utter and R. P. Behringer, “Experimental measures of affine and nonaffine deformation in granular shear,” *Phys. Rev. Lett.*, vol. 100, no. 20, p. 208302, 2008.
- [186] P. Sollich, F. Lequeux, P. Hébraud, and M. E. Cates, “Rheology of soft glassy materials,” *Phys. Rev. Lett.*, vol. 78, no. 10, pp. 2020–2023, 1997.
- [187] S. M. Fielding, M. E. Cates, and P. Sollich, “Shear banding, aging and noise dynamics in soft glassy materials,” *Soft Matter*, vol. 5, no. 12, pp. 2378–2382, 2009.
- [188] G. Picard, A. Ajdari, F. Lequeux, and L. Bocquet, “Elastic consequences of a single plastic event: A step towards the microscopic modeling of the flow of yield stress fluids,” *Eur. Phys. J. E*, vol. 15, no. 4, pp. 371–381, 2004.
- [189] G. Picard, A. Ajdari, F. Lequeux, and L. Bocquet, “Slow flows of yield stress fluids: Complex spatiotemporal behavior within a simple elastoplastic model,” *Phys. Rev. E*, vol. 71, no. 1, p. 010501, 2005.
- [190] A. Argon and H. Kuo, “Plastic flow in a disordered bubble raft (an analog of a metallic glass),” *Materials Science and Engineering*, vol. 39, no. 1, pp. 101–109, 1979.
- [191] G. Adam and J. H. Gibbs, “On the temperature dependence of cooperative relaxation properties in glass-forming liquids,” *J. Chem. Phys.*, vol. 43, no. 1, pp. 139–146, 1965.
- [192] M. D. Ediger, “Spatially heterogeneous dynamics in supercooled liquids,” *Annu. Rev. Phys. Chem.*, vol. 51, no. 1, pp. 99–128, 2000.

- [193] R. Richert, “Heterogeneous dynamics in liquids: fluctuations in space and time,” *J. Phys-Condens. Mat.*, vol. 14, no. 23, pp. R703–R738, 2002.
- [194] J. Zhu, M. Li, R. Rogers, W. Meyer, R. H. Ottewill, Sts-73, W. B. Russel, and P. M. Chaikin, “Crystallization of hard-sphere colloids in microgravity,” *Nature*, vol. 387, no. 6636, pp. 883–885, 1997.
- [195] U. Gasser, E. R. Weeks, A. Schofield, P. N. Pusey, and D. A. Weitz, “Real-space imaging of nucleation and growth in colloidal crystallization,” *Science*, vol. 292, no. 5515, pp. 258–262, 2001.
- [196] J. M. Lynch, G. C. Cianci, and E. R. Weeks, “Dynamics and structure of an aging binary colloidal glass,” *Phys. Rev. E*, vol. 78, no. 3, p. 031410, 2008.
- [197] V. Prasad, D. Semwogerere, and E. R. Weeks, “Confocal microscopy of colloids,” *J. Phys-Condens. Mat.*, vol. 19, no. 11, p. 113102, 2007.
- [198] N. Lacey, F. W. Starr, T. B. Schröder, and S. C. Glotzer, “Spatially heterogeneous dynamics investigated via a time-dependent four-point density correlation function,” *J. Chem. Phys.*, vol. 119, pp. 7372–7387, 2003.
- [199] A. S. Keys, A. R. Abate, S. C. Glotzer, and D. J. Durian, “Measurement of growing dynamical length scales and prediction of the jamming transition in a granular material,” *Nature Physics*, vol. 3, no. 4, pp. 260–264, 2007.
- [200] T. Narumi, S. V. Franklin, K. W. Desmond, M. Tokuyama, and E. R. Weeks, “Spatial and temporal dynamical heterogeneities approaching the binary colloidal glass transition,” *Soft Matter*, vol. 7, no. 4, pp. 1472–1482, 2011.
- [201] J. C. Crocker and D. G. Grier, “Methods of digital video microscopy for colloidal studies,” *J. Colloid Interface Sci.*, vol. 179, no. 1, pp. 298–310, 1996.
- [202] E. Rabani, D. J. Gezelter, and B. J. Berne, “Calculating the hopping rate for self-diffusion on rough potential energy surfaces: Cage correlations,” *J. Chem. Phys.*, vol. 107, no. 17, pp. 6867–6876, 1997.

- [203] B. Doliwa and A. Heuer, “Cage effect, local anisotropies, and dynamic heterogeneities at the glass transition: A computer study of hard spheres,” *Phys. Rev. Lett.*, vol. 80, no. 22, pp. 4915–4918, 1998.
- [204] A. Kasper, E. Bartsch, and H. Sillescu, “Self-diffusion in concentrated colloid suspensions studied by digital video microscopy of coreshell tracer particles,” *Langmuir*, vol. 14, no. 18, pp. 5004–5010, 1998.
- [205] E. R. Weeks and D. A. Weitz, “Properties of cage rearrangements observed near the colloidal glass transition,” *Phys. Rev. Lett.*, vol. 89, no. 9, p. 095704, 2002.
- [206] E. R. Weeks and D. A. Weitz, “Subdiffusion and the cage effect studied near the colloidal glass transition,” *Chemical Physics*, vol. 284, no. 1-2, pp. 361–367, 2002.
- [207] P. M. Reis, R. A. Ingale, and M. D. Shattuck, “Caging dynamics in a granular fluid,” *Phys. Rev. Lett.*, vol. 98, no. 18, p. 188301, 2007.
- [208] E. R. Weeks, J. C. Crocker, and D. A. Weitz, “Short- and long-range correlated motion observed in colloidal glasses and liquids,” *J. Phys-Condens. Mat.*, vol. 19, no. 20, p. 205131, 2007.
- [209] P. Sarangapani, J. Zhao, and Y. Zhu, “How does sensitivity to dynamical heterogeneity in supercooled colloidal liquids depend on tracer size?,” *J. Chem. Phys.*, vol. 129, no. 10, p. 104514, 2008.
- [210] A. Einstein, “On the movement of small particles suspended in a stationary liquid demanded by the molecular-kinetic theory of heat,” *Annalen der Physik (Leipzig)*, vol. 17, pp. 549–560, 1905.
- [211] W. Sutherland, “A dynamical theory of diffusion for non-electrolytes and the molecular mass of albumin,” *Philosophical Magazine*, vol. 9, pp. 781–785, 1905.
- [212] L. Berthier, G. Biroli, J. P. Bouchaud, W. Kob, K. Miyazaki, and D. R. Reichman, “Spontaneous and induced dynamic fluctuations in glass formers. i. general results and dependence on ensemble and dynamics,” *J. Chem. Phys.*, vol. 126, no. 18, p. 184503, 2007.

- [213] L. Berthier, G. Biroli, J. P. Bouchaud, W. Kob, K. Miyazaki, and D. R. Reichman, “Spontaneous and induced dynamic correlations in glass formers. ii. model calculations and comparison to numerical simulations,” *J. Chem. Phys.*, vol. 126, no. 18, p. 184504, 2007.
- [214] A. E. R. Westman and H. R. Hugill, “The packing of particles,” *J. Am. Ceram. Soc.*, vol. 13, no. 10, pp. 767–779, 1930.
- [215] H. E. White and S. F. Walton, “Particle packing and particle shape*,” *J. Am. Ceram. Soc.*, vol. 20, no. 1-12, pp. 155–166, 1937.
- [216] A. H. Boerdijk, “Some remarks concerning close-packing of equal spheres,” *Philips Research Rep.*, vol. 7, no. 4, pp. 303–313, 1952.
- [217] D. G. Scott, “Packing of Spheres: Packing of Equal Spheres,” *Nature*, vol. 188, pp. 908–909, 1960.
- [218] C. S. O’Hern, L. E. Silbert, A. J. Liu, and S. R. Nagel, “Reply to ‘Comment on “Jamming at zero temperature and zero applied stress: The epitome of disorder” ’,” *Phys. Rev. E*, vol. 70, no. 4, pp. 043302–043304, 2004.
- [219] R. L. Brown and P. G. W. Hawksley, “Packing of Regular (Spherical) and Irregular Particles,” *Nature*, vol. 156, pp. 421–422, 1945.
- [220] H. S. Leftwich, “Packing of Regular (Spherical) and Irregular Particles,” *Nature*, vol. 156, p. 753, 1945.
- [221] A. Donev, I. Cisse, D. Sachs, E. A. Variano, F. H. Stillinger, R. Connelly, S. Torquato, and P. M. Chaikin, “Improving the Density of Jammed Disordered Packings Using Ellipsoids,” *Science*, vol. 303, no. 5660, pp. 990–993, 2004.
- [222] K. Desmond and S. V. Franklin, “Jamming of three-dimensional prolate granular materials,” *Phys. Rev. E*, vol. 73, no. 3, pp. 031306–031310, 2006.
- [223] Y. Jiao, F. H. Stillinger, and S. Torquato, “Optimal Packings of Superdisks and the Role of Symmetry,” *Phys. Rev. Lett.*, vol. 100, no. 24, pp. 245504–245507, 2008.

- [224] L.-W. Teng, P.-S. Tu, and I. Lin, “Microscopic Observation of Confinement-Induced Layering and Slow Dynamics of Dusty-Plasma Liquids in Narrow Channels,” *Phys. Rev. Lett.*, vol. 90, no. 24, pp. 245004–245007, 2003.
- [225] C. Murray, “Phases of thin colloidal layers,” *MRS Bulletin*, vol. 23, no. 10, pp. 33–38, 1998.
- [226] Z. T. Németh and H. Löwen, “Freezing and glass transition of hard spheres in cavities,” *Phys. Rev. E*, vol. 59, no. 6, pp. 6824–6829, 1999.
- [227] D. Morineau, Y. Xia, and C. A. Simionescu, “Finite-size and surface effects on the glass transition of liquid toluene confined in cylindrical mesopores,” *J. Chem. Phys.*, vol. 117, no. 19, pp. 8966–8972, 2002.
- [228] J. Schüller, Y. Mel’nikenko, R. Richert, and E. W. Fischer, “Dielectric Studies of the Glass Transition in Porous Media,” *Phys. Rev. Lett.*, vol. 73, no. 16, pp. 2224–2227, 1994.
- [229] C. L. Jackson and G. B. McKenna, “The glass transition of organic liquids confined to small pores,” *J. Non-cryst. Solids*, vol. 131-133, no. Part 1, pp. 221–224, 1991.
- [230] K. Kim and R. Yamamoto, “Apparent finite-size effects in the dynamics of supercooled liquids,” *Phys. Rev. E*, vol. 61, no. 1, pp. R41–R44, 2000.
- [231] P. A. Thompson, G. S. Grest, and M. O. Robbins, “Phase transitions and universal dynamics in confined films,” *Phys. Rev. Lett.*, vol. 68, no. 23, pp. 3448–3451, 1992.
- [232] P. Scheidler, W. Kob, K. Binder, and G. Parisi, “Growing length scales in a supercooled liquid close to an interface,” *Philos. Mag. A*, vol. 82, no. 3, pp. 283–290, 2002.
- [233] F. He, L. M. Wang, and R. Richert, “Confined viscous liquids: Interfacial versus finite size effects,” *Eur. Phys. J Special Topics*, vol. 141, no. 1, pp. 3–9, 2007.
- [234] N. Xu, J. Blawdziewicz, and C. S. O’Hern, “Random close packing revisited: Ways to pack frictionless disks,” *Phys. Rev. E*, vol. 71, no. 6, pp. 061306–061314, 2005.

- [235] A. S. Clarke and J. D. Wiley, “Numerical simulation of the dense random packing of a binary mixture of hard spheres: Amorphous metals,” *Phys. Rev. B*, vol. 35, no. 14, pp. 7350–7356, 1987.
- [236] M. Matsumoto and T. Nishimura, “Mersenne twister: a 623-dimensionally equidistributed uniform pseudo-random number generator,” *ACM Trans. Model. Comput. Simul.*, vol. 8, no. 1, pp. 3–30, 1998.
- [237] J. Nocedal and S. J. Wright, *Numerical Optimization*. Springer, 1999.
- [238] A. Donev, S. Torquato, F. H. Stillinger, and R. Connelly, “Comment on ‘Jamming at zero temperature and zero applied stress: The epitome of disorder’,” *Phys. Rev. E*, vol. 70, no. 4, pp. 043301–043304, 2004.
- [239] A. H. Marcus and S. A. Rice, “Observations of First-Order Liquid-to-Hexatic and Hexatic-to-Solid Phase Transitions in a Confined Colloid Suspension,” *Phys. Rev. Lett.*, vol. 77, no. 12, pp. 2577–2580, 1996.
- [240] P. J. Steinhardt, D. R. Nelson, and M. Ronchetti, “Bond-orientational order in liquids and glasses,” *Phys. Rev. B*, vol. 28, no. 2, pp. 784–805, 1983.
- [241] F. Aurenhammer, “Power diagrams: properties, algorithms and applications,” *SIAM J. Comput.*, vol. 16, no. 1, pp. 78–96, 1987.
- [242] A. Okabe, B. Boots, K. Sugihara, and S. N. Chiu, *Spatial Tessellations: Concepts and Applications of Voronoi Diagram*. Wiley, 2 ed., 2000.
- [243] A. Caboussat and R. Glowinski, “Modeling and computation of the shape of a compressed axisymmetric gas bubble,” *Journal of Numerical Mathematics*, vol. 16, no. 2, pp. 107–117, 2008.
- [244] P. Poulin and J. Bibette, “Adhesion of Water Droplets in Organic Solvent,” *Langmuir*, vol. 14, no. 22, pp. 6341–6343, 1998.
- [245] F. Leal-Calderon, V. Schmitt, and J. Bibette, *Emulsion Science: Basic Principles*. Springer, 2 ed., 2007.

- [246] H. Princen, “Highly concentrated emulsions. I. Cylindrical systems,” *J. Colloid Interface Sci.*, vol. 71, no. 1, pp. 55–66, 1979.
- [247] H. Princen, “Highly concentrated emulsions. II. Real systems. The effect of film thickness and contact angle on the volume fraction in creamed emulsions,” *J. Colloid Interface Sci.*, vol. 75, no. 1, pp. 246–270, 1980.
- [248] H. Princen, “Rheology of foams and highly concentrated emulsions i. elastic properties and yield stress of a cylindrical model system,” *J. Colloid Interface Sci.*, vol. 91, no. 1, pp. 160–175, 1983.
- [249] J. Zhou, *Contact Forces and Angles in Disordered Materials*. PhD thesis, University of Massachusetts, Amherst, 2008.
- [250] O. Pouliquen, M. Belzons, and M. Nicolas, “Fluctuating Particle Motion during Shear Induced Granular Compaction,” *Phys. Rev. Lett.*, vol. 91, p. 014301, 2003.
- [251] J. C. Lagarias, J. A. Reeds, M. H. Wright, and P. E. Wright, “Convergence Properties of the Nelder–Mead Simplex Method in Low Dimensions,” *SIAM Journal on Optimization*, vol. 9, no. 1, pp. 112–147, 1998.
- [252] A. O. N. Siemens and M. van Hecke, “Jamming: A simple introduction,” *Physica A*, vol. 389, no. 20, pp. 4255–4264, 2010.
- [253] C. S. O’Hern, S. A. Langer, A. J. Liu, and S. R. Nagel, “Random Packings of Frictionless Particles,” *Phys. Rev. Lett.*, vol. 88, no. 7, pp. 075507–075510, 2002.
- [254] L. Silbert, G. Grest, and J. Landry, “Statistics of the contact network in frictional and frictionless granular packings,” *Phys. Rev. E*, vol. 66, no. 6, p. 061303, 2002.
- [255] L. E. Silbert, “Jamming of frictional spheres and random loose packing,” *Soft Matter*, vol. 6, no. 13, pp. 2918–2924, 2010.
- [256] E. Pratt and M. Dennin, “Nonlinear stress and fluctuation dynamics of sheared disordered wet foam,” *Phys. Rev. E*, vol. 67, no. 5, p. 051402, 2003.

- [257] C. Gilbreth, S. Sullivan, and M. Dennin, “Flow transitions in two-dimensional foams,” *Phys. Rev. E*, vol. 74, no. 5, p. 051406, 2006.
- [258] M. Twardos, M. Dennin, M. Twardos, and M. Dennin, “Slow steady-shear of plastic bead rafts,” *Granular Matter*, vol. 7, no. 2, pp. 91–96, 2005.
- [259] M. Twardos and M. Dennin, “Asymmetric Response of a Jammed Plastic Bead Raft,” *Phys. Rev. Lett.*, vol. 97, no. 11, p. 110601, 2006.
- [260] Liu, S. R. Nagel, D. A. Schecter, S. N. Coppersmith, S. Majumdar, O. Narayan, and T. A. Witten, “Force Fluctuations in Bead Packs,” *Science*, vol. 269, no. 5223, pp. 513–515, 1995.
- [261] M. E. Cates, J. P. Wittmer, J. P. Bouchaud, and P. Claudin, “Jamming and static stress transmission in granular materials,” *Chaos*, vol. 9, no. 3, pp. 511–522, 1999.
- [262] D. W. Howell, R. P. Behringer, and C. T. Veje, “Fluctuations in granular media,” *Chaos*, vol. 9, no. 3, pp. 559–572, 1999.
- [263] Q.-C. Sun and S.-Y. Ji, “A Pair Correlation Function Characterizing the Anisotropy of Force Networks,” *Chinese Phys. Lett.*, vol. 28, no. 6, p. 064501, 2011.
- [264] A. Tordesillas, “Force chain buckling, unjamming transitions and shear banding in dense granular assemblies,” *Philos. Mag.*, vol. 87, no. 32, pp. 4987–5016, 2007.
- [265] S. N. Coppersmith, C. H. Liu, S. Majumdar, O. Narayan, and T. A. Witten, “Model for force fluctuations in bead packs,” *Phys. Rev. E*, vol. 53, no. 5, pp. 4673–4685, 1996.
- [266] M. Otto, J. P. Bouchaud, P. Claudin, and J. E. S. Socolar, “Anisotropy in granular media: Classical elasticity and directed-force chain network,” *Phys. Rev. E*, vol. 67, p. 031302, 2003.
- [267] F. Radjai, M. Jean, J. J. Moreau, and S. Roux, “Force distributions in dense two-dimensional granular systems,” *Phys. Rev. Lett.*, vol. 77, no. 2, pp. 274–277, 1996.

- [268] C. Thornton, “Force transmission in granular media,” *KONA Powder and Particle*, vol. 15, pp. 81–90, 1997.
- [269] C. S. O’Hern, S. A. Langer, A. J. Liu, and S. R. Nagel, “Force Distributions near Jamming and Glass Transitions,” *Phys. Rev. Lett.*, vol. 86, no. 1, pp. 111–114, 2001.
- [270] J. H. Snoeijer, T. J. H. Vlugt, M. van Hecke, and W. van Saarloos, “Force Network Ensemble: A New Approach to Static Granular Matter,” *Phys. Rev. Lett.*, vol. 92, no. 5, p. 054302, 2004.
- [271] B. P. Tighe, A. R. T. van Eerd, and T. J. H. Vlugt, “Entropy Maximization in the Force Network Ensemble for Granular Solids,” *Phys. Rev. Lett.*, vol. 100, no. 23, p. 238001, 2008.
- [272] J. Zhou and A. D. Dinsmore, “A statistical model of contacts and forces in random granular media,” *J Stat Mech-Theory E*, vol. 2009, no. 05, p. L05001, 2009.
- [273] B. Chakraborty, “Statistical ensemble approach to stress transmission in granular packings,” *Soft Matter*, vol. 6, no. 13, pp. 2884–2893, 2010.
- [274] P. Claudin, J. P. Bouchaud, M. E. Cates, and J. P. Wittmer, “Models of stress fluctuations in granular media,” *Phys. Rev. E*, vol. 57, pp. 4441–4457, 1998.
- [275] S. Edwards and C. Mounfield, “A theoretical model for the stress distribution in granular matter. I. Basic equations,” *Physica A*, vol. 226, no. 1-2, pp. 1–11, 1996.
- [276] J. Brujic, S. F. Edwards, D. V. Grinev, I. Hopkinson, D. Brujic, and H. A. Makse, “3D bulk measurements of the force distribution in a compressed emulsion system,” *Faraday Disc.*, vol. 123, pp. 207–220, 2003.
- [277] R. Shah, H. Shum, A. Rowat, D. Lee, J. Agresti, A. Utada, L. Chu, J. Kim, A. Fernandeznieves, and C. Martinez, “Designer emulsions using microfluidics,” *Materials Today*, vol. 11, no. 4, pp. 18–27, 2008.
- [278] K. W. Desmond and E. R. Weeks, “Random close packing of disks and spheres in confined geometries,” *Phys. Rev. E*, vol. 80, no. 5, p. 051305, 2009.

- [279] M. P. Allen and D. J. Tildesley, *Computer Simulation of Liquids*. Oxford University Press, USA, 1989.
- [280] M. Toiya, J. Stambaugh, and W. Losert, “Transient and Oscillatory Granular Shear Flow,” *Phys. Rev. Lett.*, vol. 93, no. 8, p. 088001, 2004.
- [281] J. F. Peters, M. Muthuswamy, J. Wibowo, and A. Tordesillas, “Characterization of force chains in granular material,” *Phys. Rev. E*, vol. 72, p. 041307, 2005.
- [282] V. Prasad, D. Semwogerere, and E. R. Weeks, “Confocal microscopy of colloids,” *J. Phys-Condens. Mat.*, vol. 19, no. 11, p. 113102, 2007.
- [283] E. Gardel, E. Sitaridou, K. Facto, E. Keene, K. Hattam, N. Easwar, and N. Menon, “Dynamical fluctuations in dense granular flows,” *Phil. Trans. R. Soc. A*, vol. 367, no. 1909, pp. 5109–5121, 2009.
- [284] E. Lerner and I. Procaccia, “Locality and nonlocality in elastoplastic responses of amorphous solids,” *Phys. Rev. E*, vol. 79, p. 066109, 2009.
- [285] F. da Cruz, S. Emam, M. Prochnow, J. N. Roux, and F. Chevoir, “Rheophysics of dense granular materials: Discrete simulation of plane shear flows,” *Phys. Rev. E*, vol. 72, no. 2, p. 021309, 2005.